Charge Carrier Recombination Dynamics in Hybrid Metal Halide Perovskite Solar Cells

Dissertation zur Erlangung des
naturwissenschaftlichen Doktorgrades
der Julius-Maximilians-Universität Würzburg

15 83

vorgelegt von

David Kiermasch

aus Pleß, Polen

Würzburg 2020

Eingereicht am: 19.03.2020
bei der Fakultät für Physik und Astronomie

1. Gutachter: Prof. Dr. Vladimir Dyakonov
2. Gutachter: Prof. Dr. Christian Schneider
3. Gutachter:
der Dissertation

Vorsitzende(r):
1. Gutachter: Prof. Dr. Vladimir Dyakonov
2. Gutachter: Prof. Dr. Christian Schneider
3. Gutachter: Prof. Dr. Karl Mannheim
im Promotionskolloquium

Tag des Promotionskolloquiums: 15.07.2020
Doktorurkunde ausgehändigt am:

Contents

1. Introduction

The Need for Renewable Energy Sources

There is conclusive evidence that the increase in the Earth's temperature and the fast disappearance of snow and ice over the past decades are largely caused by the human influence on the greenhouse effect, which describes the atmosphere's ability to trap the emitted radiation from the planet's surface. The industrial revolution in combination with the population growth caused a dramatic rise of greenhouse gases like carbon dioxide (CO_2), methane (CH_4) and nitrous oxide (N_2O) over the last centuries. For example, the CO_2 concentration in the atmosphere has increased by more than 40 % from 280 ppm to 400 ppm since 1850.[1] These gases absorb energy in the infrared range of the electromagnetic spectrum and therefore have a huge impact on the observed global warming by intensifying the greenhouse effect. To counteract this process and limit the anthropogenic temperature increase to a maximum of 2 °C on average above pre-industrial levels, 197 nations negotiated an arrangement at the United Nations Climate Change Conference 2015.[2] To this date, more than 180 parties have already ratified to the so-called *Paris Agreement*.[3] To reach the goal of a maximum temperature increase of 2 °C, net zero CO_2 emissions until 2060 to 2070 are required.[4] It has been even suggested that the mean average should be limited to a lower value of 1.5 °C in order to reduce the climate-related risks for nature and mankind.[5] Calculations revealed that the existing energy infrastructure will exceed the remaining carbon budget for the 1.5 °C target if operated as historically. More than half of these emissions originate from fossil fuel-burning power plants,[6] which illustrates that the expansion of power plants based on renewable and environmental friendly energy sources will be of central importance for the civilization in the coming decades. Many nations are already focusing on increasing the contribution of renewable energy sources to power generation. In 2018, almost 35 % of the total power generation in Germany was produced by renewable energy sources. Out of these renewables, photovoltaic (PV) installations are among the largest clean energy sources with a market share of 20.5 %.[7] PV systems have great advantages over other energy sources such as direct access to sunlight over the entire Earth. The utilization of sunlight would easily cover the world's energy demand, which explains the intensified research on solar cells in recent decades.

Generations of Photovoltaic Devices

Today, the PV market is almost exclusively dominated by silicon (Si) as a photoactive layer. Solar cells of this type can be manufactured from silicon of different degrees of crystallinity. Under laboratory conditions, monocrystalline devices can reach power conversion efficiencies (PCEs) up to 26.3 %,[8] while polycrystalline silicon has a slightly lower record PCE of 21.9 %[9] due to losses at grain boundaries. Despite the lower efficiency, the majority of installed PV systems are polycrystalline.[10] As a consequence of long research activities and improved economies of scale, the dominance of Si-based solar systems can be explained by the rapid decline in prices over the previous decades.[11]

Nevertheless, research is also focused on other material systems and technologies as illustrated in Figure 1.1. While crystalline silicon solar cells belong to the 1st generation of PVs, the 2nd generation can be described as a thin-film technology since the active layer thickness of these devices is reduced from hundreds to a few micrometers. Well-known representatives of this generation include cadmium telluride (CdTe), gallium arsenide (GaAs) and copper indium gallium (di)selenide (CIGS). Although GaAs cells are expensive which is one of the main reasons why they are not widely used, they currently hold the world record in efficiency for a single-junction solar cell at 29.1 %.[11] Latest solar cell concepts are partially based on even thinner active layers in the range of a few hundred nanometers composed of organic or hybrid organic-inorganic materials. These devices are referred to as 3rd generation solar cells. The pioneers of this generation were the so-called dye-sensitized solar cells (DSSCs) and organic photovoltaics (OPVs). The former were introduced in 1991 by O'Regan and Graetzel by combining titanium dioxide (TiO_2) with a charge-transfer dye to sensitize the light harvesting layer.[12] Although research on organic semiconductors has been going on for many years, a major breakthrough for OPVs was the combination of two organic films leading to an acceptor-donor interface which paved the way to efficient organic solar cells.[13] Over the past decades, fullerenes and their derivates have been predominantly used as electron acceptor materials for organic solar cells. Very recently, fullerene-free acceptors with higher absorption coefficients have been proposed to increase the device performance.[14,15] With these newly synthesized acceptor materials, state-of-the-art OPVs can reach efficiencies of more than 15 %.[16]

Another technology that is part of the 3rd generation of PVs are perovskite solar cells. Since the first use of a perovskite absorber in 2009,[17] solar cell research was dominated by this class of semiconductors. Starting with a PCE of 3.8 % in a DSSC configuration, the efficiency quickly climbed to 10 % in the following years when the liquid electrolyte was replaced by a solid-state transport layer.[18,19] Further improvements in

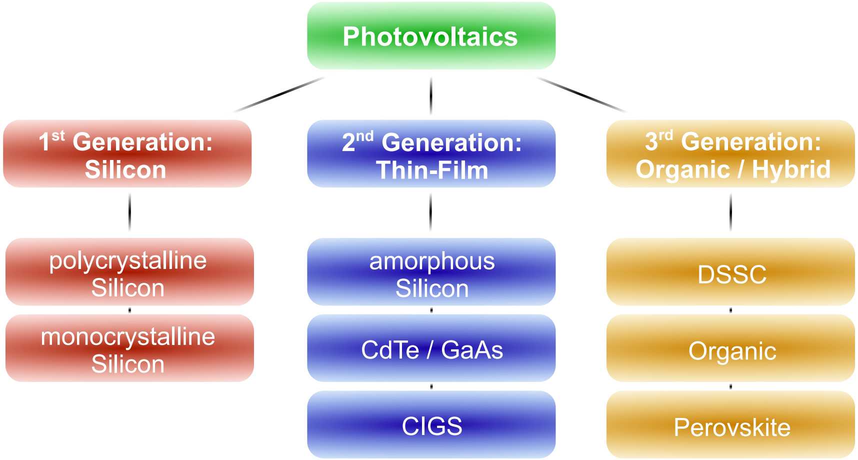

Figure 1.1.: Three generations of existing PV technologies.

material composition, the introduction of new device configurations with novel transport/interface layers and optimizations in the film formation led to a current record PCE of 25.2 %.[20] Within only ten years of intensive research, the efficiency of these devices has improved faster than ever before in the history of PVs. Despite the great attention paid to this technology, there are still many unsolved problems. The solar cells still suffer from a deficiency in long-term stability and also the use of toxic materials should be minimized. More importantly, the understanding of the basic physical properties and working principles of these devices is still largely missing and prevents further rise in efficiency. As a recent study emphasized, the greatest potential for further PCE improvements is to minimize charge carrier recombination losses.[21] However, carrier dynamics are – so far – mostly studied on pure films, whereas very little is known about recombination processes in fully operational devices as it is not straightforward to address this fundamental topic. This can be explained by the fact that solar cells are complicated devices composed of a multitude of different layers complicating the application and interpretation of the experimental methods.

Outline of the Thesis

The aim of this thesis is to contribute to a better understanding of recombination losses in fully working perovskite solar cells and the experimental techniques which are applied to determine these losses. Chapter 2 focuses on introducing the class of lead halide perovskite semiconductors and their application in PV devices. Chapter 3 addresses the main charge carrier recombination mechanisms and provides physical background for the interpretation of the herein performed measurements. The experimental background on the preparation of perovskite solar cells, the used materials and the measurement methods are summarized in Chapter 4. The main experimental results are then divided into four individual and separate studies. Chapter 5 sheds a light on the experimental techniques and provides new insights for the interpretation of the results obtained by these methods. Based on these findings, recombination dynamics under operating conditions are identified in perovskite solar cells in Chapter 6 by varying the absorber thickness. With the aim of reducing charge carrier losses, Chapter 7 investigates the impact of post-annealing on the performance and the recombination kinetics in vacuum deposited PV devices. Chapter 8 provides a detailed analysis on the commonly applied method of masking the active area during characterization of perovskite solar cells.

2. Hybrid Halide Perovskites for Photovoltaic Applications

This chapter provides a detailed overview on the material class of hybrid metal halide perovskites and their application as photoactive materials in solar cells. First, a short insight into the crystal structure is given and the precursor materials for perovskite synthesis are discussed. Afterwards the optoelectronic properties are described, which underline the suitability for PV applications. Finally, solar cells based on metal halide perovskites will be discussed in more detail including the device layout and current-voltage characterization.

2.1. Crystal Structure

The term 'perovskite' originally derives from the mineral calcium titanium oxide ($CaTiO_3$) discovered by the Prussian mineralogist Gustav Rose in 1839 in the Ural Mountains and named in honor of Lev A. Perowski.[22] Today's perovskites, which are implemented in solar cells have very little in common with that mineral except for their ABX_3 crystal stoichiometry. In case of photoactive absorbers, A is usually a large cation, B is a smaller metallic cation and X is an halogen anion. These metal halide perovskites were first described in 1893,[23] long before the solar cell was invented. As shown in Figure 2.1, the inorganic BX_3 sublattice is arranged in an octahedron and stabilized by the A-site cation which has to be small enough to fit in the interstices. During the intensive research over the last years, many different ion combinations have been identified for the use in optoelectronic applications. In most cases, lead or tin represent the B cation in the oxidation state +2 (Pb^{2+} or Sn^{2+}) at the body-center of a unit cell, while the face-centered X positions are halides such as I^-, Br^- or Cl^- which are arranged in an octahedron. Organic molecules like methylammonium ($CH_3NH_3^+$, abbreviated with MA^+) and formamidinium ($CH_5N_2^+$, abbreviated with FA^+) and inorganic atoms like Cs^+ can be located at the corner positions. The most popular compound, studied also in the first publication of a perovskite solar cell, is methylammonium lead iodide ($MAPbI_3$) which crystallizes in a tetragonal symmetry at room temperature where two

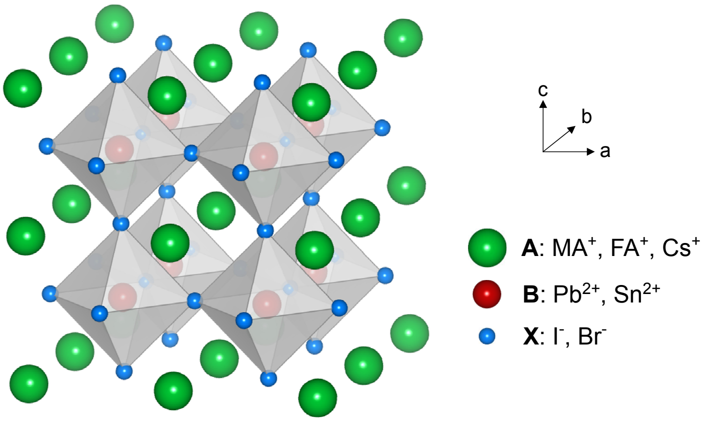

Figure 2.1.: Schematic illustration of the ABX_3 perovskite crystal structure. Inorganic BX_3 octahedra form a 3D lattice with the empty spaces being filled by the larger A cation. Widely used components for the preparation of PV devices are also listed, whereby the most frequently studied combination is $MAPbI_3$. In addition to the temperature, the choice of the materials determines the symmetry in which the perovskite is formed.

lattice constants a and b are of the same value and smaller than the third lattice constant c ($a = b = 8.86 Å < c = 12.66 Å$).[24] If $MAPbI_3$ is heated to over about 327 K degrees, a cubic crystal structure ($a = b = c = 6.33$ Å) is formed, while an orthorhombic crystal is present for temperatures below about 161 K ($a = 8.86$ Å, $b = 8.58$ Å, $c = 12.62$ Å).[25–29] While the cubic structure has the highest symmetry, both tetragonal and orthorhombic phases are formed by tilting the $PbI_6{}^{4-}$ octahedron around the c-axis resulting in a reduced symmetry.

In general, the crystal structure is not only a function of temperature but is strongly influenced by the radii of the individual ions. To predict the structure, distortion and stability of the crystal, the tolerance factor t

$$t = \frac{r_A + r_X}{\sqrt{2}(r_B + r_X)} \tag{2.1}$$

was proposed by Goldschmidt in the 1920s, where r_A, r_B and r_X are the radii of the A, B and X ions, respectively.[30] Most perovskites are characterized by a t value ranging from 0.7 to 1.1. To form a cubic crystal phase, t must be in the range of 0.9 - 1.0, while it takes lower values in the case of less symmetric lattice structures.[31] With $r_A = 0.180$ nm for the MA^+ cation, $r_B = 0.132$ nm for the Pb^{2+} cation and $r_X = 0.206$ nm for the I^- anion, t can be calculated to be 0.81 for $MAPbI_3$ in line with the tetragonal crystal phase at room temperature.[27] It is reported, that the tolerance factor is not sufficient enough to make reliable statements if a stable perovskite can be formed.[32]

Since the BX_6 octahedron defines the basic unit for the perovskite structure, the octahedral factor μ

$$\mu = \frac{r_B}{r_X} \tag{2.2}$$

was introduced as an additional criterion.[33] It usually takes values in the range of $0.44 < \mu < 0.89$ and reliably predicts, in combination with t, the formation of a perovskite lattice. If μ is smaller than 0.44, no BX_6 octahedron and consequently no perovskite structure can be formed. For $MAPbI_3$, $\mu = 0.54$ which verifies the stability of the compound.

Both the tolerance factor and the octahedral factor developed to widely used quantities in the material screening of new ions for the synthesis of light-absorbing perovskites. The successful story was triggered by the combination of different ions, such as the mixing of iodide and bromide in $MAPb(I_{1-x}Br_x)_3$.[34] In addition to the exchange of halides, many researchers tried to find new A-site cations as well. A major breakthrough was the alloying of MA^+ and FA^+ cations in $(FAPbI_3)_{1-x}(MAPbBr_3)_x$ stochiometries leading to the first reported efficiencies of around 20 %.[35–37] This material composition turned out to be also beneficial for the long-term stability, since it is reported for pure $FAPbI_3$ that two polymorphs with quite different material characteristics exist at room temperature: a black perovskite material and a yellow non-perovskite counterpart.[38] A reduction of the undesirable yellow phase impurities was enabled by the the introduction of Cs^+ into mixed cation/mixed halide perovskites.[39,40] Scientists have exploited the diversity of the periodic table even further and used additional elements in the synthesis such as the alkali metal ions Rb^+ or K^+. These ions are expected to be too small to form a stable perovskite crystal lattice if they are the only A-site cations in the system. Nevertheless, they can be incorporated into so-called quadruple cation perovskites which also include MA^+, FA^+ and Cs^+.[41,42] However, NMR studies suggest that only cesium may be integrated into the lattice, while the other smaller cations are not part of the crystalline framework.[43] With the aim of increasing the stability also larger organic cations like guanidinium ($CH_6N_3^+$) were added to $MAPbI_3$.[44] As the only A-site cation in the perovskite, they would yield a tolerance factor above 1 and the formation of a two-dimensional crystal lattice for which reason they can only be used in mixed perovskites. There are also great efforts to replace lead with less toxic or even non-toxic metals like tin or bismuth, but these have not been successful yet as the efficiencies are not yet adequate.[45,46] As a consequence of the compositional engineering during the last years, multi-cation perovskites comprising different halides are among the most stable and efficient perovskite solar cells so far.

2.2. Optoelectronic Properties

Before the first application in solar cells, perovskites were utilized in many different applications. For example, the class of oxide perovskites like barium titanate ($BaTiO_3$) are known for their ferroelectric, piezoelectric, dielelectric and pyroelectric characteristics.[47,48] Bednorz and Müller have also discovered superconducting properties at high temperatures in some perovskite compounds and were awarded the Nobel Prize for their work in 1987.[49] Although known since more than 100 years and extensively analyzed for magnetic, optical and electronic properties, the last decade has sparked an unprecedented interest in the family of perovskites.

Band Structure, Absorption and Charge Carrier Generation

The class of metal halide perovskites, where the commonly used oxide anions are replaced by halide anions shows semiconducting properties that are a precondition for PV applications. It is exclusively the anorganic ${PbI_6}^{4-}$ cage that leads to the formation of the valence and conduction bands (VB and CB, respectively) and an electronic band gap as it is schematically depicted in Figure 2.2a. The valence band maximum (VBM) consists of a Pb(6s) - I(5p) σ-antibonding (σ^*) orbital with the iodide orbital being the dominant one. The conduction band minimum (CBM) is composed of a Pb(6p) - I(5p) σ^* orbital, where most of the empty states originate from the lead.[50–52] This is in line with the formal electronic configuration of the ions in the lead iodide octaedron: $5d^{10}6s^2 6p^0$ for Pb^{2+} and $5p^6$ for I^-. The fully occupied $5p^6$ orbitals from the iodide are therefore relevant for the VBM, while empty $6p^0$ orbitals from the lead are dominant at the CBM.[53] This indicates that lead plays a central role for the optoelectronic properties and explains the difficulty of identifying high-performance lead-free alternatives. As the VBM and CBM are at the same position (Γ-point) of the first brilloin zone, $MAPbI_3$ is a direct semiconductor and features a band gap E_g of around 1.6 eV at room temperature.[24,54–56] However, there is a discussion going on whether the band gap is of direct-indirect nature since strong spin-orbit coupling could lead to Rashba splitting of the CB.[57,58] In contrast to the inorganic counterparts, the MA^+ cation does not contribute to the density of states (DOS) at the band edges, but creates deep states in the bands and thus primarily stabilizes the crystal and ensures charge neutrality.[51,52] However, calculations have revealed that molecular disorder and rotations of the organic cation can influence the band structure significantly and induce direct-indirect band gap fluctuations.[54,59,60] These rotations also affect the dielectric properties and might be responsible for the high dielectric constant of the material like suggested by several reports.[61,62] The degrees of rotational freedom of the MA^+

cation are only relevant for the tetragonal and cubic crystal phase but are restricted in the orthorhombic structure.[28]

The composition of the valence and conduction band also determines the optical absorption properties of lead halide perovskites. Figure 2.2b shows the absorption mechanisms for materials employed in first, second and third generation solar cells, namely i) Si, ii) GaAs and iii) $MAPbI_3$. According to Fermi's golden rule, the transition rate is determined by the transition matrix from states in the VB to states in the CB and the DOS in both bands. In comparison to Si, where band transitions require the assistance of phonons, $MAPbI_3$ possesses a transition probability that is two orders of magnitude larger since it is a direct semiconductor.[63] In contrast, calculations revealed no significant differences in the transition matrices of GaAs and $MAPbI_3$.[64] A closer look at the orbitals that form the VBM and CBM reveals large differences in the DOS of these two materials. While the VBs are mostly ruled by *p* orbitals in all compounds, different orbitals are dominant in the CBs. The GaAs CB is composed of *s* states, while the CB from the perovskite is derived from lead *p* orbitals. Since *p* states are less dispersive and have two additional atomic orbitals compared to *s* states, it can be concluded that the DOS of $MAPbI_3$ exceeds the DOS of GaAs as confirmed by calculations from Yin et al.[64,65] Benefiting from both the direct band gap and the *p* states in both the VB and CB, perovskites have higher absorption coefficients compared to the fully inorganic semiconductors which is indicated by the arrow thicknesses in Figure 2.2b.[64,66] As a direct consequence, thin perovskite layers in the range of a few hundred nanometers are sufficient to absorb enough light for highly efficient perovskite solar cells.

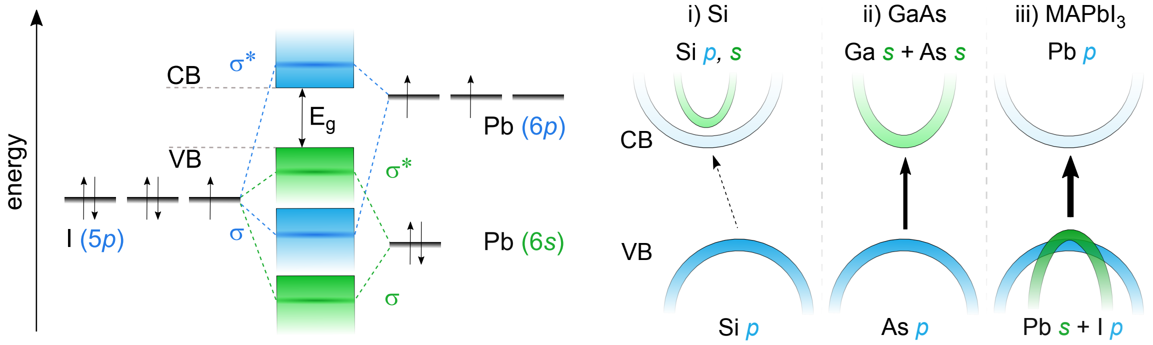

(a)

(b)

Figure 2.2.: **(a)** Simplified bonding diagramm of $MAPbI_3$ illustrating the formation of both the valence and conduction band. It is only the *s*- and *p*-orbitals of lead and iodine that are relevant while the MA^+ molecule does not lead to any states close to the VBM and CBM.[50,51] **(b)** Absorption schemes for i) Si, ii) GaAs and iii) $MAPbI_3$. As indicated by the black arrows, the perovskite has the strongest absorption due to the direct band gap and the *p* orbitals in the VB and CB.[65]

Another feature, perovskites are known for, are low exciton binding energies E_B. Depending on the E_B set by the Coulomb interaction, excitons can generally be classified into two different categories: the strongly bound Frenkel[67] excitons and the weakly bound Wannier-Mott[68] excitons whose radius exceeds the lattice spacing. First publications, conducted on $\mathrm{MAPbI_3}$ perovskites, revealed values for the binding energy in the range of $E_B = 37 - 50$ meV at 4.2 K pointing towards excitons of Wannier-Mott type.[69,70] As a result of intensified research over the last few years, lower energies in the range of $\approx 5 - 10$ meV were found in room temperature studies.[71–74] The observed values for E_B are typical for semiconductors with large dielectric constants and low effective carrier masses and are close to those reported for GaAs ($E_B \approx$ 4 meV).[74–76] As these binding energies are similar to the thermal energy ($k_B T \approx 25.7$ meV at $T = 300$ K), almost all photogenerated charge carriers are present as free charge carriers and are not bound as excitons as confirmed by theoretical and experimental studies.[77–79] The generation of free charge carriers upon photoexcitation is desirable for PV applications and in contrast to organic semiconductors, where low dielectric constants and large effective masses result in Frenkel excitons.[75] For this reason, the so-called bulk heterojunction layout[80,81] is required in OPVs to provide efficient exciton-dissociation via charge-transfer states.[82]

Charge Carrier Transport

The band structure also determines the effective mass m^* of electrons and holes and can be calculated via the relation

$$m^* = \hbar^2 \left[\frac{\partial^2 E(k)}{\partial k^2} \right]^{-1}, \tag{2.3}$$

where $E(k)$ is the energy dispersion relation with the wave vector k. The slopes at the VBM and CBM thus allow conclusions to be drawn regarding the weight of the effective masses: a flatter band is correlated with a larger effective mass and vice versa. Since the VB and CB of $\mathrm{MAPbI_3}$ are mostly dominated by p orbitals, m^* is quite similar for both types of charge carriers. The effective masses for electrons and holes in the range of $m^*_{e,h} \approx 0.1 - 0.2$ with respect to the electron mass m_0 were determined using different measurement methods[73,83] in line with predictions from density functional theory calculations.[84–86] However, this agreement can only be achieved if spin-orbit coupling is included in the calculations. The balanced effective masses in $\mathrm{MAPbI_3}$ result in an ambipolar conductivity which is beneficial for PV applications. In contrast, the effective masses of electrons ($m^*_e = 0.06\ m_0$) and holes ($m^*_h = 0.53\ m_0$) in GaAs differ significantly because the band bending is different in the VB and CB as it is a *p*-*s* type semiconductor (see Figure 2.2b).[63,87]

The most important parameter regarding charge transport is the charge carrier mobility μ. Several techniques have been employed to determine μ in lead halide perovskites which led to a wide range of reported values. Photoluminescence quenching (PLQ) measurements revealed mobilities in the range of $\mu \approx 1\,\text{cm}^2/(\text{Vs})$ for both electrons and holes in $MAPbI_3$.[88,89] Other contactless measurement methods, such as time-resolved microwave conductivity (TRMC) or time-resolved terahertz spectroscopy (TRTS), where usually the sum $\Sigma\mu$ of electron and hole mobilities is being probed, revealed values in the range of $20-70\,\text{cm}^2/(\text{Vs})$.[90–93] Even higher mobilities of more than $100\,\text{cm}^2/(\text{Vs})$ have been measured on single crystals using electrical measurement methods, like time-of-flight (TOF) or space charge limited current (SCLC).[94,95] This large range of reported values might be partially explained by different sample qualities and preparation methods of the studied perovskite films, but can also be attributed to the applied measurement techniques as the excitation intensities of steady-state and pulsed methods can vary significantly.[96] Furthermore, it is of importance whether the mobility is investigated locally within a crystal domain or long-range transport properties are measured. For example, the influence of grain boundaries on charge carrier transport is still being discussed and is not yet fully understood.[97,98] A recent study by Lim et al. has determined long-range charge carrier mobilities of $2\,\text{cm}^2/(\text{Vs})$ for polycrystalline $MAPbI_3$ films, which is lower compared to the already discussed values and indicates that these large mobilities describe short-range transport properties.[99] Although the mobilities for low temperature solution-processed materials (see Section 4.2) are considered to be high, they are rather small compared to other inorganic semiconductors such as Si or GaAs, where the electron mobility is in the range of $1500-8000\,\text{cm}^2/(\text{Vs})$.[87,100] In the simple drude picture, μ of a conductor depends only on m^*, the average scattering time of a charge carrier τ_{scat} and the elementary charge q of a charge carrier via the relation[101]

$$\mu = \frac{q \cdot \tau_{scat}}{m^*}. \tag{2.4}$$

Considering the similar values for the effective masses in perovskites and Si/GaAs, the low mobilities of $MAPbI_3$ have to result from a large variation of τ_{scat} and therefore different electron-phonon coupling. In principle, temperature-dependent measurements can reveal the nature of mobility limitations caused by scattering. Several studies found a power law of $\mu \propto T^{-1.5}$ leading to the conclusion that elastic scattering with acoustic phonons is the main limiting factor in the room temperature tetragonal phase.[91,102,103] In some cases even stronger temperature dependencies are reported.[104,105] In contrast, calculations have demonstrated that the coupling to acoustic phonons is rather weak and would limit the mobility to a few thousand $\mathrm{cm}^2/(\mathrm{Vs})$.[106,107] Recent studies concluded both experimentally[108] and theoretically[109] that scattering with longitudinal optical phonons associated with Fröhlich coupling is dominant at room temperature limiting the maximum achievable mobility to $30-80\ \mathrm{cm}^2/(\mathrm{Vs})$, which is in agreement with experimental results.[110] The theory of enhanced Fröhlich interactions is supported by the polar nature of Pb-I bond in MAPbI_3.[111] In line with this picture, Zheng et al. clarified that the formation of large polarons also plays an important role for charge carrier transport and decreases μ by a factor of two.[112] However, the temperature dependence of this scattering theory does not match with experimental results and is thus still under debate since scattering with polar optical phonons scales theoretically with $\mu \propto T^{-0.5}$.[104,113] Since the temperature dependence of mobility is typically ruled by a superimposition of different scattering processes, it is also suggested that non-conventional models should be used for the description of carrier charge transport in lead halide perovskites.[113,114]

Furthermore, the mobility as well as the charge carrier lifetime τ determine the diffusion length L_D which is defined as[115]

$$L_D = \sqrt{\frac{k_B T}{q}\mu\tau}. \tag{2.5}$$

Here, T is the temperature and k_B the Boltzmann constant. Considerations on charge carrier recombination and its impact on τ will be provided in Chapter 3. L_D specifies the mean free path length between the generation and recombination of a charge carrier in a semiconductor and is an important parameter, as it defines the optimal layer thickness of a solar cell. It is also considered to be a quality factor of a material since it comprises both the transport and recombination properties. The chronological evolution of the experimentally determined diffusion lengths for MAPbI_3 is shown in Figure 2.3, where the data is visualized with different colors depending on whether the value was determined on a film (blue) or a crystal (green). The diffusion length of a few nanometers in 2009 was increased by several orders of magnitude within a few years and now amounts to several hundred micrometers determined on single crystals.[95,116] Intensive optimization of the preparation and deposition methods of perovskites has allowed even polycrystalline films to have long diffusion lengths in the range of $\approx 10\ \mu\mathrm{m}$ and thus being close to single crystal quality.[92,117] Since state-of-the-art perovskite solar cells typically only have thin active layers of a few hundred nanometers, the high diffusion lengths allow for efficient charge carrier extraction.

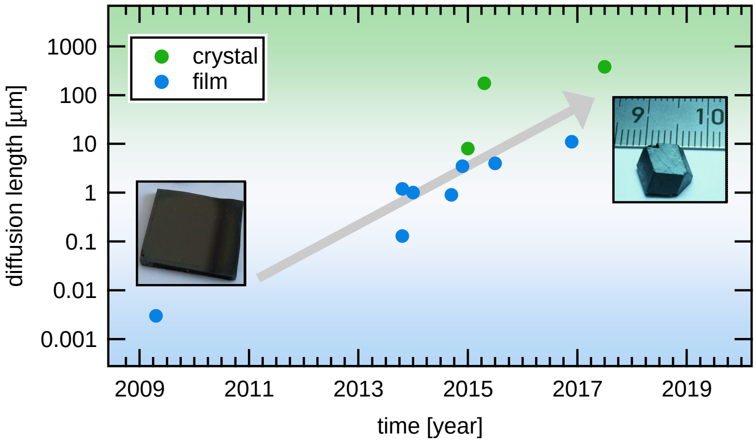

Figure 2.3.: Evolution of measured L_D values for $MAPbI_3$ in the last decade. Through process optimization, the diffusion length of the charge carriers in films (blue points) could be increased by several orders of magnitude. In addition, values determined on crystals (green points) are presented to show that the polycrystalline films are of almost single crystalline quality. Values are collected from the following References[17,88,89,92,95,115–120].

So far, mostly $MAPbI_3$ as the most representative absorber was discussed in this section. However, the exchange of individual ions can have a significant influence on the optoelectronic properties. Depending on the chemical composition, the band gap can be continuously tuned over a wide range. By replacing or intermixing I^- with Br^- or Cl^-, the band gap is increased to 2.33 eV for pure methylammonium lead bromide ($MAPbBr_3$) and 3.12 eV for methylammonium lead chloride ($MAPbCl_3$).[121,122] Other works have successfully substituted the A-site cation by Cs^+ (cesium lead iodide, $CsPbI_3$: E_g = 1.73 eV) or FA^+ (formamidinium lead iodide, $FAPbI_3$: E_g = 1.48 eV).[123,124] Band gap tuning also has been exploited by replacing the Pb^{2+} cation with other metals like tin where methylammonium tin iodide ($MASnI_3$) leads to E_g = 1.30 eV. Interestingly, the band gap does not follow a linear trend if Sn^{2+} is mixed with Pb^{2+} and E_g decreases even further to 1.17 eV for both $MASn_{0.75}Pb_{0.25}I_3$ and $MASn_{0.50}Pb_{0.50}I_3$ compounds as reported by Hao and coworkers.[125] This variability has allowed perovskites to be employed not only in single-junction devices, but also in a multi-junction configuration in tandem solar cells[126,127] and other applications. For example, extensive research efforts are also focused on the implementation in photodetectors,[128,129] light-emitting diodes (LEDs),[130,131] lasers[132,133] or scintillators[134] for the detection of ionizing radiation.[135] Due to their optoelectronic properties and versatility, lead halide perovskites thus represent a new class of interesting organic-inorganic semiconductors offering a wide range of possible applications.

2.3. Perovskite Photovoltaics

This section describes the working principle of perovskites solar cells and gives a short introduction to the variability of possible device layouts. Further, the current-voltage characteristic is explained and the most important PV parameters like the PCE are introduced. In the end, the so-called current-voltage hysteresis, often observed in perovskite solar cells, will be discussed.

2.3.1. Device Layout and Working Principle

Perovskite Solar Cell Architectures

The scientific interest in solar cells based on metal halide perovskite materials during the last decade led to a multitude of different device architectures. Kojima et al. implemented both $MAPbI_3$ and $MAPbBr_3$ in DSSCs, where the thin perovskite layer replaced a dye.[17] These electrochemical cells typically employ a μm-thick mesoporous TiO_2 layer on which the dye/perovskite layer is deposited. The photogenerated electron-hole pair is separated and the electron is transferred to the titanium dioxide lattice and further to an electrode. The mesoporous structure complicates the contact between the dye and a hole extraction layer, which is necessary to transport the positive charge to the counter electrode. To overcome this issue, a liquid electrolyte is used, allowing for a full penetration of the TiO_2/dye network. The first perovskite solar cell used the redox pair I_2/I^- as an electrolyte. In this system, the I^- ions get oxidized to elementary iodine by transferring an electron to the perovskite layer. Then, it gets reduced again at the counter electrode to close the electrical circuit. The energy of electrons in the valence band of the perovskite has therefore to match the oxidation potentials of the halides in the electrolyte. In contrast, excited electrons from the perovskite cannot flow to the liquid electrolyte since no states at the corresponding energies are available.

It took 3 years for the perovskite to re-enter the PV stage with a more than twofold increase in efficiency from 3.8 % to around 10 %.[19] This was realized by introducing the solid-state hole transport layer (HTL) 2,2,7,7–tetrakis(N,N–p–dimethoxy–phenylamine)–9,9–spirobifluorene (spiro-MeOTAD) to replace the liquid electrolyte which also improved the device stability significantly. The concept of a so-called solid-state DSSC was already introduced in the 90s by Tennakone,[136] Murakoshi[137] and Bach.[138] A milestone in the development of perovskite PVs was the replacement of n-type TiO_2 with insulating aluminium oxide (Al_2O_3) which increased the PCE even further.[18] Two important conclusions were drawn from this work: first, it became apparent that an additional capping layer of perovskite on top of mesoporous TiO_2 does not limit the efficiency, which clearly distinguishes the structure from a regular DSSC. Second, charge transfer to TiO_2 was not needed since the transport of electrons in the perovskite was faster than in mesoporous titanium dioxide, which was interpreted as a clear indication of amibipolar transport. These publications are considered as pioneering works guiding further research on perovskites and paved the way for the layouts currently in use. Figure 2.4a depicts the architecture just described, which is one of the most frequently employed designs for perovskite solar cells. A glass substrate is initially coated with the electrode, a transparent conductive oxide that must be light-transmitting since the final solar cell is illuminated from the glass side. In case of the mesoporous architecture, fluorine-doped tin oxide (FTO) is preferred because it resists the necessary sintering of the mesoporous TiO_2 layer at 400 – 500 °C. Electron transport in porous TiO_2 is usually limited by trapping and detrapping in sub-band gap states[139] and leads therefore to low mobilities of around 10^{-2} $cm^2/(Vs)$,[140] which explains the faster transport in the perovskite film observed by Lee et al. when TiO_2 is replaced by insulating Al_2O_3.[18] In the past years, a number of other mesostructures were also implemented as electron transport layers (ETL) such as zinc oxide (ZnO),[141] zirconium dioxide (ZrO_2)[142] or tin dioxide (SnO_2).[143] The porous network is then infiltrated by the perovskite with a closed capping layer. An HTL in combination with an electrode completes the solar cell. Among the HTM's, spiro-MeOTAD is the most commonly chosen material, although a variety of other compounds can also be used.[144] Gold, silver or other metals are then applied as the electrode.

The ambipolar transport and the high carrier diffusion lengths (see Section 2.2) also allow the mesoporous network to be substituted by a planar transport layer as illus-

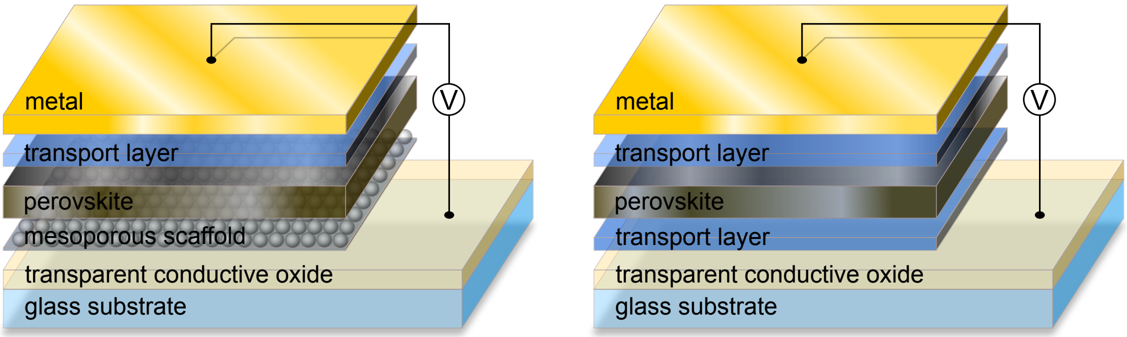

(a) mesoporous device layout

(b) planar device layout

Figure 2.4.: Device architectures for perovskite solar cells. In **(a)**, a mesoporous scaffold is used as a transport layer, while a planar configuration is shown in **(b)**. The glass substrate is coated with a transparent conductive oxide acting as an electrode and followed by a transport layer, which can be either planar or mesoporous. The active layer with the perovskite and another transport layer are located above. Finally, a metal electrode completes the solar cell.

trated in Figure 2.4b. Here, the perovskite is embedded between the HTL and ETL resulting in a p-i-n or n-i-p configuration. Instead of FTO, indium-doped tin oxide (ITO) is often implemented as an transparent conductive oxide. Various transport materials have been established in the meantime, whereby poly(3,4–ethylenedioxythiophene):poly(styrenesulfonate) (PEDOT:PSS)[145] and poly–(bis(4–phenyl)(2,4,6–trimethylphenyl)amine) (PTAA)[146] are the most prominent representatives of the HTLs and the C_{60}[145,147] fullerene or [6,6]-phenyl-C-61-butyric acid methyl ester ($PC_{61}CM$)[148,149] are frequently used as ETLs. Often a sequence of several transport layers[146,150] is combined or dopants[151,152] are added to increase the conductivity and improve charge carrier extraction. The great potential of this design, which is similar to those of organic solar cells, was demonstrated by Liu et al. in 2013, when PCEs of over 15 % were achieved.[153] The planar device architecture exhibits several advantages over the mesoporous design such as simplified fabrication and usually reduced hysteresis during current-voltage measurements as discussed in more detail in Section 2.3.2. Nevertheless, PCEs of over 20 % can be achieved regardless of layout.[154]

Operating Principle

The working principle is quite similar in both type of devices and depends strongly on the optoelectronic properties of the perovskite itself. To generate electricity, a number of different steps are necessary as summarized in Figure 2.5. In the very first step, an incident photon is absorbed. According to the photovoltaic effect,[155,156] which describes the interaction of light with matter, an electron is lifted from the valence band to a higher energetic state in the conduction band of the semiconductor (i). If the energy of the photon is not sufficient, no absorption can occur, while charge carriers with excess kinetic energy are created if the energy is higher than E_g (ii). For $MAPbI_3$, it has been shown that the cooling of these so-called hot-carriers (due to a larger effective temperature compared to the temperature of the crystal lattice) is regulated by the emission of longitudinal optical phonons, providing lifetimes in the range of 1 – 100 ps which is longer compared to conventional semiconductors.[157,158] The slow thermalization processes are attributed to a hot-phonon bottleneck caused by an increased phonon reabsorption in the presence of a non-equilibrium phonon population at high carrier densities.[74,159] Irrespective of whether charge carriers were generated according to (i) or (ii), they are initially present as excitons, which is indicated in step (iii). As already described in Section 2.2, these are weakly bound Wannier-Mott excitons which get separated on the ps time scale.[160] The fact that hot charge carriers are present as free carriers qualifies lead halide perovskites as candidates for hot carrier solar cells, where excited charge carriers with excess energy get separated and extracted before

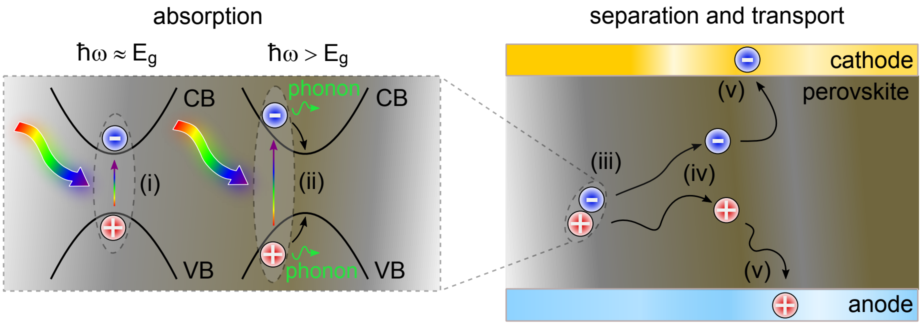

Figure 2.5.: Schematic depiction of the working mechanism of a perovskite solar cell. Photons with the energy of the band gap (i) or with a higher energy (ii) are absorbed and generate a weekly bound exciton. After the separation of the electron hole pair (iii) both types of charge carriers diffuse to the respective contacts (iv) and get extracted (v). Further details are given in the text. For clarity, charge carrier recombination is neglected and will be discussed in Chapter 3.

they relax to the VBM and CBM, respectively.[161,162] After the carriers are separated and a splitting of the electron and hole quasi Fermi levels E_{Fn} and E_{Fp} is established, they must move to separate electrodes. For this reason, every solar cell requires a build-in asymmetry that ensures that charge carriers with different polarities can be collected and extracted independently at individual contacts (steps (iv) and (v)). Accordingly, the transport layers and contacts are of central importance for the working principle of perovskite solar cells and a prerequisite to obtain a diode structure. Usually a good transport layer is characterized by a selectivity to only one carrier type. This can, for example, be achieved by energy level alignment, allowing one kind of carriers to enter the layer and blocking the opposite charge carriers due to a lack of free energetic states.[163] Würfel et al. also demonstrated that a difference in electron and hole conductivities in two regions of a device already can be sufficient to obtain charge carrier separation.[164] When the HTL and ETL get in contact with the perovskite, the Fermi level E_F equilibrates over the whole device and the difference of work functions of the transport layers results in a build-in voltage V_{bi}. Depending on the solar cell technology, V_{bi} can be present over the whole absorber width or narrowed down to a thin space charge region. The role of V_{bi} is intensively discussed in literature, since its strength and the length over which it extends has a direct influence on charge carrier separation mechanism both in the dark and under illumination.[165,166] The interplay of the build-in voltage, charge carrier drift and charge carrier diffusion was very recently investigated by the group of Nazeerudin.[167] The authors varied V_{bi} by shifting the work function of the ETL by about 1 eV and observed very similar V_{oc}'s, indicating that the build-in electrical field plays a minor role in the operation mechanism. The open-circuit voltage is therefore controlled by charge carrier recombination and the quasi Fermi levels in the perovskite with the transport layers following the respective levels. As a direct consequence, a flat band structure is assumed to exist in the perovskite and carrier transport should be ruled by diffusion and not by drift due to electrical fields.[167,168] This result is also supported by cross sectional Kelvin probe force microscopy measurements, which revealed a field-free $MAPbI_3$ layer embedded in a device configuration under both short- and open-circuit conditions.[169] The observed field-screening is attributed to the rearrangement of mobile ions in the perovskite film, which will be further addressed in Section 2.3.3. In line with previous statements, calculations[165] have demonstrated that PV devices benefit from diffusion dominated transport if the diffusion length is higher than the active layer thickness which is indeed the case for most lead halide perovskite solar cells (see Section 2.2). Nevertheless, the exact working principle of perovskite solar cells still remains topic of ongoing research and more experimental work is necessary since a better understanding would help to boost the PCE even further.

2.3.2. Current-Voltage Characterization and Photovoltaic Performance

The main characterization of PV devices is realized by measuring the current dependence on a externally applied voltage, which is usually referred to as the current-voltage (j-V) response. In order to compare different solar cells with each other, standard illumination conditions have been introduced. The AM1.5 G spectrum with an irradiance of 100 mW/cm² is often termed "1 sun" illumination and defines the incident power P_L the solar cell is illuminated with. The spectral distribution is set by the global (G) standard reference spectrum (average of direct and diffuse solar irradiance) passing the air mass (AM) under the solar zenith angle of $\cos(1/1.5) = 48.19°$.[170] The j-V characteristics normalized to the active area of a typical perovskite solar cell both in the dark and under 1 sun illumination are summarized in Figure 2.6a in a linear and in Figure 2.6b in a semi-logarithmic representation. Several points of interest are highlighted for the illuminated curve, namely the the short-circuit current density (j_{sc}), the open-circuit voltage (V_{oc}) and the maximum power point (MPP). When both contacts are connected through an external circuit and no voltage is applied, the resulting current is called j_{sc}, where the corresponding band diagram is depicted in Figure 2.6c. In this scenario, the Fermi level is equilibrated over the whole device and the photogenerated charge carriers get extracted at the respective contacts. As discussed already in the previous Section 2.3.1, charge transport can occur via both drift or diffusion, depending on V_{bi}. For clarity, mobile ions (see Section 2.3.3) and doping are not considered in Figure 2.6c. In

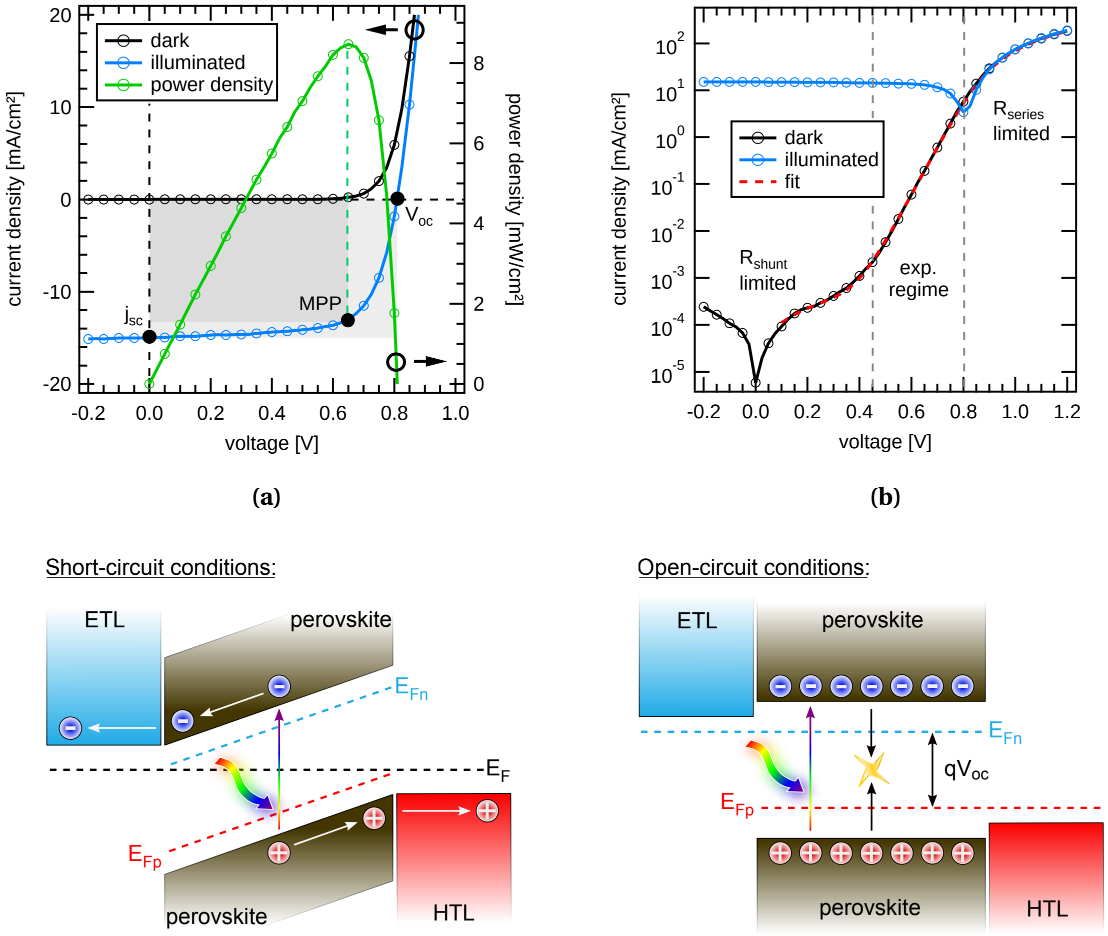

Figure 2.6.: **(a)** Current-voltage characteristics in the dark and under simulated AM1.5 G illumination (left axis) and the power density (right axis) of a perovskite solar cell. The maximum power point indicates the part of the j-V curve where the power density has its maximum (green dashed line). The fill factor is defined by the maximum power point and corresponds to the ratio of the maximum power density and the product $j_{sc} \cdot V_{oc}$. **(b)** Semi-logarithmic representation of both j-V curves including a fit according to Equation 2.8. In addition, band diagrams of a solar cell are shown under **(c)** short-circuit and **(d)** open-circuit conditions.[163,166] At short-circuit, the photogenerated charge carriers are extracted, whereas at open-circuit conditions, the generation rate equals the recombination rate and the resulting quasi Fermi level splitting creates V_{oc}.

contrast to short-circuit, current flow is suppressed and no charge carriers get extracted under open-circuit conditions when the quasi Fermi level splitting (E_{Fn} and E_{Fp}) due to photogenerated charge carriers is fully compensated by an externally applied bias, the V_{oc} (Figure 2.6d). Under these conditions, both the VB and the CB are aligned flat and the recombination rate balances the photogeneration rate. This point is therefore of particular interest for investigating recombination losses in PV devices and will be addressed in this thesis. Increasing the voltage further to values above V_{oc} leads to an injection of charge carriers, which recombine inside the device. Another feature of the illuminated j-V response is the MPP, located at the voltage where the power density $j(V) \cdot V$ (Figure 2.6a, green line) has its maximum (P_{max}). The MPP determines the fill factor FF, which is defined as

$$FF = \frac{P_{max}}{j_{sc} \cdot V_{oc}} = \frac{j_{MPP} \cdot V_{MPP}}{j_{sc} \cdot V_{oc}} \tag{2.6}$$

and can be understood as the ratio between the theoretically possible power ($j_{sc} \cdot V_{oc}$) and the maximum power output of the device which is illustrated by the two grey squares in Figure 2.6a. Thus, it describes the "squareness" of the j-V curve. With the above-mentioned PV parameters, the PCE of a solar cell can be written as

$$PCE = \frac{P_{max}}{P_L} = \frac{j_{sc} \cdot V_{oc} \cdot FF}{P_L}. \tag{2.7}$$

Highly efficient solar cells therefore require that j_{sc}, V_{oc} and FF are optimized at the same time. To obtain the maximum power, an external load must be adjusted such that the solar cell is at the MPP under illumination.

In general, the relation between current and voltage of a solar cell can be described by the generalized Shockley equation[171]

$$j(V) = j_0 \left[\exp\left(\frac{e(V - jR_{series})}{n_{id} k_B T} \right) - 1 \right] + \frac{V - jR_{series}}{R_{shunt}} - j_{ph}, \tag{2.8}$$

where j_0 is the dark saturation current density, n_{id} is the diode ideality factor, R_{series} is the series resistance, R_{shunt} is the shunt resistance and j_{ph} is the photocurrent density. The impact of these parameters is demonstrated in Figure 2.6b by fitting the j-V response in the dark ($j_{ph} = 0$) with Equation 2.8 (red dashed line). The exponential diode behavior of the device is controlled by the combination of the material properties j_0 and n_{id}. Recently, Cuevas pointed out that a more suited expression for j_0 is "thermal equilibrium recombination current" since it corresponds to the recombination of charge carriers generated by the thermal background radiation.[172] In case of ideal diodes ($n_{id} = 1$), j_0 contains all information about charge carrier recombination. However, in many cases n_{id} deviates from unity and is therefore also used as an additional parameter describing the dominant recombination processes in solar cells as discussed in Section 3.3.[173,174] The divergence of the exponential behavior is a consequence of resistive losses induced by R_{series} and R_{shunt}. Resistances inside the device and from the electrical circuit are included in R_{series}, which can negatively influence the FF. The impact of the series resistance can be observed for high voltages in Figure 2.6b. R_{shunt} accounts for leakage currents inside the device, for example caused by pinholes and affects the diode current at low voltages. In case of low R_{shunt}, it is even possible that the open-circuit voltage is reduced. High parallel resistances and low series resistances should therefore always be aimed for.

Bucket Analogy

To illustrate the introduced PV parameters, a solar cell is compared with a bucket in the following. The comparison between a bucket and a solar cell is based on lectures from Yablonovitch and was recently adopted by a book[175] from Green and co-workers. A modified version is shown in Figure 2.7 to demonstrate the different states in which the solar cell is operating under j_{sc}, MPP and V_{oc} conditions. A PV device is symbolized by an empty bucket, which gets filled with water drops representing excited charge carriers in the active layer. At the bottom, a valve controls the water flow and therefore also the water level and pressure inside the bucket. Both, water flow and water level correspond to the current and the voltage of the solar cell. The water flow drives a wheel, where the dissipated power depends on the product of flow and pressure. This is the analogy to the power generated by a PV device. Thus, the valve controls the rotational speed of the wheel and determines the current state of the bucket. In the solar cell picture, it corresponds to the resistance of the load which is connected to the device. In the

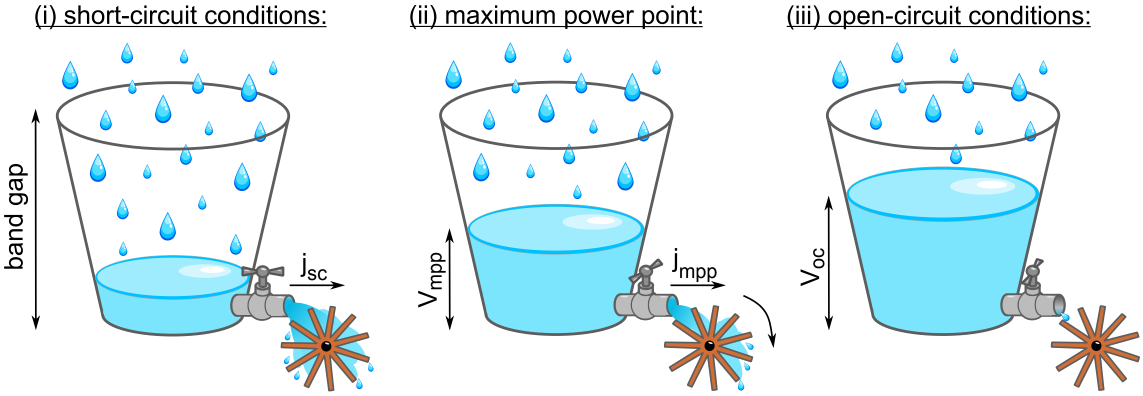

Figure 2.7.: Bucket analogy of the working principle of a solar cell. The bucket represents a PV device where the height corresponds to the band gap of the active layer. A water wheel has its equivalence in the power output of a solar cell. When it rains, the water drips into the bucket and the position of the valve determines the condition that sets inside. Under (i) short-circuit, the valve is fully open, all the water flows out and the water level, which corresponds to the voltage, is close to zero. At (ii) MPP, the valve is set so that the product of water level and water flow (current in a device) is maximized and the wheel turns at the highest rotational speed. In contrast, the valve is completely closed under (iii) open-circuit and the resulting water level is equivalent to V_{oc}.[175]

case of an open valve, the collected water drops out of the bucket, preventing the water level from increasing. Since no pressure can build up, the wheel does not turn and no power is generated. This situation corresponds to a solar cell under (i) short-circuit conditions. The power output can by increased by closing the valve continuously until it reaches the MPP. At this point, the water level and water flow are optimized such that wheel rotates with the maximal rotational speed, which is equivalent to a solar cell operating at its (ii) MPP. If the valve is further closed, the wheel gets slower again and the dissipated power decreases towards zero in the case of a closed bucket. This state corresponds to (iii) open-circuit conditions, where the maximum water height is reached and the solar cell provides the V_{oc}. However, under these conditions, the water level would increase until it finally spills over which cannot be observed in real devices since the V_{oc} is always smaller than E_g. Therefore, additional loss processes, the recombination of charge carriers, must be considered and will be discussed in Chapter 3.

2.3.3. Hysteresis Effects

One of the most controversial phenomena in perovskite solar cells is the so-called hysteresis. It describes slow, time-dependent processes that usually occur in electrical measurements. During current-voltage characterization, the direction of the measurement, i.e. whether the voltage is swept from negative to positive (forward) or vice versa (backwards), can have a large influence on the resulting current. Figure 2.8 shows two sets of j-V curves in the dark and under illumination, where the degree of hysteresis differs significantly and complicates the determination of PCE. The scan rate was 0.5 V/s such that the entire measurement was performed on a time scale of seconds. Both devices show a higher performance when the current response is measured from positive to negative voltages. The difference between the studied devices are the transport layers surrounding the $MAPbI_3$ film. In case of Figure 2.8a, a p-i-n architecture is used with PEDOT:PSS as the HTL and a combination of $PC_{61}BM$ and C_{60} as ETL's. In Figure 2.8b, the perovskite is sandwiched between planar TiO_2 and poly(3-hexylthiophene-2,5-diyl) (P3HT) leading to a n-i-p layout. Obviously, the implemented transport materials and the structure of the device strongly influence the gap between the forward and backward scans in line with other reports.[176–183] The composition of the perovskite also determines the extent of hysteresis, where the incorporation of FA^+, Cs^+, Rb^+ and K^+ as the A-position cations having a diminishing effect.[184–186] However, it is not only the materials involved that play a role, but also the conditions under which the solar cell is being measured. Numerous publications have shown that the bias prior to a j-V loop,[180,187,188] the applied voltage range[189]

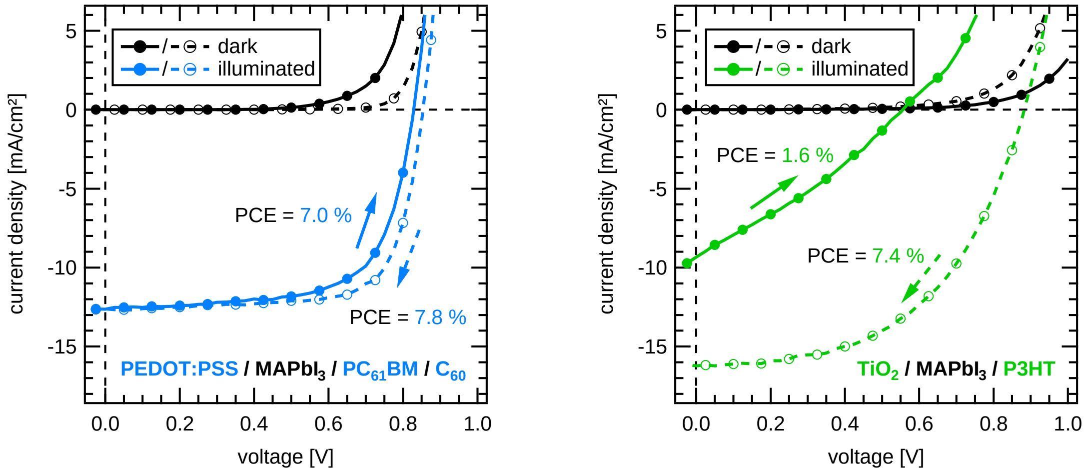

(a) **(b)**

Figure 2.8.: Examples of j-V characteristics from MAPbI$_3$ solar cells with hysteresis. When a voltage is applied, the measured current in the dark and under 1 sun illumination depends on the direction of the voltage sweep which complicates the PCE determination. The device in **(a)** uses PEDOT:PSS as a HTL and a combination of PC$_{61}$BM and C$_{60}$ as ETL's and corresponds therefore to a p-i-n layout. In contrast, the curves in panel **(b)** are determined on a n-i-p solar cell, where a compact TiO$_2$ layer acts as the ETL and P3HT as the HTL. In both cases, ITO and gold are employed as electrodes and the scan rate was set to be 0.5 V/s.

and the scan rate[187,190] are also important. The anomalous behavior can also be affected by light soaking[191,192] and temperature.[193,194]

In principle, hysteresis during j-V characterization is a property common to all types of solar cells. For example, silicon PVs or DSSCs also reveal differences between forward and backward sweeps at sufficiently high scanning speeds.[195,196] This is ascribed to capacitive effects in the device, where charge carriers cannot follow the voltage cycling. In the simplest case, the solar cell acts as a plate capacitor and gets charged during the forward scan and discharged during the backward scan. Additional contributions to hysteresis may be caused by trapping and release of charge carriers, when the release rate of traps is slower compared to the scan velocity. However, these effects only become visible during short measurement times in the millisecond range, which is in clear contradiction to perovskite solar cells. Here, the hysteresis is more pronounced and sometimes still present at very slow scan rates.[187] It has been even shown that the PL intensity measured on films or the V_{oc} and PCE of full devices can build up to several hundred of seconds.[182,190,197] Consequently, additional effects must be taken into account to explain the observed anomalies.

Ferreoelectricity

The physical origin of the hysteresis effect has been debated for a long time and various explanations have been proposed. Initially, polarization of the perovskite was suggested to be responsible for hysteresis, because a large variety of ABX_3 compounds is known for its polarizability which causes, for example, ferroelectric behaviour. However, there are a several conflicting works on the presence of ferroelectricity. Theoretical studies opened up the possibility that lead halide perovskites show spontaneous electric polarization in the tetragonal phase. Different origins have been suggested like oriental polarization from the MA^+ dipole or ionic polarization induced whether by a displacement between MA^+ and the lead iodide sublattice or a shift of Pb^{2+} within the ${PbI_6}^{4-}$ octahedral.[198–200] Out of these possible contributions, the largest part is attributed to the asymmetric organic cation.[198,200] In line with these reports, Pecchia et al. proposed ferroelectric order in $MAPbI_3$ at length scales of 8 – 10 nm where electrons and holes can accumulate separately.[201] In contrast, it is also calculated that the ferroelectric behaviour is not stable at room temperature and can only be observed for temperatures below 50 K.[202] Additionally, experimental works spread further confusion within the scientific community as contradictory results on the question, if lead halide perovskites are[203–206] of ferroelectric nature or not,[207,208] exist. It is postulated that dipoles in the perovskite would result in an internal electrical field which can strengthen or weaken an externally applied field leading to the observed differences in scan directions during j-V characterization.[180,209] However, this theory seems unlikely to be the main origin of hysteresis since the timescale of switching domains are reported to be in the range of ~ 0.1 – 1 ms and thus intrinsically too fast compared to the observed effects on the timescale of seconds (see Figure 2.8).[210] It is also demonstrated, that the rotations of the organic cation do not influence photogenerated charge carriers at all.[62]

Trapping and Detrapping of Charge Carriers

Further speculations exist, that charge trapping and detrapping processes may be involved in hysteresis during j-V measurements.[211] Trap states are associated with defects in the crystal lattice that are able to trap electrons or holes. These processes can occur in the bulk of the perovskite and at the interfaces to the transport layers. It is suggested that photogenerated charge carriers are trapped when a forward bias is applied and then released again when the voltage is set to zero again during a measurement. This mechanism can then result in differences between the forward and backward scans.[212] The theory is supported by different works where passivating layers are implemented in devices to reduce the amount of traps states leading to a decreased hysteresis. For example, the group of Snaith passivated the surface of TiO_2 with the fullerene C_{60} resulting in an increased PCE and a reduced current-voltage discrepancy between both scan directions.[213] Similarly, Shao et al. deposited $PC_{61}BM$ on top of a perovskite layer and measured that the amount of surface trap states is reduced by more than two orders of magnitude, again decreasing the hysteresis significantly.[176] This theory therefore supports the large influence of the transport layers on the emergence of hysteresis. However, since the presence of trap states is not a property that is exclusively encountered in perovskite solar cells, there must be further explanations for j-V hysteresis.

Mobile Ions

Over the past few years, a consistent majority of publications have identified mobile ions as the main cause of the observed dynamic phenomena. Ionic conduction in fully anorganic perovskites like $CsPbCl_3$ or $CsPbBr_3$ has already been demonstrated in 1983 by Mizusaki et al., where the authors concluded that the halogen ions are highly mobile.[214] Possible movement of mobile ions is depicted in Figure 2.9, where the vacancies V_I, V_{Pb} and V_{MA} are filled by adjacent ions. Iodide migration occurs along the edges of the octahedron, while lead and methylammonium have to diffuse longer distances to find neighbouring empty positions. In addition, interstitials can also contribute to the ionic conductivity. Many researchers focused on the identification of the dominant mobile species in both theoretical and experimental works. Calculations revealed a huge range of activation energies E_A for ion migration in lead halide perovskites with $E_A^I = 0.1 - 0.6$ eV, $E_A^{MA} = 0.5 - 1.1$ eV and $E_A^{Pb} = 0.8 - 2.3$ eV.[215–217] From these values it can be concluded that the ionic transport is predominantly driven by A- and X-site ions. Various experimental works confirmed the movement of individual ions and their vacancies. It is shown that I^-,[197,219–221] MA^+,[221–226] and in some cases even

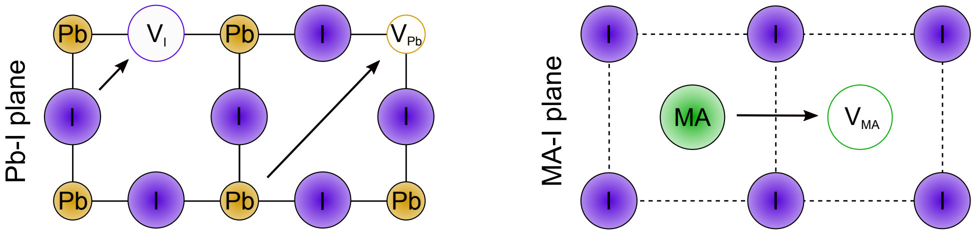

Figure 2.9.: Schematic illustration of possible transport mechanisms for ions in $MAPbI_3$. V_I, V_{Pb} and V_{MA} represent the different vacancies in the crystal lattice. Ionic transport is not necessarily related to vacancies, but can also be supported by interstitials.[215,218]

Pb^{2+} [222,227] ions are moving in the crystal lattice under electrical fields. Further, the diffusion coefficients have been determined to be in the range of 10^{-9} cm^2/s for iodide and 10^{-12} cm^2/s for methylammonium. However, the concentration of MA^+ ions is one order of magnitude higher compared to mobile I^- ions.[221] Senocrate et al. concluded that the experimentally observed ionic conductivity in $MAPbI_3$ is higher than it is calculated in the case of pure MA^+ movement pointing towards iodide-driven hysteresis effects.[226] The effect of illumination on the ionic conductivity has also been investigated leading to the conclusion that light generates additional iodine vacancies in the perovskite.[228] Very recently, Meggiolaro et al. tried to obtain a more comprehensive picture of mobile ions and they linked the variation of measured activation energies and diffusion parameters to the polycrystallinity of perovskite films where the surfaces dominate ion migration behavior.[229] This is in line with reports, where grains boundaries have been identified as the main transport pathways for ions.[230]

The extact mechanism how mobile ions influence electrical measurements like j-V characterization is still under debate. Figure 2.10 illustrates the ion distribution and its impact on band alignment at both short-circuit and open-circuit conditions under equilibrium. For clarity, only methylammonium and iodide ions/vacancies (MA^+, I^-, V_{MA}^- and V_I^+) are included in the scheme since these are believed to contribute most to hysteresis effects like discussed before. Under j_{sc} conditions (Figure 2.10a), mobile ions move trough the perovskite film according to the build-in electrical field (see Figure 2.6c). This results in the screening of the built-in potential, which can not further act as a driving force for the extraction of charge carriers leading to a reduced j_{sc} as shown in Figure 2.8b. When a forward voltage is applied and the scanning speed is faster compared to the moving ions, band valleys are generated in the CB and VB forcing excited electrons to accumulate close to the HTL and holes close to the ETL. Both types of charge carriers are therefore trapped at the wrong electrodes which leads in case of non-selective contacts to increased charge carrier recombination at the interfaces reducing both FF and V_{oc}.[231,232] If the applied voltage approaches and exceeds V_{oc}, the driving force that separates ions, vanishes. This situation is summarized in Figure 2.10b, where the ions are uniformly redistributed again. In the backward scan, FF and V_{oc} are increased since the charge carrier transport and recombination are not negatively affected by an unfavorable ion distribution in the device. It is obvious that hysteresis effects therefore can be described as a combination of ionic and electronic charge carrier distributions in the device. The hypothesis of non-selective transport layers in combination with mobile ions is supported by a large number of transient experiments, like the slow build-up of open-circuit voltage after switching on the light

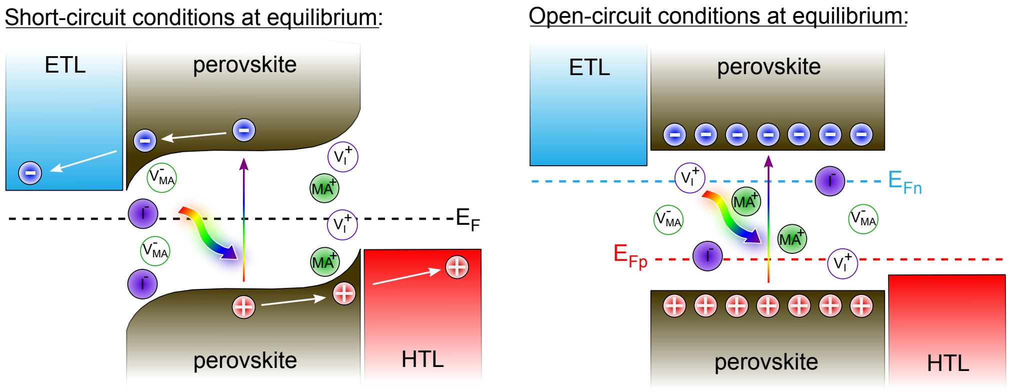

(a) **(b)**

Figure 2.10.: Impact of mobile ions on band energetics at **(a)** short-circuit and **(b)** open-circuit conditions under equilibrium.[231,232] At j_{sc} conditions, the build-in potential forces the ions to move close to the interfaces to the transport layerts. This results in a screening of the build-in field, where the extracted charge carriers are mostly driven by diffusion. In contrast, when the device is stabilized under V_{oc} conditions, the ions are redistributed again. Further explanations on how mobile ions can influence current-voltage measurements are provided in the main text.

and drift-diffusion simulations and is therefore widely accepted to be the main cause of hysteresis.[218,232–237]

During the last years, many researchers focused on the elimination of current-voltage hysteresis in perovskite solar cells. Various approaches were applied to both the perovskite itself and the surrounding transport layers. To suppress ion movement, Ferdani et al. substituted the organic cation to increase the activation energy for ion diffusion. It was demonstrated, that partial replacement of methylammonium by guanidinium in $MAPbI_3$ suppressed iodide transport.[238] Other attempts optimized the transport layers and the interfaces to reduce charge carrier recombination and the observable hysteresis.[176,179,239,240] To quantify the extend of hysteresis effects, several publications introduced the hysteresis index HI,[241–244] which quantifies the difference between the forward and the backward j-V scan. To give an example, according to Li et al., it can be expressed as follows[244]

$$HI = \frac{PCE_{back} - PCE_{for}}{PCE_{back}}, \tag{2.9}$$

where PCE_{for} and PCE_{back} correspond to the PCE determined from forward and backward scan directions, respectively. A solar cell without hysteresis thus has a HI value of zero, which increases the larger the difference between forward and reverse direction gets. However, it is under debate if HI is a useful parameter to describe hysteresis in perovskite-based devices since it does not account for all relevant conditions like for example the material system or the scan speed.[245] In contrast, it is suggested to monitor the stability of the important parameters such as j_{sc}, V_{oc} and PCE over time. For this reason, several authors developed protocols and guidelines for a correct PCE determination of perovskite solar cells highlighting the importance of stabilized PV parameters.[246–248]

3. Charge Carrier Recombination in Semiconductors

The following chapter provides insights into loss processes in semiconductors, namely charge carrier recombination. Carrier recombination dynamics are very relevant for the functionality of optoelectronic devices. An overview over the most important recombination mechanisms will be given, including their impact on the charge carrier lifetime τ. Finally, it will be highlighted how these recombination mechanisms are connected to PV parameters like V_{oc} in fully working devices.

3.1. Recombination Mechanisms

Recombination of charge carriers is of fundamental importance for semiconductors in electronic devices like solar cells, LEDs and transistors. In general, all processes which lead to a depopulation of the excited species are described by recombination mechanisms and are therefore considered as charge carrier losses. In PV devices, these carriers cannot consequently get extracted anymore. Thus, in order to increase the efficiency of a solar cell, every researcher strives for a reduction of unwanted recombination processes. An overview over possible loss mechanisms relevant for the operation of PVs is provided in Figure 3.1. These processes can be categorized according to the number of involved particles. Monomolecular or first-order recombination describes processes with only one particle. This can, for example, be the recombination of an exciton. As discussed in Section 2.2, photoabsorption yields mostly free charge carriers instead of excitons. Accordingly, this type of recombination can be neglected for perovskites, but plays an important role in OPVs.[249] On the other hand, Shockley-Read-Hall (SRH) recombination is considerably more important for perovskite solar cells (see (i) in Figure 3.1). In this case, a trap (defect) leads to an energetic state within the band gap which captures an electron or hole by simultaneous emission of phonons and mediates therefore a recombination event. Since only one charge carrier is required for the process, it also represents first-order recombination. At higher charge carrier concentrations, (see (ii)) band-to-band or second-order (bimolecular) recom-

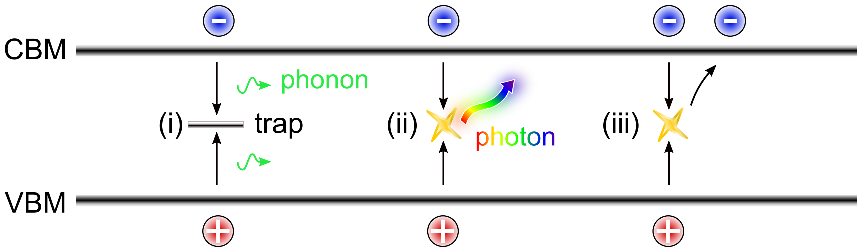

Figure 3.1.: Overview of different charge carrier recombination mechanisms in semiconductors. Trap–assisted recombination is shown in (i), which is induced by energetic states inside the band gap. This process is usually dominating at low carrier concentrations, where the density of trap states rules. This mechanism is often described by Shockley–Read–Hall theory and corresponds to a first-order process. A direct recombination of an electron in the CB and a hole in the VB with the emission of a photon is called (ii) band–to–band recombination. Since two particles are involved in the process, it is often referred to as a second-order process. A three particle loss mechanism is (iii) Auger recombination, where the energy which results from a direct electron-hole recombination is transferred to another electron or hole. For all these processes energy and momentum conservation must be fulfilled.

bination starts to be dominant which involves both an electron in the CB and a hole in the VB. Here, the recombination event depends on the product of the electron and hole carrier concentrations n and p, which can be summarized as n^2. The recombination of free charge carriers normally induces the emission of photons, for which reason these processes are also referred to as radiative recombination. If the excess energy is directly reabsorbed by a third charge carrier, the process is called Auger recombination and corresponds to a third-order mechanism scaling with n^3. The excited carrier, independent if it is an electron or a hole, thermalizes then back to the band edge by emitting phonons. Just like SRH recombination, this mechanism is also part of non-radiative recombination processes and dominates under high charge carrier densities.[250] Since non-radiative recombination losses lead to the emission of phonons, they increase the lattice temperature of the solar cell absorber.

Taking all these processes into account, the time-dependent change of charge carrier density n can be determined by the differential equation

$$\frac{\mathrm{d}n}{\mathrm{d}t} = -k_1 n - k_2 n^2 - k_3 n^3, \tag{3.1}$$

with k_1, k_2 and k_3 as the respective rate constants of first-, second- and third order recombination. For simplicity, the generation, diffusion and drift of charge carriers is neglected in this expression. Since the dominating processes for each rate constant are known, k_1, k_2 and k_3 can also be substituted by the rate constants k_{SRH}, k_{rad} and k_{Aug}.

These processes can be divided into two categories: avoidable and unavoidable charge carrier recombination as will be further outlined in this chapter.

3.1.1. Shockley-Read-Hall Recombination

Charge carrier recombination via defects is an important loss mechanism in semiconductor devices. This type of recombination is usually described within the framework of Shockley-Read-Hall recombination, developed in the middle of the 20th century.[251,252] A localized trap can result in an energetic state within the band gap which can mediate recombination events between electrons and holes from the CB and VB, respectively. If a trap captures a charge carrier, this carrier can either be released again by thermal activation or it recombines with a particle of opposite polarity. Therefore, the time until both carrier types are captured is in competition with the release time of the trapped carrier and therefore determines the effectiveness of the defect state. Impurities, where the time of capturing both charge carriers is shorter than the release time are called recombination centers.[253] In order to ensure energy conservation, trapping and detrapping is always related to the emission and absorption of phonons. The energetic position of the defect state and thus the energy difference to the CB or VB determines the number of phonons required for capturing a charge carrier. It follows intuitively that defect states which are located in the middle of the band gap have the highest probability of mediating a SRH recombination event since energy exchange with the crystal lattice is less likely when the energetic distance between two states is large. Hence, a separation into deep traps which act as SRH recombination centers and shallow traps which are prone to release the captured charge carriers is therefore useful and frequently used in literature.

According to Shockley-Read-Hall theory, the recombination rate R_{SRH} of photogenerated charge carriers via a recombination center with the energy E_T can be expressed using the equation

$$R_{SRH} = \frac{np - n_i^2}{\tau_p(n + n_t) + \tau_n(p + p_t)}, \tag{3.2}$$

where n and p are the electron and hole concentrations, n_i is the equilibrium carrier concentration of electrons/holes and τ_n and τ_p are electron and hole carrier lifetimes. n_t and p_t describe the electron and hole densities when the Fermi level equals the energy of the trap through which the charge carriers recombine and equals

$$\begin{aligned} n_t &= N_C \exp\left(-\frac{E_C - E_T}{k_B T}\right) \\ p_t &= N_V \exp\left(-\frac{E_T - E_V}{k_B T}\right) \end{aligned} \tag{3.3}$$

with the N_C and N_V as the effective density of states close to the band edges. The charge carrier lifetimes τ_n and τ_p depend on the defect state density N_T, the capture cross section σ and the thermal velocity v_{th} via

$$\tau_{n,p} = \frac{1}{v_{th}\sigma_{n,p}N_T} \tag{3.4}$$

and correspond to the smallest mean time for a charge carrier between generation and capture. The detailed derivation of these equations can be found in References[170,253]. In case of multiple defects, the SRH rate is a sum over all energies E_T. Under the assumption that photogenerated carriers and one SRH lifetime τ_{SRH} dominate ($np > n_i^2$, $n \gg n_t$, $p \gg p_t$), the rate can be approximately simplified to[254–256]

$$R_{SRH} \propto \frac{n}{\tau_{SRH}}. \tag{3.5}$$

A closer look on Equation 3.2 reveals that SRH recombination is the largest, when the energy level of the defect is in the center of the band gap (both $E_C - E_T$ and $E_T - E_V$ are maximized) and the semiconductor is undoped, such that $n \approx p$. However, it does not explain the physical origin why recombination via defect states of different energies proceeds differently.[256]

To get more insights into the physics behind SRH recombination, the parameters defining Equation 3.4 have to be discussed in more detail, namely v_{th}, $\sigma_{n,p}$ and N_T. The product of the thermal velocity and the capture cross section is often referred to as the capture coefficient $k_{n,p}$ which is expressed in units of m^3/s.[257] This kinetic factor has been widely described by the theory of multiphonon processes as introduced by Huang and Rhys[258] and others.[259,260] In this model, a band-like state and a defect state are represented by two parabolas with the same shape, but shifted in energy E and the configuration coordinate Q, which represents the potential energy surface. This situation is exemplary visualized in Figure 3.2. The configurational space or coordinate includes all changes of a defect state and its neighbors and is therefore a more comprehensive parameter than the bond length alone.[261,262] A non-radiative transition from the upper parabola is enabled by tunneling and/or thermal excitation to a vibrationally excited state of the lower parabola. The energetic difference of the two minima of the parabolas ΔE corresponds, for example, to the energy difference between the CBM and the impurity state and defines the number of phonons P needed for a transition via $\Delta E/\hbar\omega$, where $\hbar\omega$ corresponds to the phonon energy. In general, a high number of P results in a low value of the capture coefficient.[257] However, it is not only the number of phonons which is important for a transition but also the shift in Q, which is quantified by the so-called Huang-Rhys factor S_{HR}. It describes the strength

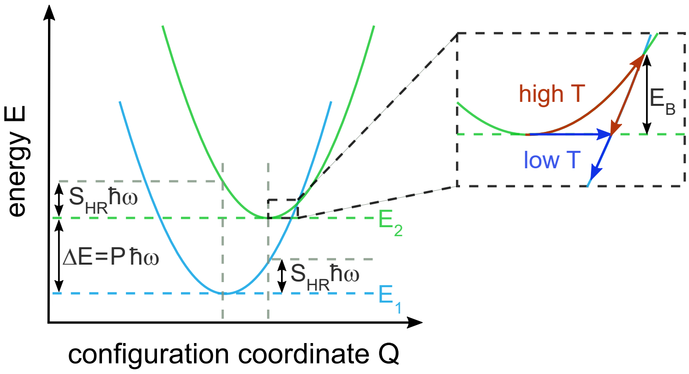

Figure 3.2.: Schematic illustration of a phonon-assisted transition between two states which are represented by the green and blue parabolas, where the upper one describes the CB and the lower one a defect state. E_1 and E_2 correspond the energetic positions and define the number of photons P needed to mediate the transition. The shift in Q is described by the Huang-Rhys factor S_{HR}. In order to couple to a vibronic state of the lower parabola, an electron needs to be thermally activated (high T, characterized by the energy barrier E_B) or to rely on a tunneling process (low T) as shown in the zoomed part. Modified from Reference [257].

of electron-phonon coupling with higher values indicating a stronger coupling. As discussed in Chapter 2.2, lead halide perovskites are polar semiconductors and thus polar coupling seems justified. For this case, Ridley developed a complicated, but still analytical solution for S_{HR}, which depends on several parameters such as the phonon energy, the lattice constant, the high- and low-frequency limit of the permittivity ϵ and ϵ_∞ and the radius of the defect.[260] The Huang-Rhys factor includes therefore the microscopic characteristics of the involved states and is different for every single defect or for example band-to-band transitions (see Section 3.1.2). It scales with the difference in Q with a high shift in Q leading to large S_{HR} values and vice versa. With the knowledge of both S_{HR} and P, the capture coefficient/transition rate $k_{n,p} = v_{th}\sigma_{n,p}$ between the parabolas can be calculated for differently charged defects as recently demonstrated by Kirchartz et al.[256] The authors assumed a longitudinal optical phonon energy of 16.5 meV corresponding to Pb-I modes as determined by Sendner et al.[113] Thus, a trap located in the middle of the band gap (0.8 V from the band edges) would require 49 phonons to be emitted making SRH recombination in general unlikely to occur. Further, it was found that the defect energy level has a strong impact on $k_{n,p}$ with midgap impurities leading to the highest transition rate. In addition, it is concluded that polar materials with heavy elements and low phonon energies like $MAPbI_3$ are highly sensitive to ΔE, where the transition rate from non-midgap defects is substantially lower compared to classical semiconductors.[256] This feature provides lead halide perovskites with the ability to be tolerant to defects as long as they are not in the middle of the band gap. The defect density N_T, also part of Equation 3.4, and the nature of defects will be addressed in the next section.

Nature of Defects in Lead Halide Perovskites

Various theoretical publications focused on the calculation of energetic states and their formation energies for all different types of defects like vacancies, interstitials and anti-sites. For $MAPbI_3$, it follows that 12 different intrinsic defects are possible which can be divided into 3 vacancies, 3 interstitials and 6 anti-sites. Many publications agree with the statement that most defects do not create states in the middle of the band gap, but that these states are rather located in the bands or close to the band edges. For example, Kim et al. conclude that vacancies such as V_{Pb} and V_I only generate levels close to the band edges opening up the possibility to act as doping sources.[263] Schottky defects, where anion and cation vacancies occur together, do not even lead to traps states inside the band gap. Another study by Yin et al. agrees with these results that most intrinsic defects create only shallow energy levels except anti-site substitutions like iodine on a lead or methylammonium position.[264] Luckily, these anti-sites suffer from high formation energies and are thus unlikely to be present in a large quantity. In 2015, a more fundamental study suggested the iodine interstitial and the iodine occupying a methylammonium position as possible candidates for recombination centers.[265] However, most of the theoretical studies focus on bulk defects and do not take into account surfaces or grain boundaries, which are always present in polycrystalline films. For this reason, some studies also analyzed defects related to grain boundaries and predicted no appearance of deep trap states.[64,266] This is in line with Uratani et al. where the authors predicted high formation energies for surface defects in case of stoichiometrically balanced growth conditions.[267]

In contrast to theoretical works, experiments usually focus on the determination of trap state energies and the corresponding defect densities since many experimental techniques do not allow for the identification of the exact nature of the studied defects. Using thermally stimulated current measurements, Baumann et al. reported on traps with a depth of 0.5 eV with a rather low density of 10^{15} cm^{-3}, probably not relevant under operating conditions.[268] This energy level was confirmed by Martin et al. and additional traps were found at 0.18 eV by applying the same experimental technique.[269] A large variation of defect energies (0.16 – 0.66 eV) was measured via admittance spectroscopy, where the densities were determined to be in the range of 10^{15} – 10^{17} cm^{-3}.[270,271] A trap density of 10^{16} cm^{-3} was also implemented as a fitting parameter to model transient PL decays.[78] Further, it has been highlighted that grain boundaries do not act more dominant as recombination centers than the bulk of the material and therefore no changes in trap energies or densities are generally expected.[272] Measurements were not only conducted on polycrystalline films, but also on crystals as demonstrated by Adinolfi et al. Performing space-charge limited current measurements on $MAPbI_3$ single crystals, trap densities were calculated to be in the order of 10^{11} – 10^{12} cm^{-3}, distributed within 0.25 eV near the band edges.[273] The fact that mostly defects, which are not located in the middle of the band gap and moderate trap densities are reported is in line with the theoretical predictions. The high distribution of the reported values can be probably related to different preparation methods, the choice of precursor materials and the different measurements techniques.

The defect properties of lead halide perovskite can be attributed to electronic structure already discussed in Chapter 2.2. As depicted in Figure 2.2a, the CBM of $MAPbI_3$ is mainly derived from empty Pb 6p orbitals, while the VBM is composed of Pb 6s and I 5p orbitals. Since the VB originates from an antibonding coupling, the VBM is above the atomic Pb and I orbitals. If, for example, an Pb vacancy is formed, it is surrounded by I dangling bonds leading to an energetic defect state between the I p orbital and the VBM and thus not within the band gap. Similar considerations can be also made for an iodine vacancy, when the defect is formed by Pb dangling bonds. The energy level of the corresponding state should be located between Pb p atomic orbital and the CBM forming a shallow trap state.[65] Obviously, the defect tolerant nature can be ascribed to the antibonding orbitals forming the bands. This is in contrast to many classical semiconductors like Si or GaAs, where the VB is formed of bonding orbitals and the CB is formed of antibonding orbitals both originating from the same atomic states. Any vacancy therefore induces defects with energies deep inside the band gap.[257,274] The unusual feature of the antibonding character in the VBM of lead halide perovskites is considered to be the origin for their defect tolerance,[275] which can mostly be found in metal-non-metal systems.[51]

3.1.2. Radiative Recombination

Band-to-band recombination describes a process, where an excited electron from the CB recombines directly with a hole from the VB. This process is accompanied by the emission of a photon, hence the term radiative recombination is often applied. To satisfy the momentum conservation, semiconductors with an indirect band gap rely on the additional emission of phonons during the recombination event. For this reason, recombination between carriers from the VBM and CBM is disfavored in contrast to direct semiconductors like $MAPbI_3$. Considering the multiphonon model, as discussed for the description of SRH recombination, direct recombination via the emission of multiple phonons is highly unlikely to occur, hence it can be neglected for inorganic lead halide perovskites.[256] This is in contrast to OPVs, where it has been demonstrated very recently that direct non-radiative recombination occurs in organic semiconductors and scales with the energy levels of the donor-acceptor materials.[276] This is ascribed to intramolecular vibrations, whereby the C-C double bond in particular plays a significant role due to a large vibrational energy of 160 meV, for which reason only a few phonons are required to mediate transitions. Since these bonds are unavoidable in conjugated polymers, it sets an undesirable intrinsic limitation for OPVs.

The radiative recombination rate is typically expressed by[253]

$$R_{rad} = k_{rad}(np - n_i^2). \tag{3.6}$$

Under thermal equilibrium, the principle of detailed balance between absorption and emission links the radiative recombination coefficient k_{rad} to the absorption coefficient α. According to van Roosbroeck and Shockley,[277] the relation can be written as

$$k_{rad} n_i^2 = \int_0^\infty 4\pi n_r^2 \alpha(E) \phi_{bb}(E) dE, \tag{3.7}$$

where n_r is the refractive index and ϕ_{bb} spectral black-body radiation. The equation shows, that the radiative rate under thermal equilibrium equals the generation of electron-hole pairs by thermal background radiation. It is noted, that k_{rad} is carrier density independent and a material property which cannot be influenced by traps or defects like SRH recombination. Further, the van Roosbroeck-Shockley equation implies that highly absorbing materials also have high radiative rate constants. Recently, Davies et al.[278] measured absorption spectra and applied Equation 3.7 in order to calculate k_{rad} and compared the obtained values to extracted fitting parameters from previously published transient terahertz photoconductivity measurements.[91] The authors found coincidence between both methods and determined $k_{rad} = 0.5 - 1.0 \cdot 10^{-9}$ cm^3/s at room temperature, clearly showing that a radiative recombination in $MAPbI_3$ event can be treated as an inverse absorption process. These values for the radiative rate constant are in a similar range as reported in a multitude of publications obtained by fitting transient optical experiments.[92,279] The small variation of reported values underlines the intrinsic nature of the parameter. To put the values in perspective, indirect semiconductors such as Si demonstrate lower radiative rate constants ($k_{rad} = 5 \cdot 10^{-15}$ cm^3/s).[280]

Nevertheless, the determination of k_{rad} is often complicated due to a multitude of different effects that result in the rate appearing lower. For example, it has been suggested that a direct-indirect nature of the band gap due to the Rashba effect slows down radiative recombination.[281] The strong spin-orbit coupling in combination with an inversion symmetry breaking rising from polar distortion could split the spin degenerate band edges in k-space.[282,283] Therefore, it is speculated that a phonon-assisted recombination pathway could decrease the observed values for k_{rad}. However, the effect of Rashba splitting on recombination rates is under debate, since a recent publication verified the direct band gap via fast transient absorption and photoluminescence measurements.[284] The authors observed an increase in PL intensity within the first picoseconds indicating that radiative recombination has an increased probability if the carriers thermalize to the band edges, which is a unique feature of direct semiconductors. Another effect, which can effectively prolong the measured lifetimes, is the reabsorption of a previously emitted photon.[285] This process is called photon recycling and is known to occur in direct semiconductors with high absorption coefficients. It has been shown for lead halide perovskites, that photon recycling can increase carrier lifetimes and mask internal radiative recombination rates. Further, it can increase the device performance.[286–288]

Since radiative recombination is determined by the material and is unavoidable, it sets an intrinsic limit for the open-circuit voltage and efficiency of any PV device. For this reason, it is also considered as the basis for the calculation of the Shockley-Queisser limit, which expresses the maximum theoretical efficiency of a single-junction solar cell.[289]

3.1.3. Auger Recombination

Similar to SRH recombination, Auger recombination describes a non-radiative recombination event, when the energy and momentum of an electron-hole recombination is transferred to a third particle which subsequently thermalizes back to the VBM or CBM. This type of recombination is usually important, when the carrier density is high. Then, the probability that the third particle is close enough to recombination event of two other charge carriers is increased. Auger recombination strongly depends on the electronic band structure and is also affected by impurities and phonons which are involved in the conservation of the momentum.[290] The inverse process of Auger recombination is called impact ionization, where an highly energetic electron collides with another electron in a crystal and creates an electron-hole pair.[291]

In general, the recombination rate can be expressed as[163,291]

$$R_{Aug} = (k_{Aug,n} \cdot n + k_{Aug,p} \cdot p)(np - n_i^2), \tag{3.8}$$

where $k_{Aug,n}$ and $k_{Aug,p}$ are the corresponding Auger rate constants, depending on if an electron or a hole is involved as a third particle. Similar to radiative second-order recombination, Auger recombination also represents an unavoidable loss channel in solar cell materials. Wang et al. have demonstrated the impact of Auger recombination under high illumination intensities in perovskite-based concentrator PVs.[250]

3.2. Charge Carrier Lifetimes

As already indicated in Equation 3.1, all discussed recombination processes occur in parallel and therefore shorten the lifetime of photogenerated charge carriers and prevent them from surviving in the valence and conduction bands. For this reason, each charge carrier has a finite lifetime, which represents the time until it returns back to a non-excited state via one of the possible recombination processes. In general, the charge carrier lifetime describes the carrier concentration as a function of time.

The total recombination rate R is therefore the sum of the rates of all possible recombination processes[170]

$$R = R_{SRH} + R_{rad} + R_{Aug}. \tag{3.9}$$

Inserting Equations 3.2, 3.6 and 3.8 yields the full expression

$$R = \left[\frac{1}{\tau_p(n+n_t) + \tau_n(p+p_t)} + k_{rad} + (k_{Aug,n} \cdot n + k_{Aug,p} \cdot p) \right] (np - n_i^2), \tag{3.10}$$

which represents a more detailed reflection of Equation 3.1. Since no analytical solutions exist for the full expression, numerical solutions usually need to be taken into account. Nevertheless, the focus on special cases with the involvement of several simplifications can still lead to analytical solutions[163,292] as will be exemplary shown in the next paragraph.

Considering the SRH process as the only recombination mechanism in combination with one SRH lifetime τ_{SRH} and a photogenerated charge carrier population as previously discussed in Equation 3.5, the recombination rate is

$$R = \frac{dn}{dt} = -\frac{n}{\tau_{SRH}}. \tag{3.11}$$

Thus, the solution of this differential equation reads

$$n(t) = n(0) \cdot \exp\left(-\frac{t}{\tau_{SRH}} \right), \tag{3.12}$$

where $n(0)$ corresponds to the initial photo-induced charge carrier density. In this case, the charge carrier lifetime τ_{SRH} is a constant value and independent of charge carrier density and includes characteristics of the material and the involved states (see Equation 3.4). However, this case is far from being general, as usually different recombination processes exist in real materials.

Generally, the presence of one recombination mechanism in a device allows to define a lifetime which characterizes this single process. If each of the recombination processes summed up in Equations 3.9 and 3.10 are described by a lifetime, the total lifetime τ can be calculated by adding up the different lifetimes reciprocally[170,293]

$$\frac{1}{\tau} = \frac{1}{\tau_{SRH}} + \frac{1}{\tau_{rad}} + \frac{1}{\tau_{Aug}}. \tag{3.13}$$

It is worth to note here, that the total lifetime is charge carrier density dependent and thus varies with time.[163] As a direct consequence, lifetime comparison between different material systems and PV devices can only be conducted as the charge carrier density is simultaneously measured as highlighted by Pivrikas et al.[294] and Stranks et al.[295] in a scientific discussion. Nevertheless, many publications only report pure lifetimes but fail to provide information regarding the measurement (illumination) conditions and therefore the charge carrier density. By conducting PL measurements, for example, it is only possible to determine the lifetime, but the carrier concentration in the sample cannot be measured directly. For this reason, the intensity of the laser pulse is used to estimate the charge carrier density in the film. In contrast, the present thesis will focus on the determination and analysis of charge carrier lifetimes in relation to the corresponding measured charge carrier densities. This is a huge benefit of the herein employed transient electrical methods (see Section 4.3 for details on the working principle of these techniques) as they allow to identify how carrier lifetime scales with carrier concentrations. As a consequence, the dominant recombination mechanism can also be calculated as it is shown in Chapter 6.

3.3. Relationship between Recombination and PV Parameters

In the previous sections, various recombination processes that can occur in semiconductors and thus also in solar cells were explained. So far, no connection has been established to PV parameters such as the open-circuit voltage. In an ideal case, a semiconductor absorbs all photons corresponding to energies, which are higher than the band gap. Since real devices do not have an external quantum efficiency of unity over the whole spectral range of sunlight, j_{sc} is lower compared to a perfectly absorbing solar cell. However, under j_{sc} conditions, all photogenerated charge carriers should leave the device as long as extraction time is longer than the recombination lifetime. This assumption is justified for perovskite solar cells, since high mobilities and diffusion lengths in combination with thin active layers allow for a fast extraction. The situation can be different in OPVs, when excitons move trough large polymer domains providing low carrier mobilities and promoting therefore a recombination event prior to charge separation at an acceptor-donor interface.[249]

However, maximizing only the photocurrent is not sufficient to increase the efficiency as the electrical power depends on the product of both current and voltage. Hence, V_{oc} has also to be increased for prepare high performing solar cells. Under steady-state open-circuit conditions, the externally applied voltage compensates the generated voltage from the device such that generation equals recombination and carrier extraction is completely suppressed. Recombination losses therefore prevent the quasi Fermi level splitting from reaching its full potential and decrease the maximum achievable voltage. Accordingly, the V_{oc} itself is already a quantity which describes the amount of recombination losses in fully working devices. For this reason, a connection between recombination parameters (such as charge carrier lifetime and density and the diode ideality factor) and the open-circuit voltage is necessary and will be introduced in the next part.

After charge carrier generation and thermalization to the VBM and CBM, both electrons and holes are in their respective bands for a finite lifetime until they disappear by recombination. Under steady-state illumination, the electrons and holes are in thermal equilibrium with the lattice and the charge carriers occupy the states in their bands according to a Fermi distribution at the device temperature. It follows for density of electrons in the CB[170]

$$n = N_C \exp\left(-\frac{E_C - E_{Fn}}{k_B T}\right) \tag{3.14}$$

and in the same way for holes in the VB

$$p = N_V \exp\left(-\frac{E_{Fp} - E_V}{k_B T}\right). \tag{3.15}$$

From these equations, the quasi Fermi levels can be determined to be

$$E_{Fn} = E_C - k_B T \ln\left(\frac{N_C}{n}\right) \tag{3.16}$$

for the electron quasi Fermi level and

$$E_{Fp} = E_V + k_B T \ln\left(\frac{N_C}{p}\right) \tag{3.17}$$

for the hole quasi Fermi level. From a thermodynamic perspective, the quasi Fermi levels of electrons and holes correspond to their electrochemical potentials η_n and η_p.[170,296] The total energy of an electron and a hole can be calculated as the sum of their electrochemical potentials corresponding to the externally measurable voltage V via

$$eV = \eta_n + \eta_p = E_g - k_B T \ln\left(\frac{N_C N_V}{np}\right). \tag{3.18}$$

It follows that the electrochemical energy of an electron-hole pair is not exclusively determined by the band gap, but also ruled by the effective densities of states and the charge carrier concentrations. This expression links the external parameter voltage with internal parameters such as the carrier density and corresponds to the starting point for the discussion on the impact of different recombination mechanisms on V_{oc}.

Under open-circuit, the generation rate G and recombination rate R cancel out, such that $G = R$. Assuming pure radiative recombination, the recombination rate can be written as $R \approx \mathrm{k}_{rad} np$ according to Equation 3.6 if the photogenerated charge carrier densities are substantially higher than the intrinsic ones. In this case, the product np in Equation 3.18 can be replaced by G/k_{rad} and it follows

$$eV_{oc,rad} = E_g - k_B T \ln\left(\frac{N_C N_V k_{rad}}{G}\right). \tag{3.19}$$

This equation quantifies the impact of the radiative rate constant on V_{oc}. For a given generation rate, it ultimately sets an intrinsic limit for the V_{oc} of a solar cell, since both E_g and k_{rad} are material constants. This limit is often referred to as the radiative limit since it describes the maximum achievable photovoltage $V_{oc,rad}$ in a PV device. More details regarding this parameter will be provided in Chapter 7.

Analogous to the previous consideration, the voltage for pure SRH recombination can also be calculated under the assumptions that n and p are predominantly photogenerated ($n \approx p$) and one dominant SRH lifetime as in Equation 3.5. It follows for the SRH limited voltage $V_{oc,SRH}$

$$eV_{oc,SRH} = E_g - k_B T \ln\left(\frac{N_C N_V}{\tau_{SRH}^2 G^2}\right) = E_g - 2k_B T \ln\left(\frac{\sqrt{N_C N_V}}{\tau_{SRH} G}\right). \tag{3.20}$$

In this case, the photovoltage depends on the SRH lifetime, which is a parameter that is determined by material properties like the defect density (see Equation 3.4). Thus, it can be addressed in order to increase V_{oc} by the reduction of non-radiative recombination losses.

However, the cases of pure radiative or SRH recombination rarely occur in real solar cells and a simultaneous combination of both mechanisms is more suited to describe carrier dynamics. If both recombination processes are present, $G = R \approx k_{rad}np + n/\tau_{SRH}$ and the $V_{oc,rad+SRH}$ can be calculated in analogy to both above-mentioned cases based on Equation 3.18 and reads

$$eV_{oc,rad+SRH} = E_g - k_B T \ln\left[N_C N_V \cdot \left(\frac{-\frac{1}{\tau_{SRH}} + \sqrt{4Gk_{rad} + \frac{1}{\tau_{SRH}^2}}}{2k_{rad}}\right)^{-2}\right]. \tag{3.21}$$

Equation 3.19, Equation 3.20 and Equation 3.21 underline, why V_{oc} is sometimes referred to as the recombination parameter since it exclusively depends on the interplay between generation and recombination.

In the next step, a connection between the dominant recombination mechanism and n_{id} will be developed. Under open-circuit, the Shockley Equation 2.8 can be solved for V_{oc} with $j = 0$ and $j_{ph} = j_{sc}$

$$V_{oc} = \frac{n_{id}k_B T}{q} \ln\left(\frac{j_{sc}}{j_0} + 1\right) \approx -\frac{n_{id}k_B T}{q} \ln\left(\frac{j_0}{j_{sc}}\right). \tag{3.22}$$

It has to be noted, that the impact of R_{series} is ignored since external current flow is suppressed under these conditions. In addition, R_{shunt} is neglected as the current is small compared to the recombination current trough the diode at sufficiently high voltages. Subsequently, the + 1 term in the logarithm of Equation 3.22 can also be ignored as the fraction j_{sc}/j_0 is usually orders of magnitude larger. By comparing the second term in Equation 3.19 and Equation 3.20 with Equation 3.22, the similarity of the logarithmic expression is noticeable as G corresponds to j_{sc}.[174] Accordingly, the prefactor in front of $k_B T$ can be identified as n_{id}. It follows from Equation 3.19, that for pure radiative recombination $n_{id} = 1$. In case of pure SRH recombination, Equation 3.22 reveals $n_{id} = 2$. The ideality factor can therefore be used as a direct measure of the dominant recombination mechanism, where a value of $1 < n_{id} < 2$ indicates that both types of recombination are present.[297]

In addition to the already discussed cases in Equation 3.19 and Equation 3.20, there are also further limits for n_{id}. A detailed analysis of recombination pathways and their relation to n_{id} can be found in References[174,298,299]. For example, $n_{id} = 1$ also applies to SRH recombination in heavily doped semiconductors since $n \approx p$ does not hold anymore. In case of a n-doped material, n corresponds to the density of ionized dopants N_D^+ ($n \approx N_D^+$) and $n \gg p$ in the low injection regime. It follows for a pn-junction that the ideality factors are different depending if a SRH recombination event takes place in the quasi-neutral or the depletion region. Surface recombination due to non-selective contacts can lead to $n_{id} \leq 1$. If SRH recombination takes place through a series of recombination centers and the recombination is dominated by more than one trap, n_{id} can exceed values of 2.[174,299]

After j_{sc} and V_{oc} are discussed, the influence of recombination on the last important parameter, the FF, is still missing. The fill factor depends on both, the resistive losses in the device (including shunt and series resistance) and the recombination losses and is therefore the most complicated parameter in solar cells. Since no closed form solution for the FF exist, it can only be described empirically as will be demonstrated in Chapter 8.

Extending the Bucket Analogy

Once the basics of charge carrier recombination have been introduced, the unfinished picture of the water bucket from Chapter 2.3.2 can be completed. Recombination processes prevent solar cells from reaching their full voltage potential and therefore hinder the water bucket from being completely filled. Figure 3.3 depicts a water bucket under open-circuit conditions (closed valve), as it has already been shown on the right-hand side in Figure 2.7. Because the valve is closed, no water flows out of the bucket and

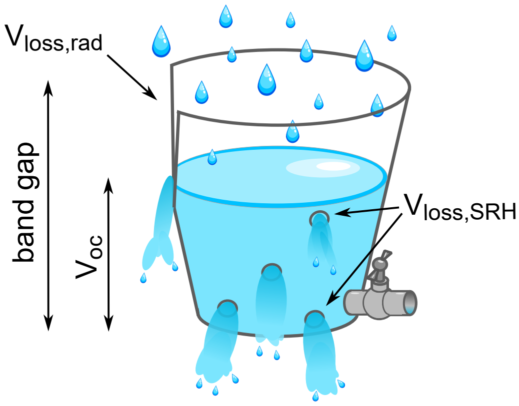

Figure 3.3.: Extented water bucket analogy under open-circuit conditions from Figure 2.7 where charge carrier recombination prcoesses are included. Recombination processes lead to a leaky bucket where the shape and the size of the holes characterize the recombination mechanisms. The lateral opening of the bucket represents unavoidable losses due to radiative recombination and accordingly limits the water level/the maximum achievable voltage. The other holes represent SRH recombination which can be avoided.

the water level reaches a maximum, which originates from the interplay between the incident water drops (generation) and charge carrier recombination processes. The introduced recombination losses correspond to holes of different sizes and shapes reducing the water height significantly. SRH processes are illustrated as holes close to the bottom of the bucket, since they are usually dominant at low charge carrier concentrations. Because SRH recombination is avoidable, the holes also can be closed, for example by a reduction of the defect density. Further, there is an opening over the whole height of the bucket corresponding to radiative recombination losses. This mechanism is not visualized by a circular hole, but by a larger opening that cannot be closed and extends all the way to the bottom. This ensures that generation equals recombination under very low light intensities even in case of no SRH processes being present. It accordingly limits the water height if all SRH recombination holes are closed and prevents the water bucket from overflowing. As real devices always suffer from recombination losses, the leaky bucket is a better representation in comparison to the bucket in Figure 2.7.

4. Experimental Methods

As already introduced in Section 2.3.1, perovskite solar cells consist of individual layers of both organic and inorganic nature. In the following chapter, the materials used in this thesis will be discussed and a short introduction into solar cell preparation will be given. Furthermore, the working principle of the experimental methods will be presented. Different measurement techniques are used to investigate recombination processes in fully working devices under operation conditions. Open-Circuit Voltage Decay and and Transient Photovoltage are measured to determine the lifetime of the charge carriers, while the Charge Extraction method is applied in order to calculate the corresponding charge carrier concentration.

4.1. Materials

Optoelectronic devices based on perovskite semiconductors rely on a complicated interplay between different materials. As already introduced in Figure 2.4, different device layouts are established in the field of perovskite PV. The versatility of these layouts has also contributed to a multitude of different transport layers and electrodes which are used to prepare solar cells. In this thesis, both n-i-p and p-i-n solar cells are studied in a planar device configuration. A mesoporous TiO_2 scaffold is not employed as an electron transport layer, since it usually suffers from more pronounced j-V hysteresis (see Section 2.3.3) and demonstrates slow transient behavior in optical and electronic measurements.[300] Since the PCE of a perovskite solar cell is not exclusively determined by the active layer, but also affected by charge selective layers, extensive studies on the identification of high-performing transport materials exist.[144,301] Figure 4.1 provides an overview over the herein investigated transport layers. VB and CB energies of $MAPbI_3$ and the energies of the highest occupied molecular orbital (HOMO) and the lowest unoccupied molecular orbital (LUMO) of the different organic compounds are included in the diagram. The HOMO and the LUMO correspond to the VB and CB in organic materials and originate from different hybridizations of the s and p orbitals of carbon. The hybridization leads to alternating single and double bonds and therefore creates a delocalized π-electron system,

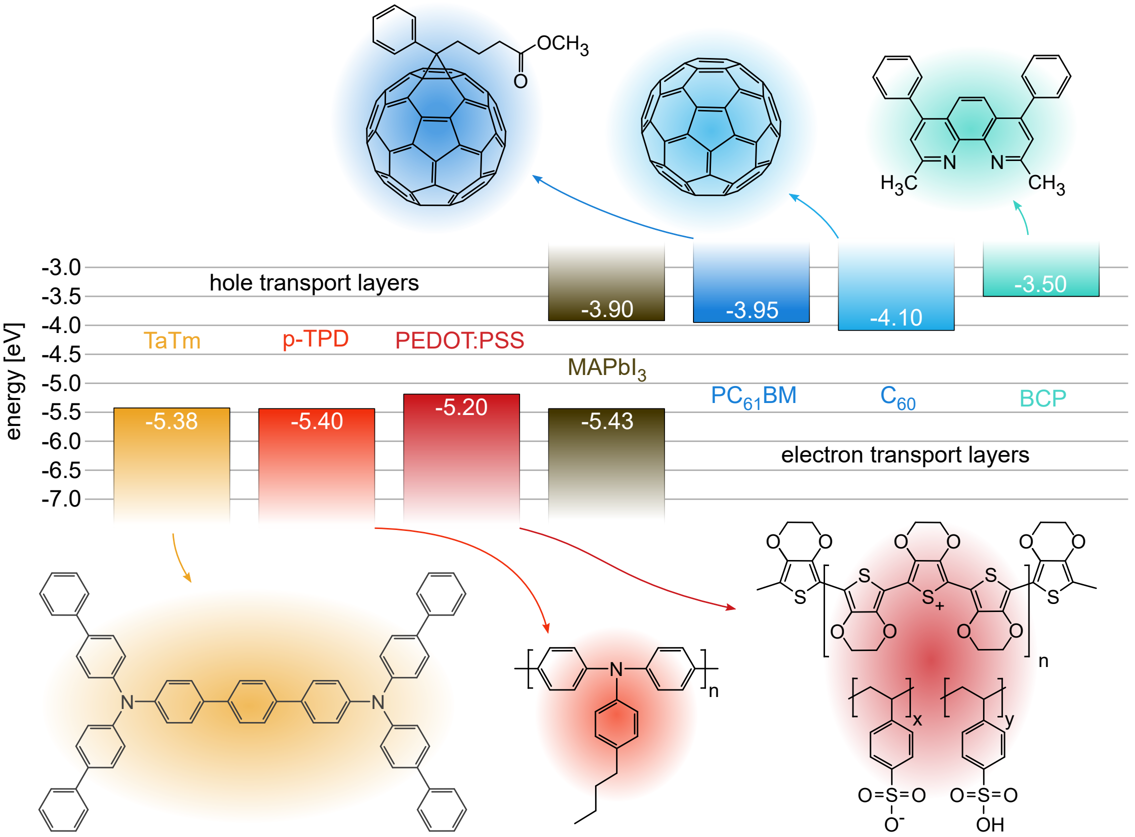

Figure 4.1.: Energy levels of the HOMO's and LUMO's and the corresponding chemical structures of the hole and electron transport materials used in the herein presented studies. For comparison, the VBM and CBM of MAPbI$_3$ are included. All organic transport layers have the conjugated π-electron system in common. Values for energy levels are taken from References [144,145,302,303].

which provides semiconducting properties.[304] The chemical structures are also illustrated in Figure 4.1, highlighting that all molecules are composed of such conjugated π-electron systems. As HTL's, N4,N4,N4",N4"-tetra([1,10’-biphenyl]-4-yl)-[1,1’:4’,1"-terphenyl]-4,4"-diamine (**TaTm**), poly[N,N-bis(4-butilphenyl)-N,N-bis(phenyl)-benzidine] (**p-TPD**) and poly(3,4-ethylenedioxythiophene):polystyrene sulphonate (**PEDOT:PSS**) are used, while **C$_{60}$**, **PC$_{61}$BM** and 2,9-dimethyl-4,7-diphenyl-1,10-phenanthroline (**BCP**) represent the ETL's. In the following, a brief description of these materials will be given.

TaTm

The arylamine derivative TaTm is a HTL, where the HOMO energy of -5.38 eV matches with the VB of the perovskite. With a LUMO energy of -2.30 eV, it provides an energetic barrier for electrons from the CB of MAPbI$_3$.[303] It is often implemented in fully evaporated n-i-p and p-i-n perovskite solar cells, since it exhibits reproducible sublimation conditions and allows for highly efficient PV devices.[303,305,306]

p-TPD

Another wide band gap semiconducting arylamine, which is also serves as an HTL, is p-TPD. It consists of a nitrogen atom with three aryl groups and belongs to the class of polymers. With a HOMO level of -5.4 eV, it demonstrates good band alignment for the injection of holes from the perovskite. Additionally, the LUMO energy of -2.4 eV enables an efficient blocking of electrons. Its first implementation in perovskite PV was reported in 2013 by Malinkiewicz et al.[302] It developed into a frequently used transport material, not only in perovskite PV,[307,308] but also in the field of organic LEDs.[309] After the preparation of thin p-TPD layers, the material displays hydrophobic character due to the butylene group, which complicates the perovskite deposition on top, since perovskites precursors are typically dissolved in hydrophilic solvents (see Section 4.2). To overcome the wetting issue, several strategies[310,311] have been proposed, like the additional deposition of an amphiphilic interfacial compatibilizer between p-TPD and the perovskite.[308]

PEDOT:PSS

The last HTL is the water-based PEDOT:PSS, which is a mixture consisting of two components. Figure 4.1 shows the chemical structure of the individual ingredients, with the upper structure representing the PEDOT and the lower structure the PSS. The conjugated polymer PEDOT is consists of polythiophene and is mainly responsible for the high electrical conductivity with values up to 4600 S/cm,[312] while the PSS counterpart is based on polystyrene sulfonate. In thin films, both polymers are strongly interlinked, which results in a high transparency in the visible part of the electromagnetic spectrum. Furthermore, by tuning the PEDOT:PSS ratio, the conductivity can be controlled over several orders of magnitude.[313] In aqueous solution, PEDOT:PSS forms micelles, with PSS forming the interface to H_2O molecules while PEDOT is embedded in the inner part of the aggregates, which leads to a high solubility and excludes toxic solvents.[314] Over the past decades, these properties have contributed to the development of PEDOT:PSS into a frequently encountered material in organic and perovskite solar cells.[315,316]

C_{60}

Nowadays, a large number of different fullerenes exists with the most popular being the buckminsterfullerene C_{60}. For its discovery in 1985, Kroto and coworkers were awarded the Nobel Prize in chemistry in 1996.[317] Within a short period of time, considerable improvements in synthesis have contributed to the fact that the material could be produced in larger quantities and thus also studied more easily.[318,319] It consists of 60 carbon atoms, which together form 12 pentagons and 20 hexagons arranged in an spherical configuration, for which reason the molecule is often called *buckyball*. Due to its high electron affinity, it is often employed as a electron transport layer in perovskite solar cells. Electron mobilities in the range of $10^{-3} - 10^{-2}$ cm^2/(Vs) are usually reported[320,321] in combination with diffusion lengths of 400 nm allowing for sufficient transport in PV devices.[322] Furthermore, the material features a LUMO energy matching to the CB of the perovskite and has a band gap of about 1.9 eV.[323] Since it is not soluble in organic solvents, it is usually deposited by thermal evaporation, as shown in Section 4.2.

$PC_{61}BM$

In order to make the C_{60} molecule solution processable, Hummelen et al. synthesized $PC_{61}BM$, which is functionalized with a phenyl and methyl butyrate side chain.[324] This chain increases the solubility in organic polar solvents and leaves the optoelectronic properties of pure C_{60} almost unaffected. Both, the energy levels and the electron mobilities are similar in both fullerene derivates.[302,321,325] The molecule has a successful history in OPVs, as it has been applied as an electron acceptor for many years until the efficiency was outnumbered by introducing fullerene-free acceptors.[14,15] Together with the C_{60} and other fullerene derivates, it is one of the most commonly used ETL's in perovskite PV.

BCP

With a LUMO energy of -3.5 eV, BCP is not considered as a conventional transport layer, but acts as a buffer layer between the fullerene and the metal electrode. It was often employed in OPVs to reduce recombination losses at the acceptor-electrode interface[326] and therefore also adopted for perovskite solar cells. Even though its working principle is not yet fully understood, recent studies suggest that thin BCP layers reduce undesired charge accumulation in the ETL and replace the Schottky barrier with an ohmic contact, which increases the PCE and improves device stability.[327,328]

4.2. Device Preparation

Intensive research over the past years has allowed the development of various methods for the preparation of perovskite solar cells. All devices studied in this work were fabricated in a planar device configuration as depicted in Figure 2.4b. For this approach, a glass substrate coated with ITO provides the basis (VisionTek Systems Ltd., United Kingdom). With typical film thickness of only 100 – 200 nm, ITO exhibits a high average transmission in the visible range of up to 92 % and a low specific electrical resistance in the order of 10^{-4} Ωcm.[329] In order to define the active area precisely and prevent short circuits when contacting the device, the substrate is patterned with a chemical photolithography process. Afterwards, the substrate is prepared for further processing by different cleaning steps. It is cleaned for 10 minutes each in water, acetone and isopropanol before being treated for 30 seconds in an oxygen plasma to completely remove organic contamination.

Preparation of the HTL

An HTL is first deposited on the cleaned glass substrate. As already mentioned in the previous section, this can be either TaTm, p-TPD or PEDOT:PSS. In case of TaTm (Novaled, Germany), the substrate is transferred to a vacuum chamber integrated into a nitrogen-filled glovebox and evacuated to a pressure of $\approx 10^{-6}$ mbar. The material are then sublimed at temperatures around 250 °C to achieve a constant evaporation rate of 0.5 Å/s. The evaporation rate and thickness (10 – 50 nm) are controlled by quartz crystal microbalance sensors. In contrast, p-TPD and PEDOT:PSS are processed from solution via spin coating. p-TPD (1-Material, Canada) is dissolved in 1,2-Dichlorbenzene with a concentration of 7 mg/ml and spin cast in an inert nitrogen-filled glovebox resulting in a layer thickness of 10 nm. Afterwards, the substrates is annealed at 110 °C to remove residual solvent. Aqueous PEDOT:PSS solution (Clevios™ P VP AI 4083, Heraeus, Germany) is deposited (40 nm) under ambient conditions without any further modification and annealed at 130 °C inside the glovebox.

Preparation of the Perovskite

The herein investigated perovskite layers are prepared by various methods, as schematically illustrated in Figure 4.2. Most methods involve the use of lead iodide (PbI_2) and methylammonium iodide (CH_3NH_3I or MAI) as reactants, whereby the formation of the perovskite is described by the reaction equation

$$PbI_2 + CH_3NH_3I \longrightarrow CH_3NH_3PbI_3. \tag{4.1}$$

Similar to the HTL's, perovskite films can be prepared either from solution or by thermal evaporation in a inert nitrogen-filled glovebox. When processing from solution, a distinction is made between the one-step and the two-step process. At the beginning of the one-step process, often denoted as the *mixed precursor* approach, a PbI_2 (Sigma-

Aldrich, Germany) stock solution is prepared by dissolving 1.5 mol in a 4:1 volume mixture of N,N-Dimethylformamide (DMF) and Dymethylsulfoxide (DMSO) and stirred over night on a hotplate adjusted to 25 °C. Afterwards, a small amount of MAI (Lumtec, Taiwan) is added to a second vial. Shortly before use, the PbI_2 solution is heated to 180 °C to ensure that the lead iodide is completely dissolved. After cooled down to room temperature again, the PbI_2 solution is added to the MAI vial such that the molar ratio between PbI_2 and MAI is 1:1 to obtain the required ratio from Equation 4.1. The resulting PbI_2/MAI solution is than stirred for at least 2 hours to ensure optimum intermixing and deposited by spin casting. During rotation of the spin coater, additional (non-dissolving) solvent (usually Chlorbenzene) is dispensed on the sample to wash out the solvents from the perovskite solution. Since the solvent is not dissolving the perovskite, but helps to remove the other solvents, the procedure is often referred to as anti-solvent washing. Introduced in 2014, it is considered as a major breakthrough in the preparation of perovskite films as it improves the horizontal growth conditions and reduces unwanted vertical elevations, resulting in much smoother and more homogeneous layers.[330–332] Further, it also increases the device reproducibility. The substrate is then annealed at 100 °C for 15-30 minutes to remove residual solvents and allow for full perovskite conversion. Further details on the application of the one-step approach can be found in Reference[333].

In the two-step process, which has been established by Xiao et al. in 2014, two individual solutions have to be prepared.[334] First, a 600 mg/ml solution of PbI_2 in DMF is prepared and stirred over night at 70 °C before use. The solution is then spin cast on the substrate, followed by an annealing step of 15 minutes at 70 °C. After cooled down to room temperature, a MAI solution (40 mg/ml in Isopropanol) is deposited by spin coating. It is important to use an orthogonal solvent in this to prevent the dry PbI_2 layer from being washed away. The substrate is then annealed at 100 °C for 1 hour to start the interdiffusion process and allow for the chemical reaction between the two layers. However, this approach often suffers from low PCE values and an insufficient reproducibility due to unreacted PbI_2 at the bottom of the substrate. To avoid this issue, it was suggested to add a small amount of MAI already to the PbI_2 solution.[335,336] In this case, MAI is already present in the PbI_2 layer leading to a larger disorder and therefore an increased volume of the crystal. If the MAI solution is spin coated in the next step, it is easier for the MAI to penetrate trough and react with the PbI_2 leading to an accelerated conversion and less unreacted salts afterwards. The best results are usually obtained with a molar ratio of 0.2 with respect to PbI_2. In addition, it has been shown that it is beneficial to anneal perovskites in DMSO solvent vapor atmosphere in order to increase the domain size of the polycrystalline layers and ensure a complete

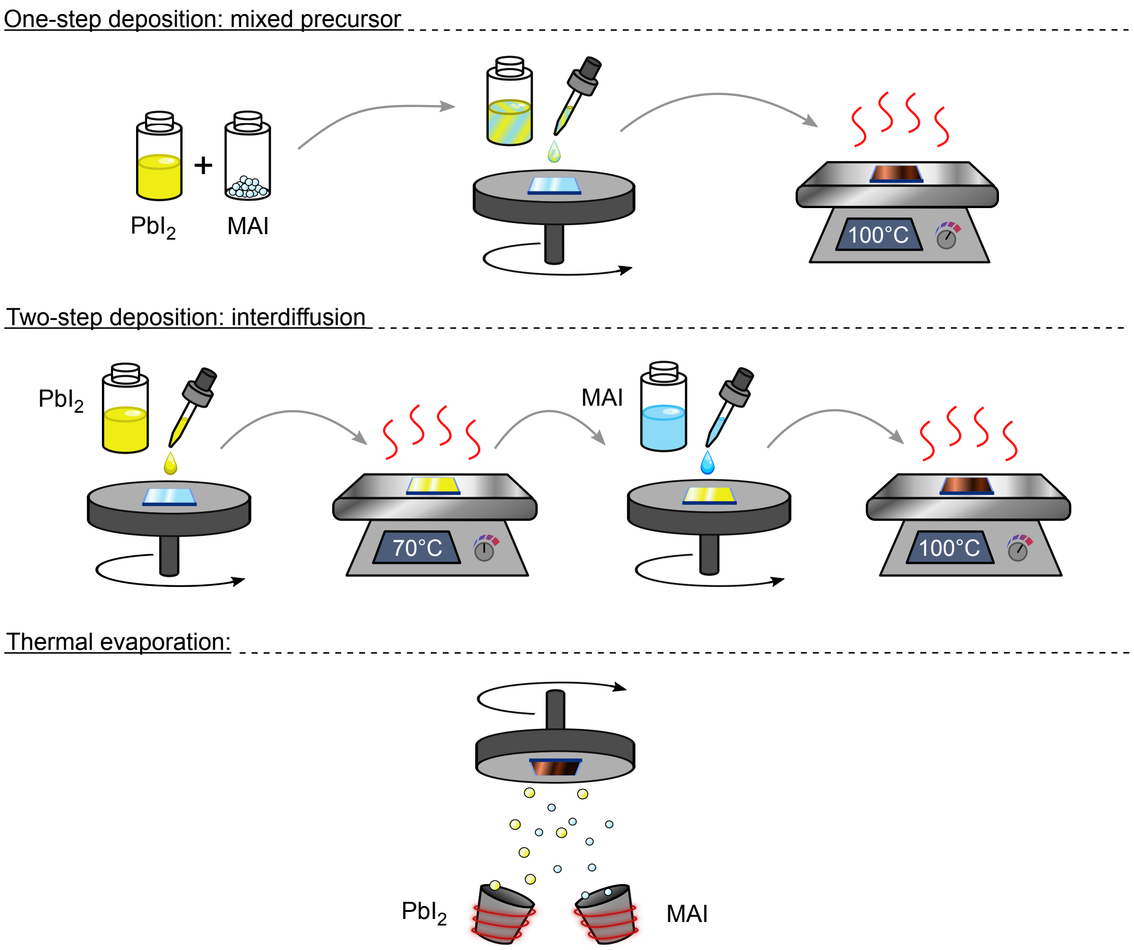

Figure 4.2.: Overview of different fabrication methods for perovskite films. Perovskite layers can be prepared either by dissolving both salts (PbI_2 and MAI) and depositing the solution via spin-coating or by applying thermal evaporation. Solution-based methods are usually divided into one-step and two-step deposition. Further explanations are provided in the main text.

reaction.[118] For this reason, the substrate is annealed at 100 °C in a closed metal box with a few μl of DMSO after spin coating the MAI salt. Both modifications (adding a small amount of MAI in the PbI_2 solution and annealing in a solvent atmosphere) improve the PCE and reproducibility of the solar cells noticeably and are applied to all studied devices in this work, which were prepared by the two-step approach.

The third method for preparing thin perovskite layers is thermal evaporation. Two crucibles, one filled with PbI_2 (TCI Chemicals, Japan) and the other one filled with MAI (Lumtec, Taiwan) are heated in an evacuated evaporation chamber under a pressure of 10^{-6} mbar. To achieve evaporation rates of 0.5 Å/s for PbI_2 and 1.0 Å/s for MAI, the crucibles were heated to 250 °C and 70 °C, respectively. The co-deposition of both materials leads to perovskite films, where the thickness can easily be controlled via the deposition time. To obtain homogenous substrate coverage, the substrate holder, which is located above both crucibles, is rotating during evaporation. All fully evaporated perovskite solar cells studied in this work are prepared by the group of Dr. Henk Bolink from the University of Valencia (Spain). Further information on vapor-deposited perovskites is provided in Reference[337].

Preparation of the ETL

After the preparation of the perovskite film, the electron transport layers are deposited. If the perovskite absorber is prepared by spin coating, it is necessary to smooth the surface with a 20 nm $PC_{61}BM$ (Solenne, Netherlands) layer. For this reason, a 20 mg/ml solution from 1,2-Dichlorbenzene is spin cast on the perovskite, followed by annealing for 1 hour at 100 °C resulting in a film thickness of 10-20 nm. In the next step, the substrate is transferred into an evaporation chamber, where 20 nm of C_{60} (Solenne, Netherlands), 8 nm BCP (Sigma-Aldrich, Germany) and a 60 nm gold electrode are deposited via evaporation under a pressure of 10^{-6} mbar. The evaporation rate is kept constant at ≤ 0.5 Å/s for C_{60} and BCP, but is higher for the gold (≥ 1.0 Å/s). In case of fully evaporated solar cells, C_{60} (Sigma-Aldrich, Germany) is directly employed on top of the perovskite layer with an evaporation rate of 0.5 Å/s until a thickness in the range of 10 and 50 nm is reached.

4.3. Transient Electrical Techniques

The following section briefly introduces the transient electrical methods which are applied in this thesis to study charge carrier recombination processes in perovskite solar cells. In complete devices, charge carrier recombination parameters, like the charge carrier lifetime or the density are not directly accessible. For this reason, steady-state and transient behavior of V_{oc} is often studied, since charge carrier generation equals recombination under open-circuit. As discussed in Chapter 3, first insights on recombination can be already obtained by determining the diode ideality factor. To gain further information, both charge carrier lifetime and the corresponding density are herein measured with optoelectrical methods. All time-resolved measurements are performed in a closed-cycle helium cryostat to avoid water-induced degradation processes within the solar cells and precisely control the device temperature (by a Lakeshore 332 cryogenic temperature controller). In order to obtain recombination parameters for different open-circuit voltages, the illumination intensity is varied over several orders of magnitude. For all measurements, a high power LED array, which is driven by a Keithley 2602 Source Meter, is employed to generate steady-state illumination conditions. To calibrate the LED current, j_{sc} of every device is first measured in an inert glovebox under a simulated AM1.5 G spectrum with an irradiance of 100 mW/cm². Then, the device is transferred into the cryostat and the LED current is adjusted such that the device generates the same j_{sc} as previously determined in the glovebox. This intensity is defined as 1 sun illumination. The intensity can be changed by varying the LED current and using neutral density filters.

4.3.1. Open-Circuit Voltage Decay

Open-Circuit Voltage Decay (OCVD) experiments are a simple tool to study internal recombination losses in solar cells. First recombination studies by employing voltage decay measurements on germanium were conducted already in 1955 by Lederhandler and Giacoletto.[338] After broad application in classical pn-junctions, OCVD was also adopted to study charge carrier dynamics in DSSCs,[339,340] OPVs[341] and very recently in perovskite solar cells.[342]

A schematic presentation of the measurement procedure is shown in Figure 4.3. During the whole experiment, the device is kept under open-circuit conditions via a 1 TΩ high-impedance voltage amplifier (Femto Messtechnik GmbH). The solar cell is then illuminated with a LED to generate an excited carrier population which leads to an open-circuit voltage. It is important to illuminate for a sufficiently long time (usually in the order ms to s) to ensure that steady-state conditions are reached in the device. At time t_0, the illumination source is turned off and the voltage decay is monitored as

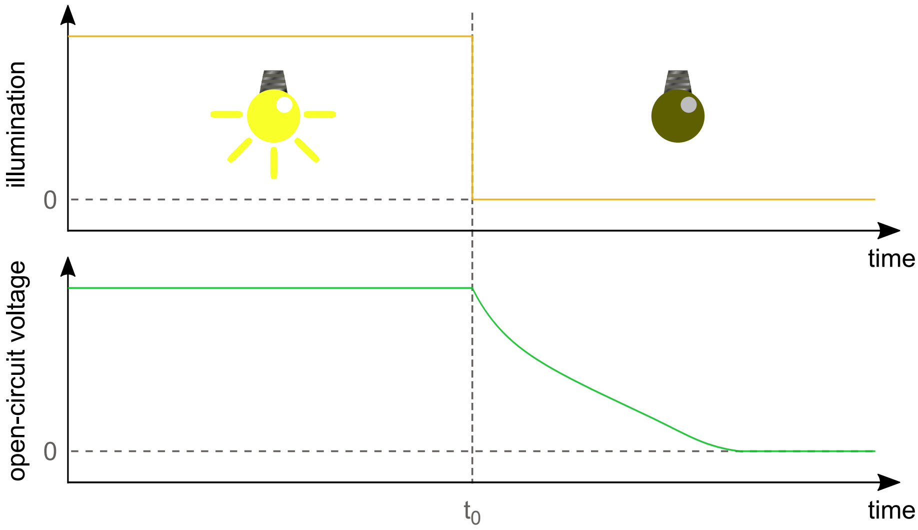

Figure 4.3.: Working principle of OCVD measurements. A solar cell is kept under open-circuit and illuminated with a constant light source. After reaching steady-state conditions, the light is switched off and the voltage decay is recorded as a function of time. The resulting decay curve can be analyzed by using Equation 4.3 to obtain the carrier lifetime τ_{OCVD}.

a function of time using an Agilent Infinium 90254A digital storage oscilloscope. Since electrical current is impeded all the time, the only way for charge carriers to relax back to their equilibrium states is via recombination processes inside the device. V_{oc} is then affected by the decreasing carrier density since it follows the relationship

$$V_{oc} = \frac{k_B T}{q} \cdot \ln\left(\frac{np}{n_i^2}\right). \tag{4.2}$$

This expression can be directly obtained, if Equations 3.14 and 3.15 are multiplied with each other and $N_C N_V \cdot \exp\left(-\frac{E_g}{k_B T}\right)$ is replaced by n_i^2. Since recombination processes are not instantaneous, the time evolution of the open-circuit voltage allows conclusions to be drawn regarding the charge carrier lifetime. As previously demonstrated in a various publications,[340,343,344] the charge carrier lifetime τ_{OCVD} can be determined from the slope of the voltage decay according to

$$\tau_{OCVD} = -\frac{n_{id} k_B T}{q} \left(\frac{\mathrm{d}V_{oc}(t)}{\mathrm{d}t}\right)^{-1}. \tag{4.3}$$

The main benefit of employing lifetime determination from OCVD signals arises from the fact that it is a continuous measurement providing high resolution in voltage and is collected in short time. All OCVD results shown in this work were usually averaged over 4 – 8 individual measurements to increase the signal-to-noise ratio, which is important for the analysis of the data. To increase the signal quality even further, additional mathematical smoothing is employed prior to taking the derivative.

4.3.2. Transient Photovoltage

Another possibility to determine the charge carrier lifetime in solar cells is the small-signal method Transient Photovoltage (TPV). The basic idea of the method can be dated back to 1955, where it was developed to study germanium and silicon.[345] The method experienced great attention during the last decade in the investigation of novel thin-film solar cells such as OPVs[346,347] and perovskites.[348,349]

A simplified overview on the working principle is provided in Figure 4.4. A solar cell is first illuminated with constant bias light and kept under open-circuit conditions during the whole measurement by using the same experimental setup as for OCVD measurements. The steady-state V_{oc} is then perturbated by a small optical pulse generated by a Nd:YAG (neodymium-doped yttrium aluminium garnet) laser ($\lambda = 532$ nm, EKSPLA PL-2210) with a pulse duration of 80 ps. Upon laser excitation, the additionally created charge carriers lead to an increase in voltage ΔV_{oc}. In order to maintain quasi-equilibrium conditions, the laser intensity is attenuated with neutral density filters such that the relation $\Delta V_{oc} \ll V_{oc}$ holds, which is relevant for further evaluation of the voltage transient as will be explained in the next paragraph. Since the device is kept under open-circuit conditions the whole time, the additionally generated charge carriers Δn have to recombine until the steady-state carrier concentration originating from the bias LED light is reached again.

The small optical perturbation leads to an increased total charge carrier density, which can be expressed as $n + \Delta n$. With insertion into Equation 3.1 it follows

$$\begin{aligned}\frac{\mathrm{d}(n+\Delta n)}{\mathrm{d}t} &= -\left(k_1(n+\Delta n) + k_2(n+\Delta n)^2 + k_3(n+\Delta n)^3\right)\\ &= -\left[k_1 n\left(1+\frac{\Delta n}{n}\right) + k_2 n^2 \underbrace{\left(1+\frac{\Delta n}{n}\right)^2}_{1+2\left(\frac{\Delta n}{n}\right)+\left(\frac{\Delta n}{n}\right)^2} + k_3 n^3 \underbrace{\left(1+\frac{\Delta n}{n}\right)^3}_{1+3\left(\frac{\Delta n}{n}\right)+3\left(\frac{\Delta n}{n}\right)^2+\left(\frac{\Delta n}{n}\right)^3}\right].\end{aligned} \tag{4.4}$$

Considering the small-perturbation approximation $\Delta V_{oc} \ll V_{oc}$ such that $\Delta n \ll n$, all terms $(\frac{\Delta n}{n})^x$ with x being larger than 1 are neglected and the expression can be rearranged

$$\begin{aligned}\frac{\mathrm{d}(n+\Delta n)}{\mathrm{d}t} &\approx -\left[k_1 n\left(1+\frac{\Delta n}{n}\right) + k_2 n^2\left(1+2\frac{\Delta n}{n}\right) + k_3 n^3\left(1+3\frac{\Delta n}{n}\right)\right]\\ &= -\underbrace{\left[k_1 n + k_2 n^2 + k_3 n^3\right]}_{\frac{\mathrm{d}n}{\mathrm{d}t}} - \Delta n \underbrace{\left[k_1 + 2k_2 n + 3k_3 n^2\right]}_{k_{eff}}.\end{aligned} \tag{4.5}$$

The first bracket can be identified as the rate equation without the small perturbation, while the second bracket is independent of Δn and can be treated as an effective recombination coefficient k_{eff}. Thus, the recombination rate for the additionally generated charge carriers (being proportional to ΔV_{oc} can be written as

$$\frac{\mathrm{d}\Delta V_{oc}}{\mathrm{d}t} \propto \frac{\mathrm{d}\Delta n}{\mathrm{d}t} \approx -k_{eff}\Delta n = \frac{\Delta n}{\tau_{\Delta n}}. \tag{4.6}$$

Here, k_{eff} is expressed by the small-perturbation lifetime $\tau_{\Delta n}$. Solving the differential equation yields an exponential relationship between Δn and $\tau_{\Delta n}$ according to

$$\Delta n = \Delta n_0 \exp\left(-\frac{t}{\tau_{\Delta n}}\right) \tag{4.7}$$

and the measurable voltage decay back to the steady-state V_{oc} via

$$V_{oc}(t) = V_{oc} + \Delta V_{oc} \exp\left(-\frac{t}{\tau_{\Delta n}}\right). \tag{4.8}$$

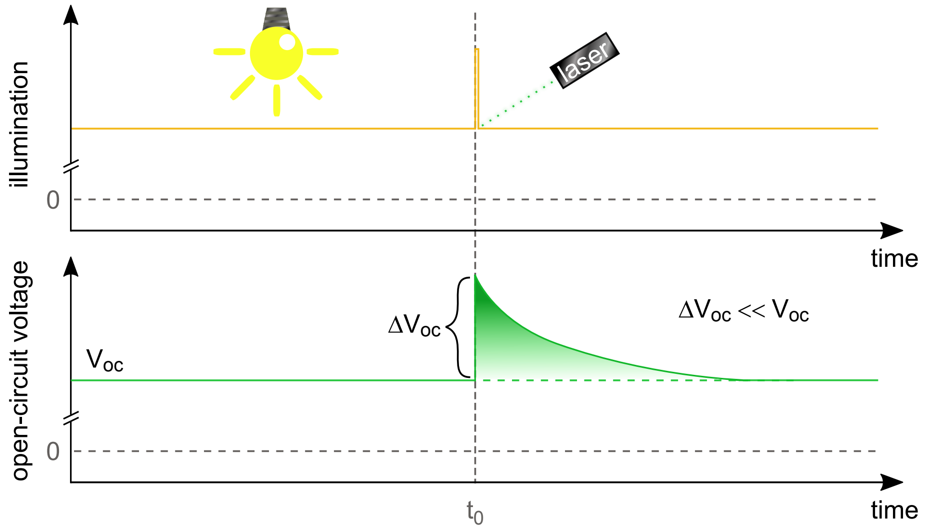

Figure 4.4.: Schematic illustration of an TPV experiment. The solar cell is kept under open-circuit conditions and illuminated with constant background illumination. At $t = t_0$, a short laser pulse generates additional charge carriers in the device such that the voltage rises by ΔV_{oc}. If the small perturbation meets the requirement $\Delta V_{oc} \ll V_{oc}$, the resulting voltage transient can be used to determine the charge carrier lifetime at the particular background illumination/open-circuit voltage.

By fitting the measured voltage transient with an exponential decay, the charge carrier lifetime can be determined as a function of illumination/open-circuit voltage. Usually TPV experiments are conducted at a multitude of different background illumination intensities, where $\Delta V_{oc} \approx 5 - 15$ mV to meet the requirement $\Delta V_{oc} \ll V_{oc}$. The advantage of TPV consists in the simpler evaluation with an exponential fit function compared to OCVD, where the derivative of an large and equally noisy transient signal needs to be calculated. In order to increase the signal quality also for TPV, a transient is recorded 100 times and then averaged. Since the measured lifetimes are a function of V_{oc} and therefore n, the equally important parameter of carrier density needs also to be determined to correctly understand recombination dynamics under operating conditions.

4.3.3. Charge Extraction

Charge Extraction (CE) is often selected to determine the charge carrier density in a solar cell under a specific illumination intensity.[249,350–352] A CE experiment is conducted directly after TPV at the same illumination intensity to correlate the obtained values with each other. Prior to each measurement, an j-V measurement under illumination is performed (Keithley 2602 Source Meter) to identify V_{oc}. The CE procedure itself is divided into two different steps, as illustrated in Figure 4.5: first, the solar cell is illuminated with constant light and the previously measured V_{oc} is applied,

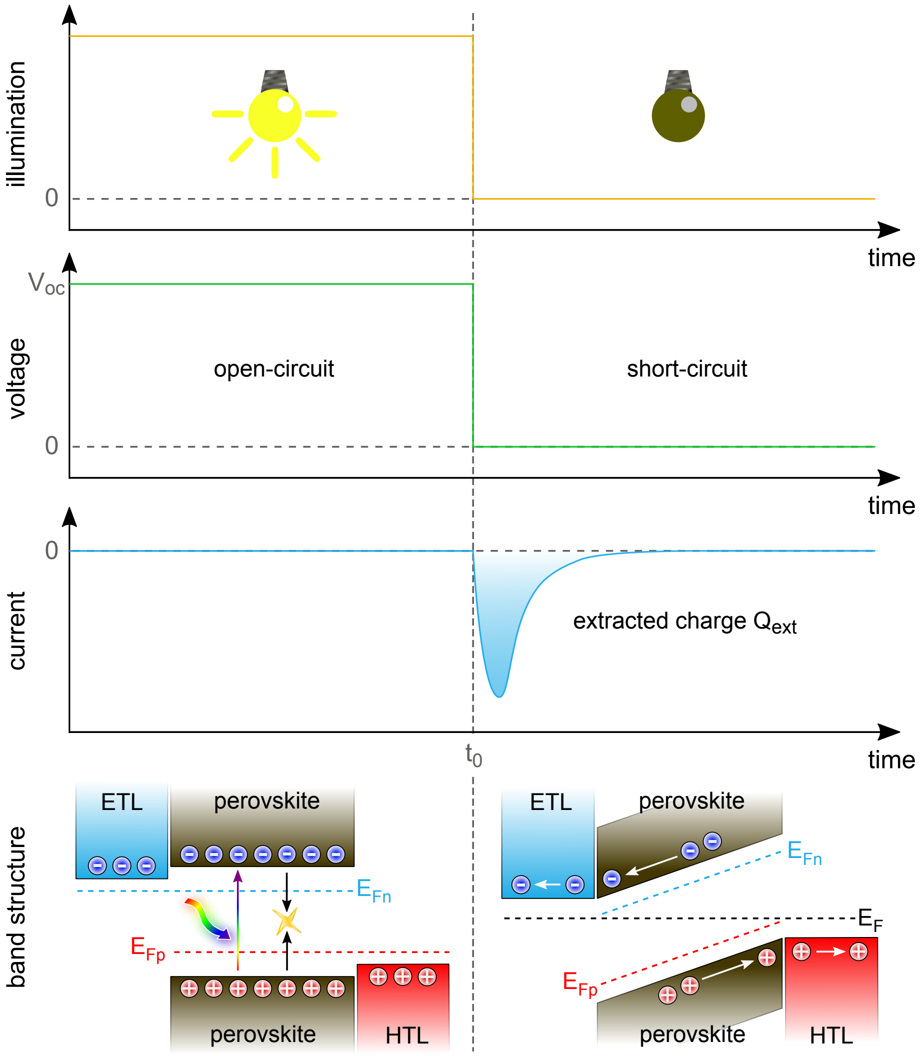

Figure 4.5.: Simplified scheme of a CE experiment. In the first step, the solar cell is illuminated with a constant illumination source and the measured V_{oc} is applied. Under these conditions, no current is flowing and the device is under open-circuit. In the second step, the illumination source is turned off and the solar cell is simultaneously switched from open-circuit to short-circuit conditions. The resulting current transient is then recorded, integrated and normalized to the volume of the active area to calculate the charge carrier density, which was stored in the device under the particular illumination intensity.

such that the device is kept under open-circuit and a steady-state carrier population is generated. At $t = t_0$, the illumination source is turned off and the device is simultaneously switched to short-circuit conditions. This is realized by a fast Texas Instruments SN74LVC1G3157 analog switch (with response time of 3 ns), which is triggered by an Agilent 81150A pulse generator. The resulting current transient is amplified by a Femto DHPCA-100 current-voltage amplifier and recorded by the same digital storage oscilloscope as used for OCVD and TPV. The current transient is then averaged 15 times to improve the signal-to-noise ratio. By integrating the obtained current to get the extracted charge Q_{ext}, the charge carrier density stored inside the device under the particular illumination intensity can be calculated via

$$n = \frac{Q_{ext}}{Adq} = \frac{1}{Adq} \int_{t_0}^{t_{stop}} I(t)\, \mathrm{d}t, \tag{4.9}$$

where A is the active area of the device, which is defined by the overlap of ITO and the metal electrode (see Section 4.2). The thickness d of the active layer is individually measured for every solar cell with a Veeco Dektak 150 profilometer. The time t_{stop} is defined by the moment, where $I(t_{stop}) \approx 0$, which is typically reached on the μs timescale for perovskite solar cells. The combination of both TPV and CE measured at the same illumination conditions allows for a detailed analysis of recombination losses in fully working devices under operating conditions and provides a powerful toolbox to determine the rates and orders of recombination processes.

However, the recorded current transients do not necessarily have to originate from charge carriers inside the active layer, but also can be affected by charges stored in the transport layers or at the electrodes. For this reason, additional measurements are performed in the dark to account and correct for these capacitive charge carriers. The exact procedure and discussion will be provided in Section 5.6 and the general influence of capacitive effects on the introduced transient electrical techniques will be studied in Chapter 5.

5. Capacitive Effects in Transient Electrical Measurements

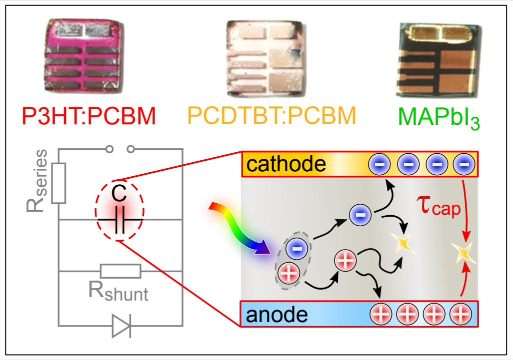

Abstract. Lifetime evaluation of solar cells is frequently conducted via both optical and electrical means with the purpose of obtaining a deeper understanding of the dominant performance limiting recombination mechanisms. Here, these previously assigned lifetimes are re-evaluated as often being severely influenced by capacitive decay rates of spatially separated charge carriers. This misconception hence explains the sometimes observed irregularities between optically and electrically determined lifetimes. In addition, it is revealed that not only the lifetimes determined by OCVD and TPV, but also charge carrier densities derived from CE measurements can be affected by capacitive charge carriers. It is shown that capacitive effects are very often ruling these measurements and therefore interfere with the assignment of important recombination parameters. To explore this limitations in more detail, an analytical expression outlining under which conditions relevant bulk recombination parameters are electrically accessible in thin-film solar cells is provided. In order to make general statements regarding different PV devices, the study includes not only perovskite solar cells, but comprises also other technologies such as OPVs and Si solar cells.

This chapter is partially based on

D. Kiermasch, A. Baumann, M. Fischer, V. Dyakonov and K. Tvingstedt. Revisiting lifetimes from transient electrical characterization of thin film solar cells; a capacitive concern evaluated for silicon, organic and perovskite devices. *Energy & Environmental Science*, 11, 629-640 (2018). DOI: 10.1039/C7EE03155F

5.1. Introduction

Thin film solar cells made from novel materials with high absorption coefficients are generally much cheaper to produce than their thicker counterparts and therefore represent a promising alternative to low-cost large-scale electricity production. However, thin solar cells made from innovative materials such as organics or metal halide perovskites need to have high PCE's to be able to compete with the already commercially established technologies. To grasp what limits the voltage produced by solar cells under illumination, it is necessary to understand the mechanisms behind the disappearance rate of the photogenerated electrons and holes in the device. The build-up and disappearance of charge carrier densities in solar cells involve a variety of processes including absorption and charge carrier generation, separation, transport via drift and diffusion, recombination in the bulk, via traps, at the surfaces or from the electrodes themselves. All these processes occur on a time scale ranging from sub-picoseconds [353,354] to in some cases several seconds or even hours. [355] Effectively designing PV components for optimized PCE always relies on maximizing the carrier generation and transport processes and simultaneously minimizing the recombination processes towards the radiative limit of the corresponding material. [354]

The lifetime of photogenerated charge carriers is one of the most important parameters in solar cells, as it rules the recombination rate that defines the open-circuit voltage (see Chapter 3) and the required minimum extraction time. Identifying the dominant recombination mechanism and the corresponding rate (lifetime) is accordingly an important subject of any PV researcher, independent of material and technology. Both optical and electrical transient measurements are therefore frequently employed with the purpose to approach this. Contactless optical methods such as terahertz spectroscopy, [356] transient absorption, [357] transient photoluminescence, [91,358–361] and transient microwave photoconductivity [92,362] all provide information related to the overall disappearance rate of excited states or charge carriers in the active material. These methods are widely performed on pure absorber materials without transport layers and at excitation intensities that differ from operating conditions. Direct electrical measurements on PV materials embedded in a device configuration probe instead the disappearance rate of excess carrier densities and the corresponding quasi Fermi level splitting as introduced in Section 4.3. Monitoring the rate at which this property decays provides accordingly the sought-after information of how the associated excess charge carriers disappear in a solar cell. In the time-domain, the most common methods employed are based on measuring the decay of V_{oc}, either by the full signal OCVD method or by the small-perturbation technique of TPV. In the corresponding frequency-domain, the rates are monitored by impedance spectroscopy[363–366] or intensity modulated voltage or current spectroscopy.[237] All rate determination methods need a complementary technique to identify the relationship between carrier density and voltage. In case of the time-domain methods, this is provided by either combining Transient Photocurrent (TPC) with TPV (usually referred to as Differential Charging) or alternatively by the CE method. The frequency-domain-methods rely instead on the integral of various forms of differential capacitance–voltage measurements.[364,367] Both the time-domain and frequency-domain methods are therefore in principle able to determine the charge carrier lifetime as a function of carrier density.

However, there is caveat with these methods originating from that they were initially developed for thicker indirect band gap germanium or silicon solar cells.[338] Devices comprising these inorganic crystalline materials are very different compared to many novel thin-film solar cells mostly in terms of their carrier lifetimes, but also in their band gaps, thicknesses, capacitances and layouts. Thin-film solar cells are necessarily relying on materials with higher absorption coefficients leading to active layer film thickness in the range of 20 – 500 nm. The high absorption coefficient allows a smaller thickness that however leads to devices with larger (geometric) capacitance values. Electrical characterization methods employed to determine recombination dynamics under operating conditions are therefore not always easily transferable to new generation thin-film PV devices.

Charge carrier lifetimes determined from the analysis of electrical transients are for most of the mentioned PV technologies ranging typically from 1 microsecond at sun intensities up to several milliseconds or even seconds at reduced intensities. These long lifetimes of excess charge carriers are quite peculiar, as they are several decades longer than those determined via complementary optical measurements such as transient photoluminescence. This discrepancy in lifetimes has not only been frequently observed in OPVs,[368,369] but also in perovskite solar cells during the last years.[370,371] Both optical and electrical methods are claiming to probe charge carrier lifetimes relevant for steady-state conditions, but obviously cannot both be correct if determined at equal carrier densities. In addition, a strong non-linear dependence of charge carrier lifetimes on voltage is observed, when transient electrical methods are employed to study recombination losses. The observed strong dependence on illumination intensities has been interpreted as that the dynamics cannot be described by first-order recombination processes, where the lifetime should be constant over at least a small range of excess carrier densities (and consequently V_{oc}'s). In case of DSSCs, the very long lifetimes up to several seconds[340] are generally attributed to a slow second-order chemical reaction rate between electrons and ions present in the electrolyte. However,

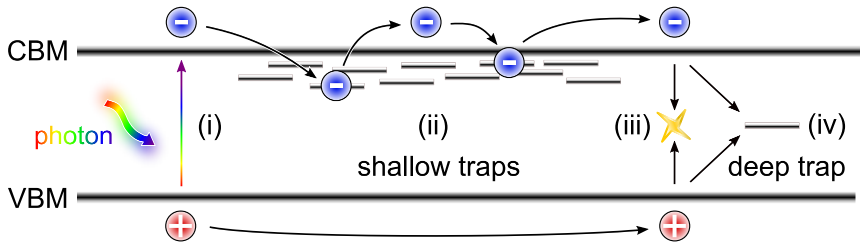

Figure 5.1.: Principle of increased carrier lifetimes by carrier trapping and detrapping processes. An electron is trapped and released at shallow traps, which do not act as SRH recombination centers until it finally recombines radiatively or non-radiatively via a deep trap. This procedure can prolong the effective carrier lifetime.

a quite identical dependence is also observed in most organic and perovskite based solar cells studied so far. In these solid-state components, slow chemical reactions are not suitable to generally explain the charge carrier kinetics. A power law dependence of recombination rates with second- or higher-order recombination kinetics in combination with assumptions of trapped charges in a broad DOS has often been ascribed to account for both the strong dependency of voltage and the very long lifetimes. In this common picture, the long lifetimes originate from a non-linear relationship between trapped and free charges, where shallow traps slow down the overall recombination rate and not speed up recombination as it is generally the case for deep mid gap trap states.[370] This trapping-detrapping procedure is illustrated in Figure 5.1, where an electron gets trapped and detrapped until it recombines radiatively with a hole or non-radiatively via a deep trap. However, it is unclear why the long lifetimes often occur exclusively in electrical measurements on devices while optical methods are not affected. Obviously, the presence of transport layers and electrodes influences the measured lifetimes.

In this chapter, both theoretical and experimental evidence is provided for that carrier trapping is not responsible for the slow recombination rates often encountered in thin-film solar cells. Charge carrier lifetimes are determined via both OCVD and TPV methods on a multitude of different PV technologies indicating that some of the obtained lifetimes are very often associated with a capacitive discharging rate instead of bulk recombination in the active layer. In addition, it is revealed that the same effects also influence CE experiments, which also complicates the determination of the corresponding charge carrier densities. The objective of this study is therefore to experimentally clarify the general influence of quasi-static capacitive effects on charge carrier lifetime and density determination by electrical time-domain approaches.

5.2. Devices and Current-Voltage Characteristics

For sake of technological generality, four different solar cells with very diverse properties are experimentally evaluated to highlight the overall message. Three of these devices correspond to novel thin-film solar cells, while the fourth one is a classical monocrystalline Si photodiode (S1787-04, Hamamatsu) included as an additional reference. Further information regarding the Si device can be found in Reference[372]. Figure 5.2 summarizes the different device architectures of the thin organic and perovskite solar cells. In both organic devices, 30 nm of PEDOT:PSS act as the hole transport layer (see Section 4.1) and 3 nm calcium with 110 nm of aluminium are used as the electron selective contact. Both metals are deposited via thermal sublimation. For the active layers, a mixture of an electron donor and electron acceptor were dissolved and deposited via spin coating resulting in the well-known bulk heterojunction layout. The P3HT and $PC_{61}BM$ active layer was deposited by spin coating a chlorobenzene solution (36 mg/ml total concentration with a molar ratio of 1:0.8) to obtain a layer thickness of 150 nm. For the other OPV device, Poly[N–9'–heptadecanyl–2,7–carbazole–alt–5,5–(4',7'–di–2–thienyl–2',1',3'–benzothiadiazole)] (PCDTBT) was dissolved together with $PC_{61}BM$ in molar ratio of 1:4 and a total concentration of 20 mg/ml. This configuration rendered a film thickness of 80 nm. The perovskite device is based on p-TPD as HTL and a combination of C_{60}, $PC_{61}BM$, BCP and gold as the electron selective contact. The $MAPbI_3$ active layer was prepared by the two-step interdiffusion process outlined in Section 4.2. Since all devices employ the same fullerene, it is further abbreviated with PCBM instead of $PC_{61}BM$.

To put the selected set of photovoltaic devices and their performance in relation to each other, their dark and illuminated j–V curves are presented in Figure 5.3. Measure-

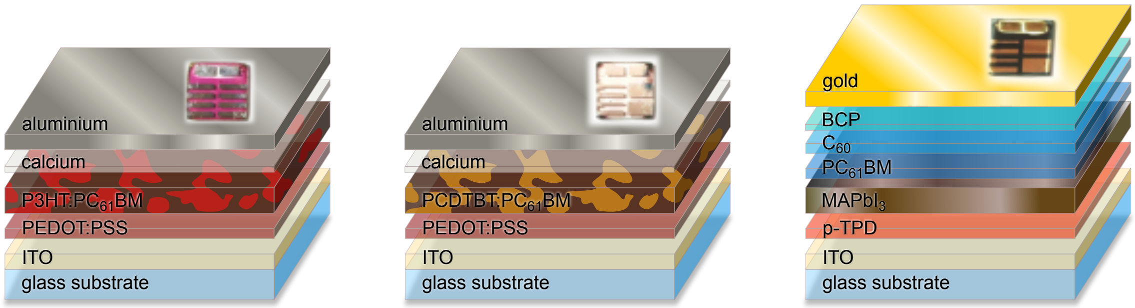

(a) P3HT:$PC_{61}BM$ **(b)** PCDTBT:$PC_{61}BM$ **(c)** $MAPbI_3$

Figure 5.2.: Device layouts of the studied thin-film PVs. Two organic solar cells in a bulk heterojunction architecture consisting of **(a)** P3HT:$PC_{61}BM$ and **(b)** PCDTBT:$PC_{61}BM$ and a perovskite **(c)** $MAPbI_3$ based device are investigated.

ments in the dark are presented on a logarithmic scale, while the illuminated curves are depicted on a linear scale. In order to determine n_{id} and j_0, the exponential term of the Shockley Equation 2.8 is used as a fit function and the obtained values are summarized in Table 5.1. The extracted n_{id}'s vary from exactly one for the Si photodiode to exactly two for the perovskite cell, with both OPV devices ranging in between. A closer look at the illuminated j-V characteristics reveals that the PCDTBT:PCBM solar cell shows the lowest PCE of 2.8 %. Both, the Si and the P3HT:PCBM devices have a PCE of 3.9 %, while the perovskite solar cell is the most efficient device with a PCE of 12.2 %. In case of the perovskite device, both the forward and backward measurements are shown, proving that only minor hysteresis behavior can be observed.

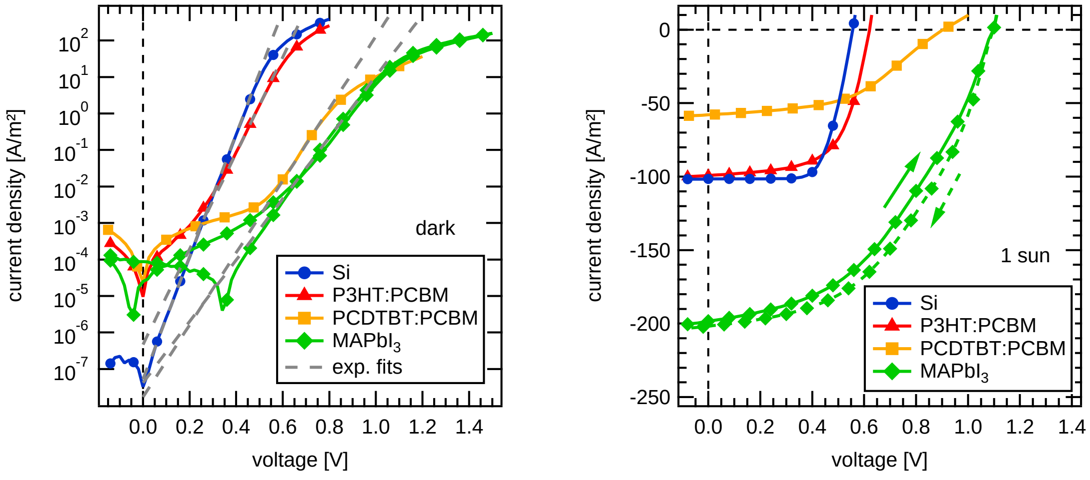

(a) **(b)**

Figure 5.3.: j-V characteristics for all four studied PV devices **(a)** in the dark and **(b)** under illumination. The grey dashed lines correspond to exponential fits according to Equation 2.8 in order to determine j_0 and n_{id}. For the MAPbI$_3$ solar cell, both the forward and backwards scans are shown to illustrate only minor current-voltage hysteresis. All extracted PV parameters are summarized in Table 5.1

device	n_{id}	j_0 [Am^{-2}]	j_{sc} [Am^{-2}]	V_{oc} [V]	FF [%]	PCE [%]
Si photodiode	1.0	$5.2 \cdot 10^{-8}$	101	0.56	69	3.9
P3HT:PCBM	1.3	$4.6 \cdot 10^{-7}$	99	0.63	62	3.9
PCDTBT:PCBM	1.7	$1.7 \cdot 10^{-8}$	58	0.90	52	2.8
MAPbI$_3$	2.0	$4.2 \cdot 10^{-8}$	198	1.10	56	12.2

Table 5.1.: Extracted PV parameters from Figure 5.3 for all studied devices from j-V characteristics in the dark and under 1 sun illumination.

5.3. Determination of Charge Carrier Lifetimes

In this section, charge carrier lifetimes are determined using transient electrical methods and different recombination regimes are identified. These techniques have advantages in comparison to optical measurements, as they are able to determine recombination dynamics on a wide range of timescales in fully working devices. Figure 5.4a shows normalized TPV transients in a semi-logarithmic plot for the set of studied devices. The background illumination intensity was adjusted to be 1 sun. The decays of all thin-film devices are well-described by a single-exponential fit according to Equation 4.8, revealing the shortest lifetime for the perovskite ($\tau = 0.39\ \mu s$) and the longest transient for the P3HT:PCBM device ($\tau = 2.87\ \mu s$). The decays for the Si device are summarized in the inset, where the illumination intensity corresponds to 1 sun and 0.001 suns. In case of the lower intensity, the data is fitted by a single exponential function leading to $\tau = 142.7\ \mu s$, whereas at 1 sun illumination, a double exponential nature is detected with time constant of $\tau_1 = 2.53\ \mu s$ and $\tau_2 = 48.1\ \mu s$. OCVD transients for the same devices are presented in Figure 5.4b. Prior to the decay, every device was illuminated with 1 sun intensity. Quite different decay dynamics can be observed between the studied devices: for example, the P3HT:PCBM solar cell displays the shortest

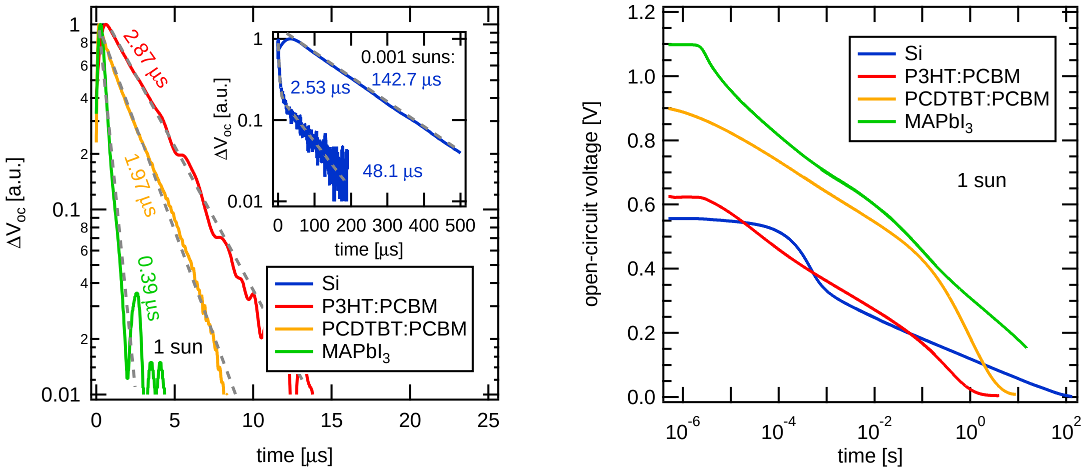

(a)

(b)

Figure 5.4.: (a) TPV decays for the studied thin-film PVs at an illumination intensity of 1 sun. The data is fitted with an exp. decay according to Equation 4.8 in order to extract the TPV lifetime τ. The logarithmic representation clearly shows that all decays are well described by a single-exponential decay. This is contrary to the Si device, which is shown in the inset. Here, at low light intensities (0.001 suns), a single exponential decay is observed while at higher intensities (1 sun) a double-exponential decay is measured and hence two lifetimes can be extracted. **(b)** OCVDs for all devices, where the solar cells were illuminated with 1 sun prior to the decay.

time to reach 0 V among the thin-film PVs even though its TPV lifetime is the longest one. The perovskite and the Si device demonstrate the longest OCVD decays with up to 115 s for the silicon device. Furthermore, all devices have different slopes strongly depending on the time after the light was switched off which indicates differences in the responsible recombination mechanisms during each decay.

To examine how the obtained TPV lifetimes scale with open-circuit voltage, measurements are performed for a plethora of different logarithmically spaced steady-state light intensities ranging from a minimum of 10^{-6} suns up to a maximum of 3 suns. It is noted that for this range of intensities the requirement $\Delta V_{oc} \ll V_{oc}$ is ensured for every measurement (see Section 4.3.2). The determined lifetimes are plotted as a function of V_{oc} in Figure 5.5a. In addition, OCVD lifetimes (solid lines) determined from Figure 5.4b by applying Equation 4.3 are included. The obtained lifetimes vary from a few hundred nanoseconds to even seconds for the range of measured open-circuit voltages. It can be confirmed that the measured lifetimes and their relation to V_{oc} indeed are identical within very respectable accuracy for all materials such that $\tau_{TPV} \approx \tau_{OCVD}$. TPV additionally provides two clearly identifiable lifetimes in the high-voltage regime of the Si device, whereas the OCVD only succeeds in identifying the longer lifetime. That the inverse derivative of the large signal OCVD generally equals small-perturbation lifetimes from TPV or Intensity-Modulated Photovoltage Spectroscopy (IMVS) was also observed for DSSC[340,344] and recently for perovskites.[373] After having confirmed the overall identity between OCVD and TPV lifetimes in all four devices, the general behavior of how the determined lifetimes relate to internal voltage is evaluated. For the Si photodiode, two quite constant charge carrier lifetimes are found for all voltages above 0.4 V. These lifetimes are individually associated with the thin back p-layer and the front thicker n-layer. Accordingly, the recombination is truly of first-order type with constant lifetimes in this regime as expected for heavily doped semiconductors. At lower voltages (< 0.4 V), only one value can however be recognized, where the determined lifetime is rapidly increasing with decreasing voltage. The large set of TPV illumination intensities as well as the OCVD measurements easily allow to identify that in this region the logarithm of the lifetime scales linear with voltage. As it is impossible that the dominant recombination dynamics should make a transition from a first-order process at high carrier densities to a higher-order process at low carrier densities, this cannot be the origin of the voltage-dependent lifetimes below 0.4 V. These voltage-dependent lifetimes are also observed for the other PV devices. While the perovskite solar cell shows an almost constant slope over the whole intensity range, both organic devices exhibit regions of different slopes. In case of the PCDTBT:PCBM device, a transition occurs from a nearly constant lifetime at voltages below 0.5 V to a steeper

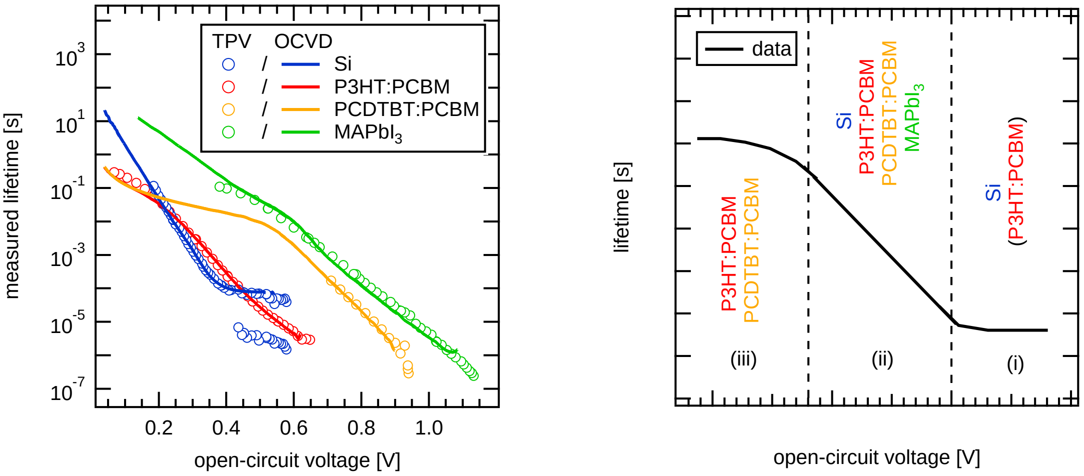

(a) **(b)**

Figure 5.5.: **(a)** Charge carrier lifetimes determined via TPV and OCVD for the four solar cells. Slope alterations lead to the presence of different regimes, where the lifetimes can be constant (at high or low voltages) or voltage-dependent (for intermediate voltages). For a better overview, a simplified scheme of these different regimes is provided in **(b)**, where the solar cells are categorized according to the presence of different slope alterations.

slope for higher V_{oc}'s. A similar transition is visible for P3HT:PCBM at around 0.2 V with the addition of another slope alteration being evident at roughly 0.5 V. A simplified scheme of the observed lifetime transitions is illustrated in Figure 5.5b. All devices have the highest slope at intermediate voltages in common. However, both organic cells demonstrate a transition to a more constant lifetime at low voltages, whereas the Si and to a minor extend also the P3HT:PCBM solar cell exhibit another transition to a constant lifetime at higher V_{oc}'s. To explain these different lifetime regimes, a complete picture of the underlying recombination mechanisms will be developed in the following based on experimental and theoretical results.

5.4. Effect of External Conditions on Voltage Decay

To understand the electronic behavior of PV devices, research is very often based on equivalent circuit modeling. This allows for a detailed description of all currents and voltages present in a solar cell, which opens up the possibility to study the different electrical components a solar cell consists of. In this section, the impact of these components will be investigated in more detail to obtain a better understanding of how they affect lifetime determination by transient electrical methods.

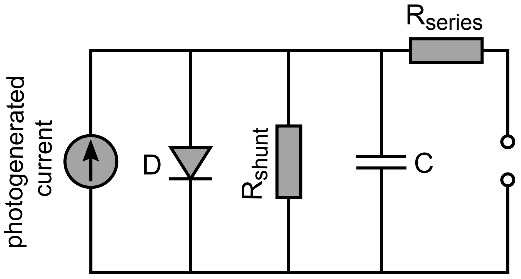

Figure 5.6.: Equivalent circuit of a solar cell. Photocurrent source, shunt resistance and a capacitor are connected in parallel to a diode. In addition, a series resistance is included. In order to describe real solar cells correctly, all these components need to be considered.

Figure 5.6 displays a widely used equivalent circuit model for solar cells. In the ideal case, a PV device can be described only by a photocurrent source, which generates the current and a diode being connected in parallel.[374,375] Sometimes, additional diodes are included to account for different recombination mechanisms.[170,376] In reality, such ideal devices do not exist, since resistive losses are always present and have to be accounted for by implementation of additional components in the equivalent circuit. The influence of resistive losses is well-recognized in literature and often included in the evaluation of j-V characteristics and other experimental observations.[355,374,377] Since the transient electrical methods employed in this work are conducted under open-circuit conditions, R_{series} does not affect these measurements and accordingly can be ignored in further analysis. On the contrary, the capacitor connected in parallel is only poorly considered in literature. Thin-film PVs consist of active layers with thicknesses of several hundred nanometers, which are embedded between two electrodes leading to capacitances that are often not negligible. For this reason, the influence of the capacitor on transient electrical methods is studied in this section. In addition, the impact of R_{shunt} and the illumination intensity will be evaluated in order to obtain a complete picture of all parameters and determine the conditions under which relevant recombination parameters can be obtained.

Effect of Illumination Intensity

By first changing the starting steady-state voltage by employing different light intensities covering several decades, the influence of light intensity on OCVD can be examined. Figure 5.7 summarizes the decays for starting light intensities ranging between 10^{-6} and 2.7 suns. For the Si device, the curves can be separated into a fast recombination regime at early timescales ($< 10^{-3}$ s) and a slower recombination regime, where all measurements converge into the same decay at longer time scales. Although the start-

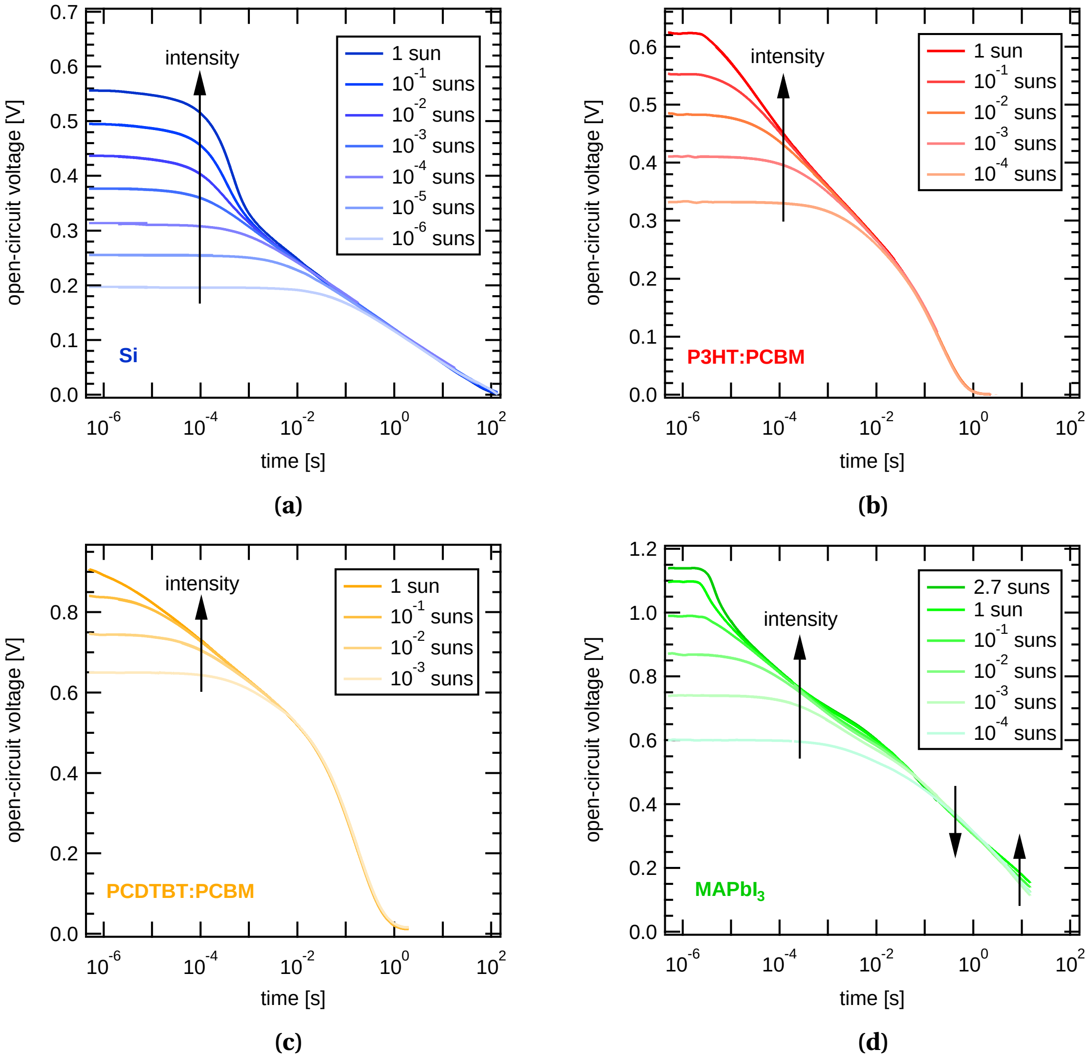

(a) (b) (c) (d)

Figure 5.7.: OCVD curves with different starting open-circuit voltages for the **(a)** Si, **(b)** P3HT:PCBM, **(c)** PCDTBT:PCBM and **(d)** MAPbI$_3$ solar cells. The voltages are varied by changing the light intensity over several orders of magnitude.

ing (steady-state) voltage scales perfectly with the logarithm of the light intensity, the initial decay is quite different depending on the starting value. Thus, the attendance of the early regime is intensity dependent and can be observed for all voltages above 0.4 V corresponding to illumination intensities ranging between 10^{-3} and 10^{-2} suns. The P3HT:PCBM and MAPbI$_3$ devices require 1 sun or even higher intensities to identify a slightly differing decay at early time scales. In case of the PCDTBT:PCBM solar cell, no attendance of an additional initial decay can be observed. Both organic devices show an additional slope alteration after the decays merged to one single curve at around 0.2 V for the P3HT:PCBM and 0.5 V for the PCDTBT:PCBM solar cell. This behaviour will be addressed in the next section. Further, the most complicated decays are found for the perovskite solar cell, where the whole decay is intensity dependent and the curves do not end up in the same trace like observed for the other devices. Obviously, the initial light intensity determines the shape of the decay also at long timescales. In addition, a shoulder around 0.7 V appears, when the device was illuminated with high light intensities prior to the decay, which is known as a "persistent photovoltage" effect often observed for perovskites.[342] Even though the main origin is not fully clarified yet, it is assumed that the presence of mobile ions is responsible for this behavior (see Section 2.3.3). In addition, mobile ions could also explain the recorded slope alterations at longer times scales since the initial ionic displacement can indeed be intensity dependent, if, for example, additional ions are generated upon photoexcitation.[235,237,378,379]

Effect of Capacitance and Shunt Resistance

To ascertain the rationality of the lifetime assignment, both external parameters, the capacitance and shunt resistance, are varied by placing these additional components in parallel to the set of studied solar cells. These additional components should demonstrate their impact on the obtained lifetimes without affecting the bulk recombination dynamics.

Figure 5.8 displays the influence of both external components on the OCVD traces. By placing additional capacitors (of 6.8 or 15 nF) in parallel with the solar cells under study, the decay is prolonged in a linear fashion. In case of the Si device, this is however only the case in the later region of the decay, whereas the initial drop is unaffected by this modification. Obviously, the additional capacitors dominate large parts of the measurements, which is the first experimental confirmation that also the pure cells are (to a very different extent) here ruled by the relaxation of spatially separated capacitive, and not bulk, charge carriers. In case of the PCDTBT:PCBM device, even the entire voltage range is completely modified by the external capacitor, while the P3HT:PCBM solar cells shows a larger deviation only at longer timescales. To then finally ascertain that this long-lived decay is indeed only associated with carriers stored at or in the direct vicinity of the electrodes, various shunt resistances are connected in parallel with the device. These external loads evidently speed up the decay and substantially reduce the assigned lifetimes, but again only in the time region that was ruled by capacitive discharging. The charges located at the electrodes are now provided with an alternative faster route to relax, a simple external resistor. Bulk carrier recombination rates certainly remain unaffected (as shown by the fast initial decay in Figure 5.8a) by external shunting, as long as R_{shunt} is not also limiting the steady-state V_{oc} itself as it is the case for both organic devices for very low shunt resistances in the kΩ-range.[355] Here, the starting V_{oc} is heavily reduced even though the illumination intensity is kept

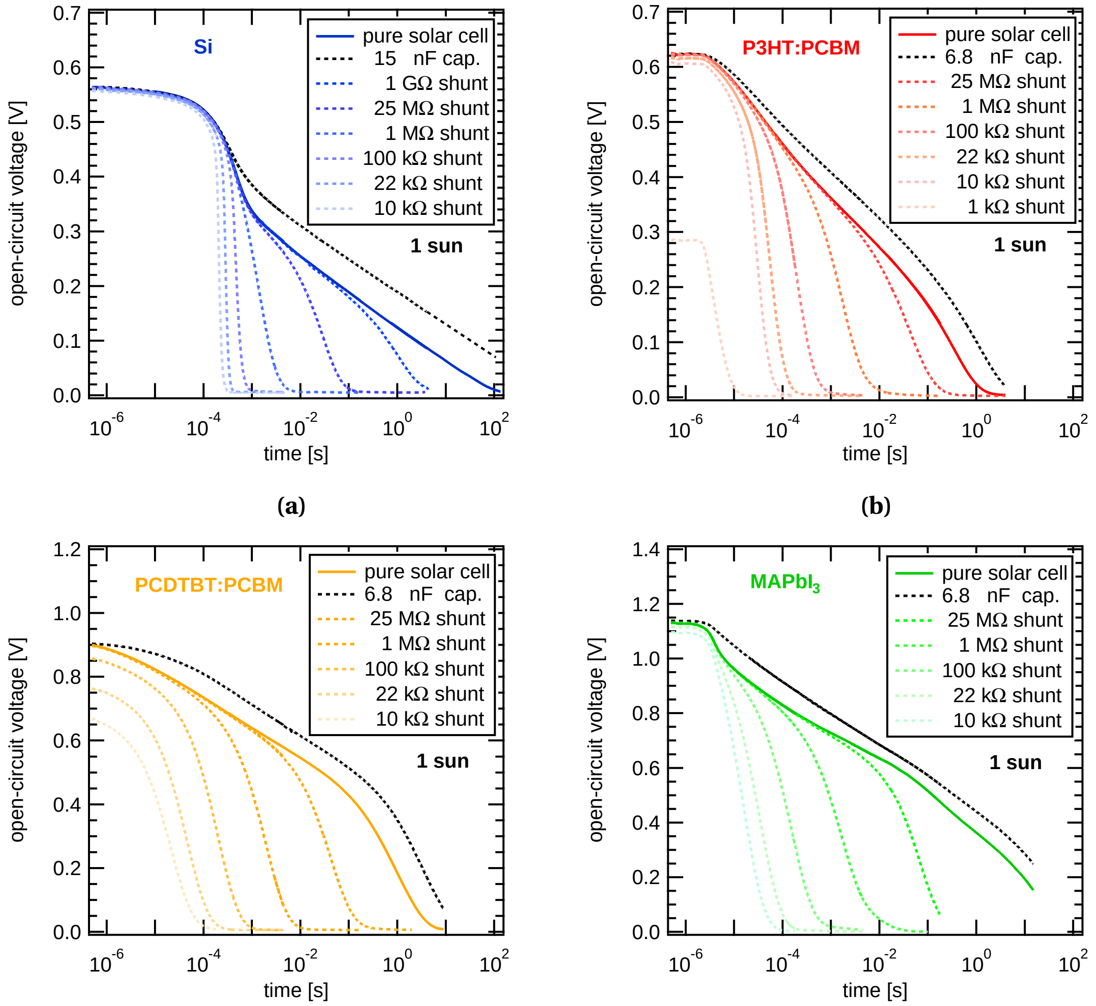

(a) (b)

(c) (d)

Figure 5.8.: OCVD decays with additional capacitors and resistances placed in parallel to the **(a)** Si, **(b)** P3HT:PCBM, **(c)** PCDTBT:PCBM and **(d)** MAPbI$_3$ solar cells at an illumination intensity of 1 sun. The capacitors prolong the decay, while the additional resistances decrease the time until V_{oc} relaxes back to zero again.

constant at 1 sun. Thus, charge carrier recombination via the external shunt is faster compared to internal bulk recombination, preventing the quasi Fermi level splitting to build up as much as in the unshunted case. Figure 5.9 displays the corresponding dark j-V curves of the shunted devices. While the Si device has a high shunt resistance preventing any leakage currents even at low voltages, both organic thin-film solar cells demonstrate leakage recombination trough internal shunts. However, by introducing additional resistors, which are lower compared to the internal shunts, the leakage current is increased by several orders of magnitude and subsequently hiding the exponential diode behavior. From these observations it can be concluded, that the OCVD slope alteration for the pure solar cells in Figure 5.7b at 0.2 V and Figure 5.7c at 0.5 V

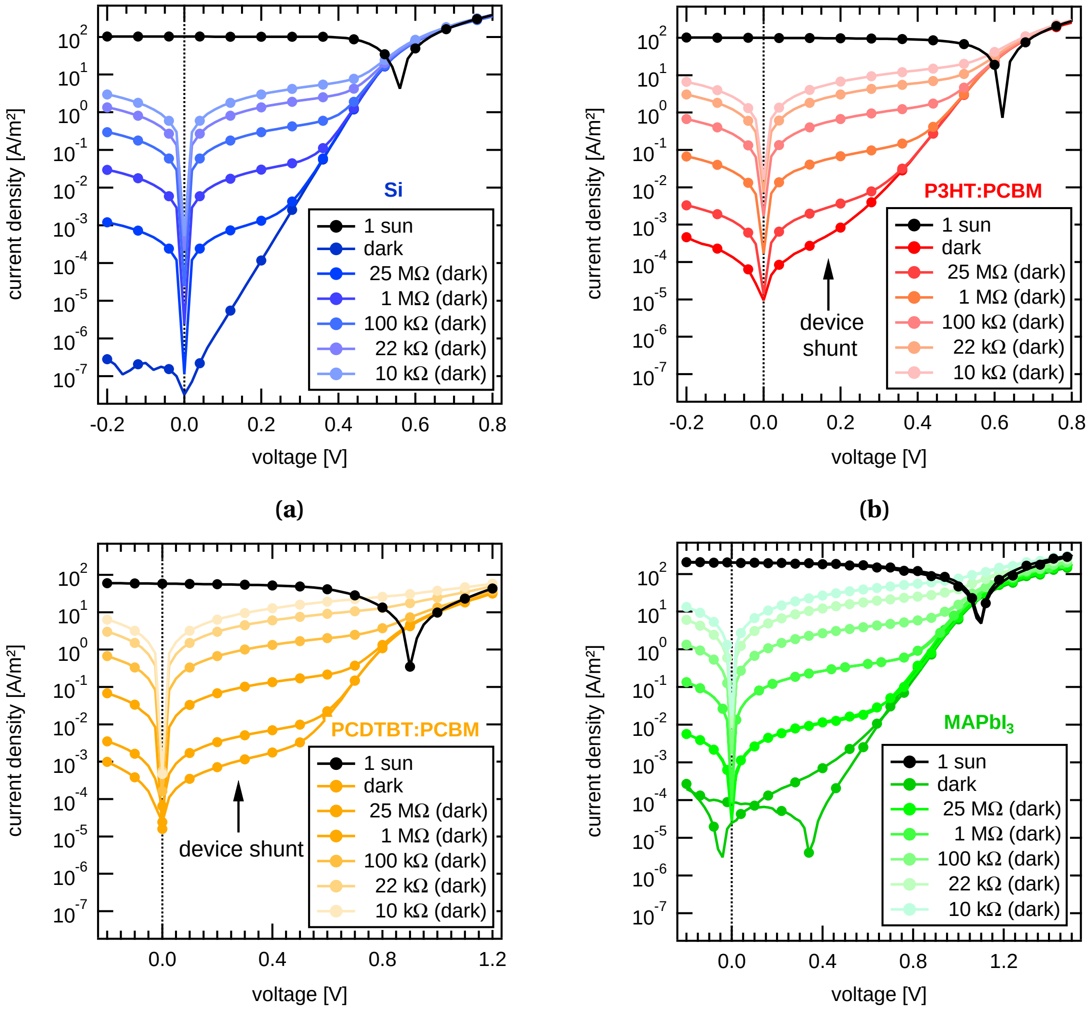

(a) (b) (c) (d)

Figure 5.9.: Current-voltage characteristics in the dark with additional resistors placed in parallel to the **(a)** Si, **(b)** P3HT:PCBM, **(c)** PCDTBT:PCBM and **(d)** MAPbI$_3$ solar cells. Additional measurements under 1 sun illumination are included to identify the conditions under which V_{oc} is affected by leakage recombination.

is correlated with the internal shunt resistance. Accordingly, this is the first hint that the lifetimes of both organic devices are ruled by the $R_{shunt}C$-time at these low voltages (region (iii) in Figure 5.5b). Furthermore, it can be stated that C does not only play a role at the lowest voltages, but also for intermediate voltages in region (ii) in Figure 5.5b, since OCVD is influenced by both external components in this regime. This is nicely demonstrated for the Si cell for voltages lower than 0.4 V (Figure 5.8a) or for the PCDTBT:PCBM device for voltages above 0.5 V (Figure 5.8c). Since the Si solar cell has a high internal shunt resistance, this part of the decay is not related to the $R_{shunt}C$-time, but is also characterized by another form of capacitive discharge. It is accordingly a strong confirmation that the decay at intermediate voltages, where the lifetime scales exponentially with voltage (Figure 5.5), is indeed only associated with capacitive carriers and not necessarily with charges trapped in tail states of the DOS in the bulk of the material as explained in Section 5.1.

As already noticed for the OCVD transients in Figure 5.8, the placing of additional capacitors in parallel to the solar cell slows down the decay and therefore increases the recombination lifetime in a wide range of voltages. In contrast, additional shunt resistors have the opposite effect by speeding up the voltage decay. The influence of the external components on the calculated charge carrier lifetimes determined by TPV and OCVD is exemplary summarized in Figure 5.10 for the Si solar cell. The introduction of a low shunt resistances results in a constant lifetime at the smallest voltages. By combining the 6.8 nF capacitor and the 25 MΩ resistor, the $R_{shunt}C$ time can be calculated to be 0.17 s, matching perfectly with the determined constant lifetime via TPV of around 0.18 s. If only the 25 MΩ resistance is included during the measurements, the constant $R_{shunt}C$ time at low voltages can be calculated to be 0.033 s. From this value, it can be concluded that $C = 1.32$ nF. The exact origin of this internal device capacitance will be discussed later. To summarize, the constant lifetimes at low V_{oc}'s in region (iii) in Figure 5.5b originate from capacitive charge carriers which are stored at the electrodes and recombine via the device shunt resistance. This process results in the $R_{shunt}C$-time of the device measured by TPV and OCVD. Furthermore, for inter-

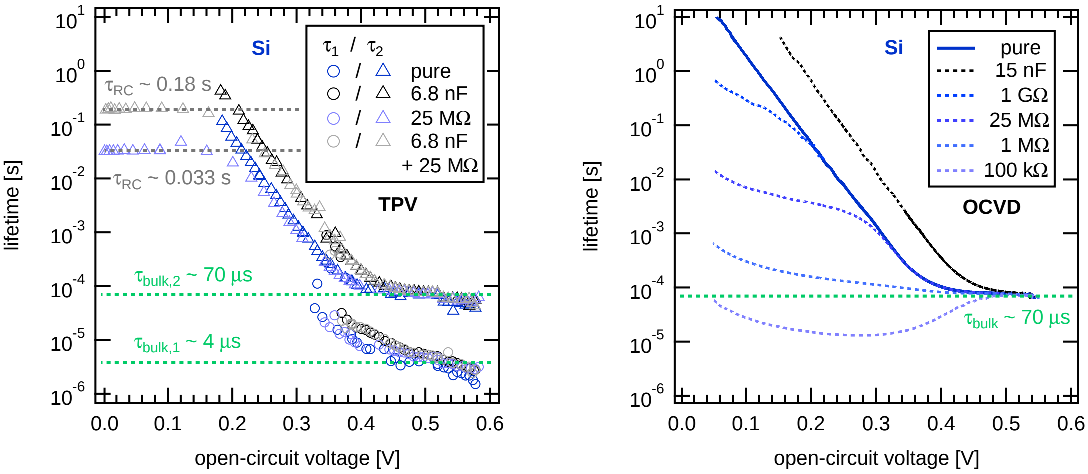

(a) (b)

Figure 5.10.: Impact of additional capacitors and shunt resistances on charge carrier lifetimes determined by **(a)** TPV and **(b)** OCVD for the Si solar cell. Additional capacitors increase the calculated lifetimes, while placing additional shunt resistances in parallel to the device has the opposite effect. For low voltages, the lifetimes correspond to the *RC* time constant. In contrast, for high open-circuit voltages, the obtained lifetimes are not affected by the external components, since real bulk carrier lifetimes are measured.

mediate voltages in the range of 0.2 V to 0.4 V in Figure 5.10 or region (ii) in Figure 5.5b, it is obvious that the external components have a huge impact on the obtained lifetimes. Considering the equivalent circuit in Figure 5.6, the assumption follows that it corresponds to a capacitive discharge not via the shunt resistor, but via the diode itself. This hypothesis will be examined in more detail in the following section. For high V_{oc}'s above 0.4 V, both measurement techniques lead to lifetimes, which are not affected by the addition of external components. This confirms finally, that these lifetimes originate from the bulk of the Si device and correspond therefore to real internal charge carrier lifetimes. Bulk carriers can only be released thermally or by applying an external electric field but would not notice whether the electrodes are shunted or not. The aim of employing transient electrical methods is therefore to identify the slope deviation of determined lifetimes at high voltages in order to study charge carrier recombination in the absorber of the device. Taking again Figure 5.5 into account, it can be concluded that no one of the studied thin-film PVs shows an as clear slope alteration as it is the case for the Si device. Accordingly, no bulk recombination lifetimes of the photoactive layers can be identified and the determined lifetimes are ruled by the discharge of capacitive charge carriers.

5.5. Analytical Description of OCVD and Lifetimes

Following the findings of the previous section, the focus shifts now to an analytical description of the capacitance affected lifetimes. Firstly, it will be demonstrated how large parts of the OCVD transient can be described via discharge of a capacitor either via the shunt resistor or the diode, but only in the time region where the device capacitance is the main contributor to the decay. Secondly, the obtained lifetimes will be analyzed in more detail and described as the sum of the real bulk carrier recombination lifetime and the capacitive discharging time.

Modeling of OCVD Transients

In the following, the voltage resulting from capacitive effects will be described for different cases of the equivalent circuit introduced in Figure 5.6. Starting with the most simple case, it can be assumed that the device consists of a shunt resistance in parallel with a capacitor. Here, the current I in the circuit results from the discharge of the capacitor through the resistor, such that

$$I = -C\frac{\mathrm{d}V}{\mathrm{d}t} = \frac{V}{R_{shunt}}. \tag{5.1}$$

Thus, it follows for the relationship between voltage and time

$$V(t) = V_{t=0} \cdot \exp\left(-\frac{t}{R_{shunt}C}\right), \tag{5.2}$$

where $V_{t=0}$ is the initial voltage at time $t = 0$ and $R_{shunt}C$ in the denominator of the exponential function can be identified as the previously measured time constants for the lowest open-circuit voltages.

A more sophisticated case is a capacitor placed in parallel to a diode without the inclusion of any resistive effects. To describe this circuit, the time derivative of the charge on the capacitor leads to a current through the diode, which has already been introduced in Equation 2.8. The differential equation can thus be written as

$$I = -C\frac{\mathrm{d}V}{\mathrm{d}t} = I_0\left(\exp\left(\frac{qV}{n_{id}k_BT}\right) - 1\right), \tag{5.3}$$

where I_0 is the dark saturation current. According to Ref.[380], the solution reads

$$V(t) = -\frac{n_{id}k_BT}{q}\ln\left[1 - \left(1 - \exp\left(-\frac{V_{t=0}q}{n_{id}k_BT}\right)\right)\exp\left(-\frac{I_0qt}{Cn_{id}k_BT}\right)\right]. \tag{5.4}$$

This expression describes the decaying voltage of diode-capacitor (DC) circuit, where the measured lifetime cannot be identified as easy as in the RC circuit. The parameters n_{id} and I_0 can, for example, be determined from current-voltage characteristics in the dark, whereas C can be used as a fit parameter or determined via other techniques, like CE (see Section 5.6) or Impedance Spectroscopy.[381–383] It should be noted, that the DC decay differs significantly from a RC decay, since it scales with the logarithm of time. This expression can be further simplified depending on the time region under focus. Taylor expansion of the t-dependent exponential term under the condition $\frac{I_0qt}{Cn_{id}k_BT} \ll 1$ leads to

$$V(t) = -\frac{n_{id}k_BT}{q}\ln\left[\exp\left(-\frac{V_{t=0}q}{n_{id}k_BT}\right) + \frac{I_0qt}{Cn_{id}k_BT}\left(1 - \exp\left(-\frac{V_{t=0}q}{n_{id}k_BT}\right)\right)\right]. \tag{5.5}$$

Since the initial voltage $V_{t=0}$ for the set of studied devices is larger compared to the thermal voltage k_BT/q, the second exponential term is negligible compared to 1, such that

$$V(t) = -\frac{n_{id}k_BT}{q}\ln\left[\exp\left(-\frac{V_{t=0}q}{n_{id}k_BT}\right) + \frac{I_0qt}{Cn_{id}k_BT}\right]. \tag{5.6}$$

From Equation 5.6, two cases can be investigated in more detail. For short times ($t \to 0$), the second term in the bracket can be neglected leading to the intuitive result $V(t) = V_{t=0}$.

For intermediate times, where the second term in the bracket dominates and the condition $\exp\left(-\frac{V_{t=0}q}{n_{id}k_BT}\right) \ll \frac{I_0qt}{Cn_{id}k_BT} \ll 1$ holds, Equation 5.6 becomes

$$V(t) = -\frac{n_{id}k_BT}{q}\ln\left[\frac{I_0qt}{Cn_{id}k_BT}\right]. \tag{5.7}$$

On this time scale, where the condition is satisfied for most parts of the OCVD transient, the voltage decay demonstrates a logarithmic dependency on time. For very long times, where $\exp\left(-\frac{V_{t=0}q}{n_{id}k_BT}\right) \ll \frac{I_0qt}{Cn_{id}k_BT}$ (includes also the previous time region), Equation 5.4 can be simplified to

$$V(t) = -\frac{n_{id}k_BT}{q}\ln\left[1-\exp\left(-\frac{I_0qt}{Cn_{id}k_BT}\right)\right], \tag{5.8}$$

which satisfies the necessity of decaying to zero for long times. Equations 5.6 and 5.7 provide analytical and quite simple expressions to fit OCVD traces in the intermediate time regime and verify the assumption if an DC circuit describes the long decays correctly. Furthermore, in order to estimate when the decay reaches $V(t) = 0$ V, Equation 5.7 can be solved for t, resulting in the following relationship

$$t_{end} = \frac{n_{id}k_BTC}{qI_0}. \tag{5.9}$$

This expression is only valid, if the device has a high shunt resistance such that any leakage currents are suppressed, otherwise the $R_{shunt}C$ decay outlined in Equation 5.2 would provide an alternative faster route for the voltage to drop.

In order to investigate the impact of the discussed capacitive effects on OCVD, Figure 5.11 summarizes the measured OCVD decays in combination with modeled $R_{shunt}C$ and DC circuits. Panel 5.11a displays the light-dependent transients for the Si device, where the data is described by a DC decay according to Equation 5.6. All necessary parameters are taken from dark j-V curves (Figure 5.3 and Table 5.1) and a value for the internal device capacitance is determined from the constant $R_{shunt}C$ lifetimes at low voltages in Figure 5.10a. Accordingly, not additional fit parameters are needed. In case of low light intensities ($\leq 10^{-3}$ suns), the entire voltage transient can be described by a DC decay. From Equation 5.9, the time when the voltage has decayed to zero can be calculated to be $t_{end} \approx 100$ s matching the observed time. This clearly confirms the previous assumption that the intermediate part of the OCVD trace is a DC decay. It should be noted here, that the position and slope of the curve at around 10^{-3} s - 10^{-2} s is not exactly reproduced, which might be not surprising since only a constant capacitance is used for the calculations. It is well known for Si pn junctions, that also a deple-

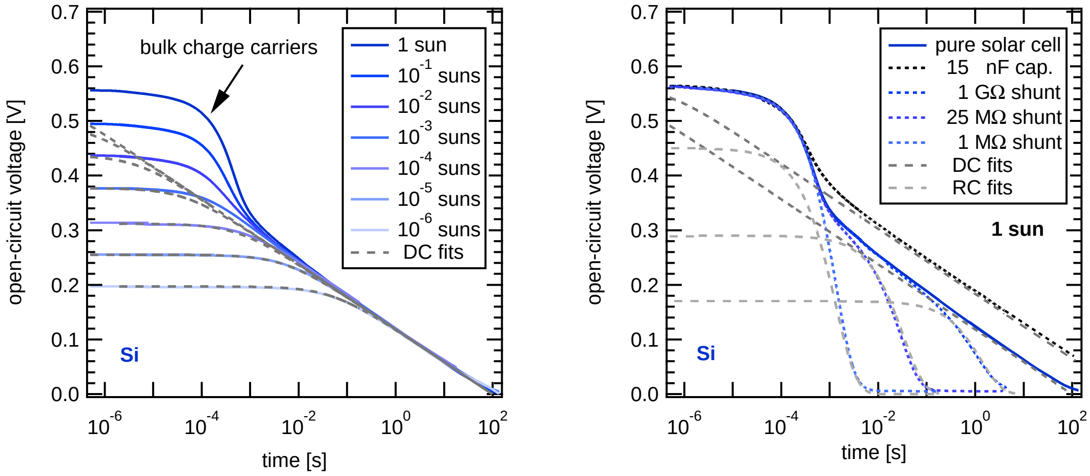

(a) **(b)**

Figure 5.11.: **(a)** Intensity-dependent OCVD transient for the Si device proving that at low light intensities the entire decay can be well described by a *DC* decay according to Equation 5.6. Bulk recombination dynamics can only be detected by combining high light intensities ($\geq 10^{-3}$ suns) and measuring on short time scales ($\leq 10^{-3}$ s). **(b)** OCVD transients for the same device with additional components clearly proving that the emerging differences are modeled by both $R_{shunt}C$ (Equation 5.2) and *DC* circuits.

tion layer capacitance is present in these kind of devices as they rely on doped materials. Since a depletion layer capacitance is voltage-dependent, the analysis introduced above lacks of providing analytical solutions and numerical methods need to be used instead. Furthermore, taking into account the early time regime at higher light intensities, the models fails to describe experimental data. This is accordingly the next proof, that this regime is dominated by recombination of charge carriers in the bulk and is not affected by capacitive effects. It is therefore important to always perform the measurements at sufficiently high intensities in order to prevent measuring only capacitive discharges. To further assure the capacitive assignment in these measurements, Figure 5.11b illustrates the impact of additional capacitors and shunt resistors, where again the *DC* circuit and now also the $R_{shunt}C$ circuit (Equation 5.2) provide quite accurate descriptions of the decays over wide range of time scales.

Having confirmed that large parts of OCVD decays are indeed superimposed by capacitive effects for the Si device, the studied set of thin-film PVs is also analyzed by means of the introduced models. OCVD transients under 1 sun for these devices are summarized in Figure 5.12 together with modeled $R_{shunt}C$ and *DC* decays. Values for the geometric capacitance are determined from CE measurements in the dark, as it shown in Section 5.6. In case of the P3HT:PCBM device, the decay between 10^{-4} s and 10^{-2} s cannot be perfectly described by the *DC* decay indicating that a geometric ca-

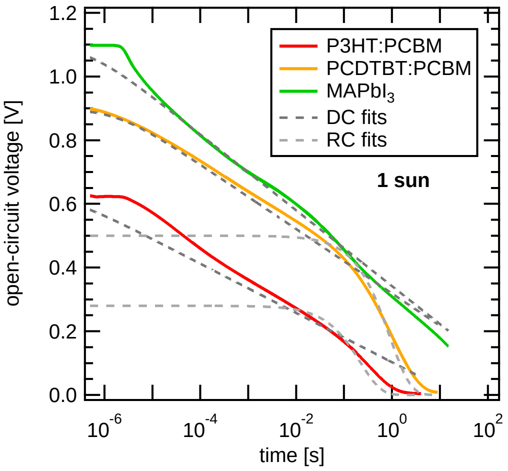

Figure 5.12.: OCVD measurements for all thin-film PVs studied in this chapter indicating that large parts of the transient are ruled by $R_{shunt}C$ (for both organic solar cells) and DC (for all three devices) decays, where it is assumed that $C = C_{geo}$ (C_{geo} is determined from CE measurements without illumination as demonstrated in Section 5.6). While the PCDTBT:PCBM solar cell is completely dominated by a pure geometric capacitance, the P3HT:PCBM device suffers obviously from an additional depletion layer capacitance as the DC circuit is not able to precisely describe the decay. The decay of the MAPbI$_3$ solar cell fits mostly to a geometric capacitance, but is affected by ionic displacement.

pacitance is not sufficient. Therefore, it is concluded that this device also has a additional depletion layer capacitance similar to the Si diode. Indeed, Lee et al. suggested that a depleted layer in the active material can occur close to the cathode interface.[384] However, at the highest voltages, a small onset is identified pointing towards recombination of charge carriers in the bulk. At lowest voltages, a $R_{shunt}C$ circuit describes the decay more accurate in line with the observation of shunt recombination in dark current-voltage characteristics. The PCDTBT:PCBM device is however fully ruled by a capacitive discharge via the diode ($\leq 10^{-1}$ s) and via the shunt resistance at longer times. Neither one of these regions has therefore anything to do with charge carrier lifetimes in the bulk under steady-state conditions. Here, the determined geometric capacitance is sufficient to describe the entire decay which confirms the absence of additional capacitive effects. It can accordingly be concluded that no recombination of charge carriers in the bulk is observed and OCVD fails in the determination of recombination parameters. The perovskite solar cells displays a tiny onset of bulk recombination at shortest times, but is to a large extent also ruled by a DC decay originating from a capacitance most probably of geometric type. The small deviations at longer times originate from ionic effects as previously discussed.

Analytical Limit for the Identification of Bulk Carrier Lifetimes

To narrow down the regions of useful lifetime information available in electrical transient measurements of solar cells, the analytical approach for charge control in a diode as proposed by Castaner and co-workers will be reevaluated in this section.[385,386] The two clear processes identified in the Si diode allow for a analytical expression of the entire voltage decay of the device and the lifetimes ruling in both regimes. The differential equation for charge control ($Q(t)$) in a diode with the inclusion of an arbitrary form of capacitance (internal or external) reads

$$\frac{\mathrm{d}Q(t)}{\mathrm{d}t} = -\frac{Q(t)}{\tau_{bulk}} - C\frac{\mathrm{d}V(t)}{\mathrm{d}t}, \tag{5.10}$$

where τ_{bulk} is a real lifetime of excess charge carriers and C is the introduced device capacitance, which may also be voltage dependent if, for example, a depletion layer approximation is instead suited. The second capacitive term has in many earlier rate equations for thin-film PVs unfortunately not been accounted for, but is very necessary, if the sample has electrodes present. Analytical solution to Equation 5.10 exists and is provided already in Reference[385] for $t(V_{oc})$, if a constant geometric capacitance is assumed, which to a first approximation is sufficient for the herein intended message. It reads

$$t = \tau_{bulk}\frac{q}{k_B T}\left(V_{t=0} - V_{oc}(t)\right) + \frac{q}{k_B T}\cdot\frac{C_{geo}}{j_0}\left[\exp\left(-\frac{qV_{oc}(t)}{k_B T}\right) - \exp\left(-\frac{qV_{t=0}}{k_B T}\right)\right]. \tag{5.11}$$

Figure 5.13 shows the analytical solution to Equation 5.11 with the same constant capacitance used previously of 1.32 nF. Different values for the bulk carrier lifetime τ_{bulk} ranging over six decades from 7 ns to 7 ms are chosen. It has to be noted, that x- and y-axis are switched for a better comparison to the OCVD measurements. The OCVD transient for the Si device under 1 sun illumination is included, where the relevant bulk carrier lifetime has been determined to be in the range of 70 μs (Figure 5.5a and 5.10). The calculated decay for an internal bulk carrier lifetime of 70 μs matches perfectly with the measured decay, which is the final confirmation that charge carrier recombination lifetimes are observed at high voltages/short time scales. Only if such a regime can accordingly be identified, it is possible to assign the decay to originate from bulk carrier recombination. These internal carrier lifetimes can thus only be measured if the capacitive lifetimes from a *DC* decay are exceeded. In case of shorter lifetimes in the ns range, the decay would be entirely ruled by the capacitive discharge over the diode. However, independent of τ_{bulk}, all decays finally catch up with the *DC* decay

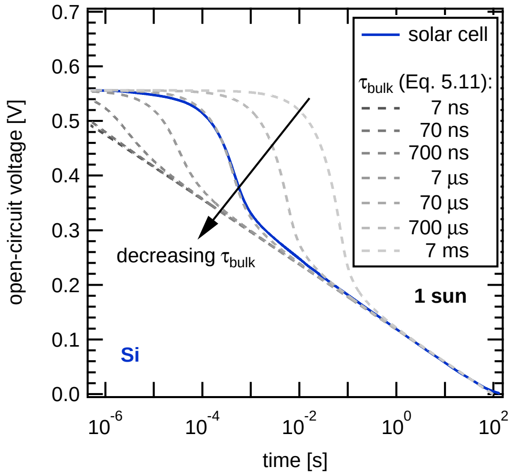

Figure 5.13.: Analytical description of charge carriers in a diode as calculated from Equation 5.11. The effect of different bulk recombination lifetimes is clearly visible in the early time regime where τ_{bulk} is longer compared to the *DC* lifetime. In addition, the OCVD trace for the Si device under 1 sun is also shown matching perfectly with the calculated decay if a internal bulk carrier lifetime of 70 μs is inserted.

for times above 10^{-1} s. This is however the regime where the determined lifetime has actually lost its original relevant physical meaning.[387]

With the insertion of Equation 5.11 into Equation 4.3, the charge carrier lifetime as a function of open-circuit voltage can be calculated according to

$$\tau = \tau_{bulk} + \frac{n_{id} k_B T}{q} \cdot \frac{C_{geo}}{j_0} \exp\left(-\frac{qV_{oc}}{n_{id} k_B T}\right), \tag{5.12}$$

where the second term on the right hand side corresponds to the measured *DC* decay time. The influence of the different contributions to lifetimes becomes obvious and the analytical expression clearly shows when the relevant steady-state bulk carrier lifetime is measurable. The *DC* term is exponentially dependent on the value of the voltage itself. Accordingly, for an accurate assignment of bulk-related carrier lifetimes via transient electrical methods, the following relation must always hold

$$\tau_{bulk} \gg \frac{n_{id} k_B T}{q} \cdot \frac{C_{geo}}{j_0} \exp\left(-\frac{qV_{oc}}{n_{id} k_B T}\right) = \frac{C n_{id} k_B T}{q j_{sc}(V_{oc})}, \tag{5.13}$$

independent if it is a first-order constant lifetime or higher-order density dependent lifetimes. Herein, the diode ideality factor is also included and the total recombination current density at V_{oc} is identified as the short-circuit current density ($j_{rec}(V_{oc}) = j_{sc}$).[173] All parameters of Equation 5.13 are hence experimentally directly accessible and provide an easy method to prove, if the determined lifetimes correspond to capacitive discharging times. This equation embodies the main message of this chapter:

only if the condition holds, electrical measurements can be employed to determine bulk carrier lifetimes relevant under operating conditions. From a strict experimental lifetime determination point of view, it becomes clear that two things should always be strived for: large recombination currents i.e. higher voltages (and thus higher illumination intensities) and low capacitances (thicker devices). The main limitation of lifetime determination via electrical means arises accordingly from the fact that the relaxation of charges associated with the quasi-static capacitance of geometrical or space-charge regions in the device is a negative exponential function of the open-circuit voltage, like often observed for thin-film PVs. With a depletion layer capacitance instead of the above assumed geometric capacitance, the small voltage dependence of C in Equation 5.13 will alter the minimum lifetime slightly, but the overall expression with a constant geometric capacitance suffices as an analytically derivable and very useful rule, since electrodes always lead to the presence of C_{geo}.

Figure 5.14 finally plots the outcome of the calculated minimum lifetime from Equation 5.13 together with the measured lifetimes from OCVD and TPV for all solar cells. Values for the geometric capacitance are obtained from CE measurements shown in the next Section 5.6. The Si photodiode has a sufficiently long lifetime to easily pass the test of Equation 5.13 as long as high light intensities are evaluated (which is the case for measured lifetimes above 0.4 V), whereas the other devices are more questionable. The minor difference between measured and calculated lifetimes for the Si device

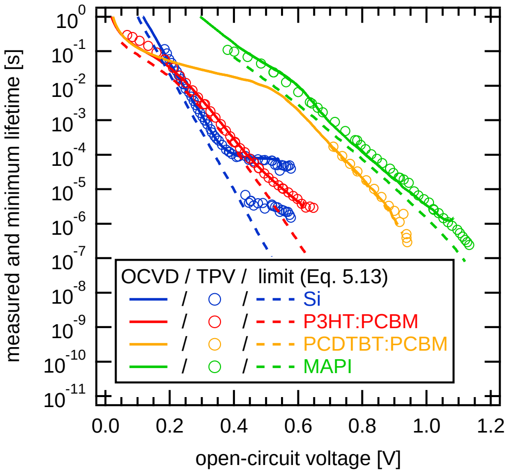

Figure 5.14.: Electrical lifetime limit calculated from Equation 5.13 (dashed lines) plotted together with measured lifetimes via OCVD (solid lines) and TPV (empty circles). The lifetime limit is calculated with a constant geometric capacitance. It is only the Si device that certainly passes the constraint of Equation 5.13 for measured lifetimes above 0.4 V. In case of the thin-film PVs, the P3HT:PCBM device shows the onset of bulk carrier lifetimes at highest voltages, whereas the PCDTBT:PCBM and $MAPbI_3$ solar cells do not show any clear distinction from the calculated limit in any region.

at lower voltages results from the fact that a depletion layer capacitance is responsible for the *DC* time. The PCDTBT:PCBM device is not safe in any region and every assigned lifetime is, as stated earlier, a full geometric capacitive decay. For the P3HT:PCBM cell, a departure from the geometric capacitive lifetime at the highest voltages is observed, yet its slope alteration is not large enough to not still be partly affected. For this device, it is again reminded that the capacitance itself does show a pronounced voltage dependence, probably originating from a depletion layer capacitance. Such additional junction capacitive effects in combination with ionic motion are also likely the reason for that a small offset remains between the calculated geometric minimum lifetime and the measured one for the perovskite device. Also this solar cell does not show a clear slope deviation at highest voltages. At intermediate and low voltages, none of the measured lifetimes in Figure 5.14 are thus related to steady-state bulk carrier lifetimes. Our observations are in line with recent publications, where similar concerns on lifetime assignment where raised for thin-film PVs like DSSCs,[388], OPVs[389] PbS[390] and perovskite solar cells.[237,373] Furthermore, a theoretical study by Sandberg and coworkers based on numerical simulations has very recently reproduced and confirmed the herein presented findings and results.[391]

5.6. Impact of Capacitive Effects on Charge Carrier Density

After proving that lifetimes determined by OCVD and TPV can often be dominated by capacitive charge carriers, the question arises if these effects also disturb the methods for the determination of the corresponding charge carrier densities. The first raised concerns should be evident when plotting electrically determined extracted amount of charge carriers over the V_{oc}. Numerous publications do this, but often note merely a small increase of carrier density when the internal voltage is increased by several hundreds of millivolts. This is clearly in contrast to the expected strong exponential relationship outlined in Equation 4.2 between excess charge carrier densities and open-circuit voltage (or quasi Fermi level splitting). Excess charge carriers in the bulk are expected to show an exponential relationship to internal voltage following the definition of their chemical potential, whereas geometrical or space charge capacitive charge carriers show a much weaker (linear or power law) dependence.

Figure 5.15a summarizes CE measurements for the Si device performed at an illumination intensity of 1 sun. The current pulse from the device is linked to the axis on the left-hand side, while the integrated current corresponding to total extracted charge is connected to the axis on the right-hand side. After a time span of 10^{-4} s, the experiment is completed and approximately 40 nC of charge are extracted from the pure device. Placing a capacitor (6.8 nF) next to the device results in an additional contribution in the current signal (grey area) and accordingly to more extracted charge of 43.7 nC. Considering a V_{oc} of 0.56 V at 1 sun, it can be calculated that 3.8 nC are stored on the additional capacitor which matches the increased amount of charge during the CE experiments. It is accordingly concluded that also this method is affected by capacitive charge carriers. The presence of such general capacitive contribution to the overall carrier density is nonetheless already recognized in literature and also considered to be attended to. One capacitive correction method for carrier density determinations is mostly employed: it is based on the assumption of a linear dielectric geometrical capacitance ("charges on the plates") being identical in forward and reverse bias direction measurements. By measuring extracted charges from reverse biased solar cells in the dark one knows the capacitive correction (C_{geo}) needed also under forward illuminated bias. CE measurements in the dark are shown in Figure 5.15b when negative voltages in the range of -0.35 V up to -0.05 V are applied prior to extraction. At these low voltages, only a negligible current is flowing trough the reverse-biased diode as it is illustrated in Figure 5.3a. Obviously, the amount of extracted charge increases linearly the more negative the applied voltage is (dashed lines in Fig-

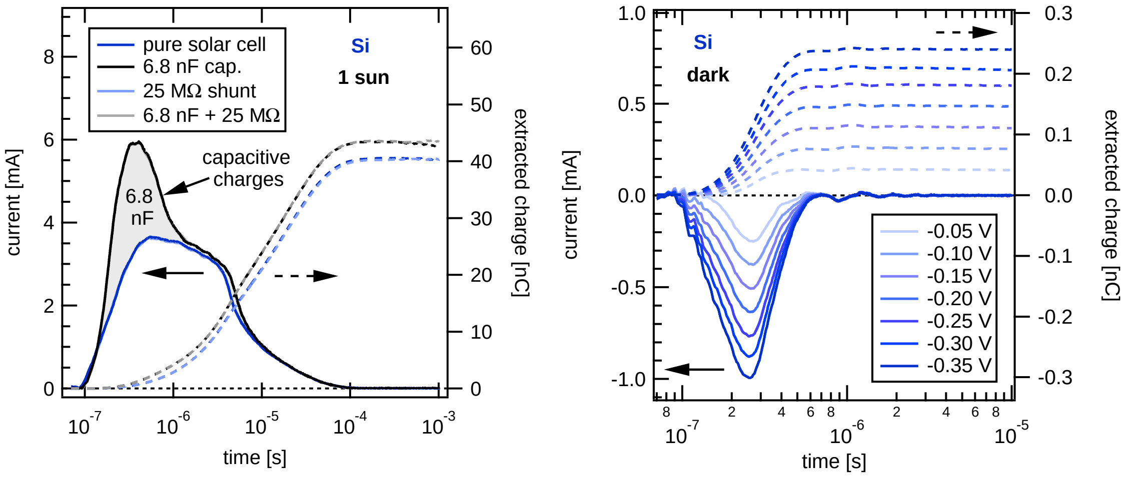

(a) (b)

Figure 5.15.: **(a)** CE measurements performed on the Si device under 1 sun illumination. Solid lines represent the recorded current (left axis), while the integral of the current is shown on the right axis corresponding to the amount of extracted charge. An additional 6.8 nF capacitor leads to more extracted charge carriers at early time scales, since these carriers are extracted faster than charges from the active layer. **(b)** CE experiments in the dark under low negative applied voltages probing only the geometrical capacitance of the device.

ure 5.15b) and the geometric capacitance $C_{geo} = Q/U$ can be calculated to be 0.66 nF or $9.9{\cdot}10^{-5}$ F/m^2 (normalized to the active area) for the studied Si device. This value matches the stated value of 0.7 nF from Hamamatsu[372] and verifies the conducted method for the determination of the C_{geo}. It follows, that the previously determined value of 1.32 nF from Figure 5.10a must therefore be the sum of both the geometric and the depletion layer capacitance. For the other solar cells, the same linear behavior can be observed and C_{geo} is calculated analogously and the following values are obtained: C_{geo} (P3HT:PCBM) = 0.87 nF or $2.9{\cdot}10^{-4}$ F/m^2, C_{geo} (PCDTBT:PCBM) = 1.6 nF or $5.4{\cdot}10^{-4}$ F/m^2 and C_{geo} (MAPbI$_3$) = 0.91 nF or $6.0{\cdot}10^{-4}$ F/m^2. These values have been used to calculate the lifetime limit according to Equation 5.13 for Figure 5.14. Further, the conclusion can be drawn, that all thin-film PVs demonstrate a higher geometric capacitance compared to the Si device resulting from the thinner active layer thickness. Another method to determine C_{geo}, implemented when performing impedance measurements, is based on the assumption of different frequency response of different species in C–V sweeps.[367] Capacitive charges at the electrodes are assumed to respond very fast, whereas excess minority bulk carriers in the neutral region are assumed to be much slower. The sought-after bulk excess carrier density is then determined by evaluating the difference of a low and a high frequency C–V sweep.

With the knowledge of the geometric capacitance it is now possible to correct regular CE measurements under illumination, as it is summarized for all devices in Figure 5.16. CE experiments were performed at a wide range of illumination intensities similar to the already discussed TPV measurements in order to vary the open-circuit voltage. The raw data provided directly from the integral of CE measurements are represented by circles and solid lines, whereas the corrected charge is drawn as triangles and dashed lines. The correction is done by calculating the amount of extracted charge stored on the plates via $C_{geo} \cdot V_{oc}$ and subtracting this value from the raw extracted charge determined under illumination. For the Si diode, additional corrected and uncorrected CE measurements are shown in case of a 6.8 nF external capacitor to demonstrate the overall impact of capacitive charge on these measurements. In addition, a 25 MΩ shunt resistance is also placed in parallel to the device. Measurements performed on the Si cell in panel 5.16a easily allow for the clear identification of a strong exponential contribution from carriers in the bulk at voltages above 0.4 V as well as of a clear depletion layer capacitive contribution at lower voltages being in line with lifetime determination via OCVD and TPV. The 6.8 nF capacitor increases the capacitive contribution by a constant offset, while the shunt resistance reduces the open-circuit voltages at lower light intensities and affects also the amount of extracted charge, since the lower shunt resistance provides a fast pathway for the carriers to recombine instead of being ex-

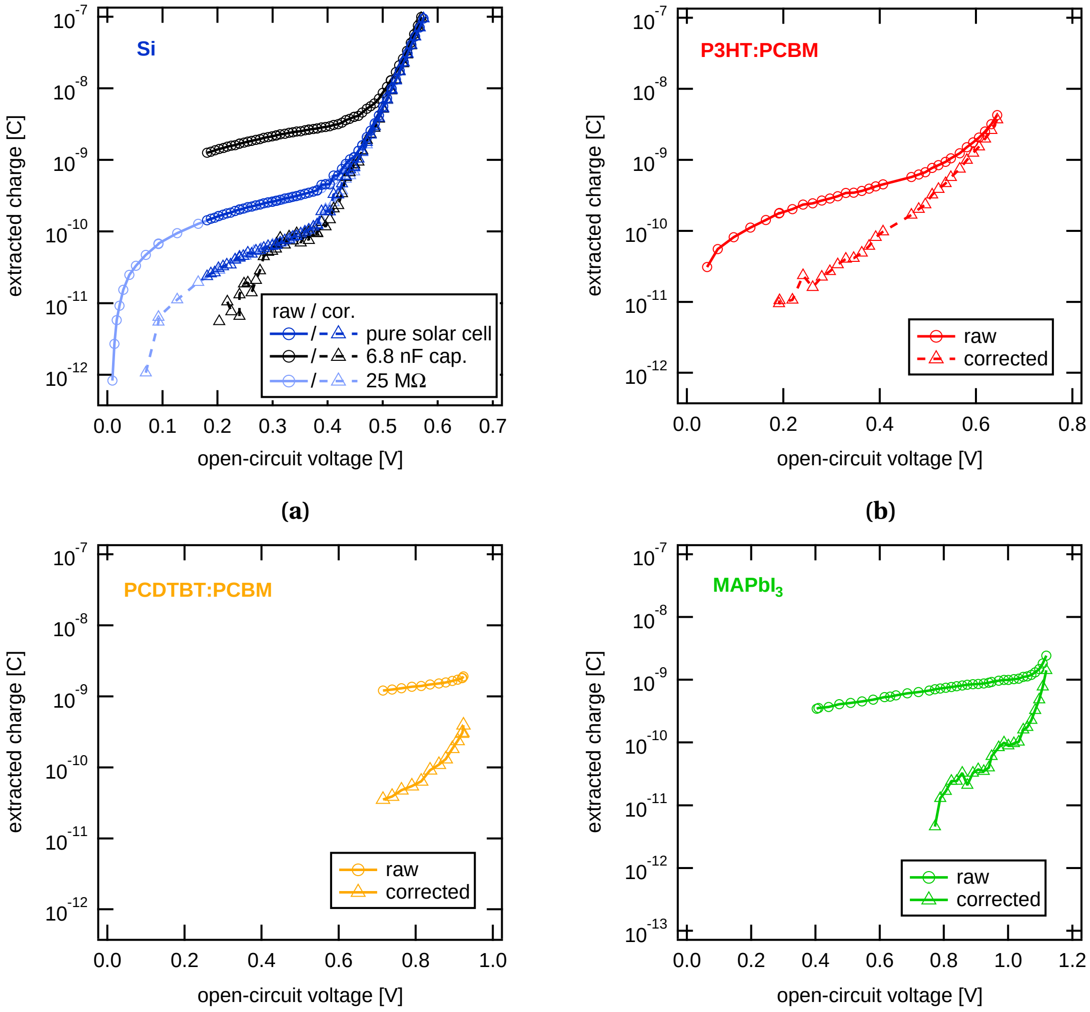

(a)

(b)

(c)

(d)

Figure 5.16.: Measured uncorrected (circles) and corrected (triangles) charge from CE experiments plotted over the open-circuit voltage for the **(a)** Si photodiode and the three thin-film solar cells comprising **(b)** P3HT:PCBM, **(c)** PCDTBT:PCBM and **(d)** $\mathrm{MAPbI_3}$ as active layers. The Si panel also includes CE data obtained from additional measurements with a 6.8 nF capacitor in parallel to effectively demonstrate the capacitance contribution in CE. In contrast, the 25 MΩ shunt resistance reduces V_{oc} at low light intensities and therefore also the amount of extracted charge.

tracted. For all measurements it is obvious that the capacitive correction is difficult to perform. Subtracting weak dependencies (linear geometric capacitance) from an exponential relation at best gives improvement in accuracy of carrier concentration in a rather narrow voltage range but does not at all help at lower voltages. Accordingly, the charge carrier density plotted on a logarithmic scale versus V_{oc} must provide a clear and distinguishable transition from the capacitive contribution in the low voltage region to a clear and exponential function at higher internal voltages. The raw extracted charge from the two organic cells does on the other hand not noticeably display the expected exponential region whereas the corrected charge shows a steeper, yet still not clearly exponential relation to voltage. In contrast, the perovskite cell appears to show a quite steep rise at the very highest voltages, all obtained from intensities exceeding 1 sun, pointing towards the possible onset of extraction of bulk charges. At voltages lower than 1 V, it is however fully ruled by capacitive charges. Thus, in line with OCVD and TPV measurements, it is found that CE is to the same extend also affected by capacitive charge carriers. These measurements are often just not able to collect the total average excess carrier densities from the bulk but still mostly remaining spatially separated capacitive charge carriers from the electrodes or other types of capacitive charge carriers. Similar observations were also obtained for a Si device by means of Impedance Spectroscopy, where the transition from capacitive to bulk carriers was also noticed at around 0.4 V.[364] In general, the reliability of electrical charge extraction methods was studied partially in literature[392–395] with overall similar observations and conclusions as compared to the herein presented results.

5.7. Summary

This chapter proposes a resolution to the long-standing controversy of reported charge carrier lifetimes and densities often observed in thin-film PV devices such as OPVs, PbS, DSSC, as well as in perovskite solar cells. Clear experimental and theoretical evidence is provided that the voltage decays of these solar cells are mostly governed by capacitive electrode associated charges which complicate bulk carrier lifetime assignments relevant under steady-state conditions. The introduced $R_{shunt}C$ and DC models are very accurately able to the describe large parts of the measured transients. It is clearly revealed that these long-lived carriers are not allocated in the bulk of the absorbing semiconductor, but are located either close to the charge selective layers, in the charge selective layers, or in the actual conducting metal electrodes. The problem of relevant lifetime determination via electrical means arises solely from that the relaxation of charges associated with a capacitance of geometric or space-charge regions in the device is always a decaying exponential function of the open-circuit voltage as outlined by Equation 5.13. If the restrictions of this expression do not hold, one is measuring mostly capacitive discharging rates as well as charge densities stored in or at the surfaces of the device, as opposed to the sought-after bulk region. Therefore, it is concluded that only if the relevant steady-state decay rate of bulk charge carriers is slower than the decay rate of capacitive space charges, it can be safely measured via electrical transient techniques such as OCVD, TPV and CE. Some of these concerns were identified long ago within the field of older inorganic PV technologies, where electrical lifetime measurements were initially developed for. These devices were however less affected by capacitive carriers due to larger active layer thicknesses and demonstrated partially long carrier lifetimes like demonstrated here for the Si diode. Even if carrier densities have previously been partly corrected for capacitance in most novel thin-film solar cells,[351] the discharging rate and redistribution of these still present carriers has not been accounted for in lifetime assignments. Considering the vast literature where many researchers are observing very slow recombination rates, the description presented herein is in many cases more probable compared to other effects like trapping and release from shallow trap states. From the theoretical analysis shown here, it is possible to distinguish between capacitive and real bulk carriers and a guideline for the interpretation of optoelectrical data is provided.

6. Bulk Recombination in $MAPbI_3$ Solar Cells Revealed by Active Layer Thickness Variation

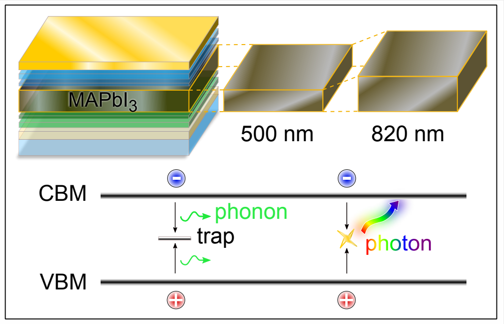

Abstract. Identifying the dominant recombination mechanisms in perovskite solar cells is of crucial importance for further improvements. To ascertain the identification of bulk charge carrier dynamics via electrical methods, it is beneficial to evaluate thick films to minimize the capacitance. Herein, very efficient co-evaporated n–i–p solar cells with varied active layer thicknesses from 500 nm to 820 nm in comparison to a solution-processed device with 350 nm thickness are studied. In the case of the n–i–p cells, the higher capacitance of the 500 nm solar cell leads to longer decay times at low V_{oc}'s, while in the high voltage regime quite similar kinetics independent of active layer thickness are observed, allowing for the identification of the transition from capacitance-affected to bulk carrier dynamics. It is further revealed that increasing the $MAPbI_3$ thickness by more than 50 % does not affect the recombination dynamics, confirming the high quality of the devices. For the first time for perovskite solar cells it is demonstrated that the recombination order ranges between 1.6 and 2.0, pointing towards trap-assisted and free-carrier recombination under operating conditions.

This chapter is partially based on

D. Kiermasch, L. Gil-Escrig, A. Baumann, H. J. Bolink, V. Dyakonov and K. Tvingstedt. Unravelling steady-state bulk recombination dynamics in thick efficient vacuum-deposited perovskite solar cells by transient methods. *Journal of Materials Chemistry A*, 7, 14712 (2019). DOI: 10.1039/c9ta04367e

6.1. Introduction

Perovskite solar cells are expected to be very cost-effective as they, just like OPVs, can be easily processed via simple printing and vacuum techniques. A low cost of module production is hence envisaged, but as for any PV technology, a high PCE and long-term stability are paramount for making devices attractive for the energy market. The remarkable rise in PCEs for perovskite photovoltaics can be mainly attributed to a very exhaustive optimization of material combinations and deposition methods that today has enabled high crystal quality of the formed photoactive layers. Despite this development, there however remains a deficiency in the overall fundamental understanding of the physics of charge carrier recombination. Further improvements in the performance can now only be achieved with a higher detailed understanding of the dynamics that govern the remaining loss mechanisms. The correct assignment of non-radiative losses and their carrier density dependence is yet to be completed. A first step towards this identification requires assigning both the recombination rate and order to the dominant loss process at each charge carrier density. Currently, several speculations exist,[286,358] for example regarding a non-radiative second-order process. For this process, however, no clear physical origin can be easily identified. In OPVs, similar non-radiative recombination was described and assigned to coupling to high energy vibrational modes, of which not many are needed to allow for non-radiative transitions.[276] In perovskites, such high energetic phonons do not exist[256] and justifying the existence of second order non-radiative recombination behavior becomes harder.

Although lead halide perovskites are considered defect tolerant as discussed in Section 3.1.1,[396] solar cells still partially suffer from deep energy states acting as charge carrier traps and the associated recombination centers are believed to still be a prominent source of non-radiative recombination. In addition to this, the influence of imperfect charge carrier selectivity of the currently employed electrodes embodies a potential source of surface recombination.[297,397,398] Most efforts on recombination dynamics made up to now have however been focused on lifetime assignments of the pure absorber layer itself. More recent studies have also included the contribution of trap-mediated recombination in the bulk of the perovskites, leading to longer assigned lifetimes indicative of the existence of a distribution of shallow trap states.[357] This is in contrast to earlier assignments of mid-gap defect distributions which instead have the effect of speeding up recombination. Staub and coworkers later clarified the role of photon recycling effects that strongly enhances the perceived lifetime obtained from PL decay measurements.[399] Nevertheless, they were able to account for this and provided internal radiative rate constants as well as trap-assisted SRH lifetimes in pure perovskite films. A work on complete devices by Paulke showed in contrast that the recombination can be described by second-order free-carrier dynamics, however with the need to invoke a “time-dependent” rate constant.[400] A clear picture of the true nature and dynamics of photogenerated charge carriers in the perovskite layer itself as well as at the electrode interfaces in actual operational devices, is generally still largely missing.

Insights into recombination losses, which occur in complete devices, can be gained by studying the transient behavior of V_{oc}. Carrier lifetime and density determination via transient methods is therefore widely implemented for perovskites.[300,342,348,401,402] First attempts of employing these methods for mesoporous perovskite devices were carried out by O’Regan and coworkers who emphasized the difficulties of obtaining the correct number of extracted charge carriers and the necessity to distinguish bulk and interface contributions.[300] These methods may therefore in principle provide very useful information on full devices, but only if conducted with care and interpreted correctly as discussed in Chapter 5. Furthermore, Kirchartz et al.[403] and Deledalle et al.[404] have previously shown that for organic solar cells the most crucial necessity to carry out evaluation of recombination dynamics of complete devices is to ensure both high light intensities and thick devices. The basis of these requirements is that it is impossible to access the recombination order in devices where the spatial distribution of excess carriers is not homogeneous.[405] Recent works conducted on perovskite solar cells have up until now observed a quite strong dependence of the carrier lifetime on charge carrier concentration.[300,370,401,406–408] These studies accordingly provided kinetics in devices with recombination orders ranging between 3 and 7 by employing electrical transient methods. Reconciling such high recombination orders under steady-state operational conditions is however not straightforward.

To be able to reliably determine correct recombination orders in thin-film solar cells it is accordingly imperative to reduce the factors that are known to obstruct the assignment of lifetimes and carrier densities. In this chapter, TPV and CE are conducted on solar cells based on $MAPbI_3$ as an active material and the requirement of thick devices is ensured by studying optimized and highly efficient n-i-p solar cells with perovskite layer thickness of 500 nm and 820 nm. In addition, high illumination conditions are applied in order to reach very homogeneous carrier distributions inside the active layer allowing for the observation of recombination orders which are in line with those measured on pure films and noticeably lower than what have been observed previously in complete devices. While the conducted measurements are affected by capacitive contributions at low light intensities/open-circuit voltages, a transition to bulk-related charge carrier dynamics is identified for high light intensities in both devices. This allows the assignment of loss processes to be mainly of Shockley-Read-Hall and free-carrier recombination type. In addition, it is shown that increasing the perovskite thickness, advantageous to achieve high photocurrents, does not affect the recombination dynamics significantly confirming the high quality of the vacuum-processed solar cells studied herein. To strengthen the presented results, additional reference measurements on a thinner solution-processed perovskite device are performed, which has a larger capacitance, a more inhomogeneous carrier distribution and shorter charge carrier lifetimes due to a larger amount of interface recombination losses at a poorly selective PEDOT:PSS interface.[355] This solar cell does not reveal any bulk recombination parameters at all as it is universally ruled by the capacitive discharge of spatially separated charge carriers, even though measured at intensities of up to 3 suns.

6.2. Devices and Current-Voltage Characteristics

As introduced in Section 4.2, perovskite active layers can be processed either from solution[18,409] or by co-evaporation[153,302] of the constituting materials. Even though research is mostly focused on solution-based preparation techniques, the 20 % PCE limit was recently exceeded by co-evaporation methods as well.[305,410] To avoid substantial changes in the morphology,[411] topography[412] and surface coverage[413] observed when varying the thickness via solution-based methods, the more controlled process of co-evaporation is employed to establish uniform $MAPbI_3$ thicknesses of 500 nm and 820 nm. The devices are prepared in Valencia (Spain) by the group of Dr. Henk Bolink. Scanning electron microscopy images of the surfaces of two prepared films with thicknesses of 500 nm and 820 nm are shown in Figure 6.1a and 6.1b. Independent of layer thickness, both films demonstrate the same crystalline domains sizes in the range of tens to hundreds of nanometers. In addition, X-ray diffraction pattern of these films is summarized in Figure 6.1c, confirming a similar crystallinity independent for both films. The appearance of different $MAPbI_3$ peaks leads to the conclusion that both PbI_2 and MAI were fully converted to perovskite as no residual reflections of the constituents are detectable.[414] Complete details on film and device preparation are provided in Section 4.2. Thus, the analysis of the pure films confirms that the method of co-evaporation is able to produce perovskite layers with different thicknesses but keeping other structural properties identical at the same time. It therefore allows to study the impact of the active layer thickness on both device capacitance and recombination dynamics.

In the following, solar cells were manufactured based on the same perovskite thicknesses of 500 nm and 820 nm in a device configuration which is depicted in Figure 6.2.

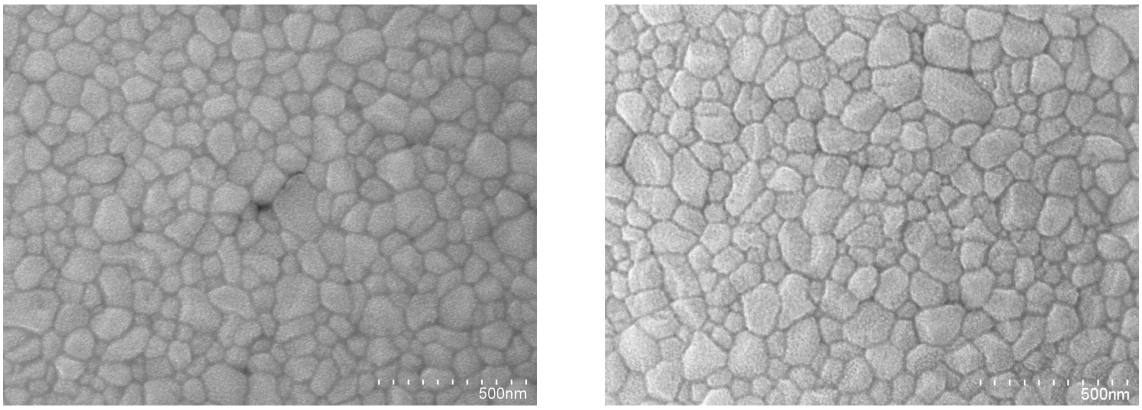

(a) 500 nm **(b)** 820 nm

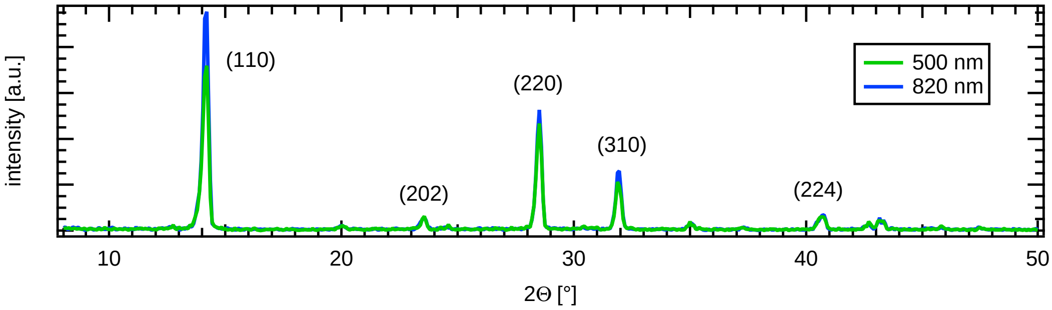

(c)

Figure 6.1.: SEM images for the **(a)** 500 nm and **(b)** 820 nm thick $MAPbI_3$ films showing the same surface topography with similar crystal domain sizes in the range of 10 – 300 nm. **(c)** X-ray diffraction pattern revealing that the studied films are of the same crystalline quality. The determined peaks in the spectra are assigned to the well-known reflections from $MAPbI_3$ perovskite in the tetragonal crystal structure.[415,416] Data is provided by Lidón Gil-Escrig.

The n-i-p layout employs doped-undoped double transport layers located above and underneath the perovskite layer. As an ETL, a combination of 10 nm pure C_{60} close to the perovskite and 40 nm of C_{60}, which is doped with N1,N4–bis(tri–p–tolylphosphoranylidene)benzene–1,4–diamine (PhIm), is used. A similar stacking is also implemented as an HTL, where 10 nm of pure TaTm are followed by 40 nm of doped TaTm. Here, 2,2'–(perfluoronaphthalene–2,6–diylidene)dimalononitrile (F_6–TCNNQ) is utilized as a dopant. As a metal top contact, 100 nm of gold are deposited at the end. The combination of thin pristine organic layers close to the perovskite and thicker doped layers increases the conductivity of the transport layers speeding up the extraction of charge carriers and keeping the interface recombination losses at the same level as in the undoped case. A detailed study on how these devices were optimized by adjusting the thickness of the layers and the necessary amount of doping needed for optimal device performance can be found in Reference[305].

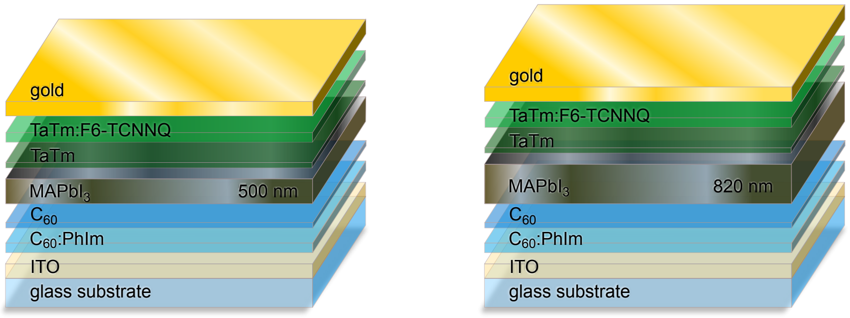

(a) 500 nm **(b)** 820 nm

Figure 6.2.: Device layouts of the **(a)** 500 nm and **(b)** 820 nm n-i-p perovskite solar cells. As an ETL and HTL, a combination of thin undoped organic layers (C_{60} and TaTm) and thicker doped layers (C_{60}:PhIm and TaTm:F_6–TCNNQ) is used. All layers are prepared by the co-evaporation method.

Figure 6.3a shows the current–voltage characteristics under simulated AM1.5G solar irradiation for both devices with different $MAPbI_3$ layer thicknesses in forward (solid) and backward (dashed) directions. Interestingly, both kinds of solar cells show the same fill factor of 72 % and similar V_{oc}'s exceeding 1.1 V. The identical FF thus confirms that charge transport is not the main limitation of the PCE. In contrast to several earlier publications, where an increase in perovskite layer thickness resulted in a decreased performance due to drops in the V_{oc},[417] j_{sc}[411,412] and FF,[411,417] only an increase in j_{sc} due to increased light absorption is observed herein. The 820 nm device (64 % thicker) retains a slightly higher short-circuit current density leading to a higher PCE of 18.2 % compared to 17.6 % for the 500 nm solar cell. Furthermore, no changes in hysteresis behavior upon increasing the active layer thickness is observed in the set of studied devices as it was very recently reported by Li et al.[183] The corresponding j–V curves in the dark are presented in Figure 6.3b together with the $j_{sc}(V_{oc})$ relation[173] determined by measuring both PV parameters at different illumination intensities in the range of 10^{-5} suns to almost 3 suns. The j-V response is fitted by Equation 2.8 to determine the ideality factor (fits are drawn as dashed lines). Since real devices suffer from R_{series}, the intensity(V_{oc}) or $j_{sc}(V_{oc})$ method is more suited to provide accurate values of n_{id} at higher voltages.[173,174,355,374] Since R_{series} can be neglected under open-circuit and R_{shunt} is sufficiently high to prevent affecting the determined V_{oc}'s, Equation 2.8 can be solved for j_{ph} (which equals j_{sc}) in case of $j(V_{oc}) = 0$

$$j_{ph} = j_{sc}(V_{oc}) = j_0 \left(\exp\left(\frac{qV_{oc}}{n_{id} k_B T} \right) - 1 \right). \tag{6.1}$$

This expression allows to determine n_{id} directly from $j_{sc}(V_{oc})$ measurements. Both, j-V characteristics in the dark and the $j_{sc}(V_{oc})$ method however lead to quite simi-

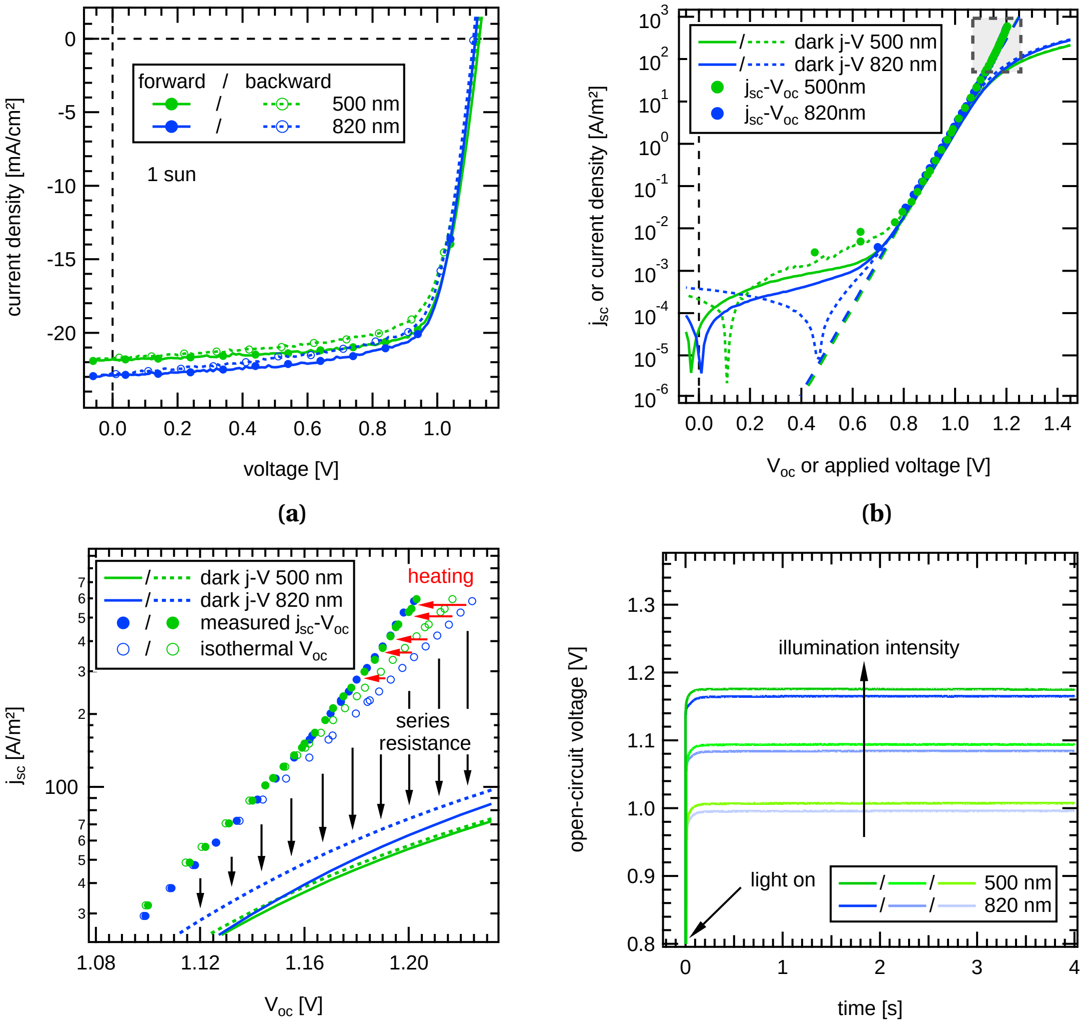

(a) **(b)** **(c)** **(d)**

Figure 6.3.: **(a)** Current–voltage characteristics for the 500 nm and 820 nm n-i-p devices under 1 sun illumination. **(b)** Corresponding j–V curves in the dark (lines) including $j_{sc}(V_{oc})$ measurements for illumination intensities ranging from 10^{-5} suns to 3 suns (dots). The dashed lines correspond to Shockley fits according to Equation 2.8. The grey dashed rectangle is enlarged in **(c)** to demonstrate the influence of device heating and series resistance on the measurements. **(d)** Evolution of V_{oc} for both solar cells after switching on the light for three different light intensities. Independent of illumination intensity, the voltage saturates within a few hundred milliseconds.

lar values of the ideality factor in the range of 1.54 – 1.58 for the 500 nm device and 1.58 – 1.60 for the 820 nm device in the voltage regime between 0.8 V and 1.0 V. These values indicate that SRH recombination is present in the set of studied devices[174] as discussed in Section 3.3 and furthermore that the active layer thickness does not have a significant influence on n_{id}. Figure 6.3c shows an enlarged view of the grey rectangle in Figure 6.3b, where the benefit of measuring $j_{sc}(V_{oc})$ instead of j-V curves becomes apparent. While the j-V's in the dark are heavily affected by series resistance at high forward bias, the $j_{sc}(V_{oc})$ measurements (solid circles) better follow the expected exponential relation described by the Shockley Equation. However, an additional minor bending at voltages higher than 1.1 V can be observed. This is in line with previously observed voltage saturation effects, often seen in a multitude of solar cells when evaluated at higher intensities.[173,349,418,419] Such a behavior was earlier assigned to an increased recombination rate due to enhanced surface recombination,[173,420] but was very recently suggested to have a much simpler origin instead, namely device heating, since a large part of the energy is converted into heat under open-circuit conditions as any current flow is suppressed. Ullbrich et al. showed that just accounting for the thermal resistance Θ of the cell is quite accurately able to explain such voltage saturation effects at higher illumination intensities.[421] The authors extended the Shockley Equation with a modified temperature $T = T_{amb} + \Delta T$, where T_{amb} is the ambient temperature and ΔT is expressed as the product of thermal resistance and the incident illumination intensity. The heating effect is not surprising in the set of herein studied samples as intensities of around 3 suns are approached. The reduced voltages at higher intensities thus can be explained by the fact that the heated device has an increased number of thermally generated background carriers present, forcing the V_{oc} to saturate. To demonstrate the effect of device heating, the $j_{sc}(V_{oc})$ data is fitted at intermediate voltages (0.75 – 1.00 V), where heating is negligible. This allows to determine isothermal values for n_{id} and j_0. By then extrapolating this relation to higher voltages (intensities), the isothermal open-circuit voltage also at higher corresponding illumination intensities/short-circuit currents can be calculated (shown as empty circles in Figure 6.3c). The difference between the measured (heated) and isothermal voltages reveals that the voltage saturation of the thicker and thus more absorbing device is slightly more pronounced and a larger thermal resistance is, as expected, associated. To reduce the effect of device heating, transient electrical measurements in this thesis are performed with illumination times as short as possible but still paying attention to that a steady-state voltage has been established. As can be seen in Figure 6.3d, it takes only a few hundred milliseconds for the n-i-p devices to reach a stable V_{oc}, which is much faster compared to TiO_2-based perovskite solar cells, where times up to hundreds of seconds are sometimes needed.[182,197] Thus, the illumination time is kept very short (< 1 s) to reduce the effect of device heating. With the ambition to determine as accurately as possible how the excess charge carrier density and charge carrier lifetime vary with internal voltage (and not device heating), the measured charge carrier density and lifetime are presented versus the determined isothermal 300 K voltages.

In order to point out the effect of short recombination lifetimes and larger device capacitances, an additional solar cell based on PEDOT:PSS as the HTL is studied. A fully solution-processed device with a similar p-i-n structure as introduced in Figure 5.2c is prepared, where the p-TPD is replaced by PEDOT:PSS. This transport layer is known to be a potential source of leakage and surface recombination[355,422] due to its semi-metallic nature which leads to an inefficient electron-blocking ability.[423] Despite its benefits in perovskite PVs such as simple processing, high reproducibility or suppressed hysteresis, PEDOT:PSS-based devices suffer from decreased V_{oc}'s which are usually up to 0.2 V lower in comparison to other HTL's.[316,355,424,425] This is a direct consequence of decreased charge carrier lifetimes as the $MAPbI_3$/PEDOT:PSS interface speeds up recombination. Figure 6.4 illustrates j-V curves in the dark and under 1 sun illumination for the solar cell comprising 350 nm of $MAPbI_3$ as an active layer. The low V_{oc} of 0.88 V indicates increased charge carrier losses in comparison to the co-evaporated n-i-p devices introduced in Figure 6.3. On the other hand, the highly conductive polymer allows for a high fill factor of 80 %. The extracted PV parameters of the PEDOT:PSS-based cell and the thicker n-i-p devices are summarized in Table 6.1.

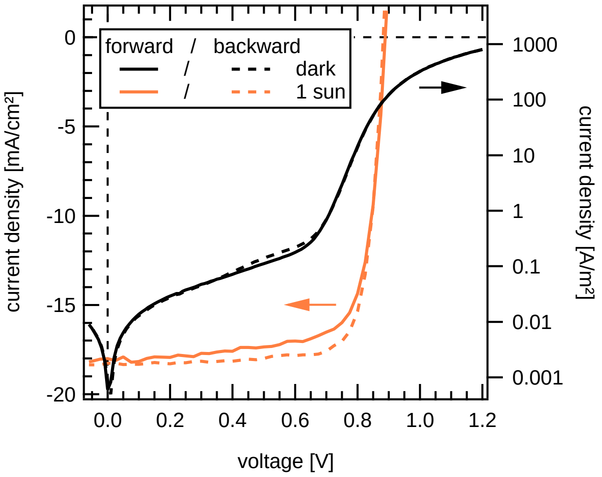

Figure 6.4.: Illuminated (left y-axis) and dark (right y-axis) j-V curves of a 350 nm solution-processed $MAPbI_3$ device with PEDOT:PSS as a hole transport layer and the combination of C_{60}, $PC_{60}BM$ and BCP as electron transport layers.

device	n_{id}	j_0 [Am^{-2}]	j_{sc} [$mAcm^{-2}$]	V_{oc} [V]	FF [%]	PCE [%]
500 nm (n-i-p)	1.54-1.58	$5.5 \cdot 10^{-11}$	21.8	1.12	72	17.6
820 nm (n-i-p)	1.58-1.60	$8.5 \cdot 10^{-11}$	22.7	1.11	72	18.2
350 nm (p-i-n)	1.24	$2.1 \cdot 10^{-10}$	18.3	0.88	80	12.8

Table 6.1.: Extracted PV parameters from j-V characteristics (Figure 6.3 and 6.4) for all devices.

6.3. Relation between Charge Carrier Density and Open-Circuit Voltage

In this section, CE is applied to determine the geometric capacitance of the introduced devices and to study the charge carrier density under illumination at open-circuit conditions. Analogous to Section 5.6, the amount of charge carriers stored at the electrodes is determined via CE experiments without illumination. The solar cells are prebiased with low negative voltages ranging from -0.35 V to -0.05 V, where it can be assumed that the devices act as plate capacitors. The extracted charge normalized to the device area is shown in Figure 6.5a. A linear relationship between the amount of extracted charge and the applied voltage can be confirmed and the following values for the geometric capacitance can be calculated: 114 nF/cm^2 for the 350 nm thick device based on PEDOT:PSS, 54 nF/cm^2 for the 500 nm n-i-p solar cell and 42 nF/cm^2 for the 820 nm n-i-p device confirming that a thicker perovskite layer decreases the device capacitance. These values are used in the following to correct the CE measurements under illumination. Earlier publications stated that CE measurements performed on mesoporous perovskite solar cells display long extraction times in the range of tens of microseconds[426] leading to an unrealistically high amount of extracted charge,[300] which is probably caused by ion migration. In contrast, CE signals obtained in this chapter are

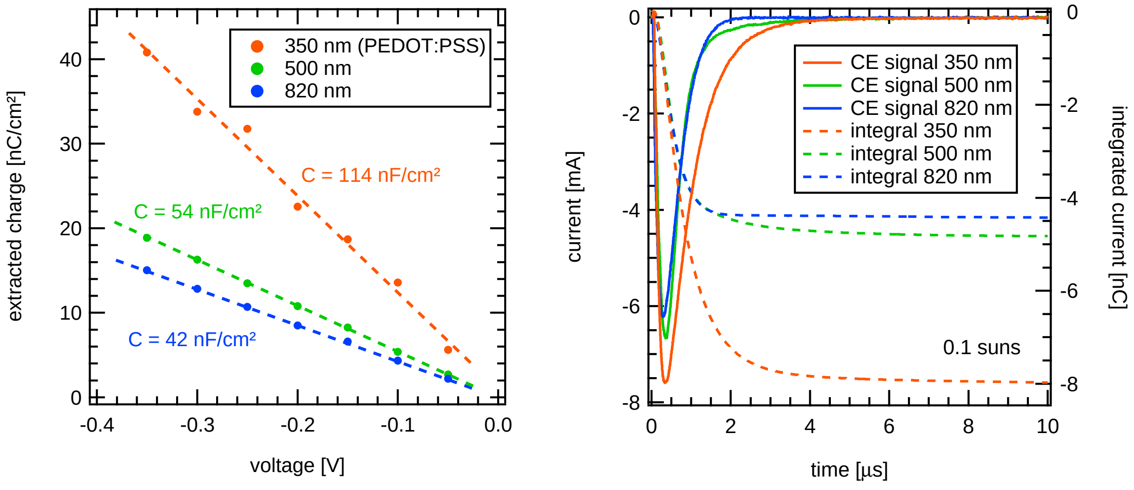

(a) (b)

Figure 6.5.: (a) Extracted charge from CE experiments without illumination under negative voltages in the range of -0.05 V down to -0.35 V. From a linear fit, the geometric capacitance of each device is calculated. **(b)** Raw charge extraction signals (solid lines, left y-axis) and the integral (dashed lines, right y-axis) for all devices measured under 0.1 sun illumination conditions. A fast charge extraction pulse within a few hundred nanoseconds can be observed.

usually characterized by a very realistic extraction time of only a few hundred nanoseconds as it is demonstrated in Figure 6.5b. Thus, a very reasonable amount of total extracted charge is accordingly obtained. This is also in line with a previous publication, where it was shown that planar TiO_2-free devices do not necessarily lead to an unrealistic amount of extracted charge.[401]

Figure 6.6a summarizes the extracted charge (normalized to the active area) of the studied devices over a plethora of open-circuit voltages measured at illumination intensities ranging from 10^{-5} suns to almost 3 suns. The dashed lines represent the geometrical capacitance multiplied with the studied open-circuit voltages to quantify the amount of geometric capacitive charge carriers. This charge are subtracted from the illuminated measurements to correct for the geometrical capacitance. The measured CE data for the illuminated case is shown as filled circles and shows a clear transition into a much steeper slope at an open-circuit voltage of around 1.05 V. At low voltages, both n–i–p devices demonstrate differences in the amount of total extracted charge, while it appears more similar after the 1.05 V transition. At higher voltages, the total extracted charge from the 820 nm cell however still outnumbers the amount of charge measured for the 500 nm device. The larger amount of charges in the thinner device at lower V_{oc}'s (< 1.05 V) confirms that these are indeed capacitive charge carriers located at the surfaces (electrodes), as these carriers originate from the solar cell with larger C_{geo}. In contrast, the larger amount of charges at the highest V_{oc}'s (> 1.05 V) in the thicker device (highlighted by dashed arrows) indicates bulk-dominated volume charges instead. In comparison to both n–i–p cells, more charges are extracted at substantially lower voltages in the thinner PEDOT:PSS solar cell. In addition, no transition can be observed leading to the conclusion that the extracted charge carriers are purely dominated by the capacitance of the device. It is extremely important to consider here that, in general, the spatial distribution of excess charge carriers in a device can be very inhomogeneous[403–405] and accordingly that the determination of excess carrier density from the measured amount of extracted charge is not at all straightforward. Only in the case of a homogeneous excess carrier distribution is it reasonable to divide the total extracted charge with the active layer thickness to obtain a relevant density value. As outlined in the above-mentioned studies, ensuring thick devices and higher illumination conditions will force the distribution of excess carriers to become more homogeneous. As a consequence, for thinner devices and lower light intensities, the gradients of excess carrier concentration inside the active layer are simply too large to allow for the assumption of one single average carrier concentration and decay rate at each evaluated intensity. In addition, the voltage dependence of inhomogeneously distributed excess carriers will be weaker than that of evenly spatially distributed excess

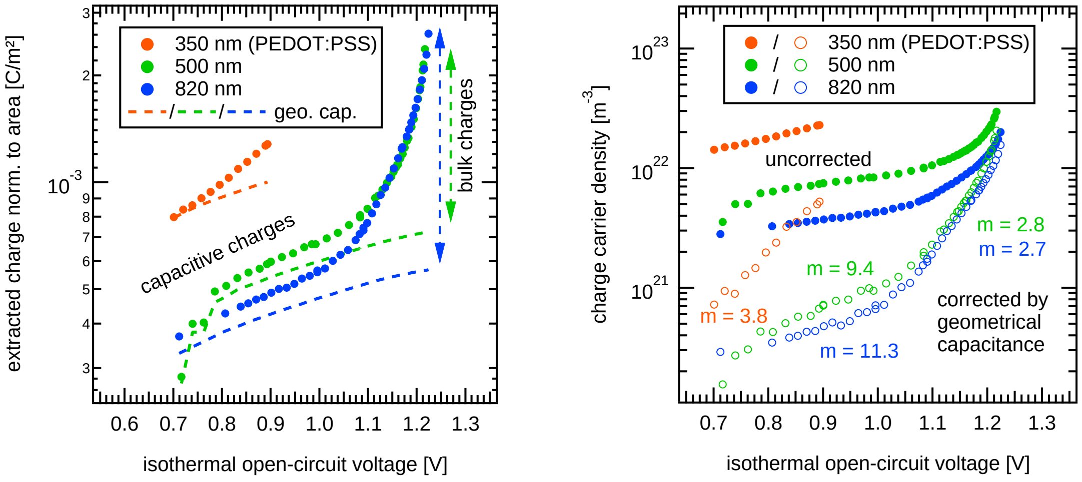

(a) **(b)**

Figure 6.6.: (a) Measured extracted charge from CE experiments plotted over 300 K isothermal open-circuit voltages for the 500 nm and 820 nm n–i–p and 350 nm PEDOT:PSS devices. In the case of the n–i–p cells, a clear transition is visible at around 1.05 V allowing for the identification of a capacitance affected regime at low voltages and bulk-related charges at higher voltages. The PEDOT:PSS solar cell does not show a transition and displays therefore only the capacitive contribution. Dashed lines correspond to geometrical capacitance approximation from CE experiments in the dark at low negative voltages (see Figure 6.5a). The calculated charge carrier densities are shown in **(b)**, where both the raw (filled circles) and capacitance-corrected (empty circles) data is included.

carriers.[391,403,404] However, as the device thickness and light intensities are increased, the flatter the distribution of excess charge carriers becomes. In case of the two thicker n–i–p devices, these conditions are ensured as the active layer thickness is larger compared to other thin-film PVs and the measurements are performed at high illumination intensities. When accounting for the different volumes, the charge carrier density can be calculated as carried out in Figure 6.6b. Here, the filled circles show the uncorrected densities while the empty circles represent the capacitance corrected densities originating from the difference between circles and dashed lines in Panel 6.6a. For the n-i-p devices, it can be confirmed that both the determined excess charge carrier densities in the bulk of the perovskite and their voltage dependency are in fact quite similar, something that would not have been the case if the carrier profiles would be inhomogeneous. In contrast, the uncorrected extracted charge carrier density of the thinner PEDOT:PSS solar cell shows much weaker voltage dependence, signifying that this device displays a much more inhomogeneous excess carrier distribution and is ruled by capacitive charges. The corrected extracted charge in both n–i–p devices is covering more than one entire order of magnitude of excess carrier densities, far exceeding that in a majority of earlier published studies, allowing for the assignment of the slope of the exponential relationship between voltage and excess carrier density with greater certainty. This relationship is usually described by[403]

$$n = n_0 \exp\left(\frac{qV_{oc}}{mk_BT}\right), \tag{6.2}$$

where n_0 corresponds to the equilibrium carrier density and m accounts for the slope deviation from the thermal voltage k_BT/q. Using this expression, the m-values in both the capacitive and bulk regime for both n–i–p devices are determined. While the low voltage data for the n–i–p devices is assigned to the capacitive regime show ($m = 9.4$ for the 500 nm device and $m = 11.3$ for the 820 nm device) very high and different m-values of no siginificant meaning, the relevant high voltage regime can be described by substantially lower and very similar m-values of 2.8 and 2.7 for both devices, respectively. This again points to the fact that steady-state m-values should not be affected by the active layer thickness, but only by the representative recombination process. The PEDOT:PSS based solar cell reveals a considerably higher m-value of 3.8. An early study on thickness variation[406] noted different slopes when instead altering the thickness of their transport layers (PEDOT:PSS and $PC_{70}BM$), highlighting also that these layers substantially contribute to the overall capacitance of the device, obstructing meaningful deductions of the bulk carrier density slope parameter m.

6.4. Relation between Charge Carrier Lifetime and Open-Circuit Voltage

After the successful identification of bulk charge carriers in the previous section, it is proceed with the determination of how charge carrier lifetimes vary with V_{oc} by means of TPV. Similar to the previous CE experiments, the same range of steady-state background intensities ($10^{-5} - 3$ suns) is used. The induced small-voltage transients are analyzed with a mono-exponential decay function to extract charge carrier lifetimes. In recent literature regarding perovskites, it is found that both single[95,234,401,407,427] and double[234,241,300,402,428] exponential functions are used to determine TPV decay times. Thereby, it appears that studies employing a double exponential fit have the presence of TiO_2 in common, while planar devices in the p–i–n layout more often show single exponential TPV decays. This is in line with reports[300,402,428] where (mesoporous) TiO_2 was proposed as the main cause of the second and slower exponential decay, also in the small-perturbation regime, where the condition $\Delta V_{oc} \ll V_{oc}$ is satisfied. Figure 6.7 summarizes the measured TPV lifetimes for the three perovskite solar cells calculated by fitting the transients with a single exponential decay. However, for high light intensities ($V_{oc} \geq 1.10\,\mathrm{V}$) the transients start to reveal more of a double exponential nature (with two lifetimes τ_1 and τ_2) in case of the n–i–p devices. The high voltage part is enlarged in the inset of Figure 6.7 and reveals a difference by a factor of 3 to 4 between the observed τ_1 and τ_2 for both layer thicknesses. Since the studied solar cells do not contain planar or mesoporous TiO$_2$ it cannot be the origin of the two measured lifetimes. Furthermore, in the high intensity region it has to be noted that τ_1 exhibits a stronger voltage-dependence than τ_2, which seems to be nearly constant at around 1 μs. It is noted that voltage-independent charge carrier lifetimes describe a first-order recombination process and accordingly that it is conceivable that both first- and second-order carrier lifetimes are being measured at these high voltages. Another possible explanation could be that one lifetime corresponds to the interface and the other one can be assigned to charge carriers from the bulk of the perovskite.

In general, the dependency of lifetime on the open-circuit voltage can be expressed by

$$\tau = \tau_0 \exp\left(-\frac{qV_{oc}}{\vartheta k_B T}\right) \tag{6.3}$$

with τ_0 as the intercept at 0 V corresponding to the equilibrium carrier lifetime and the factor ϑ accounts again for the slope deviation from the thermal voltage $k_B T/q$. Please note, that this expression is in form quite identical to the capacitive discharging lifetime introduced in Equation 5.13 apart from that the prefactor $\frac{n_{id} k_B T}{q} \cdot \frac{C_{geo}}{j_0}$ is now replaced by τ_0. The unit remains time in both cases, but the fact that it is ruled by ratio between the capacitance and the dark saturation current in Equation 5.13 explains the high values it often needed to take in earlier literature. In line with the voltage dependency of the charge carrier density, the small-perturbation lifetimes also show a clear transition at around 1.05 V for both thicker n-i-p devices, where the slopes change substantially. It is emphasized that this transition in the relationship between charge carrier lifetime and V_{oc} has previously not been identified in perovskite solar cells. For the 500 nm device, ϑ is determined to be 1.6 in the low voltage regime and 2.4 in the high voltage regime. Quite similar values are obtained for the 820 nm device where ϑ equals 1.7 at voltages below 1.05 V and 2.5 for voltages above 1.05 V. However, in agreement with previous reports, the PEDOT:PSS device does not show any slope alterations over the studied open-circuit voltage range and reveals ϑ to be 1.4. Under 1 sun illumination conditions, the PEDOT:PSS cell shows a charge carrier lifetime of about 400 ns, while both thicker n–i–p devices demonstrate a lifetime of around 800 ns. It is accordingly unphysical, that the huge difference in V_{oc} of these devices could be caused by such a small discrepancy in the charge carrier lifetime. This fact indicates that the measured lifetimes cannot be related to bulk carriers at the same time but that the PEDOT:PSS cell displays kinetics associated with a capacitive discharge instead. In order to solidify

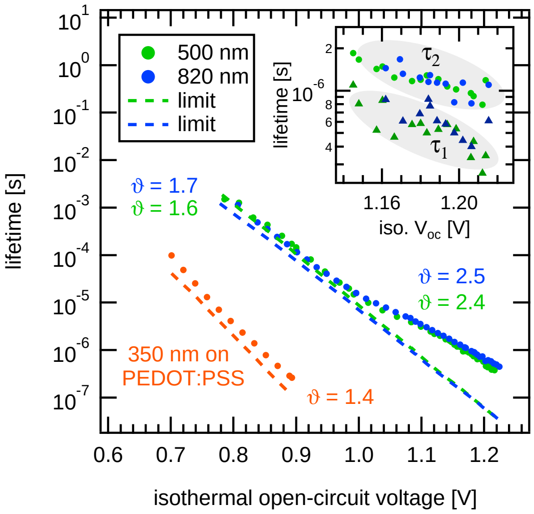

Figure 6.7.: Small-perturbation charge carrier decay times determined by TPV for the 350 nm PEDOT:PSS device and the 500 nm and 820 nm n–i–p cells. The data has been analyzed with single exponential fits. For the highest intensities, double exponential decays are observed in both n–i–p devices as shown in the inset, where both τ_1 and τ_2 times are plotted. Dashed lines correspond to the characteristic time limit according to Equation 5.13 resulting from the discharge of charge carriers at the electrodes. This limit must be exceeded in order to make statements about relevant bulk lifetimes, which is the case for voltages higher than 1.05 V.

the statements made so far and to distinguish between bulk recombination lifetimes and capacitive discharging rates, the characteristic time τ_{cap} according to Equation 5.13 is calculated using n_{id} from Table 6.1 and the $j_{sc}(V_{oc})$ relation from Figure 6.3b and the geometrical capacitance determined from Figure 6.5a. The obtained values are depicted as dashed lines in Figure 6.7. The following can therefore be concluded for both n–i–p devices: at low voltages ($V_{oc} < 1.05$ V), the measured TPV lifetime is determined by the time it takes for charge carriers located at the respective majority carrier electrode or interface of the electrodes to find their counterpart at the other end of the device. The lifetime is accordingly well described by a capacitor that is discharged via the diode itself. For voltages above 1.05 V, the charge carriers get more evenly distributed and the measured lifetimes clearly exceed the limit set by Equation 5.13, allowing for the identification of bulk carrier lifetimes. For the highest intensities, the difference between the theoretical capacitive limit and the measured lifetimes is more than one order of magnitude. In the case of the thinner PEDOT:PSS device, no clear difference between the calculated capacitive limit and the measured decay times can be observed, which is clearly proving that these lifetimes are not real bulk carrier lifetimes. Even at the highest illumination intensities, the capacitive discharge is still longer than the bulk carrier lifetimes, which are usually in the range of a few ns in PEDOT:PSS-based devices[429,430] since these cells suffer more from surface/interface recombination.[355,422] The small difference between the calculated and measured lifetimes for the PEDOT:PSS device can be explained by the fact that the measured lifetimes do not originate from a pure geometric discharge but are rather a combination of voltage independent (geometric) and voltage dependent (e.g. depletion layer) capacitive effects.

6.5. Charge Carrier Dynamics and Recombination Order

Performing TPV and CE at the same illumination intensities and thus open-circuit voltages allows to correlate the measured lifetimes with the corresponding charge carrier density as displayed in Figure 6.8a for the PEDOT:PSS device and Figure 6.8b for both n–i–p devices. The dashed lines correspond again to the capacitive lifetime limit but now plotted versus the charge carrier density instead of V_{oc}. While the PEDOT:PSS solar cell has a constant slope and is completely limited by capacitive discharge as illustrated in Figure 6.8c, both n–i–p devices show the transition from a steeper slope below $1{\cdot}10^{21}$ m^{-3} to a flatter slope at high charge carrier densities. At low carrier concentrations (grey region), the decay times are longer for the 500 nm device at a fixed charge carrier density. This behavior is expected since these decay times originate from a device with a larger capacitance (and the discharging time of a capacitor is directly proportional to its capacitance) and thus confirms the statements made so far. In contrast, the lifetime–density correlation is quite similar for both devices at higher carrier densities, which means that these cells are ruled by very similar bulk carrier recombination dynamics. This situation is depicted in Figure 6.8d, where internal bulk recombination lifetimes are longer compared to τ_{cap}. The capacitance-to-bulk transition can be already observed at slightly lower carrier densities for the thicker device, which can be explained by the reduced impact of capacitive charge carriers on the charge carrier dynamics. In addition, τ_2 is included in Figure 6.8b, showing an almost constant lifetime–density relationship pointing towards the contribution from a pure first-order recombination process.

Combining Equation 6.2 and 6.3, the relationship between lifetime and carrier density can be described by the power law expression

$$\tau = \tau_0 \left(\frac{n}{n_0} \right)^{-\lambda} \tag{6.4}$$

where the ratio m/ϑ is now abbreviated with λ. The parameter λ, describing the slope of the power law, represents the recombination order via the relation $\delta = \lambda + 1$.[346,431]

Values for δ are provided in Figure 6.8, revealing a high recombination order of 3.8 for the PEDOT:PSS sample, in line with values presented in earlier studies.[370,401,406–408] In the case of the n–i–p devices, even higher values of 6 – 7 for the 500 nm device and 8 – 9 for the 820 nm device are obtained for densities below $1{\cdot}10^{21}$ m^{-3}, but without any physical meaning as they originate from the capacitive regime. However, for charge carrier densities above $1{\cdot}10^{21}$ m^{-3}, quite similar recombination orders in the range of 1.7 – 2.0 (500 nm) and 1.6 – 2.0 (820 nm) can be determined. Whereas most of the earlier publications on both perovskite and organic solar cells have commonly observed

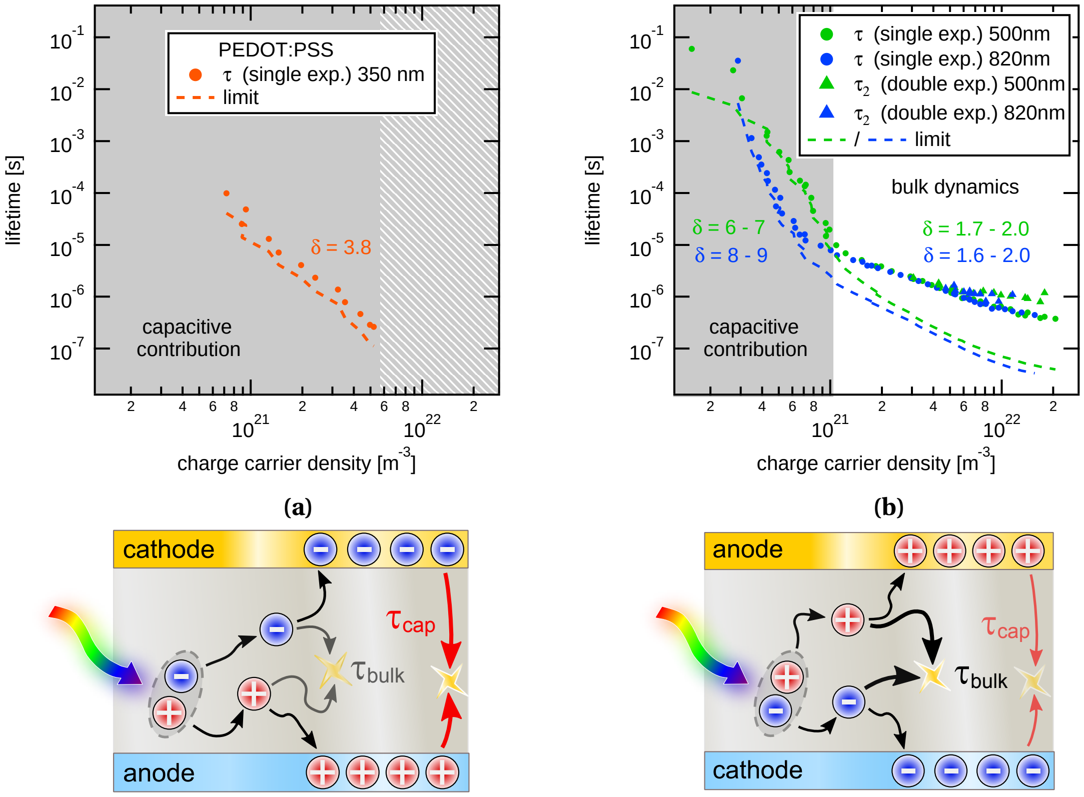

(a) **(b)**

(c) **(d)**

Figure 6.8.: Recombination dynamics for the **(a)** PEDOT:PSS based and **(b)** two thicker 500 nm and 820 nm perovskite solar cells. The PEDOT:PSS device is completely dominated by capacitive charge carriers and shows a constant slope of $\delta = 3.8$. In the case of the n-i-p devices, the transition between capacitance and bulk related dynamics can be observed at $1{\cdot}10^{21}$ m^{-3}. While the capacitive parts show a longer lifetime for the thinner 500 nm device at a fixed carrier concentration, the bulk regimes are quite similar. In addition, the capacitive part demonstrates unphysically high recombination orders, while the bulk related dynamics point towards first- and second-order processes. **(c)** Schematic depiction of the situation in the PEDOT:PSS device, where τ_{cap} is longer compared to τ and thus dominates the measurements. **(d)** In contrast, both n-i-p devices show a regime where bulk recombination lifetimes can be determined.

noticeably higher recombination orders, the thicker n–i–p devices reveal recombination orders lower than or around 2 when determined by electrical means on complete perovskite solar cells. The deduced recombination order in the relevant carrier density regime thus largely rules out the occurrence of Auger effects and confirms that devices are mostly ruled by first- and second-order dynamics independent of the active layer thickness. Accordingly, it can be concluded that these devices suffer from SRH and radiative recombination under operating conditions. These values for the recombination order are also in line with literature where TRMC and PL measurements revealed similar values in neat MAPbI$_3$ films (not integrated into a device architecture) at similar charge carrier densities of around ~10^{22} m^{-3}.[286,432,433] In line with the j–V characteristics in Figure 6.3, it is concluded from the transient optoelectrical analysis that the additional 320 nm of perovskite in this device configuration do not affect the recombination dynamics negatively, which is remarkable compared to the existing literature.[406,411,417] This points towards the interfaces to contribute to a large extend to the recombination losses in these solar cells. Further, it is emphasized that under 1 sun illumination conditions, a steady-state excess charge carrier concentration of $7 \cdot 10^{21}$ m^{-3} is identified which is a value of carrier concentration that non-electrical methods such as TRPL, TA, THz spectroscopy and TRMC should strive for in the future in order to determine perovskite PV relevant decay kinetics.

6.6. Transient and Steady-State Parameters

Transient electrical techniques can be used not only to determine charge carrier lifetimes and densities but also steady-state parameters like the ideality factor n_{id}.[434] The ideality factor is linked to the determined experimental parameters m and ϑ via

$$\frac{1}{n_{id}} = \frac{1}{m} + \frac{1}{\vartheta}. \tag{6.5}$$

By combining Equation 6.5 with the relation $\delta = (m/\vartheta) + 1$, the recombination order can be determined by

$$\delta = \frac{m}{n_{id}}. \tag{6.6}$$

This clarifies that the recombination order is in principle also accessible by determining merely the voltage dependence of charge carrier density and the steady-state parameter n_{id}. Both Equations 6.5 and 6.6 are therefore of general importance for the herein intended message, since they link steady-state and transient recombination parameters with each other and provide an alternative route to the one illustrated in Figure 6.8 for the determination of δ. A few rules of thumb are worthy of bearing in mind with respect to the above equations; if the steady-state ideality factor n_{id} equals the charge carrier density slope m, then the dynamics must be first-order ($\delta = 1$). If on the other hand the lifetime slope ϑ equals the density slope m, pure second-order recombination ($\delta = 2$) dominates. The latter is for example the case for an intrinsic solar cell operating in the radiative limit with pure band-to-band recombination. Then m and ϑ are not only equal but must also have the value 2, which will always result in an ideality factor of unity. However, these clear cases are often not observed in real thin-film solar cells.[298]

Table 6.2 summarizes the measured and calculated recombination parameters determined in this chapter. For the n–i–p devices, the values are separated into parameters determined in the capacitive and the bulk regime as already discussed. Using Equation 6.5, four calculated values for n_{id} are thus provided and compared to the values obtained from the steady-state $j_{sc}(V_{oc})$ measurements. Depending on which regime the n_{id} has been determined in, the values are close or slightly underestimated compared to the steady-state value. Please note that the ideality factor determined in the higher voltage regime, which is assigned to reliable bulk values, still might be limited by a minor contribution from capacitive effects. A lower n_{id} is also observed for the PEDOT:PSS based device (Equation 6.5 leads to 1.02, while the dark j–V in Figure 6.4 revealed 1.24). The recombination order δ was also subsequently calculated in two ways: first, by using the slopes in Figure 6.8 (and thus relying only on TPV and CE) and second, taking Equation 6.6 with m-values from CE and n_{id}'s from steady-state experiments in Figure 6.3b and 6.4. Both methods demonstrate that the parameters determined in the capacitive regime yield completely unrealistic values for δ, while representative and realistic orders (1.6–2.0) can be obtained only in the higher voltage regime for the 500 nm and 820 nm n–i–p devices, justifying the focus on the separation of the measured transient data into these two regimes. The agreement of both

	350 nm	500 nm		820 nm	
region	capacitive	capacitive	bulk	capacitive	bulk
m (Figure 6.6b)	3.8	9.4	2.8	11.3	2.7
ϑ (Figure 6.7)	1.4	1.6	2.4	1.7	2.5
n_{id} (Equation 6.5)	1.02	1.37	1.29	1.48	1.30
n_{id} (Figure 6.3 and 6.4)	1.24	1.54-1.58		1.58-1.60	
δ (Figure 6.8)	3.8	$\approx 6-7$	$\approx 1.7-2.0$	$\approx 8-9$	$\approx 1.6-2.0$
δ (Equation 6.6)	3.2	≈ 6	≈ 1.8	≈ 7	≈ 1.7

Table 6.2.: Recombination parameters determined by steady-state (j–V characteristics and $j_{sc}(V_{oc})$ measurements) and transient (TPV and CE) techniques.

methods in the determination of the recombination order confirms the reliability of the performed analysis.

After the lifetime and density of the charge carriers and thus the recombination rate in conjunction with the dominant recombination order have been determined, further parameters such as the recombination current j_{rec} and V_{oc} can be directly calculated. According to References[300,434,435], the recombination current at open-circuit can be calculated via

$$j_{rec} = \frac{qd}{\delta} \cdot \frac{n}{\tau}. \tag{6.7}$$

Inserting the determined values for lifetime, density and recombination order obtained from the bulk regime, j_{rec} is calculated and the values are summarized Figure 6.9a in case of the 500 nm thick n-i-p device, which serves as an example for the both n-i-p solar cells. For reasons of comparison, the measured j_{sc}'s are also included in the plot as empty circles. Obviously, j_{rec} equals j_{sc} at open-circuit over the range of studied voltages. Accordingly, voltage-independent charge carrier generation can be confirmed for the n-i-p devices. This is in contrast to a multitude of OPVs, where electric fields are usually necessary to separate the excitons prior to extraction.[249,436] It has to be noted, that different lifetimes for Equation 6.7 have been used to calculate the recombination current density. The dashed line illustrates the transition from lifetimes determined from a single-exponential fit to lifetimes calculated from the double-exponential fit at higher intensities (see Figure 6.7). At highest voltages, j_{sc} is described best by inserting τ_2 into Equation 6.7. Thus it is accordingly concluded that charge carrier recombination processes are characterized by this lifetime. Further, by combining Equation 6.2, 6.3 and 6.7 and solving for V_{oc}, the voltage can be calculated according to

$$V_{oc} = \frac{mk_BT}{q\delta} \ln\left(\frac{j_{sc}\delta\tau_0}{qdn_0}\right). \tag{6.8}$$

It is noted, that the recombination current is set to be j_{sc} which is a valid assumption as previously shown in Figure 6.9a. The reconstructed open-circuit voltages are compared to the measured values in Figure 6.9b for the whole range of studied illumination intensities. The measured V_{oc}'s can be quite accurately reproduced if it is considered that most of the input parameters for Equation 6.8 do have a noticeable error margin as they are extracted from strong exponential functions. However, for low light intensities, a deviation becomes apparent which is most probably caused by the impact of shunt recombination losses on the open-circuit voltage. These losses are not accounted for in the herein presented model, hence the calculated values overestimate the measured (reduced) voltages. Since the derived recombination framework presented in this chapter is able to reproduce the steady-state parameters j_{rec} (j_{sc}) and

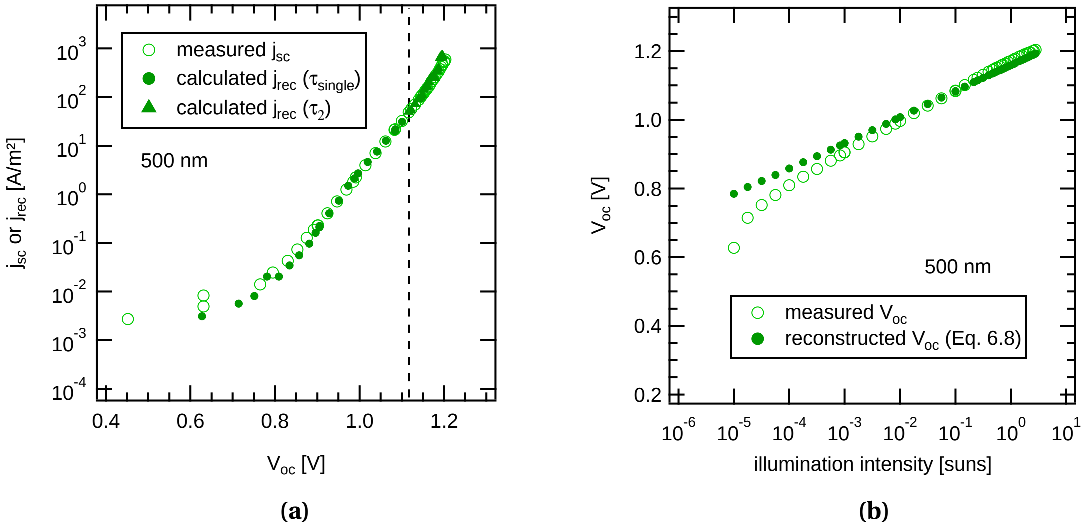

Figure 6.9.: (a) Measured j_{sc} and calculated j_{rec} for the 500 nm n-i-p device proving that the recombination current density at open-circuit equals the short-circuit current density. The dashed line indicates that different values for the lifetime (originating from a single- and a double-exponential fit) have been used to calculated the recombination current. **(b)** Measured and reconstructed open-circuit voltages according to Equation 6.8.

V_{oc} over the whole range of studied intensities, it is concluded that the experimental methods provide a powerful tool to describe the kinetics of photovoltage generation in fully working devices.

6.7. Summary

In conclusion, it is demonstrated that highly efficient planar perovskite devices can be manufactured with active layer thicknesses exceeding 800 nm without any noticeable loss in efficiency. Furthermore, accounting for the increase of the equilibrium charge carrier density, originating from the induced temperature rise at the highest intensities, steady-state relevant charge carrier concentrations and lifetimes versus isothermal voltages are provided and analyzed. While it is not possible to extract useful bulk recombination parameters from the thinner PEDOT:PSS device due to short lifetimes and a high device capacitance, a capacitance-to-bulk transition in the studied n–i–p perovskite PV devices is identified. With these thick and well-performing solar cells and by measuring in the high intensity regime of up to 3 suns, it is possible to generate homogeneously distributed excess carrier concentrations which allow to calculate accurate and meaningful values of charge carrier densities and lifetimes in complete devices. Having minimized the influence of spatially separated carriers, the obtained densities, lifetimes and associated recombination orders (1.6 – 2.0) are in line with reported values for pure perovskite films, as determined by optical contact-less transient methods and in strong contrast to earlier literature and the PEDOT:PSS device, where noticeably higher values for δ are found. Under operating conditions, the main loss processes in these devices are therefore assigned to be of SRH and free-carrier recombination type. By comparing devices with thicknesses of 500 nm and 820 nm but otherwise identical intrinsic properties, it is found that the recombination dynamics are not depending on the perovskite thickness in accordance with the very similar open-circuit voltages indicating that the interfaces towards both transport layers still remain to be a dominant source of non-radiative recombination losses. The reliability of the measured data is finally confirmed by calculating the recombination current density and open-circuit voltage and comparing to the parameters determined from steady-state j-V characteristics. This work demonstrates that transient electrical techniques can, if correct bulk dynamics are identified, help to understand recombination losses in solar cells that will allow future opportunities to also study how to suppress them. The work further contributes to the enduring discussion on the correct analysis of electrical transient data which was initially addressed in Chapter 5, where long lifetimes and high recombination orders are sometimes observed for low carrier concentrations/illumination intensities in different solar cells technologies, possibly originating from measurements performed in the capacitance-limited region. It is clearly shown that these optoelectrical methods can be used to determine reliable recombination parameters in fully working perovskite devices under operating conditions if both thick active layers and high illumination conditions are ensured.

7. Improved Open-Circuit Voltage of Evaporated Perovskite Solar Cells by Post-Annealing

Abstract. Perovskite layers can be prepared by various methods with the source materials being deposited either by solution-based methods or by thermal evaporation. In this study, a post-annealing procedure is applied to co-evaporated n-i-p and p-i-n perovskite solar cells leading to PCE improvements, which can be mainly attributed to an increased open-circuit voltage. With a V_{oc} of around 1.11 V after preparation, the voltage is improved to more than 1.18 V by annealing the device to 320 K and cooling back to room temperature again. The observed photovoltage is among the highest reported V_{oc}'s for $MAPbI_3$ solar cells featuring also an excellent stability of more than half a year. J-V characteristics in the dark reveal a reduction of both n_{id} and leakage recombination, indicating a significant impact of the post-annealing procedure on the recombination losses. To investigate carrier dynamics in more detail, transient optoelectrical techniques are applied and confirm that the bulk carrier lifetime is increased. Finally, high radiative efficiencies of more than 1 % are obtained from electroluminescence measurements, demonstrating that the solar cells are also suitable for LED applications.

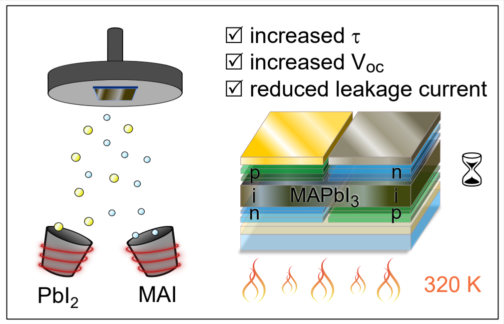

This chapter is partially based on

D. Kiermasch, L. Gil-Escrig, A. Baumann, H. J. Bolink, K. Tvingstedt and V. Dyakonov. High open-circuit voltages above 1.18 V in planar perovskite solar cells due to post-annealing: insights into charge carrier dynamics from transient electrical techniques. *in preparation*

7.1. Introduction

Even though organic-inorganic hybrid perovskite solar cells have become a promising candidate for a next generation PV technology, the PCEs have reached a bottleneck after the rapid development during the last years since the first application of $MAPbI_3$ as a photoactive absorber in 2009.[17] Further increase in photovoltaic performance requires a correct understanding of the elementary physical processes, which lead to energy conversion, such as charge carrier generation, transport or recombination dynamics. As outlined in Equation 2.7 in Section 2.3.2, the PCE of a solar cell is defined by the short-circuit current density, the fill factor and the open-circuit voltage. In case of the most popular perovskite compositions like $MAPbI_3$, which is characterized by a band gap in the range of 1.6 eV, the maximum value of j_{sc} corresponds to ~25 – 26 mA/cm^2.[296] Several publications have already demonstrated high currents close to 24 mA/cm^2 in case of $MAPbI_3$[437,438] and even higher values[36] for other perovskites comprising different organic molecules and halides. This indicates that there is not much room for further improvements since the reported values for j_{sc} are close to the theoretical limit. However, to exploit the PCE maximum for a 1.6 eV band gap material of 30.5 %[296] according to Shockley-Queisser,[289] the other PV parameters have to be addressed, namely FF and V_{oc}.

The fill factor can be affected by parasitic losses like shunt and series resistance, depending on the intensity the solar cell is illuminated with. While leakage currents due to a small shunt resistance are usually dominant at low illumination intensities,[355] losses caused by a high series resistance are more important at solar relevant conditions as will be clarified in Chapter 8.[439] Therefore, every device engineer tries to minimize ohmic losses either by introducing new materials with higher conductivities (charge carrier mobilities) or by optimizing the established layers by changing the thickness and/or the chemical doping. In addition, FF also depends on the type of dominating charge carrier recombination processes in the diode, which are usually described by the ideality factor. In 1981, Green showed that the FF of an ideal solar cell exclusively depends on n_{id} and V_{oc} if the impact of both R_{shunt} and R_{series} is negligible, as it is illustrated in the exponential part of the dark j-V relation in Figure 2.6b.[440] Since FF is sensitive to these recombination parameters, it should be aimed for ideality factors close to unity and high open-circuit voltages to increase its value. In the radiative limit of $MAPbI_3$, which corresponds to a $V_{oc,rad}$ of 1.33 V[441,442], the FF can even exceed 90 % at 1 sun illumination.[21,296,443] Summing up all these considerations, it can be concluded that the reduction of recombination losses is detrimental for further PCE improvements as they do not only affect V_{oc} (see Section 3.3 for further details) but the FF as well. Recent literature has therefore identified non-radiative recombination losses as the main limiting factor in state-of-the-art perovskite solar cells.[21,297,444] For this reason, many scientists are engaged in characterizing non-radiative recombination processes and minimizing these losses to increase the performance even further.

Charge carrier recombination is described by the underlying mechanism and the rate at which charge carriers recombine and can be generally characterized by the different processes introduced in Chapter 3. While it is always strived for minimizing SRH losses, higher-order mechanisms like band-to-band (radiative) free carrier and Auger recombination are carrier density dependent and cannot be avoided and accordingly define the already introduced radiative limit as the maximum achievable $V_{oc,rad}$. When lead halide perovskites were implemented for the first time as absorber materials in DSSCs, a low voltage of only 0.61 V has been achieved.[17] By replacing TiO_2 with Al_2O_3 and using Spiro-OMeTAD instead of a liquid electrolyte, a noticeable increase in V_{oc} to values exceeding 1.0 V was obtained, boosting the PCE to more than 10 % and clearly demonstrating the potential of this novel PV technology.[18] In 2014, Tvingstedt et al. highlighted the promising radiative efficiency (EQE_{EL}) in the range of 10^{-2} % for planar p-i-n devices with a V_{oc} of 1.08 V, outnumbering state-of-the-art fullerene-containing OPVs by more than 2 orders of magnitude.[441] To address losses due to trap-mediated SRH recombination, the composition of the perovskite absorber has been widely modified. Incorporation of rubidium into the crystal lattice pushed V_{oc} to 1.24 V for a 1.63 eV band gap quadruple cation perovskite and led to a remarkable EQE_{EL} of 3.8 %.[41] Similarly, Cs compounds were utilized as additives[39] resulting in an increased V_{oc} due to a reduced defect density as pointed out by Hu et al.[445] In line with these reports, potassium iodide was also implemented as an additive.[42] The employement of these different components usually aims to modify the bulk of the perovskite. However, another route to reduce parasitic losses is to improve the interfaces to the surrounding transport layers. Long PL lifetimes over 8 μs under solar relevant carrier densities have for example been demonstrated on polycrystalline $MAPbI_3$ layers, if the surfaces were treated with additives after preparation.[446] Very recently, surface passivation also helped to approach the radiative limit with a quasi Fermi level splitting of 1.28 eV in solution-processed films as determined by optical measurements.[447] Having a closer look on solar cells in full device configuration, replacing PEDOT:PSS with p-TPD can help to increase the voltage substantially.[355] Further, a high open-circuit voltage of 1.21 V was realized by stacking a guanidinium bromide interface layer on top of a mixed-cation perovskite (featuring a band gap of 1.62 eV).[448] The highest V_{oc} for $MAPbI_3$ reported so far is 1.26 V as recently published by Liu et al.[449] The outstanding photovoltage was achieved by a light-induced activation process, whose origin was not clarified. All these results demonstrate that new perovskite compositions, improved deposition methods and interface engineering[450–452] are necessary to push the PV parameters closer to the radiative limit.

As introduced in Section 4.2, different routes can be applied to synthesize uniform perovskite films of high quality. Most of the above-mentioned studies are based on solution-processed devices as still the largest part of research is focused on preparation out of solution. Here, the substrate is usually annealed to around 100 °C after depositing the material to ensure complete crystallization. Nevertheless, preparation techniques like spin-casting are generally not directly applicable to large scale production and therefore do not promote a rapid introduction of perovskite solar cells on the PV market. In contrast, vapor-deposition methods avoid the use of toxic solvents, allow for an easier scalability and are therefore considered as a promising approach to realize commercialization.[337] These techniques are characterized by simultaneous evaporation of the reactants, with crystallization being driven by the excess kinetic energy of the condensating particles, thus avoiding additional annealing steps. In the present chapter, a novel post-annealing procedure is applied to fully co-evaporated planar n-i-p and p-i-n perovskite solar cells, where the complete device is heated to 320 K for several hours and cooled back to room temerature again. As a consequence, the PCE of the devices is increased which can be mainly attributed to an improved V_{oc} reaching more than 1.18 V. To demonstrate that the increase in V_{oc} is not a temporary effect, stability measurements over more than half a year are performed and supported by additional MPP tracking. Further, the origin of the voltage increase is studied by investigating the changes in recombination dynamics. From current-voltage characteristics in the dark, a reduction of both the ideality factor and shunt recombination losses is tracked, indicating that recombination losses at low and also more relevant higher light intensities are reduced. In addition, a transient optoelectrical analysis is performed to study recombination dynamics in more detail, demonstrating that bulk recombination lifetimes are increased by the post-annealing process. Finally, the solar cells are studied by means of electroluminescence measurements and noteworthy radiative efficiencies exceeding 1 % are obtained, being among the highest reported values for perovskite devices and outnumbering many other PV technologies.

7.2. Devices and Current-Voltage Characteristics

To ensure the general validity of the statements made in this chapter, the study is conducted on planar $MAPbI_3$-based n-i-p and p-i-n solar cells. 820 nm are selected for the active layer thickness since the efficiency is slightly increased compared to thinner de-

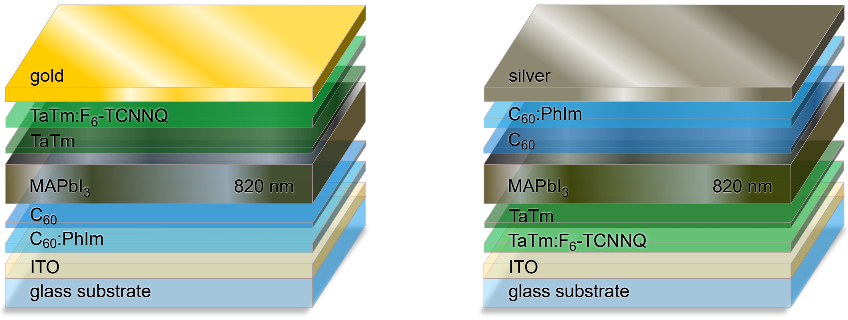

(a) n-i-p **(b)** p-i-n

Figure 7.1.: Device layout of the **(a)** n-i-p and **(b)** p-i-n perovskite solar cells with an active layer thickness of 820 nm. As transport layers, a combination of thin undoped organic layers (C_{60} and TaTm) and thicker doped layers (C_{60}:PhIm and TaTm:F_6–TCNNQ) is used. All layers are prepared by co-evaporation.

vices as shown in Figure 6.3a. The solar cells are fully evaporated with the same combination of electron (C_{60} and C_{60}:PhIm) and hole (TaTm and TaTm:F_6-TCNNQ) transport layers as already used in the previous study in Chapter 6. Further details on material properties and device preparation is provided in Chapter 4.

Current-voltage characteristics under 1 sun illumination for the the n-i-p and p-i-n devices after preparation are summarized in Figure 7.2a. Both types of solar cells demonstrate quite similar open-circuit voltages of more than 1.1 V. Differences in FF (72 % for n-i-p and 70 % for p-i-n) and j_{sc} (22.7 mA/cm^2 for n-i-p and 20.2 mA/cm^2 for p-i-n) lead to different PCEs ranging from ~18 % for the n-i-p device to ~16 % for the p-i-n configuration. While the n-i-p device shows minor but still detectable hysteresis, the p-i-n cell does not display any differences between the forward and backward scan. This demonstrates that the interfaces and the regions close to the interfaces influence the hysteresis behavior significantly as discussed already in Section 2.3.3. Figure 7.2b illustrates the evolution of V_{oc} for both solar cells during the time after preparation and induced by a simple post-annealing procedure. Post-annealing of the full devices was performed in a closed helium cryostat, where the temperature was carefully increased from 300 K up to 320 K, at which the solar cells were kept for several hours, followed by cooling down to room temperature again. The temperature was not further increased to higher values as it is known for $MAPbI_3$ that heating over 363 K (90 °C) of full devices can lead to irreversible degradation.[453–455] For this reason, deliberate care was taken to avoid increasing the temperature too much. A steep rise in V_{oc} can be observed during the first days where the initial voltage of around 1110 mV increases to approximately 1140–1150 mV. Post-annealing of both solar cells improves the V_{oc} even further to more than 1180 mV being stable for a time span of more than half a year. Red arrows indicate the day the post-annealing was conducted at. In order to disentangle

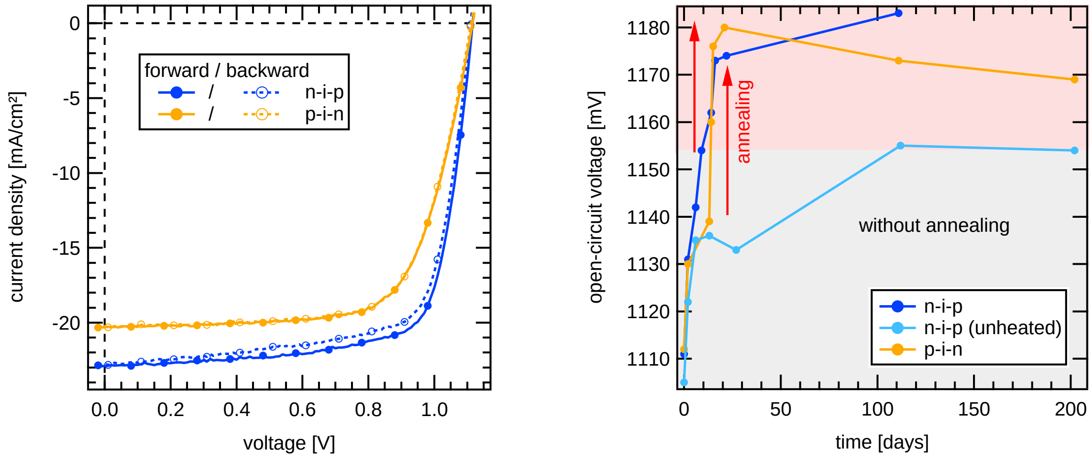

(a) **(b)**

Figure 7.2.: **(a)** j-V characteristics of n-i-p and p-i-n solar cells after preparation determined under 1 sun illumination. Both solar cells display only minor hysteresis effects. **(b)** V_{oc} evolution during a time span of 202 days for both type of devices. The post-annealing procedure (heating to 320 K for several hours and cooling down back to 300 K) increases the V_{oc} up to more than 1180 mV as indicated by the red arrows. For reasons of comparison, V_{oc} development for a n-i-p device without the heating treatment is shown, demonstrating that the voltage is lower in comparison to the the treated solar cells.

the processes between time and heating, the V_{oc} development of an additional n-i-p device without post-annealing treatment was studied in the same time range. For this device, the voltage stabilizes at around ~1150 mV after 100 days. From this, it is concluded that the processes increasing the voltage from ~1110 mV to ~1150 mV are time-induced as indicated by the grey area, while the improvement from ~1150 mV to more than ~1180 mV is activated by the post-annealing procedure (red area). Several reports exist, where it is demonstrated in a similar way that the V_{oc} (and PCE) of perovskite solar cells can increase during aging in the dark and under heating.[455–458] It has been also shown that the occurrence of an improved PCE during continuous measurements might be characteristic for planar devices without a mesoporous scaffold (see Figure 2.4). While the identification of the origin for the PCE improvement over time requires further research, speculations already exist that these improvements are caused by the passivation of (surface) defects by small amounts of PbI_2 which can play a role if the perovskite starts to decompose.[455,459–461] However, as this still remains an open task for further studies, the focus of this chapter is to investigate the changes induced by the post-annealing procedure in more detail.

In order to support the above-mentioned stability measurements, additional maximum power point tracking measurements are conducted and summarized in Figure 7.3. MPP tracker are commonly used for PV systems to guarantee that a solar cell op-

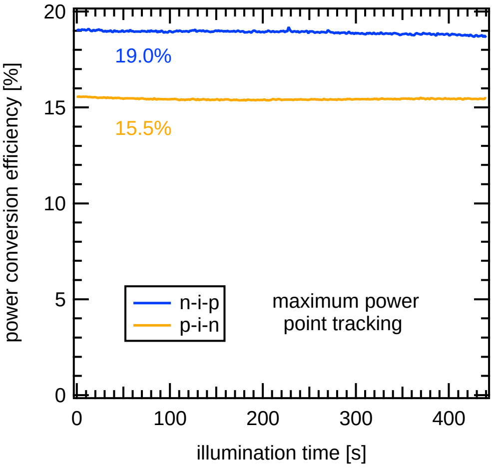

Figure 7.3.: Maximum power point tracking of both devices at 1 sun illumination after the post-annealing procedure. A stable power output is detected.

erates under optimal conditions and the extracted power is maximized. Here, both devices do not show losses in efficiency upon 1 sun illumination supporting again that the increase in V_{oc} due to post-annealing is not a temporary effect. For the n-i-p device, the PCE is increased to around 19 %, while the p-i-n solar cell is characterized by a similar PCE (15.5 %) as directly after preparation since it suffers from minor losses in FF due to an increased series resistance as will be discussed in the next section.

7.3. Ideality Factor from Current-Voltage Characteristics in the Dark

To gain further insights into the underlying mechanisms which are responsible for the observed V_{oc} changes, j-V characteristics measured in the dark are analyzed in the following. Figure 7.4 summarizes the current-voltage scans which are performed within a period between 0 and 111 days for the n-i-p device (Panel 7.4a) and for the p-i-n device (Panel 7.4b). For clarity, only measurements from the forward scan direction between -0.2 V and 1.5 V are shown, since these devices only have negligible hysteresis behavior as outlined in the previous section. Information about dominant recombination processes are accessed by studying the ideality factor. In case of an intrinsic semiconductor, an n_{id} of unity is an indication of pure band-to-band recombination while SHR recombination leads to $n_{id} = 2$. Surface recombination due to non-selective contacts would correspond to $n_{id} \leq 1$. Further information on the relation between ideality fac-

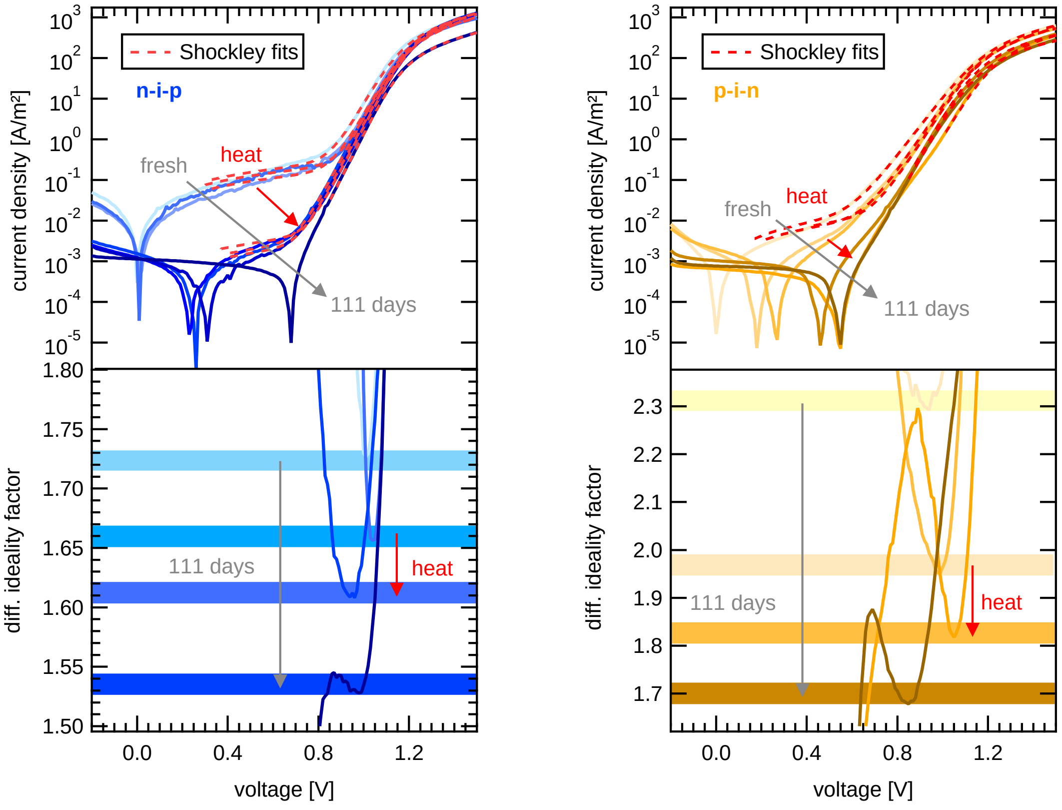

(a)

(b)

Figure 7.4.: j-V curves in the dark for the studied **(a)** n-i-p and **(b)** p-i-n solar cells. Aging and heating increases the shunt resistance and reduces leakage currents in both type of devices. The red dashed lines correspond to Shockley fits according to Equation 2.8. Differential ideality factors derived from Equation 7.1 are summarized in the lower parts of the graphs, demonstrating a reduction of n_{id} and thus reduced non-radiative recombination.

tor and the dominant recombination processes is provided in Section 3.3. To determine the differential ideality factor n_{id}^{diff}, the current-voltage curves are analyzed with

$$n_{id}^{diff} = \left(\frac{k_B T}{q} \cdot \frac{\mathrm{d} \ln j(V)}{\mathrm{d}V} \right)^{-1}, \tag{7.1}$$

which is a direct outcome of the exponential term of the Shockley Equation 2.8. It describes the slope of the dark j-V curves and allows to extract the ideality factor as a function of the applied voltage. The calculated n_{id}^{diff}'s for the set of dark j-V's are plotted in the bottom half of Figure 7.4 showing a noticable reduction of n_{id} within the studied time span of 111 days. It is obvious that the ideality factor changes due to both time and annealing in line with the observed changes in V_{oc}. This indicates that the recombination dynamics are changing in both devices. For the n-i-p cell, n_{id} decreases from 1.73 to 1.53, while the p-i-n device exhibits an even greater shift from 2.30

to 1.69. These values are in line with a multitude of different studies, where similar values for the ideality factors have been determined for perovskite PV.[174,297,298,355,408,462] The decrease in n_{id} is usually correlated with an decrease of SRH recombination via defects. Thus, this is the first evidence that non-radiative SRH is efficiently decreased by the introduced post-annealing procedure.

To extract further information from the measured j-V curves, the full expression of the generalized Shockley Equation 2.8 is used to quantify the observed changes in R_{shunt} and R_{series}. Fits are illustrated as red dashed lines in Figure 7.4, while the extracted parameters for R_{shunt} and R_{series} are provided in Figure 7.5. Induced by the post-annealing process, the shunt resistance is increased by more than one order of magnitude in both devices, proving that leakage recombination pathways have been removed efficiently. This can also be observed in the increased open-circuit voltage in the "dark", which is caused by room light and scattered light from the sun simulator during the j-V sweep and demonstrates the potential application as indoor light applications or photodetectors. It has to be noted that the exact values for the R_{shunt} after more than 20 days of storage could not be determined as no leakage currents can be observed due to the photovoltage from scattered light. The inset of Figure 7.5a shows the measured V_{oc}'s at low light intensities ($10^{-5} - 10^{-3}$ suns) before (blue) and after (red) post-annealing to illustrate an the increase in voltage. It has been reported for perovskite solar cells, that shunt recombination losses seem to be more pronounced in devices that suffer from non-perfect selectivity of the transport layers.[355,463] This results in increased interface recombination between the perovskite and the transport layers and reduces the ability of appropriate quasi Fermi level splitting and therefore high $V_{oc}'s$. While shunt recombination losses are usually dominant at low light intensities, interface or surface recombination also plays a crucial role under operating illumination conditions. To give an example, PEDOT:PSS is known to be a large source of interface recombination as it can only inefficiently block electrons.[355,422] In contrast to the R_{shunt}, R_{series} (Figure 7.5b) does not reveal a clear trend from the post-annealing procedure. Even though the n-i-p cell shows a small drop in R_{series} after post-annealing, no general conclusion can be made, since the p-i-n shows the opposite trend. In the studied time span, R_{series} increases by approximately 4 Ωcm^2 in case of the n-i-p and even 8 Ωcm^2 for the p-i-n cell. This can be explained by the degradation of the top electrode (and the transport layers underneath) as the metal reacts with some components of the perovskite.[464,465] The movement of halides in perovskites crystals[466] allows for a reaction between the electrode material and e.g. iodine, as it has already been demonstrated for silver electrodes with the formation of silver iodide.[467,468] As silver is chemically less inert in comparison to gold, the degradation of

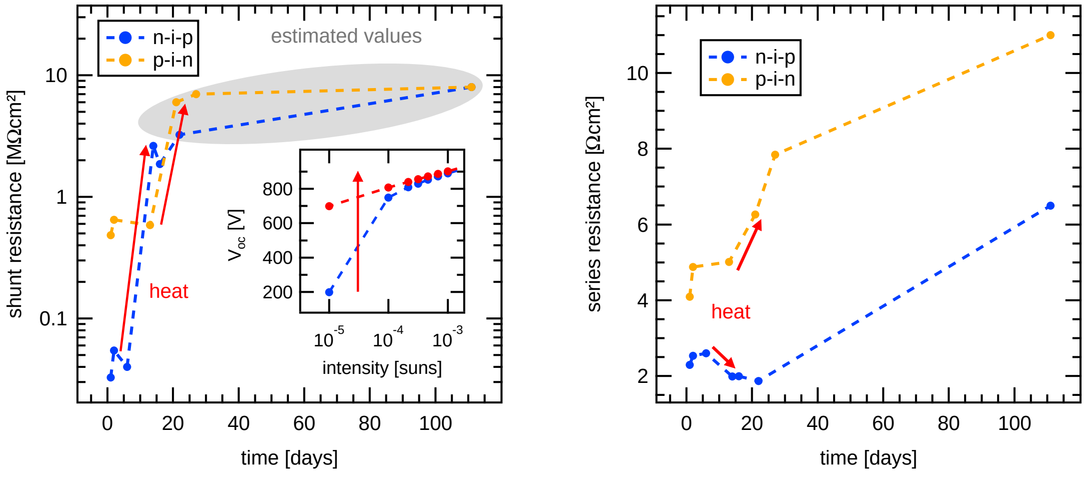

(a) **(b)**

Figure 7.5.: Observed changes in **(a)** shunt and **(b)** series resistance as determined from j-V measurements in the dark (Figure 7.4). The post-annealing procedure reduces shunt recombination losses significantly, increasing the open-circuit voltage at low light intensities as it is exemplary shown in the inset for the n-i-p soar cell. In contrast, there is no clear trend observable for the series resistance. For both devices, R_{series} increases as the electrodes starts to degrade in time.

the p-i-n devices is more severe than for the n-i-p solar cells. Nevertheless, as there is no correlation between V_{oc} and R_{series}, it is unlikely that charge transport is responsible for the herein studied effects, especially since both devices show a stable open-circuit voltage even though the series resistance is increasing in time.

7.4. Analysis of Charge Carrier Lifetimes

To further analyze charge carrier recombination processes, CE in combination with TPV is employed. In line with the previous study in Chapter 6, the measurements are performed over a large range of illumination intensities up to 3 suns, where the solar cells are heated up by the LED even though all experiments are performed in a closed-cycle helium cryostat. To account for this, the isothermal open-circuit voltage is calculated according to the method outlined in Section 6.2.[421] Figure 7.6 depicts the determined charge carrier densities for the n-i-p and p-i-n devices. Filled circles summarize CE measurements performed under illumination intensities in the range of 10^{-5} up to 3 suns, while the dashed lines correspond to measurements in the dark. Here, the charge carriers stored on the electrodes are extracted by applying a small negative bias without illumination prior to switching to short-circuit conditions. This is analogous to Figure 6.5a, where the calculated capacitance can be used to determine the amount of capacitive charge at the corresponding V_{oc}'s. Under illumination, both devices show a transition from a shallow slope to a steeper slope at around 1.05 V. At lower voltages, only minor differences between the illuminated and dark measurements can be observed, while the light induces a substantial increase in charge carrier density at higher voltages. It can be therefore concluded, that mostly capacitive charge carriers rule at low voltages in both devices. For the p-i-n solar cell, the similarity between the geometric capacitance and the charge carrier density obtained under illumination ($V_{oc} \leq 1.05$ V) is pointing towards a pure geometric capacitance. In contrast, a voltage-dependent offset can be noticed for the n-i-p solar cell for voltages below 1.05 V, which results from an additional contribution to the geometric capacitance. These charges, for example, can have their origin in a depletion-layer capacitance in the perovskite film like already proposed in complete solar cells under certain conditions.[469,470] It is therefore important to note, that even though the same transport layers have been used and the perovskite layer was prepared within the same batch, both devices show different capacitive contributions indicating that the crystallization of the active layer is different depending on if the n- or p-layer is underneath. Thus, the differences in the capacitive behavior between both studied solar cells indicates that the perovskite is intrinsically doped if it is deposited on top of C_{60} instead of TaTm. The post-annealing procedure does not influence the voltage-dependence of the capacitive charge carriers

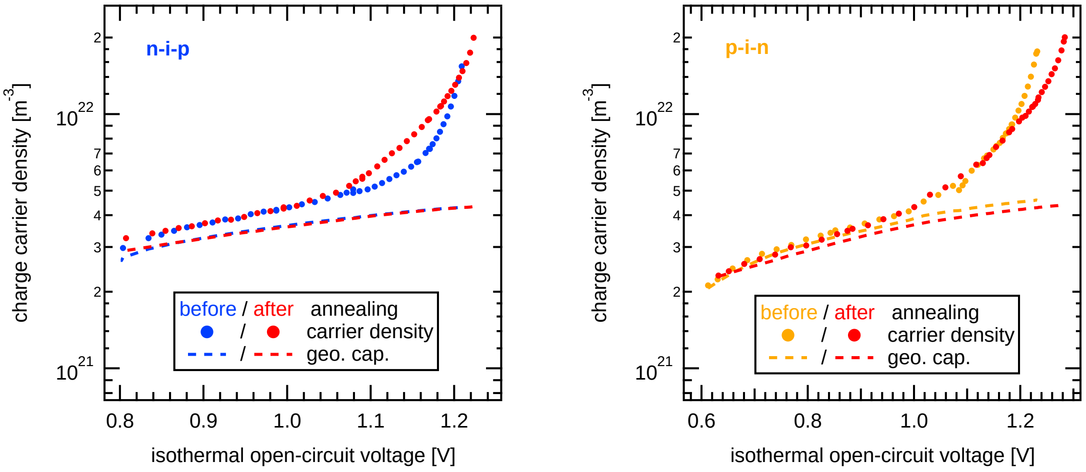

(a) **(b)**

Figure 7.6.: Charge carrier density from CE plotted over the open-circuit voltage for the **(a)** n-i-p and **(b)** p-i-n devices before (blue/orange filled circles) and after (red filled circles) annealing. Dashed lines represent extracted charge carrier from geometric capacitance measured with CE experiments in the dark. In both type of devices, a transition from a shallow slope at low voltages ($V_{oc} \leq 1.05$ V) to a steeper slope at higher light intensities can be observed. While the low voltage part of the extracted densities coincides with the geometric capacitance for the p-i-n device, a voltage dependent offset can be observed for the n-i-p cell.

at low voltages. This is contrary to high voltage regime, where charge carriers from the bulk dominate. Here, the post-annealing procedure shows differences in the extracted charge carrier density clearly pointing towards modified bulk recombination dynamics which will be further investigated by means of TPV.

In the following, the impact of post-annealing on charge carrier lifetimes is studied. A detailed description of the method is provided in Section 4.3.2, whereas the interpretation and analysis of the data is discussed in Chapter 5. The solar cells were illuminated with the same illumination intensity array that has been used for CE in order to ensure the same open-circuit voltages and correlate the lifetime with the corresponding charge carrier density. To distinguish between capacitance affected lifetimes and bulk carrier lifetimes, it is emphasized that the measured lifetimes have to exceed the characteristic limit set by Equation 5.13. To compare the change in carrier dynamics induced by the post-annealing, it is necessary to analyze how lifetime scales with carrier density rather than voltage, which is summarized in Figure 7.7 for both devices together with the time limit from the geometric capacitance. In both kind of solar cells, the measured lifetimes, which are extracted from a single exponential fit, are close to the capacitive limit for densities below $4{\cdot}10^{21}$ m^{-3} (capacitive regime, grey background), whereas for higher voltages, the limit is surpassed and bulk dynamics can

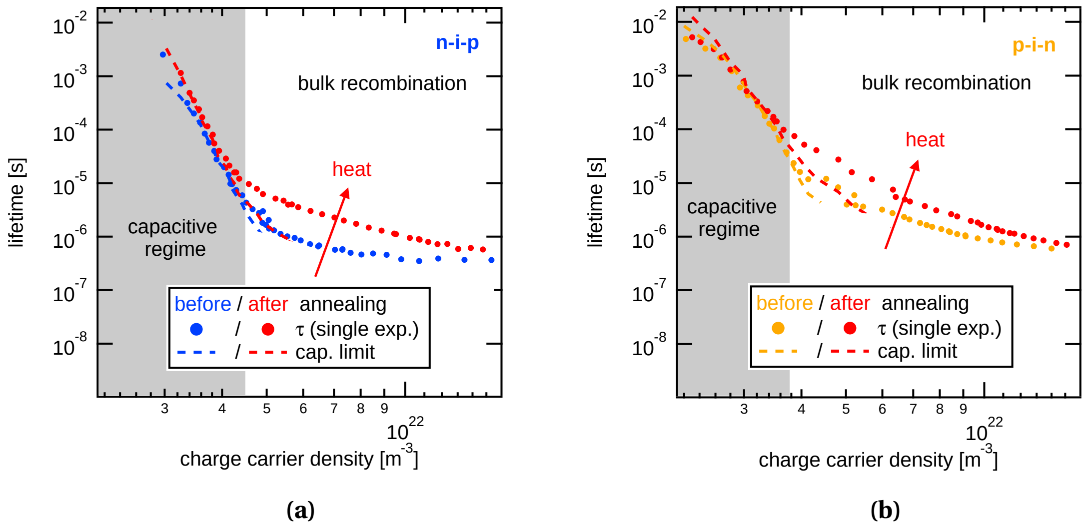

Figure 7.7.: Charge carrier lifetimes as determined from single exponential fits plotted over the charge carrier density for the **(a)** n-i-p and **(b)** p-i-n device. Dashed lines correspond to the capacitive discharging time, which was calculated via Equation 5.13. At lower charge carrier densities ($\leq 4{\cdot}10^{21}$ m^{-3}), the measured data originates from the recombination of spatially separated capacitive charge carriers, while bulk carrier dynamics can observed at higher densities. Charge carriers from the bulk demonstrate that post-annealing leads to a higher carrier lifetime at the same densities, resulting in an improved open-circuit voltage under operating conditions.

be identified in line with Figure 7.6. Obviously, post-annealing does not influence the capacitive discharging times, while the bulk carrier lifetimes at fixed concentrations are increased. This justifies again the separation of the measured data into these two regimes. Furthermore, at carrier concentrations below $4{\cdot}10^{21}$ m^{-3}, the lifetime strongly depends on carrier density, while the slope gets more shallow for higher concentrations. As demonstrated in Chapter 6, the slope only remains a useful indication of the dominant carrier recombination mechanism if bulk charge carriers are measured. At high carrier densities, the slope is increased, suggesting that post-annealing increases the dominant recombination order as it is expected if SRH recombination centers have been passivated. This is completely in line with the observed reduction of n_{id} in Section 7.3, which also indicates decreased SRH recombination. Thus, the transient optoelectrical analysis directly proves that the reason for the increase in V_{oc} (see Figure 7.2b) is linked to improved carrier lifetimes and reduced recombination losses.

After having identified bulk charge carrier lifetimes in fully working n-i-p and p-i-n perovskite solar cells, the general effect of these recombination lifetimes on the resulting open-circuit voltage at 1 sun illumination conditions can be explored. The impact of charge carrier lifetimes on V_{oc} is generally described by Equation 3.19 and 3.20 in case of pure radiative and SRH recombination processes. If both recombination mechanisms are present, Equation 3.21 is a more appropriate expression since it takes radiative and SRH recombination into account. The outcome of Equation 3.19, 3.20 and 3.21 is depicted in Figure 7.8, which is in line with calculations from Pazos-Outón.[471] The values are calculated for 1 sun illumination conditions (in order to de-

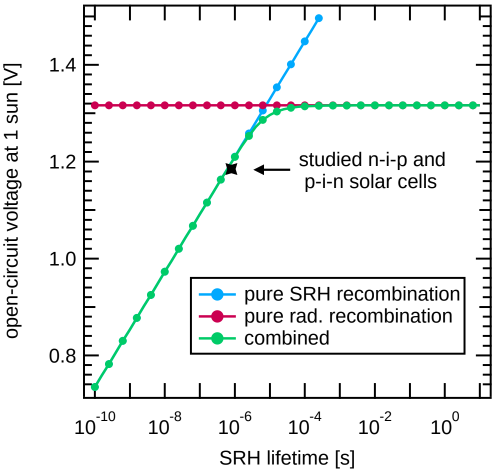

Figure 7.8.: Calculated influence of the SRH lifetime on the open-circuit voltage based on Equation 3.19, 3.20 and 3.21. The inserted parameters are listed in the main text. In addition, the obtained values for lifetime and V_{oc} for the herein studied devices is included.

termine G), a band gap of 1.6 eV, a device thickness of 820 nm, $k_{rad} \approx 10^{-17}$ m^3/s[433] and $N_{C,V} \approx 3.1{\cdot}10^{24}$ m^{-3}. In case of pure radiative recombination, SRH lifetime has no influence and the open-circuit voltage is limited to about 1.32 V, matching with reported values.[441,442,449] If SRH recombination is present and the lifetimes are sufficiently low, V_{oc} can be decreased to values below the radiative limit. The voltage-lifetime correlation for the set of herein studied devices is also included (black star) proving that the determined lifetime perfectly matches with the theoretical prediction. This supports the validity of the determined recombination parameters and demonstrates that both SRH and radiative processes are the main loss mechanisms in these devices. The measured lifetimes of 800 ns under 1 sun are among the highest carrier lifetimes reported so far for $MAPbI_3$-based perovskite solar cells raising the hope that further improvements can help to reach SRH lifetimes in the range of 10 – 100 μs to minimize limitations caused by trap-assisted SRH recombination and maximize V_{oc} close to the radiative limit.[21]

7.5. External Quantum Efficiency of Electroluminescence

Further quantification of non-radiative recombination losses after post-annealing is performed by measuring the external electroluminescence quantum efficiency. It is determined by measuring the total electroluminescence flux (integrated over all energies) in dependency of the applied voltage and divided with the total injection current (corresponding to the current density in the dark). The calculated EQE_{EL} for both devices after post-annealing is summarized in Figure 7.9. At an injection current which corresponds to j_{sc} at 1 sun (and therefore a charge carrier density under realistic operating conditions), the solar cells show high radiative efficiencies of around 1 %, which increases up to 1.8 % for a higher driving voltage of 1.5 V. These high values allow the studied perovskite solar cells for an application as LEDs. First publications[441,442] on radiative efficiencies of perovskite PVs in 2014 reported rather low EQE_{EL} values in the range of 0.001 % – 0.01 %, which is outnumbered by the herein presented devices by more than 2 orders of magnitude. Furthermore, the obtained values are comparable with the highest efficiencies reported so far of 1 % for a quadruple cation perovskite (containing Rb, Cs, MA, FA, I and Br),[41] 7 % for $FA_{0.92}MA_{0.08}PbI_3$[472] and 8 % for $MAPbI_3$.[449] The highest certified values for EQE_{EL} are in the range of 3 – 6 % as very recently summarized by Green and Ho-Baillie.[473] Perovskites can accordingly also compete with other PV technologies such as Si (1.6 %) and CIGS (2.4 %) and are

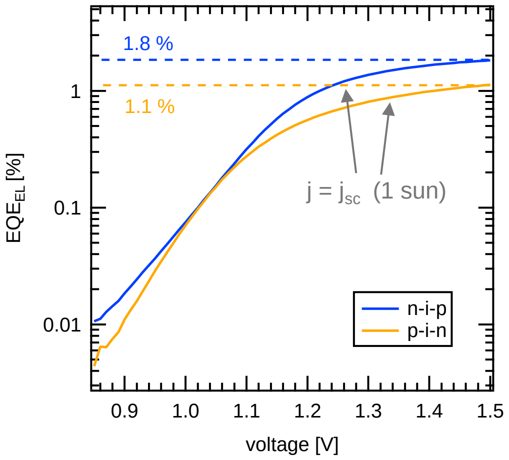

Figure 7.9.: EQE_{EL} as a function of applied voltage for both type of devices after the post-annealing process. The solar cells demonstrate high radiative efficiencies in the range of 1 % at an injection current j corresponding to j_{sc} (1 sun).

substantially better than OPVs (0.004 %) and DSSCs (~10^{-6} %).[473] These improvements over the last few years strongly underline the successful story of perovskite solar cells, which has his main origin in the defect tolerant nature and the suppression of non-radiative recombination losses.[21]

7.6. Discussion

Finally, the structural changes which are induced by the thermal post-annealing process will be discussed. Similar observations also have been obtained by Sheikh et al. while studying the effect of thermal cycling on the PV performance.[474] After the first cycle, an improved V_{oc} was observed, which the authors attributed to an improvement of hole mobility in the spiro-OMeTAD transport layer. Since this material is not employed in the herein studied devices and the results show that the series resistance increases (Figure 7.5b) while the improved V_{oc} remains constant, it is concluded that transport and recombination phenomena are decoupled and the observed changes are not linked to mobility variations. Another possible explanation could be found in the induced changes by the tetragonal-cubic phase transition which occurs at approximately 310 K to 338 K and therefore in the range of the post-annealing temperature of 320 K.[27,29,91,475] However, it is stated for $MAPbI_3$ that no abrupt optical changes take place across this phase transition, but that the ion activation energy decreases at approximately 318 K from 0.7 to 0.5 eV which is probably not relevant for the herein observed phenomena.[476] This is in line with another report,[475] where the solar cell performance has been studied in the temperature range of 298 K to 343 K. It was found, that the phase transition did not lead to any discontinuity in device performance, indicating that optoelectronic properties are insensitive to the phase transition. Interestingly, some devices showed an improvement in V_{oc} after heating and cooling back, which the authors did not pay any attention to. These observations lead to the conclusion that the phase transition is probably not the origin of the performance improvements.

Very recently, Tsai et al. showed how light-induced lattice expansion can help to improve the PCE and in particular the V_{oc} of $MAPbI_3$ and mixed perovskites.[477] It is suggested, that a decrease in the energetic barrier near the perovskite interfaces and the reduction of non-radiative recombination both in the bulk and at the interfaces are the reason for the observed device improvements. This is in line with other reports,[478,479] where the impact of crystal strain on recombination dynamics has been studied, demonstrating that strain-free films and devices are associated with reduced defect concentrations and therefore suppressed non-radiative recombination pathways. This coincides with a report by Nishimura et al., where the effect of lattice strain on Sn-based perovskite solar cells was investigated by substituting different cations.[480] The authors found a strong correlation between strain and the device efficiency and concluded that strain-free devices provide the highest PCE (and V_{oc}). It therefore appears very likely, that the increased open-circuit voltage after the post-annealing procedure is related to a release of strain in the perovskite layer. Local strain inhomogeneities already can appear during device preparation and post-annealing releases the strain (especially close to the interfaces) and thus provides a reduced amount of defects and an improved device performance. This is supported by the fact, that the volumetric expansion coefficient α_V for $MAPbI_3$ is significantly higher compared to other thin-film solar cell materials like CIGS or CdTe as reported by Jacobsson et al.[27] and a higher expansion coefficient increases the probability of removing crystal strain if the temperature is increased. Very recently, Lohmann and co-workers studied the effect of different substrate temperatures during co-evaporation on the performance of vacuum deposited $MAPbI_3$ solar cells.[481] By varying the temperature from 271 K to 296 K, a strong correlation with the PCE was found, demonstrating that a higher substrate temperature indeed improves the device, which supports the herein presented findings.

This chapter underlines that further research on perovskite PV do not necessarily has to focus on optimizing material combinations and preparation routes, but also on simple post-processing methods like illumination with light,[449,477] treatment of the perovskite surface with other solutions[482,483] or post-annealing in solvent-atmosphere.[382] It is further believed that the post-annealing procedure of complete devices might be even applicable to solution-processed devices as similar device improvements were also observed in literature.[474,475]

7.7. Summary

To conclude, the effect of device post-annealing of planar co-evaporated n-i-p and p-i-n perovskite solar cells was studied. It was found that the open-circuit voltage can be improved from 1.11 V to more than 1.18 V by storing the devices in a nitrogen-filled glovebox and annealing them to 320 K for several hours and cooling back to 300 K again. Stability measurements over more than half a year and MPP tracking confirm that the increase in voltage is a permanent feature. Current-voltage characteristics in the dark revealed an increase of the shunt resistance, proving that leakage currents are reduced up two orders of magnitude since shunt recombination channels are efficiently passivated. In contrast, no significant changes in the series resistance are induced by post-annealing. The j-V curves are also analyzed with respect to the ideality factor, which shows a reduction by post-annealing pointing towards decreased SRH recombination losses. Recombination dynamics are then investigated in more detail by transient optoelectrical techniques, namely TPV and CE. It is demonstrated that the charge carrier lifetime increases with post-annealing, which is an indication of reduced amount of traps in the bulk of the perovskite and at the interfaces to the transport layers. Furthermore, a high radiative efficiency of more than 1 % is determined from electroluminescence measurements, showing that the set of studied devices is competitive with the most efficient perovskite PVs reported so far. Finally, possible explanations for the observed device improvements are discussed, like the temperature-induced release of strain in the perovskite film which is the most probable origin for the observed phenomena. It is therefore suggested that future works on co-evaporated perovskite solar cells should consider a post-annealing step after preparation or control the substrate temperature during evaporation in order to reduce recombination losses and increase the PCE.

8. Impact of Active Area Masking on Current-Voltage Characterization of Solar Cells

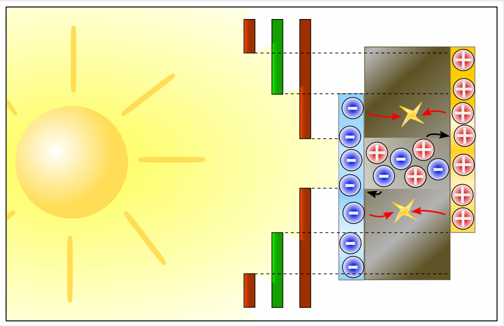

Abstract. Guidelines for the correct measurement protocol of novel PV technologies are becoming more frequent in literature as it is not straightforward to accurately measure the efficiency parameters of laboratory solar cells. This is particularly the case for small-area research devices, which are prone to overestimate the short-circuit current density due to edge effects of various types. The common practice is therefore to utilize masks with well-defined apertures. In this chapter, it is shown experimentally and theoretically that active area masking leads to erroneous determination of both open-circuit voltage and fill factor. Although the errors induced in these parameters by using a mask are generally smaller than what the errors in current can amount to when not using a mask, they are omnipresent and can be well described. As these errors in V_{oc} and FF can be characterized by means of analytical equations, the consequences for the resulting PCE is also examined. Based on the obtained results, it is concluded that masks should be chosen that match the active area as close as possible to prevent overestimating the PCE. The herein presented study focuses on perovskite solar cells, but the conclusions are valid independent of PV technology.

This chapter is partially based on

D. Kiermasch, L. Gil-Escrig, H. J. Bolink and K. Tvingstedt. Effects of Masking on Open-Circuit Voltage and Fill Factor in Solar Cells. *Joule*, 3, 16-26 (2019). DOI: 10.1016/j.joule.2018.10.016

8.1. Introduction

The concern of reporting accurate values of solar cell PCEs has increased with the improved cell performances during the last years as it is summarized in Figure 8.1a. It can be seen that the certification of efficiencies by the appropriate laboratories has become more important from 2013 onwards. The most frequent sources of contemporary PV measurement errors are usually found in spectral mismatch and erroneous estimations of the true area that takes part in generating the photocurrent.[484,485] Even though a set of routines and methods has been proposed to circumvent common measurement errors,[246,247,486,487] the number of manuscripts reporting dubious or even erroneous efficiencies is still not negligible as pointed out by Zimmermann and coworkers.[488] The authors analyzed 375 publications and compared the reported j_{sc} values from j-V characterization with the expected values from corresponding external quantum efficiency measurements. It was found that more than 30 % of these publications overestimate the photocurrent by more than 20 %.[488] The practice of active area masking was introduced mostly in the DSSC community with the motivated purpose to not overestimate the current by erroneous areas, unconsidered scattering or light piping effects. In these highly light-scattering PV devices, j_{sc} is easily overestimated under illumination without the employment of photomasks. In addition, the adjacent transport layers can unintentionally contribute to an increase in current. For example, it is well-known for PEDOT:PSS that the polymer is able to collect current from regions outside of the overlap of the electrodes due to its high conductivity (see Section 4.1).[489] For perovskite solar cells, masking is also generally recommended for the same reasons, particularly for those based on mesoporous TiO_2. The now well-established effect of photon recycling[285–287,399] in high radiative efficiency perovskite films may, in addition, also guide more light into the active area from illuminated regions outside the electrodes. Accurate knowledge of the active area for generation and recombination is therefore necessary and also quite appropriately provided for by careful use of shadow masks during device characterization.[484,490–492] Figure 8.1b illustrates the impact of masking on j_{sc} for a planar $MAPbI_3$ solar cell without a mesoporous scaffold. The unmasked device demonstrates an increased photocurrent by approximately 7 % which can be accounted for by applying an aperture that is smaller than the overlap of the electrodes.

Several academic publishers have recently started to request that any submitted PV manuscript is now accompanied by a reporting form, certifying if and how masking was employed during the measurements.[493] Point 6 of the Nature publishing group checklist now asks authors to describe the applied mask/aperture or to explain why

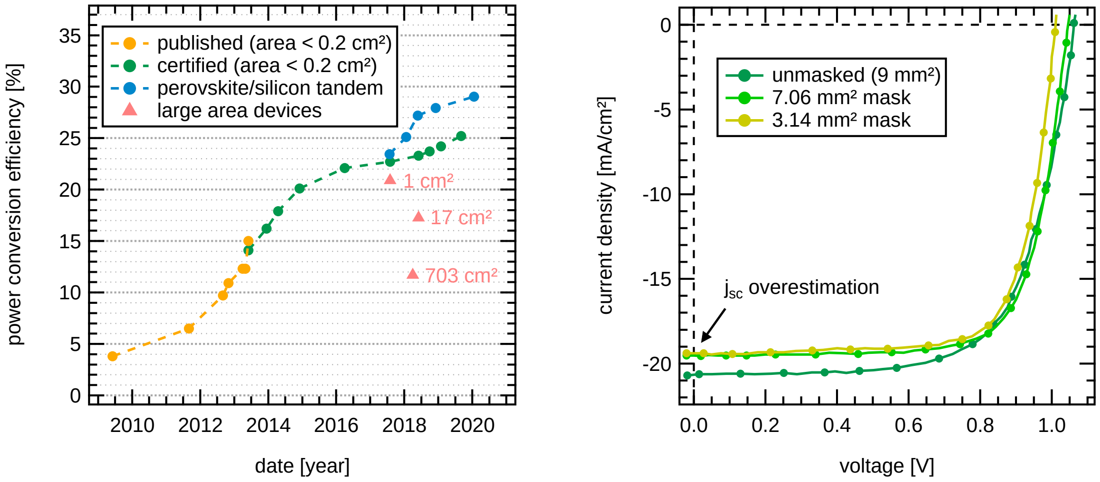

(a) **(b)**

Figure 8.1.: **(a)** Reported PCE values for perovskite solar cells since the first publication in 2009. There was a change in 2013–2014 when numerous researchers got their solar cells certified by official institutes. Data collected from the following References: [17–20,34,409,473,494–496] **(b)** Impact of masking on j_{sc} of a planar perovskite solar cell. Without a mask, the photocurrent is overestimated by approximately 7 % leading to an erroneous PCE.

a mask/aperture has not been used. It is also demanded to specify if the measured short-circuit current density of the devices vary with aperture area. These recommendations are highly justified to not let any exaggerated current density (and thus PCE) claims pass through. Most solar cell certification institutes are also commonly employing masks when asked to certify high efficiencies of novel laboratory cells. The contemporary focus of masking is thus put on its impact on j_{sc} overestimation, often leading researchers to safeguard and choose masks with apertures noticeably smaller than the active device area to accommodate to these concerns. For the best perovskite solar cells, where only little remains to be gained in photocurrent generation, the remaining improvements are, however, mainly to be expected in V_{oc} and FF. Correctly understanding and assigning the origin of V_{oc} and FF deficits in solar cells remains in fact an essential aspect of PV research. Consequently, it is crucial to measure these parameters as correctly and accurate as possible. However, the induced effects on these equally relevant parameters of PV energy conversion are usually not considered sufficiently when employing masks under illuminated characterization. Thus, the photocurrent should not be allowed to be overestimated, but equal care must be taken to prevent errors in V_{oc} and FF determination.

In the present chapter, the outcome of masking on V_{oc} and FF is investigated both experimentally and analytically. For the open-circuit voltage it is demonstrated that masking always leads to underestimated values. This is not caused by a change in recombination dynamics as proven with intensity-dependent V_{oc} and CE experiments but rather linked to the fact that the volume for generation does not equal the volume for generation when parts of the active area are not illuminated. Masking with small apertures can in addition affect the fill factor substantially in different ways, depending on the conditions the device is operating under. For high light intensities, the series resistances leads usually to an improvement in FF when the cell is masked wheres the opposite is the case for low light intensities in the shunt limited regime. The chosen mask aperture size is therefore crucial, to not over- or underestimate these two PV figures of merit. This is herein demonstrated by measurements on perovskite devices under different masking and illumination conditions, coupled to analytical expressions for solar cells operating in different recombination regimes. Finally, the impact of masking on the resulting PCE is addressed, clearly highlighting that the choice of aperture size can increase the obtained efficiencies since the loss in voltage can be overcompensated by the gain in fill factor. Although the work focuses on perovskite solar cells, the general deductions are valid independent of PV technology.

8.2. Current-Voltage Characteristics

To assess the influence of masking, a set of planar n-i-p co-evaporated $MAPbI_3$ solar cells with active layer thicknesses of 500 nm are studied, which are already introduced in Figure 6.2a. Figure 8.2 shows the outcome of evaluating a device masked with two sets of apertures (1.84 mm^2 or 0.58 mm^2) when illuminated with a calibrated solar simulator. The active area, defined as the overlap of both electrodes, is determined to be 6.77 mm^2. To calculate the corresponding current densities in Figure 8.2b, the absolute current is divided with the active area if unmasked, otherwise by the size of the aperture. First, it is highlighted that scattering or light piping effects are minimal in these planar perovskite solar cells as only minor impact on j_{sc} can be observed when the device is masked. These changes are even within the error margin originating from aperture area uncertainty. Thus, accounting for the generation area via the mask aperture provides the correct conversion into j_{sc} but also affects the other PV parameters. The most pronounced feature in Figure 8.2 is instead the clear impact of smaller masks on both V_{oc} and FF. Table 8.1 summarizes the PV parameters as calculated from j-V characteristics in Figure 8.2. Obviously, the V_{oc} is reduced substantially by more than 90 mV when comparing the unmasked case with the smallest aperture size. In contrast, FF is increased by 8.4 % when the same scans are compared. Interestingly, the largest jump in fill factor can be observed between the unmasked case and the 1.84 mm^2 mask pushing the PCE to 16.4 % which is higher compared to to unmasked measurement

(15.7 %) and the measurement with the smallest mask (15.8 %). Both, the V_{oc} and FF are therefore in fact erroneous in terms of not actually being representative of the supposed reference AM1.5 G spectrum with 100 mW/cm^2 illumination conditions. This will be addressed in more detail in the following sections by first analyzing the influence on V_{oc} and later proceed with the more intricate effects on FF and also PCE.

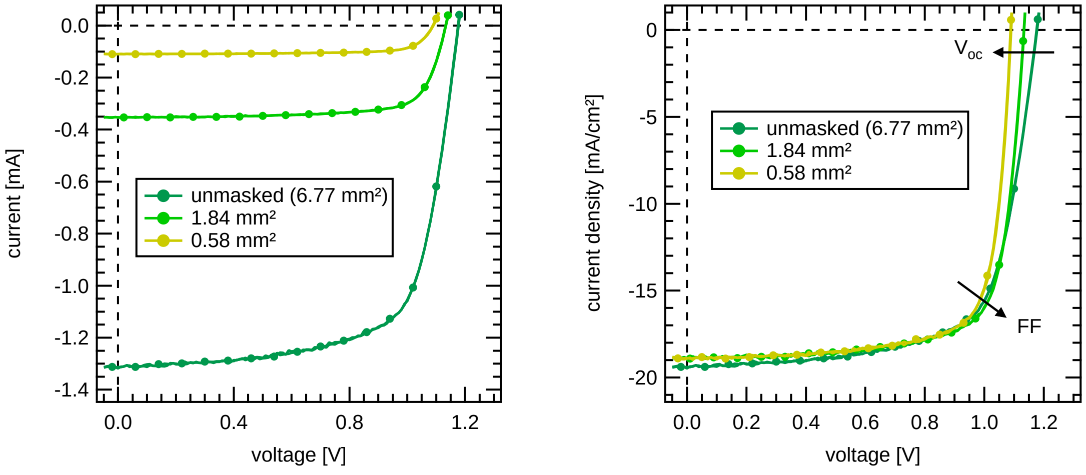

(a) **(b)**

Figure 8.2.: Current-voltage characteristics measured with a sweep rate of 100 mV/s for a planar MAPbI$_3$ perovskite solar cell with and without different mask apertures. To demonstrate the influence on V_{oc} and FF, both the **(a)** absolute and **(b)** normalized currents are depicted. For all cases, forward and backward scans are shown, indicating that no differences between both scan directions can be observed. Current densities are determined by dividing the absolute current with the active area (6.77 mm^2) or the aperture size (1.84 mm^2 or 0.58 mm^2).

	I_{sc} [μA]	j_{sc} [mA/cm^2]	V_{oc} [V]	FF [%]	PCE [%]
unmasked (6.77 ± 0.05) mm^2	1312.77	19.39 ± 0.14	1.1820	68.3	15.7
masked (1.84 ± 0.02) mm^2	353.16	19.19 ± 0.21	1.1338	75.2	16.4
masked (0.58 ± 0.02) mm^2	109.53	18.88 ± 0.65	1.0905	76.7	15.8

Table 8.1.: Extracted PV parameters from Figure 8.2 for the studied n-i-p device with different mask apertures.

8.3. Influence on Open-Circuit Voltage

As observed in Figure 8.2, the fundamental PV figure of merit of V_{oc} is underestimated when masks with an aperture area smaller than the electrode overlap during illuminated j-V characterization are employed. In order to quantify the amount of these voltage losses, the masking ratio X is defined as

$$X = \frac{A_{aperture}}{A_{device}}, \tag{8.1}$$

where $A_{aperture}$ is the area of the hole opening of the mask and A_{device} is the device area. Based on Equation 3.22, an analytical expression for solar cells not suffering from shunt resistance[355] or self-induced heating effects[421] can therefore be provided for the voltage reduction ΔV_{oc} that occur with masking

$$\Delta V_{oc} = \frac{n_{id} k_B T}{q} \ln(X), \tag{8.2}$$

which is derived by substracting V_{oc} (unmasked) from V_{oc} (masked). In the common case of un-shunted solar cell operation, the reduction of V_{oc} will accordingly scale directly with the logarithm of the mask aperture such that cells with higher ideality factors and measured at higher temperatures will suffer more in voltage losses upon masking. Accordingly, the value of j_0 has itself no influence on the extent of the induced masking voltage losses. The logarithmic relation in Equation 8.2 thus leads to omnipresent underestimations in the open-circuit voltage. It should be noted here that this simple expression still will be valid even if the cell suffers from series resistance losses. If a solar cell is heavily shunted instead, the V_{oc} will no longer follow the outlined logarithmic relation of Equation 8.2. In this case, it will turn to drop linear with reduced masking area, which is less relevant under operating conditions close to 1 sun illumination. However, the additionally induced temperature rise that complicates the situation when illuminated with stronger light intensities is more relevant. As a masked cell is partially operating in the shadow, it will be overall colder than an unmasked cell and the isothermal Equation 8.2 then becomes only an approximation, which will slightly overestimate the voltage drop due to masking. This is indeed the case for the 1 sun illuminated device in Figure 8.2, where the theoretical isothermal expression slightly overestimates the measured voltage losses with 4 to 7 mV as sum-

	V_{oc} [V]	ΔV_{oc} [mV]	ΔV_{oc} from Eq. 8.2 [mV]
unmasked (6.77 ± 0.05) mm^2	1.1820		
masked (1.84 ± 0.02) mm^2	1.1338	-48.2	-52.3
masked (0.58 ± 0.02) mm^2	1.0905	-91.5	-98.6

Table 8.2.: Extracted values for V_{oc} from Figure 8.2 summarized together with measured and calculated voltages losses induced by masking.

marized in Table 8.2. Nevertheless, Equation 8.2 remains a useful approximation of the induced voltages losses caused by small mask apertures. The explanation for the voltage reduction can be found in the fact that the non-illuminated part of the masked solar cell will still join in as volume for recombination, accordingly rendering the volume for recombination larger than the volume for generation. Any voltage provided by the cell exists all over the highly conducting electrodes and thus leads to a recombination current in the entire volume found between those electrodes. The total recombination current scales linearly with the area of the overlapping electrodes and is in the generalized Shockley Equation 2.8 an exponential function of the voltage measured at those electrodes. Its value is hence not affected by any mask aperture size (apart from potential device temperature reductions due to partly working in the shadow). On the other hand, the volume for generation is defined by the area that is illuminated, which can be either the complete active area or the aperture size if the solar cell is masked. So even if the total generation current equals the total recombination current at open-circuit conditions, the generation current density does not equal the recombination current density. This undesirable characterization condition will therefore inhibit the quasi Fermi levels from reaching its potential value and is thus not an appropriate way to estimate the true voltage potential of the PV material. With the reasoning above, the voltage provided by a masked device should correspond to the voltage from an unmasked cell that is illuminated with an intensity reduced to the same amount as the masking ratio defined in Equation 8.1. The postulate that masking will have the same effect on both V_{oc} as simply reducing the light intensity with a similar factor will be addressed in the next paragraph.

In order to prove that an reduction of illumination intensity has indeed the exact same effect on V_{oc} as masking does, Figure 8.3a depicts the measured V_{oc} versus seven decades of illumination intensity for a perovskite solar cell with (0.44 mm^2) and without (6.77 mm^2 device are) a mask and accordingly with $X = 0.065$. In the intermediate (isothermal 300 K) intensity regime from ~10^{-3} to ~10^{-2} suns, the theoretical voltage losses from Equation 8.2 fit perfectly with the measured voltage losses, both amounting exactly to 110 mV. The blue filled triangles represent the data from the masked cell just shifted in intensity with the masking factor of 0.065, rendering an overlap with the unmasked lower intensity data. The logarithmic diffusion part of the V_{oc} (suns) relation also confirms that the ideality factor of 1.55 does indeed not change with masking, as opposed to that recently suggested in the work by Xu and co-workers.[497] Accordingly, the two measurements can be fitted with the same expression just shifted in intensity. For the highest intensities, the voltage of the unmasked device demonstrates a stronger saturation compared to the masked measurements, clearly indicating

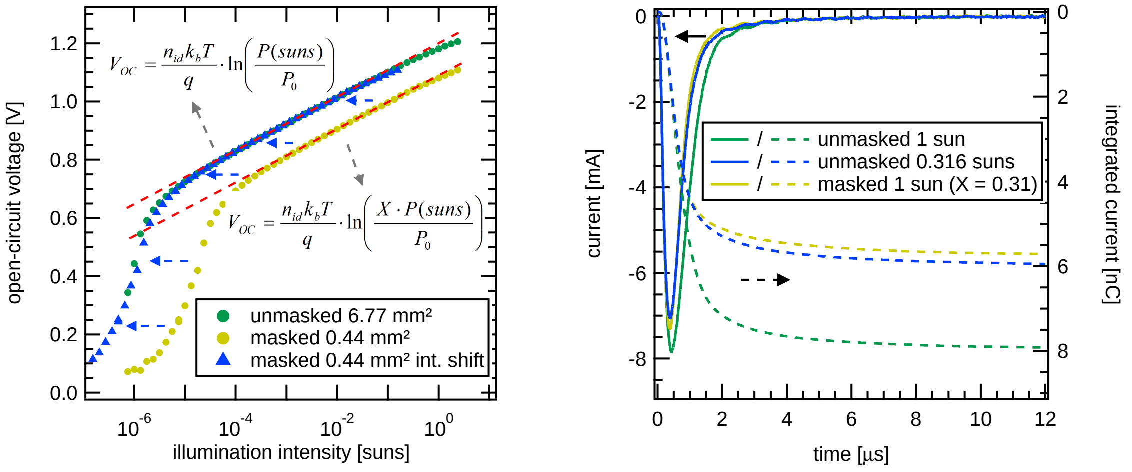

(a) **(b)**

Figure 8.3.: **(a)** V_{oc} of a 6.77 mm^2 solar cell measured as a function of light intensity with and without the utilization of a mask with a aperture of 0.436 mm^2. The fitted red dashed lines use the same equation with identical parameters apart from the inclusion of the masking aperture ratio X = 0.065. It becomes clear that the voltage should actually not be described as being reduced at a particular light intensity with masking, but instead that the light intensity is simply incorrect. **(b)** CE experiments performed on an device, which was unmasked and masked with a larger 2.06 mm^2 aperture. The extracted charge from the masked cell at 1 sun is quite similar when compared to the charge from the unmasked cell that is illuminated with an intensity close to the masking ratio X = 0.31.

that device heating is more pronounced without employing an aperture. Nevertheless, by neglecting the temperature differences between masked and unmasked cells at the highest intensities, Equation 8.2 summarizes the general effect of masking on V_{oc}. Obviously, the quasi Fermi levels of a masked solar cell are accordingly unable to reach their full potential and the V_{oc} is therefore always underestimated. Thus, the steady-state charge carrier density present in a partly masked device can never be as high as in an unmasked one. To confirm this statement, CE measurements are performed to compare the charge present in a masked and an unmasked cell at two different illumination intensities. Figure 8.3b shows the obtained current pulses (solid lines) and their integrals (dashed lines), either unmasked (6.77 mm^2) or masked with an aperture of 2.06 mm^2, resulting in $X = 0.31$. A quite similar current pulse and integral value is obtained when evaluating the unmasked cell but with a reduced intensity very close to the masking aperture-device area ratio. The similarity concludes that the lower charge density resulting in reduced voltages in masked devices is not representative of 1 sun illumination conditions. Figure 8.3 therefore directly shows that a masked cell with a mask aperture smaller than the active area is in fact never characterized under the as-

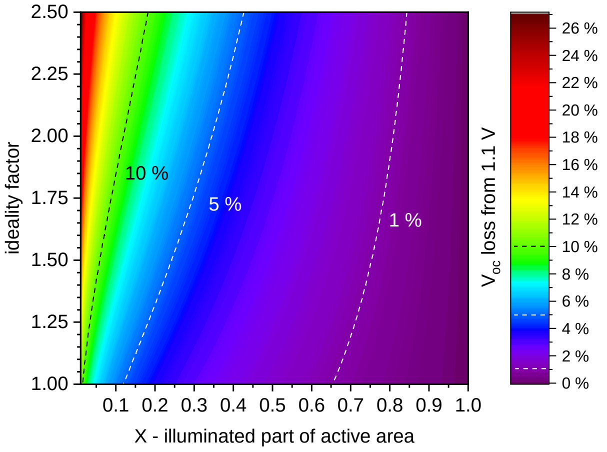

Figure 8.4.: Relative underestimation on V_{oc} as a function of masking ratio X for different ideality factors. The calculations are based on an unmasked V_{oc} of 1.1 V.

sumed 100 mW/cm^2 reference solar intensities in terms of recombination, but instead at a reduced intensity corresponding to the aperture-device area ratio X.

To quantify the induced errors in voltage by active layer masking, the calculated outcome of Equation 8.2 is illustrated in Figure 8.4. It shows the relative error in V_{oc} as a function of the employed mask aperture size (with respect to active device area) for different ideality factors. The losses are determined by assuming an unmasked V_{oc} of 1.1 V, which is representative for high-quality perovskite solar cells. In general, it can be concluded that a relative error between 1 % and 5 % can be expected if 20 % to 60 % of the active area is shaded. Accordingly, by applying masks that are noticeably smaller compared to the device area, the resulting error in voltage is not negligible.

8.4. Influence on Fill Factor

For the fill factor, the situation is slightly more complex and different outcomes can occur with masking, depending on in which regime of the recombination current curve the device is evaluated. In Figure 8.5, measured FF values of two MAPbI$_3$-based solar cells are depicted, both affected by a typical R_{series} of approximately 5 Ωcm^2. These devices are evaluated with and without masking under a similar large set of illumination intensities as in Figure 8.3a. The device in Figure 8.5a has a very high R_{shunt} as opposed to the second device shown in Figure 8.5b. The solar cell in Figure 8.5a is characterized with and without the presence of a mask with a small aperture of 0.44 mm^2, whereas the shunted device in Figure 8.5b was instead measured with a larger 2.06 mm^2 mask aperture. The FFs are determined from the forward sweep of the corresponding j-V characteristics, but due to the hysteresis-free character of these devices (Figure 8.2),

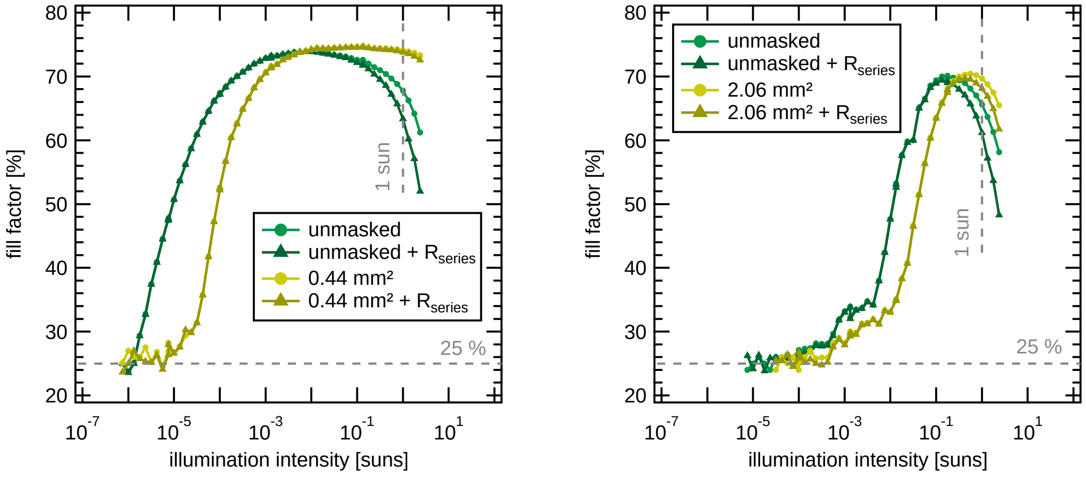

(a) **(b)**

Figure 8.5.: Measured FF as a function of light intensity and masking for two different perovskite devices, where **(a)** is less shunted (and a mask aperture of 0.44 mm^2 is used) and **(b)** is more shunted (and a mask aperture of 2.06 mm^2 is used). The active area in both cases amounts to 6.77 mm^2. To illustrate the influence of R_{series}, an additional 4 Ωcm^2 resistor is placed in series to both devices. At 1 sun illumination, the FF in the masked cases is noticeably overestimated, especially if an additional R_{series} is added.

reverse sweeps showed no noticeable differences. In order to also evaluate the effect of higher R_{series}, the j-V measurements are also performed with an included external 60 Ω resistor (~4 Ωcm^2) in series. The FFs of both devices are suffering from their series resistances at all intensities higher than ~10^{-2} suns and the losses are obviously also increased with the added external resistor. In Figure 8.5a, it clearly can be seen how the FF of the 0.44 mm^2 masked device gets overestimated when evaluated at 1 sun illumination intensity, whereas the opposite is happening in the shunted regime below 10^{-4} suns. In the intermediate diffusion limited intensity regime around 10^{-2} suns only very minor differences can be observed, even with such a small mask aperture. However, it is again noted in analogy with Figure 8.3a for V_{oc} that the measured FF values of the masked devices are in essence just the same as in the unmasked case, but only shifted in intensity. To better recognize this implication in Figure 8.5a, it is clarified that the last triangle of the masked set of measurements (at 2.4 suns) equals a value from the unmasked data lying in between the 10th and the 9th last point. As each intensity step corresponds to 75 %, it follows that the masking ratio $X = 0.44/6.77 \approx 0.065$ is the same value as reducing the intensity 75 % 9.5 times ($0.75^{9.5} \approx 0.065$). The same intensity offset is also valid for all other points in Figure 8.5a, whereas in Figure 8.5b, the larger mask aperture gives a ratio of $X = 0.31$, which corresponds to 4.1 steps. This confirms that the FF is in fact not correctly determined under the assumed reference

AM1.5 G spectrum with 100 mW/cm^2 illumination conditions when employing a mask with aperture smaller than the area defined by the overlapping electrodes.

Obviously, FF can both be over- and underestimated when using masks, but it is emphasized that the most common case is an overestimation due to the prevalence of device series resistance under 1 sun illumination conditions. Under 100 mW/cm^2 solar irradiance or comparable photon fluxes, a majority of present-day laboratory perovskite solar cells will have entered a series resistance limited region. When using masks smaller than the device active area, the operational maximum power point will be shifted to a lower voltage where the effect of series resistance is smaller and accordingly where the fill factor is getting larger and will be erroneously overestimated. If solar cells are operating in an intensity regime instead where the recombination current is fully ruled by the exponential diffusion part, there only will be very small influences on FF with masking. If no other limitations are present, the FF in this regime quite accurately can be described by an analytical equation found by Green[440]

$$FF_{ideal} = \frac{\frac{qV_{oc}}{n_{id}k_BT} - \ln\left(\frac{qV_{oc}}{n_{id}k_BT} + 0.72\right)}{\frac{qV_{oc}}{n_{id}k_BT} + 1}, \tag{8.3}$$

clarifying that the FF is completely determined by the recombination parameters V_{oc} and n_{id}. In order to rewrite this expression in terms of X, Equation 3.22 is used and the following relation is obtained

$$FF_{ideal,masked} = \frac{\ln\left(X\frac{j_{sc}}{j_0}\right) - \ln\left(\ln\left(X\frac{j_{sc}}{j_0}\right) + 0.72\right)}{\ln\left(X\frac{j_{sc}}{j_0}\right) + 1}. \tag{8.4}$$

This empirical equation for FF reductions due to masking only is valid in the intensity regime where the device is not suffering from either series or shunt resistances. It is further assumed that all other imaginable FF limitations, such as space charge limited currents,[498] field-dependent carrier generation,[499] distributed series resistance effects[500,501] and non-linear and light intensity dependent shunts[502] in addition are not present. Slightly more complex analytical expressions are also provided by Green for devices that suffer from ohmic resistive losses.[440] As the the presence of R_{series} is most common under relevant illumination conditions, an approximate expression for fill factor alterations due to masking is included here and reads

$$FF_{series,masked} = FF_{ideal,masked} \cdot \left(1 - \frac{X \cdot R_{series} \cdot j_{sc}}{\frac{n_{id}k_BT}{q}\ln\left(X\frac{j_{sc}}{j_0}\right)}\right), \tag{8.5}$$

where setting $X = 1$ will provide the FF of the unmasked but series resistance affected solar cell. Although being an empirical approximation not at all accounting for all conceivable limiting features to FF, Equation 8.5 is still a quite relevant and useful analytical expression for devices suffering from finite series resistance. Figure 8.6a shows how the FF of a theoretical PV diode suffers from both R_{series} and R_{shunt} and is generally dependent on illumination intensity/masking. If the device is operating at the common high illumination intensities where R_{series} is present, the FF will increase noticeably with masking according to Equation 8.5. If, on the other hand, the device already operates under substantially reduced light intensities, masking would here have a minor, but indeed opposite effect: marginally decreasing the FF according to the simpler expression outlined in Equation 8.4. The calculated FF of seven different cases included in Figure 8.6a, five suffering from R_{series} and one from R_{shunt} therefore may represent five differently conducting transparent electrodes and one leaky device. The more complicated expression for R_{shunt} losses can be found in Reference[440]. The black filled circles show the ideal pure diffusion limited dependence without resistive losses as described by Equation 8.4. The blue circles illustrate an identical device, which in addition also suffers from a shunt resistance. In this case, the FF will drop very rapidly with masking at intensities lower than 10^{-4} suns to finally saturate at the ohmic value of 25 %. On the other hand, the set of green colored circles illustrates the influence of R_{series}. To give a numerical example, the case with a reasonable series resistance of 10 Ωcm^2 has a fill factor of 72.2 % at 1 sun. Using a mask with an aperture of 75 % of the active area will increase the FF to a value of 75.4 %. The effect of masking on FF therefore can be summarized as follows: if the device does not suffer from series resistance and a large mask is applied, the effect almost can be neglected. However, most laboratory solar cells do suffer noticeably from R_{series} most often due to the limited conductivity of the employed transparent electrode material and a quite pronounced overestimation in FF easily can be induced when using smaller mask apertures. Thus, these calculations confirm and explain the previously observed behavior in Figure 8.5.

To calculate possible fill factor overestimates, Equation 8.5 with R_{series} and X as variables is applied for further analysis. The array $FF_{series,Masked}$ (R_{series}, X) is first generated with $n_{id} = 1.55$, $j_{sc} = 1.29 \cdot 10^{-3}$ A and $j_0 = 1.09 \cdot 10^{-16}$ A, corresponding to PV parameters at T = 300 K obtained from the device shown in Figure 8.2. Since the calculated numbers are absolute FF values, they are normalized to the unmasked case $(X = 1)$ for all R_{series} to obtain the relative overestimation shown in Figure 8.6b for 1 sun illumination. For a better overview, white dashed lines are included at 1 %, 5 % and 10 % overestimation. Already at R_{series} as low as 4 Ωcm^2, the FF overestimation is reaching 1 % when only 10 % of the active area is shadowed, highlighting the danger of

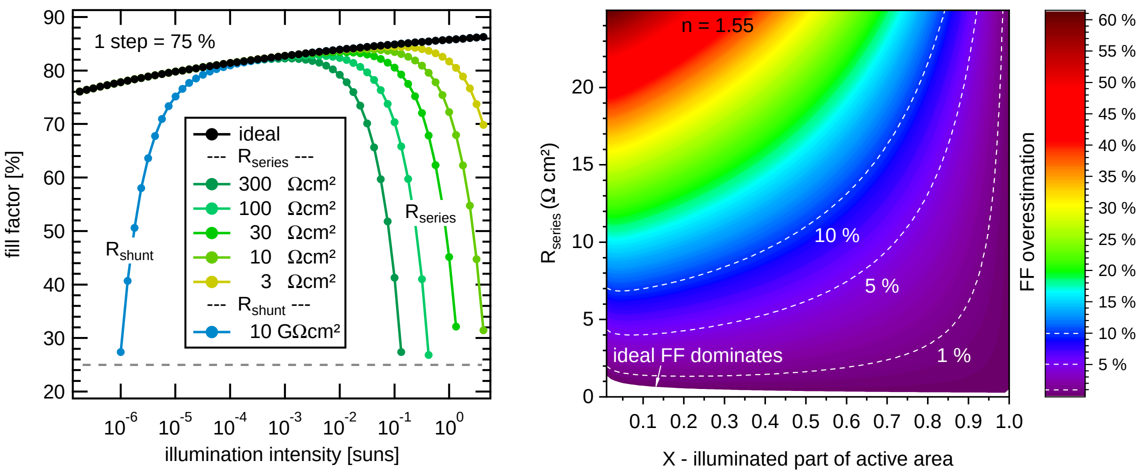

(a) **(b)**

Figure 8.6.: (a) Calculated effect of masking on FF where the black filled circles correspond to the case without resistive losses as described by Equation 8.4. The other circles show the impact of various series resistances (by using Equation 8.5) as well as one example for a shunt resistance. Masking has effectively the same consequence as altering the illumination intensity such that one step in the data corresponds to either an intensity reduction of 75 % or to the effect of using a mask with 75 % aperture of the device active area. **(b)** Calculated overestimation in FF as a function of masking ratio X and R_{series}.

an incorrect FF determination. The white area corresponds to the case, where Equation 8.4 dominates over the series resistance affected part of Equation 8.5. Accordingly, in case of very low values for R_{series} (or low light intensities), the FF will decrease with masking aperture area which is not expected to be relevant for solar cell characterization under operating conditions.

8.5. Consequences for the Power Conversion Efficiency

Finally, the total induced effect of masking on the most important figure of merit of a solar cell, the PCE, will also be summarized in the following. As different technologies and geometries have already been shown to display very different j_{sc} dependencies on masking, it is here refrained from making any general statements on the influence of this parameter. Therefore, only the present influence from the herein evaluated parameters, the V_{oc} and the FF, on PCE will be studied. By combining Equation 8.2 and

8.5, the following expression can be obtained for the relative error in efficiency ΔPCE with masking, again under the assumption of an unmasked V_{oc} of 1.1 V

$$\Delta PCE = \left(\left(\frac{(1.1 + \Delta V_{oc}(X)) \cdot FF_{series,masked}(X, R_{series})}{1.1 \cdot FF_{series,masked}(1, R_{series})} \right) - 1 \right) \cdot 100\%. \tag{8.6}$$

The numerator in the bracket quantifies the impact of ΔV_{oc} and $FF_{series,masked}$ in dependency of masking (X) and R_{series}, while the denominator normalizes the obtained values to the unmasked case $(X = 1)$. For n_{id}, j_{sc} and j_0, the same values as for Figure 8.6b provide the basis for the calculations. The outcome of Equation 8.6 is illustrated in Figure 8.7 as a function of both series resistance and mask aperture ratio. It can be concluded that the combined induced errors in PCE remain small ($\leq 1-5$ %) as long as fairly large mask apertures are employed, whereas devices with higher R_{series} will quite rapidly overestimate the PCE as the mask aperture is getting smaller. The graph is divided into two areas which are separated by a line with constant PCE. The reddish part demonstrates the dominant losses from the ΔV_{oc} term (Equation 8.2), while the greenish part is characterized by the improvements from $FF_{series,masked}$ (Equation 8.5). This combined effect is indeed the reason for the observed behavior in Figure 8.2b (summarized in Table 8.1), where the PCE of the intermediate (1.84 mm^2) mask rendered the highest PCE since with this mask aperture the FF is boosted more than what V_{oc} is suffocated.

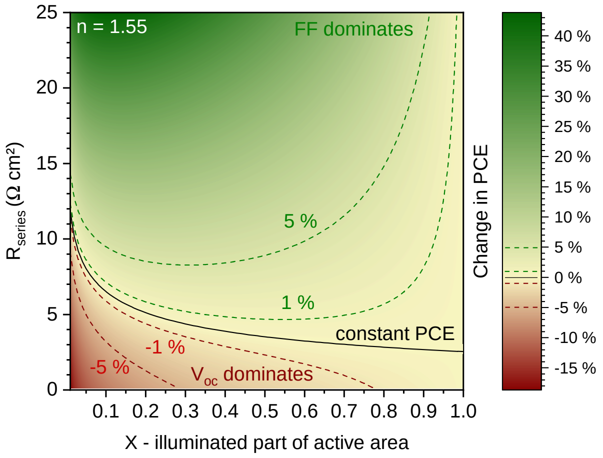

Figure 8.7.: Masking effect on PCE for a 1 sun illuminated perovskite deivce with $n_{id} = 1.55$. Neglecting possible j_{sc} alterations, the combined effect of the present V_{oc} underestimation and FF overestimation leads to a fairly large region of allowable masking apertures, where the error in efficiency is less than 5 %. For devices with very low series resistance, the V_{oc} underestimation will dominate and render the measured PCE marginally lower than its true value. On the other hand, solar cells with higher R_{series} will noticeably overestimate the PCE if the aperture size is small.

To minimize the effects outlined herein and to allow an as-truthful representation of the relevant V_{oc} as well as FF values, it is crucial to reduce the difference between any used mask aperture and the device area. However, this is something that is often not common practice, out of fear of overestimating the photocurrent. To alleviate and balance these two concerns, the best practice should be still to recommend the use of masks, but to employ masks with apertures as large as technically possible if it is strived for accurate and correct values of V_{oc} and FF. Having masks with similar areas as the active area, however, can unfortunately lead to problems in alignment. The ultimate remedy is therefore to make both cell areas and aperture areas larger. Then, not only alignment is more easily achievable, but also the accuracy in area determination is increased and the relative influence of edge effects, such as for example excessive stray light, is minimized.[503] For solar simulators with common collimation and devices using glass substrates with a thickness ≤1 mm^2, the employment of both masks and cell areas of approximately 1 cm^2 will obviously not impede V_{oc} and FF noticeably and will simultaneously also not under- or overestimate the j_{sc}. For small laboratory devices where the j_{sc} of unmasked cells is still noticeably larger than masked ones, it is instead suggested to measure the device first with a mask with a well-calibrated area which is smaller than the active area to guarantee a good estimate of j_{sc}. Then, the device should be measured with a mask slightly larger than the active area, which will provide correct values of V_{oc} and FF. The final j-V curve is then determined by normalizing the unmasked j-V data to the masked j_{sc} values. This is in line with earlier clarifications[490,491] to guarantee that substrate edges as well as other parts of the device are well masked to prevent overestimating j_{sc}, but also ensures the values for V_{oc} and FF to be as accurate as possible.

8.6. Summary

The employment of photomasks is of major importance for many novel solar cells to avoid overestimation in j_{sc}. In this chapter, possibly overlooked aspects regarding V_{oc} and FF during laboratory solar cell characterization are highlighted. The open-circuit voltage will always be underestimated as masking reduces the volume for generation without affecting the volume for recombination. Intensity-dependent V_{oc} and CE measurements revealed that the recombination dynamics are indeed not affected by masking, which consequently only corresponds to a reduction in light intensity. The expected error for common aperture sizes was estimated to range between 1 % and 5 %. For the fill factor, the situation is slightly more complex: under 1 sun illumination conditions, FF is most often overestimated with masking due to the reduced influence of

R_{series} and the smaller the employed mask, the larger these errors become. In contrast, for low light intensities and/or shunted devices, the FF will decrease with masking. In a similar way as for the voltage, both experimental and theoretical results prove that masking has essentially the same effect on FF as merely reducing the light intensity. The induced overestimation under relevant operating conditions can amount to 5 – 10 % and depends strongly on R_{series} of the device. If the used aperture is smaller than the area defined by the overlapping electrodes, masking never allows to correctly measure V_{oc} and FF under the anticipated standard reference illumination conditions. For the more advertised parameter of PCE, the combination of these two altered values often renders minor alterations but it can be generally expected that masking increases the obtained efficiencies in many cases. Since high efficiency solar cells are usually obtained on small device areas (Figure 8.1a), it remains important to determine PV parameters as accurate as possible. Even though the present study focuses on the novel field of perovskite solar cells, the conclusions are valid independent of technology and therefore also are applicable to other PV systems.

9. Summary

In order to facilitate the human energy needs with renewable energy sources in the future, new concepts and ideas for the electricity generation are needed. Solar cells based on metal halide perovskite semiconductors represent a promising approach to address these demands in both single-junction and tandem configurations with existing silicon technology. Despite intensive research, however, many physical properties and the working principle of perovskite PVs are still not fully understood. In particular, charge carrier recombination losses have so far mostly been studied on pure films not embedded in a complete solar cell. This thesis aimed for the identification and quantification of charge carrier recombination dynamics in fully working devices under conditions corresponding to those under real operation. To study different PV systems, transient electrical methods, more precisely OCVD, TPV and CE, were applied. Whereas OCVD and TPV provide information about the recombination lifetime, CE allows to access the charge carrier density at a specific illumination intensity. The benefit of combining these different methods is that the obtained quantities can not only be related to the V_{oc} but also to each other, thus enabling to determine also the dominant recombination mechanisms.

Although optoelectrical techniques have been widely used in the past to study recombination in PV devices, the interpretation of the results is not straightforward. In the first experimental **Chapter 5**, the previously determined lifetimes and densities were re-evaluated in terms of their physical origin. In order to compare different kinds of solar cells with each other, a classical Si diode, two organic solar cells composed of P3HT:PCBM and PCDTBT:PCBM and a perovskite solar cell based on $MAPbI_3$ were examined. It was found that these measurement methods are often influenced by capacitive effects caused by spatially separated charge carriers. In case of TPV and OCVD, clear evidence is provided that the observed voltage decays for the thin-film devices are mostly governed by charge carriers stored at the electrodes or in the transport layers, whereas no information about relevant bulk recombination lifetimes could be obtained. With a theoretical equivalent circuit analysis, it was possible to reveal the origin of the measured transients since $R_{shunt}C$ and DC models were quite accurately able to describe the results. Furthermore, similar observations were also obtained for CE experiments, which show that capacitive charge carriers also affect carrier density determination. In order to quantify these limitations, an analytical expression rendering the experimental conditions where bulk recombination parameters are electrically accessible in thin-film PV devices is finally provided as a guide for future interpretation of transient electrical data.

To overcome the limits found in the previous study, thicker and more efficient co-evaporated n-i-p perovskite solar cells are investigated in **Chapter 6**. The impact of geometric capacitance was reduced by increasing the active layer thickness from 500 nm to 820 nm without any noticeable loss in performance. While useful bulk recombination parameters were not accessible from a thinner (350 nm) PEDOT:PSS device due to short carrier lifetimes and a higher device capacitance, a capacitance-to-bulk transition was easily identified for the thicker n-i-p solar cells. In the case of these devices, the 500 nm solar cell revealed longer decay times due to the larger capacitance in the limited regime at low carrier concentrations, whereas similar recombination dynamics were detected in the high voltage regime independent of active layer thickness. As a direct outcome, it is concluded that increasing the $MAPbI_3$ thickness by more than 50 % does not affect the observed recombination kinetics which is pointing towards the interfaces to the transport layers to be the main source of carrier losses. It is finally revealed for the first time for perovskite solar cells that the recombination order ranges between 1.6 and 2.0 under operating conditions, indicating that the main loss processes can be assigned to be of SRH and free-carrier radiative recombination type.

The work presented in **Chapter 7** focuses on the elimination of undesired recombination losses in co-evaporated n-i-p and p-i-n perovskite solar cells. Films prepared by the sublimation of the materials are usually not annealed after preparation as the crystallization is driven by the excess of kinetic energy of the precursor materials. For this reason, a post-annealing procedure is applied to perovskite solar cells revealing PCE improvements, which can be mainly attributed to an increased V_{oc}. Starting with an open-circuit voltage of around 1.11 V, the value could be improved to more than 1.18 V by annealing the devices to 320 K and cooling back to room temperature again. The increased V_{oc}, featuring also an excellent stability of more than half a year, is one of the highest reported values for $MAPbI_3$-based perovskite solar cells. A deeper focus on the recombination behavior via j-V characteristics illustrates a reduction of both the ideality factor and leakage recombination currents. The change in n_{id} indicates the passivation of SRH trap states which is further supported by a transient electrical analysis based on TPV and CE. It is revealed that recombination losses are indeed decreased because both the charge carrier lifetime and the dominant recombination order were increased by post-annealing. This is in line with high radiative efficiencies of more than 1 % as obtained from EL measurements, which highlights the potential application as an LED. Finally, the temperature-induced strain release in the perovskite film is suggested as the microscopic explanation for the observed phenomena.

In the last study outlined in **Chapter 8**, the impact of active area masking during j-V characterization on both the open-circuit voltage and fill factor is analyzed. Applying photomasks during efficiency measurements of small-area research devices is an often recognized necessity to prevent current overestimations. For V_{oc}, it was found that it will always be reduced if masks smaller than the overlap of the electrodes will be employed since the ratio between the volumes for generation and recombination is decreased. Intensity-dependent V_{oc} and CE experiments proved that no change in recombination takes places and the effect of masking can be described by a simple reduction of light intensity. Furthermore, the expected errors in voltage amount to a range of 1 – 5 % for common aperture sizes. The more complicated situation for the fill factor showed that it can be both over- and underestimated depending on the intensity the solar cell is illuminated with. However, under operating conditions close to 1 sun intensities, FF is most often overestimated with masking due to the reduced influence of R_{series}. Both experimental and theoretical results provide evidence that masking has the same effect on FF as reducing the illumination intensity in line with the observations for V_{oc}. The combined effect on these parameters is finally also evaluated for the PCE indicating that it can generally be expected that masking increases the obtained efficiencies in many cases. From these results it is concluded that mask sizes should be chosen that match the active area as close as possible to determine all PV parameters accurately.

To conclude, this thesis contributes to the enduring discussion on the interpretation of electrical transient results obtained by experimental techniques like OCVD, TPV and CE. It was demonstrated that these methods can help to understand recombination losses in thin-film solar cells based on perovskite materials if bulk recombination dynamics are identified. The powerful toolbox of transient electrical techniques is therefore able to detect the main limiting factors in fully working devices and provides also solutions on how to suppress these carrier losses.

9.1. Zusammenfassung

Um künftig den menschlichen Energiebedarf in Zukunft mit erneuerbaren Energiequellen zu decken sind neue Konzepte und Ideen für die Stromerzeugung erforderlich. Solarzellen auf der Basis von hybriden Perowskit-Halbleitern stellen einen vielversprechenden Ansatz dar, um dieser Anforderung – beispielsweise in Tandem-Konfigurationen zusammen mit Silizium – gerecht zu werden. Trotz intensiver Forschung sind viele physikalische Eigenschaften und das Funktionsprinzip dieser neuartigen Solarzellen immer noch nicht vollständig verstanden. Insbesondere wurden die Rekombinationsverluste bisher meist nur an reinen Schichten untersucht, welche nicht in einen kompletten Solarzellenaufbau integriert waren. Die vorliegende Arbeit zielte auf die Identifizierung und Quantifizierung der Ladungsträger-Rekombinationsdynamik in voll funktionsfähigen Solarzellen unter Bedingungen, die denen im realen Betrieb entsprechen, ab. Um verschiedene PV-Systeme zu untersuchen wurden transiente elektrische Methoden, genauer gesagt OCVD, TPV und CE, angewandt. Während OCVD und TPV Informationen über die Rekombinationslebensdauer liefern, erlaubt CE die Berechnung der Ladungsträgerdichte. Die Kombination dieser Methoden hat den Vorteil, dass die erhaltenen Größen miteinander in Verbindung gesetzt werden können und somit umfangreiche Rückschlüsse auf die zugrundeliegende Rekombinationmechanismen ermöglichen.

Obwohl optoelektronische Messmethoden häufig in der Vergangenheit zur Untersuchung von Rekombinationsprozessen in Solarzellen eingesetzt wurden, ist die Interpretation der Ergebnisse nicht trivial. Im ersten experimentellen **Kapitel 5** wurde der physikalische Ursprung der ermittelten Lebensdauern und Dichten näher untersucht und erfolgreich identifiziert. Um die Unterschiede verschiedener Solarzellen-Technologien miteinander vergleichen zu können wurde eine klassische Silizium-Diode, zwei organische Solarzellen aus P3HT:PCBM und PCDTBT:PCBM und eine Perowskit-Solarzelle auf der Basis von $MAPbI_3$ in die Studie einbezogen. Dabei hat sich gezeigt, dass die Messmethoden oft durch kapazitive Effekte, verursacht durch räumlich getrennte Ladungsträger, beeinflusst werden. Im Falle von TPV und OCVD wurde nachgewiesen, dass die beobachteten Transienten bei Dünnschicht-Solarzellen meist durch Ladungsträger bestimmt werden, die sich an den Elektroden oder in den Transportschichten befinden, während keine Informationen über relevante Rekombinationsprozesse innerhalb der aktiven Schichten gewonnen werden konnten. Aufgrund einer theoretischen Analyse mittels verschiedener Ersatzschaltkreise von Solarzellen konnte der Ursprung der gemessenen Transienten aufgedeckt werden, da $R_{shunt}C$- und DC-Modelle in der Lage waren die gemessenen Ergebnisse beschreiben zu können. Darüber hinaus wurden ähnliche Beobachtungen auch für CE-Experimente gemacht, die zu dem Schluss geführt haben, dass kapazitive Ladungsträger auch die Bestimmung der Ladungsträgerkonzentration beeinflussen können. Um die Einschränkungen zu quantifizieren wurde schließlich eine Bedingung hergeleitet, mit der sich berechnen lässt unter welchen Bedingungen Rekominationsprozesse mittels elektrischer Messmethoden zugänglich sind. Dies kann als Basis für die zukünftige Interpretation von Messungen und den dazugehörigen Ergebnissen genutzt werden.

Um die in der vorherigen Studie festgestellten Limitierungen überwinden zu können wurden dickere und effizientere n-i-p Perowskit-Solarzellen in **Kapitel 6** untersucht. In einer zusätzlich analysierten dünnen (350 nm) Solarzelle, die PEDOT:PSS als Transportschicht nutzte, konnten zunächst keine relevanten Rekombinationsprozesse innerhalb des Perowskits bestimmt werden, da die Relaxation der hohen Kapazität die kurze Lebensdauer überlagert hat, weshalb nur die Rekombination der räumlich getrennten Ladungen beobachtet werden konnte. Ein verringerter Einfluss der geometrischen Kapazität wurde durch die Erhöhung der aktiven Schichtdicke von 500 nm auf 820 nm in hocheffizienten n-i-p Solarzellen erreicht. Im Gegensatz zu dem PEDOT:PSS-Bauteil konnte bei den n-i-p-Solarzellen ein Übergang von der kapazitiven Überlagerung zu den wichtigen Rekombinationsprozessen innerhalb des Perowskites gefunden werden. Während sich die gemessenen Lebensdauern bei niedrigen Ladungsträgerkonzentrationen aufgrund der unterschiedlichen geometrischen Kapazitäten unterschieden haben, zeigten die Rekombinationsvorgänge im $MAPbI_3$ keine signifikanten Unterschiede und damit keine Abhängigkeit von der Schichtdicke. Daraus konnte geschlossen werden, dass eine Erhöhung des Perowskit-Films um mehr als 50% keinen Einfluss auf die Rekombinationskinetik hat, weshalb die Grenzflächen zu den Transportschichten als Hauptursache für die Rekombinationsverluste in diesen Solarzellen gilt. Abschließend wurde das erste Mal überhaupt für Perowskit-basierte Solarzellen gezeigt, dass die Rekombination unter relevanten Beleuchtungsbedingungen hauptsächlich durch SRH und strahlende Verlustprozesse dominiert wird.

Der Fokus von **Kapitel 7** lag auf der Beseitigung der zuvor identifizierten Rekombinationsverluste in aufgedampften n-i-p- und p-i-n Perowskit-Solarzellen. Schichten, die mittels Sublimation der Ausgangsmaterialien hergestellt werden, erfordern üblicherweise kein zusätzliches Ausheizen wie bei der Flüssigprozessierung, da die vollständige Kristallisation durch den Überschuss an kinetischer Energie der Moleküle sichergestellt wird. Aus diesem Grund wurde in einer Studie ein neuartiges Heizverfahren der gesamten Solarzelle angewendet, welches zu einer Erhöhung der Effizienz geführt hat, die hauptsächlich auf ein erhöhte Leerlaufspannung zurückzuführen ist. Ausgehend von einer Spannung von etwa 1,11 V konnte der Wert auf über 1,18 V verbessert werden, in-dem die Solarzellen für mehrere Stunden auf 320 K erwärmt und anschließend wieder abgekühlt wurden. Die erhöhte Leerlaufspannung, die mit einer ausgezeichneten Stabilität von mehr als einem halben Jahr überzeugen konnte, ist eine der höchsten berichteten Werte für $MAPbI_3$-basierte Perowskit-Solarzellen. Der Fokus auf das Rekombinationsverhalten über j-V Messungen zeigte sowohl eine Reduzierung des Idealitätsfaktors als auch der Leckströme. Die Veränderung von n_{id} deutet auf eine Passivierung der SRH-Fallenzustände an, was durch eine tiefergreifende Analyse mit Hilfe von transienten elektrischen Methoden verifiziert werden konnte. Dabei hat sich gezeigt, dass die Rekombinationsverluste verringert werden konnten, da sowohl die Ladungsträgerlebensdauer als auch die dominante Rekombinationsordnung durch das Ausheizverfahren erhöht wurden. Dies steht im Einklang mit den hohen Strahlungseffizienzen von mehr als einem Prozent, wie aus EL-Messungen berechnet wurde. Als mikroskopische Erklärung für die beobachteten Phänomene wurde schließlich das temperaturinduzierte Lösen von Kristall-Verspannungen innerhalb des Perowskits vorgeschlagen.

In der letzten Studie, die in **Kapitel 8** zusammengefasst ist, wurden die Auswirkungen des Maskierens der aktiven Fläche während der Charakterisierung mittels Strom-Spannungs Messungen beleuchtet. Dabei lag der Fokus sowohl auf der Leerlaufspannung als auch auf dem Füllfaktor. Die Verwendung von Photomasken bei der Bestimmung der Effizienzen von kleinen Solarzellen ist notwendig, um die Kurzschlussstromdichte nicht zu überschätzen. Jedoch wurde festgestellt, dass die Leerlaufspannung durch das Maskieren mit Aperturen, die kleiner sind als die aktive Fläche, verringert wird. Dies lässt sich damit begründen, dass sich das Verhältnis von Generation und Rekombination von Ladungsträgern verkleinert hat. Weiterhin konnten intensitätsabhängige Messungen der Leerlaufspannung und zusätzliche CE-Experimente beweisen, dass die Rekombinations-Prozesse durch das Maskieren nicht beeinflusst werden und die Spannungsreduzierung stattdessen mit einer Verringerung der Beleuchtungsintensität beschrieben werden kann. Die Situation für den Fallfaktor ist dagegen etwas komplizierter, da dieser Parameter, abhängig von der Beleuchtungsintensität, sowohl über- als auch unterschätzt werden kann. Jedoch lässt sich festhalten, dass unter realistischen Betriebsbedingungen nahe einer Sonnenintensität der Füllfaktor aufgrund des geringeren Einflusses des Serienwiderstandes überschätzt wird. Die kombinierte Wirkung der beiden Parameter wurde anschließend im Hinblick auf die Effizienz untersucht. Dabei hat sich gezeigt, dass grundsätzlich erwartet werden kann, dass die Praxis des Maskierens in vielen Fällen die gemessene Performance der Solarzellen überschätzen kann. Aus diesem Grund wird vorgeschlagen, dass zukünftig Masken verwendet werden sollten, die möglichst genau der aktiven Fläche entsprechen, um sicherzustellen, dass alle PV Parameter zuverlässig und möglichst genau bestimmt werden.

Zusammenfassend trägt die vorliegende Arbeit zu der bereits seit langem bestehenden Diskussion über das Verständnis und die Funktionsweise von elektrischen Messmethoden wie OCVD, TPV und CE bei. Es wurden neue Interpretationsansätze für diese experimentellen Messmethoden entwickelt, die es zukünftig erleichtern werden Resultate zu analysieren und Rückschlüsse auf die Rekombinationsverluste in Dünnschicht-Solarzellen ziehen zu können. Die neu gewonnen Erkentnisse konnten erfolgreich auf Perowskit-Solarzellen angewendet werden und ermöglichten die Quantifizierung der limitierenden Prozesse. Grundsätzlich kann der Einsatz der transienten elektrischen Messmethoden zukünftig dabei helfen die Verlustmechanismen in kompletten Solarzellen zu identifizieren und zu minimieren und dadurch einen wesentlichen Beitrag zur Kommerzialisierung dieser neuen Technologie beitragen.

Bibliography

[1] Climate Change 2014: Synthesis Report. Contribution of Working Groups I, II and III to the Fifth Assessment Report of the Intergovernmental Panel on Climate Change. Report, IPCC - Intergovernmental Panel on Climate Change (2014).

[2] The Paris Protocol - a blueprint for tackling global climate change beyond 2020. European Comission. *URL: https://ec.europa.eu/commission/publications/paris-protocol-blueprint-tackling-global-climate-change-beyond-2020_en* (08.07.2019).

[3] United Nations Framework Convention on Climate Change. *URL: https://unfccc.int/process/the-paris-agreement/status-of-ratification* (accessed 08.07.2019).

[4] J. Rogelj, M. Schaeffer, M. Meinshausen, R. Knutti, J. Alcamo, K. Riahi and W. Hare. Zero Emission Targets as Long-Term Global Goals for Climate Protection. *Environmental Research Letters*, **10**, 10, 105007 (2015). doi: 10.1088/1748-9326/10/10/105007.

[5] Global Warming of 1.5°C. An IPCC Special Report on the Impacts of Global Warming of 1.5°C above Pre-Industrial Levels and Related Global Greenhouse Gas Emission Pathways, in the Context of Strengthening the Global Response to the Threat of Climate Change, Sustainable Development, and Efforts to Eradicate Poverty. Report, IPCC - Intergovernmental Panel on Climate Change (2018).

[6] D. Tong, Q. Zhang, Y. Zheng, K. Caldeira, C. Shearer, C. Hong, Y. Qin and S. J. Davis. Committed Emissions From Existing Energy Infrastructure Jeopardize 1.5°C Climate Target. *Nature*, **572**, 7769, 373 (2019). doi: 10.1038/s41586-019-1364-3.

[7] Deutlicher Rückgang des Energieverbrauchs in Deutschland im Jahr 2018. Report, AGEB - AG Energiebilanzen e.V. (2019).

[8] K. Yoshikawa, H. Kawasaki, W. Yoshida, T. Irie, K. Konishi, K. Nakano, T. Uto, D. Adachi, M. Kanematsu, H. Uzu and K. Yamamoto. Silicon Heterojunction Solar Cell with Interdigitated Back Contacts for a Photoconversion Efficiency over 26%. *Nature Energy*, **2**, 17032 (2017). doi: 10.1038/nenergy.2017.32.

[9] J. Benick, A. Richter, R. Müller, H. Hauser, F. Feldmann, P. Krenckel, S. Riepe, F. Schindler, M. C. Schubert, M. Hermle, A. W. Bett and S. W. Glunz. High-Efficiency n-Type HP mc Silicon Solar Cells. *IEEE Journal of Photovoltaics*, **7**, 5, 1171 (2017). doi: 10.1109/JPHOTOV.2017.2714139.

[10] Photovoltaics Report. Fraunhofer Institute for Solar Energy Systems Freiburg. *URL: https://www.ise.fraunhofer.de/content/dam/ise/de/documents/publications/studies/Photovoltaics-Report.pdf* (accessed 08.07.2019).

[11] M. A. Green. How Did Solar Cells Get So Cheap? *Joule*, **3**, 3, 631 (2019). doi: 10.1016/j.joule.2019.02.010.

[12] B. O'Regan and M. Gratzel. A Low-Cost, High-Efficiency Solar Cell Based on Dye-Sensitized Colloidal TiO_2 Films. *Nature*, **353**, 6346, 737 (1991). doi: 10.1038/353737a0.

[13] C. W. Tang. Two-Layer Organic Photovoltaic Cell. *Applied Physics Letters*, **48**, 2, 183 (1986). doi: 10.1063/1.96937.

[14] K. Cnops, B. P. Rand, D. Cheyns, B. Verreet, M. A. Empl and P. Heremans. 8.4% Efficient Fullerene-Free Organic Solar Cells Exploiting Long-Range Exciton Energy Transfer. *Nature Communications*, **5**, 3406 (2014). doi: 10.1038/ncomms4406.

[15] Y. Lin, J. Wang, Z.-G. Zhang, H. Bai, Y. Li, D. Zhu and X. Zhan. An Electron Acceptor Challenging Fullerenes for Efficient Polymer Solar Cells. *Advanced Materials*, **27**, 7, 1170 (2015). doi: 10.1002/adma.201404317.

[16] J. Yuan, Y. Zhang, L. Zhou, G. Zhang, H.-L. Yip, T.-K. Lau, X. Lu, C. Zhu, H. Peng, P. A. Johnson, M. Leclerc, Y. Cao, J. Ulanski, Y. Li and Y. Zou. Single-Junction Organic Solar Cell with over 15% Efficiency Using Fused-Ring Acceptor with Electron-Deficient Core. *Joule*, **3**, 4, 1140 (2019). doi: 10.1016/j.joule.2019.01.004.

[17] A. Kojima, K. Teshima, Y. Shirai and T. Miyasaka. Organometal Halide Perovskites as Visible-Light Sensitizers for Photovoltaic Cells. *Journal of the American Chemical Society*, **131**, 17, 6050 (2009). doi: 10.1021/ja809598r.

[18] M. M. Lee, J. Teuscher, T. Miyasaka, T. N. Murakami and H. J. Snaith. Efficient Hybrid Solar Cells Based on Meso-Superstructured Organometal Halide Perovskites. *Science*, **338**, 6107, 643 (2012). doi: 10.1126/science.1228604.

[19] H.-S. Kim, C.-R. Lee, J.-H. Im, K.-B. Lee, T. Moehl, A. Marchioro, S.-J. Moon, R. Humphry-Baker, J.-H. Yum, J. E. Moser, M. Grätzel and N.-G. Park. Lead Iodide Perovskite Sensitized All-Solid-State Submicron Thin Film Mesoscopic Solar Cell with Efficiency Exceeding 9%. *Scientific Reports*, **2**, 591 (2012). doi: 10.1038/srep00591.

[20] National Renewable Energy Laboratory (NREL) - Best Research-Cell Efficiencies. *URL: https://www.nrel.gov/pv/assets/pdfs/best-research-cell-efficiencies.20190802.pdf* (accessed 07.08.2019).

[21] W. Tress. Perovskite Solar Cells on the Way to Their Radiative Efficiency Limit – Insights Into a Success Story of High Open-Circuit Voltage and Low Recombination. *Advanced Energy Materials*, **7**, 14, 1602358 (2017). doi: 10.1002/aenm.201602358.

[22] A. R. Chakhmouradian and P. M. Woodward. Celebrating 175 years of perovskite research: a tribute to Roger H. Mitchell. *Physics and Chemistry of Minerals*, **41**, 6, 387 (2014). doi: 10.1007/s00269-014-0678-9.

[23] H. L. Wells. Über die Cäsium- und Kalium-Bleihalogenide. *Zeitschrift für anorganische Chemie*, **3**, 1, 195 (1893). doi: 10.1002/zaac.18930030124.

[24] E. Mosconi, A. Amat, M. K. Nazeeruddin, M. Grätzel and F. De Angelis. First-Principles Modeling of Mixed Halide Organometal Perovskites for Photovoltaic Applications. *The Journal of Physical Chemistry C*, **117**, 27, 13902 (2013). doi: 10.1021/jp4048659.

[25] A. Poglitsch and D. Weber. Dynamic Disorder in Methylammoniumtrihalogenoplumbates (II) Observed by Millimeter-Wave Spectroscop. *The Journal of Chemical Physics*, **87**, 11, 6373 (1987). doi: 10.1063/1.453467.

[26] N. Onoda-Yamamuro, O. Yamamuro, T. Matsuo and H. Suga. p-T Phase Relations of $CH_3NH_3PbX_3$ (X = Cl, Br, I) crystals. *Journal of Physics and Chemistry of Solids*, **53**, 2, 277 (1992). doi: 10.1016/0022-3697(92)90056-J.

[27] T. J. Jacobsson, L. J. Schwan, M. Ottosson, A. Hagfeldt and T. Edvinsson. Determination of Thermal Expansion Coefficients and Locating the Temperature-Induced Phase Transition in Methylammonium Lead Perovskites Using X-ray Diffraction. *Inorganic Chemistry*, **54**, 22, 10678 (2015). doi: 10.1021/acs.inorgchem.5b01481.

[28] M. T. Weller, O. J. Weber, P. F. Henry, A. M. Di Pumpo and T. C. Hansen. Complete Structure and Cation Orientation in the Perovskite Photovoltaic Methylammonium Lead Iodide between 100 and 352 K. *Chemical Communications*, **51**, 20, 4180 (2015). doi: 10.1039/C4CC09944C.

[29] E. Smecca, Y. Numata, I. Deretzis, G. Pellegrino, S. Boninelli, T. Miyasaka, A. La Magna and A. Alberti. Stability of Solution-Processed $MAPbI_3$ and $FAPbI_3$ Layers. *Physical Chemistry Chemical Physics*, **18**, 19, 13413 (2016). doi: 10.1039/C6CP00721J.

[30] V. M. Goldschmidt. Die Gesetze der Krystallochemie. *Naturwissenschaften*, **14**, 21, 477 (1926). doi: 10.1007/bf01507527.

[31] M. A. Green, A. Ho-Baillie and H. J. Snaith. The Emergence of Perovskite Solar Cells. *Nature Photonics*, **8**, 7, 506 (2014). doi: 10.1038/nphoton.2014.134.

[32] C. Li, X. Lu, W. Ding, L. Feng, Y. Gao and Z. Guo. Formability of ABX_3 (X = F, Cl, Br, I) Halide Perovskites. *Acta Crystallographica Section B*, **64**, 6, 702 (2008). doi: 10.1107/S0108768108032734.

[33] C. Li, K. C. K. Soh and P. Wu. Formability of ABO_3 Perovskites. *Journal of Alloys and Compounds*, **372**, 1, 40 (2004). doi: 10.1016/j.jallcom.2003.10.017.

[34] J. H. Noh, S. H. Im, J. H. Heo, T. N. Mandal and S. I. Seok. Chemical Management for Colorful, Efficient, and Stable Inorganic–Organic Hybrid Nanostructured Solar Cells. *Nano Letters*, **13**, 4, 1764 (2013). doi: 10.1021/nl400349b.

[35] N. J. Jeon, J. H. Noh, W. S. Yang, Y. C. Kim, S. Ryu, J. Seo and S. I. Seok. Compositional Engineering of Perovskite Materials for High-Performance Solar Cells. *Nature*, **517**, 476 (2015). doi: 10.1038/nature14133.

[36] W. S. Yang, J. H. Noh, N. J. Jeon, Y. C. Kim, S. Ryu, J. Seo and S. I. Seok. High-Performance Photovoltaic Perovskite Layers Fabricated Through Intramolecular Exchange. *Science*, **348**, 6240, 1234 (2015). doi: 10.1126/science.aaa9272.

[37] W. S. Yang, B.-W. Park, E. H. Jung, N. J. Jeon, Y. C. Kim, D. U. Lee, S. S. Shin, J. Seo, E. K. Kim, J. H. Noh and S. I. Seok. Iodide Management in Formamidinium-Lead-Halide–Based Perovskite Layers for Efficient Solar Cells. *Science*, **356**, 6345, 1376 (2017). doi: 10.1126/science.aan2301.

[38] C. C. Stoumpos, C. D. Malliakas and M. G. Kanatzidis. Semiconducting Tin and Lead Iodide Perovskites with Organic Cations: Phase Transitions, High Mobilities, and Near-Infrared Photoluminescent Properties. *Inorganic Chemistry*, **52**, 15, 9019 (2013). doi: 10.1021/ic401215x.

[39] M. Saliba, T. Matsui, J.-Y. Seo, K. Domanski, J.-P. Correa-Baena, M. K. Nazeeruddin, S. M. Zakeeruddin, W. Tress, A. Abate, A. Hagfeldt and M. Grätzel. Cesium-Containing Triple Cation Perovskite Solar Cells: Improved Stability, Reproducibility and High Efficiency. *Energy & Environmental Science*, **9**, 6, 1989 (2016). doi: 10.1039/C5EE03874J.

[40] D. P. McMeekin, G. Sadoughi, W. Rehman, G. E. Eperon, M. Saliba, M. T. Hörantner, A. Haghighirad, N. Sakai, L. Korte, B. Rech, M. B. Johnston, L. M. Herz and H. J. Snaith. A Mixed-Cation Lead Mixed-Halide Perovskite Absorber for Tandem Solar Cells. *Science*, **351**, 6269, 151 (2016). doi: 10.1126/science.aad5845.

[41] M. Saliba, T. Matsui, K. Domanski, J.-Y. Seo, A. Ummadisingu, S. M. Zakeeruddin, J.-P. Correa-Baena, W. Tress, A. Abate, A. Hagfeldt and M. Grätzel. Incorporation of Rubidium Cations into Perovskite Solar Cells Improves Photovoltaic Performance. *Science* (2016). doi: 10.1126/science.aah5557.

[42] M. Abdi-Jalebi, Z. Andaji-Garmaroudi, S. Cacovich, C. Stavrakas, B. Philippe, J. M. Richter, M. Alsari, E. P. Booker, E. M. Hutter, A. J. Pearson, S. Lilliu, T. J. Savenije, H. Rensmo, G. Divitini, C. Ducati, R. H. Friend and S. D. Stranks. Maximizing and Stabilizing Luminescence from Halide Perovskites with Potassium Passivation. *Nature*, **555**, 497 (2018). doi: 10.1038/nature25989.

[43] D. J. Kubicki, D. Prochowicz, A. Hofstetter, S. M. Zakeeruddin, M. Grätzel and L. Emsley. Phase Segregation in Cs-, Rb- and K-Doped Mixed-Cation $(MA)_x(FA)_{1-x}PbI_3$ Hybrid Perovskites from Solid-State NMR. *Journal of the American Chemical Society*, **139**, 40, 14173 (2017). doi: 10.1021/jacs.7b07223.

[44] A. D. Jodlowski, C. Roldán-Carmona, G. Grancini, M. Salado, M. Ralaiarisoa, S. Ahmad, N. Koch, L. Camacho, G. de Miguel and M. K. Nazeeruddin. Large Guanidinium Cation Mixed with Methylammonium in Lead Iodide Perovskites for 19% Efficient Solar Cells. *Nature Energy*, **2**, 12, 972 (2017). doi: 10.1038/s41560-017-0054-3.

[45] W. Ke, C. C. Stoumpos and M. G. Kanatzidis. "Unleaded" Perovskites: Status Quo and Future Prospects of Tin-Based Perovskite Solar Cells. *Advanced Materials*, **0**, 0, 1803230. doi: 10.1002/adma.201803230.

[46] F. Igbari, Z.-K. Wang and L.-S. Liao. Progress of Lead-Free Halide Double Perovskites. *Advanced Energy Materials*, **9**, 12, 1803150 (2019). doi: 10.1002/aenm.201803150.

[47] G. H. Kwei, A. C. Lawson, S. J. L. Billinge and S. W. Cheong. Structures of the Ferroelectric Phases of Barium Titanate. *The Journal of Physical Chemistry*, **97**, 10, 2368 (1993). doi: 10.1021/j100112a043.

[48] N. A. Benedek and C. J. Fennie. Why Are There So Few Perovskite Ferroelectrics? *The Journal of Physical Chemistry C*, **117**, 26, 13339 (2013). doi: 10.1021/jp402046t.

[49] J. G. Bednorz and K. A. Müller. Possible High T_c Superconductivity in the Ba-La-Cu-O System. *Zeitschrift für Physik B Condensed Matter*, **64**, 2, 189 (1986). doi: 10.1007/bf01303701.

[50] T. Umebayashi, K. Asai, T. Kondo and A. Nakao. Electronic Structures of Lead Iodide Based Low-Dimensional Crystals. *Physical Review B*, **67**, 15, 155405 (2003). doi: 10.1103/PhysRevB.67.155405.

[51] R. E. Brandt, V. Stevanović, D. S. Ginley and T. Buonassisi. Identifying Defect-Tolerant Semiconductors with High Minority-Carrier Lifetimes: Beyond Hybrid Lead Halide Perovskites. *MRS Communications*, **5**, 2, 265 (2015). doi: 10.1557/mrc.2015.26.

[52] F. Brivio, K. T. Butler, A. Walsh and M. van Schilfgaarde. Relativistic Quasiparticle Self-Consistent Electronic Structure of Hybrid Halide Perovskite Photovoltaic Absorbers. *Physical Review B*, **89**, 15, 155204 (2014). doi: 10.1103/PhysRevB.89.155204.

[53] F. Brivio, A. B. Walker and A. Walsh. Structural and Electronic Properties of Hybrid Perovskites for High-Efficiency Thin-Film Photovoltaics from First-Principles. *APL Materials*, **1**, 4, 042111 (2013). doi: 10.1063/1.4824147.

[54] C. Quarti, E. Mosconi and F. De Angelis. Interplay of Orientational Order and Electronic Structure in Methylammonium Lead Iodide: Implications for Solar Cell Operation. *Chemistry of Materials*, **26**, 22, 6557 (2014). doi: 10.1021/cm5032046.

[55] A. Amat, E. Mosconi, E. Ronca, C. Quarti, P. Umari, M. K. Nazeeruddin, M. Grätzel and F. De Angelis. Cation-Induced Band-Gap Tuning in Organohalide Perovskites: Interplay of Spin–Orbit Coupling and Octahedra Tilting. *Nano Letters*, **14**, 6, 3608 (2014). doi: 10.1021/nl5012992.

[56] Y. Yasuhiro, N. Toru, E. Masaru, W. Atsushi and K. Yoshihiko. Near-Band-Edge Optical Responses of Solution-Processed Organic–Inorganic Hybrid Perovskite $CH_3NH_3PbI_3$ on Mesoporous TiO_2 electrodes. *Applied Physics Express*, **7**, 3, 032302 (2014). doi: 10.7567/APEX.7.032302.

[57] T. Wang, B. Daiber, J. M. Frost, S. A. Mann, E. C. Garnett, A. Walsh and B. Ehrler. Indirect to Direct Bandgap Transition in Methylammonium Lead Halide Perovskite. *Energy & Environmental Science*, **10**, 2, 509 (2017). doi: 10.1039/C6EE03474H.

[58] V. Sarritzu, N. Sestu, D. Marongiu, X. Chang, Q. Wang, S. Masi, S. Colella, A. Rizzo, A. Gocalinska, E. Pelucchi, M. L. Mercuri, F. Quochi, M. Saba, A. Mura and G. Bongiovanni. Direct or Indirect Bandgap in Hybrid Lead Halide Perovskites? *Advanced Optical Materials*, **6**, 10, 1701254 (2018). doi: 10.1002/adom.201701254.

[59] R. E. Wasylishen, O. Knop and J. B. Macdonald. Cation Rotation in Methylammonium Lead Halides. *Solid State Communications*, **56**, 7, 581 (1985). doi: 10.1016/0038-1098(85)90959-7.

[60] C. Motta, F. El-Mellouhi, S. Kais, N. Tabet, F. Alharbi and S. Sanvito. Revealing the Role of Organic Cations in Hybrid Halide Perovskite $CH_3NH_3PbI_3$. *Nature Communications*, **6**, 7026 (2015). doi: 10.1038/ncomms8026.

[61] E. J. Juarez-Perez, R. S. Sanchez, L. Badia, G. Garcia-Belmonte, Y. S. Kang, I. Mora-Sero and J. Bisquert. Photoinduced Giant Dielectric Constant in Lead Halide Perovskite Solar Cells. *The Journal of Physical Chemistry Letters*, **5**, 13, 2390 (2014). doi: 10.1021/jz5011169.

[62] V. M. Caselli, M. Fischer, D. Meggiolaro, E. Mosconi, F. De Angelis, S. D. Stranks, A. Baumann, V. Dyakonov, E. M. Hutter and T. J. Savenije. Charge Carriers Are Not Affected by the Relatively Slow-Rotating Methylammonium Cations in Lead Halide Perovskite Thin Films. *The Journal of Physical Chemistry Letters*, 5128–5134 (2019). doi: 10.1021/acs.jpclett.9b02160.

[63] W.-J. Yin, J.-H. Yang, J. Kang, Y. Yan and S.-H. Wei. Halide Perovskite Materials for Solar Cells: a Theoretical Review. *Journal of Materials Chemistry A*, **3**, 17, 8926 (2015). doi: 10.1039/C4TA05033A.

[64] W.-J. Yin, T. Shi and Y. Yan. Unique Properties of Halide Perovskites as Possible Origins of the Superior Solar Cell Performance. *Advanced Materials*, **26**, 27, 4653 (2014). doi: 10.1002/adma.201306281.

[65] W.-J. Yin, T. Shi and Y. Yan. Superior Photovoltaic Properties of Lead Halide Perovskites: Insights from First-Principles Theory. *The Journal of Physical Chemistry C*, **119**, 10, 5253 (2015). doi: 10.1021/jp512077m.

[66] S. De Wolf, J. Holovsky, S.-J. Moon, P. Löper, B. Niesen, M. Ledinsky, F.-J. Haug, J.-H. Yum and C. Ballif. Organometallic Halide Perovskites: Sharp Optical Absorption Edge and Its Relation to Photovoltaic Performance. *The Journal of Physical Chemistry Letters*, **5**, 6, 1035 (2014). doi: 10.1021/jz500279b.

[67] J. Frenkel. On the Transformation of Light into Heat in Solids. I. *Physical Review*, **37**, 1, 17 (1931). doi: 10.1103/PhysRev.37.17.

[68] G. H. Wannier. The Structure of Electronic Excitation Levels in Insulating Crystals. *Physical Review*, **52**, 3, 191 (1937). doi: 10.1103/PhysRev.52.191.

[69] M. Hirasawa, T. Ishihara, T. Goto, K. Uchida and N. Miura. Magnetoabsorption of the Lowest Exciton in Perovskite-Type Compound $(CH_3NH_3)PbI_3$. *Physica B: Condensed Matter*, **201**, 427 (1994). doi: 10.1016/0921-4526(94)91130-4.

[70] K. Tanaka, T. Takahashi, T. Ban, T. Kondo, K. Uchida and N. Miura. Comparative Study on the Excitons in Lead-Halide-Based Perovskite-Type Crystals $CH_3NH_3PbBr_3$ $CH_3NH_3PbI_3$. *Solid State Communications*, **127**, 9–10, 619 (2003). doi: 10.1016/S0038-1098(03)00566-0.

[71] J. Even, L. Pedesseau and C. Katan. Analysis of Multivalley and Multibandgap Absorption and Enhancement of Free Carriers Related to Exciton Screening in Hybrid Perovskites. *The Journal of Physical Chemistry C*, **118**, 22, 11566 (2014). doi: 10.1021/jp503337a.

[72] Y. Yamada, T. Nakamura, M. Endo, A. Wakamiya and Y. Kanemitsu. Photoelectronic Responses in Solution-Processed Perovskite $CH_3NH_3PbI_3$ Solar Cells Studied by Photoluminescence and Photoabsorption Spectroscopy. *IEEE Journal of Photovoltaics*, **5**, 401 (2015). doi: 10.1109/JPHOTOV.2014.2364115.

[73] A. Miyata, A. Mitioglu, P. Plochocka, O. Portugall, J. T.-W. Wang, S. D. Stranks, H. J. Snaith and R. J. Nicholas. Direct Measurement of the Exciton Binding Energy and Effective Masses for Charge Carriers in Organic–Inorganic Tri-Halide Perovskites. *Nature Physics*, **11**, 582 (2015). doi: 10.1038/nphys3357.

[74] Y. Yang, D. P. Ostrowski, R. M. France, K. Zhu, J. van de Lagemaat, J. M. Luther and M. C. Beard. Observation of a Hot-Phonon Bottleneck in Lead-Iodide Perovskites. *Nature Photonics*, **10**, 53 (2015). doi: 10.1038/nphoton.2015.213.

[75] X. Chen, H. Lu, Y. Yang and M. C. Beard. Excitonic Effects in Methylammonium Lead Halide Perovskites. *The Journal of Physical Chemistry Letters*, **9**, 10, 2595 (2018). doi: 10.1021/acs.jpclett.8b00526.

[76] M. Dvorak, S.-H. Wei and Z. Wu. Origin of the Variation of Exciton Binding Energy in Semiconductors. *Physical Review Letters*, **110**, 1, 016402 (2013). doi: 10.1103/PhysRevLett.110.016402.

[77] V. D'Innocenzo, G. Grancini, M. J. P. Alcocer, A. R. S. Kandada, S. D. Stranks, M. M. Lee, G. Lanzani, H. J. Snaith and A. Petrozza. Excitons Versus Free Charges in Organo-Lead Tri-Halide Perovskites. *Nature Communications*, **5** (2014). doi: 10.1038/ncomms4586.

[78] S. D. Stranks, V. M. Burlakov, T. Leijtens, J. M. Ball, A. Goriely and H. J. Snaith. Recombination Kinetics in Organic-Inorganic Perovskites: Excitons, Free Charge, and Subgap States. *Physical Review Applied*, **2**, 3, 034007 (2014). doi: 10.1103/PhysRevApplied.2.034007.

[79] C. Sheng, C. Zhang, Y. Zhai, K. Mielczarek, W. Wang, W. Ma, A. Zakhidov and Z. V. Vardeny. Exciton versus Free Carrier Photogeneration in Organometal Trihalide Perovskites Probed by Broadband Ultrafast Polarization Memory Dynamics. *Physical Review Letters*, **114**, 11, 116601 (2015). doi: 10.1103/PhysRevLett.114.116601.

[80] G. Yu and A. J. Heeger. Charge Separation and Photovoltaic Conversion in Polymer Composites with Internal Donor/Acceptor Heterojunctions. *Journal of Applied Physics*, **78**, 7, 4510 (1995). doi: 10.1063/1.359792.

[81] J. J. M. Halls, C. A. Walsh, N. C. Greenham, E. A. Marseglia, R. H. Friend, S. C. Moratti and A. B. Holmes. Efficient Photodiodes from Interpenetrating Polymer Networks. *Nature*, **376**, 6540, 498 (1995). doi: 10.1038/376498a0.

[82] V. Coropceanu, X.-K. Chen, T. Wang, Z. Zheng and J.-L. Brédas. Charge-Transfer Electronic States in Organic Solar Cells. *Nature Reviews Materials*, **4**, 11, 689 (2019). doi: 10.1038/s41578-019-0137-9.

[83] J.-P. Yang, M. Meissner, T. Yamaguchi, X.-Y. Zhang, T. Ueba, L.-W. Cheng, S. Ideta, K. Tanaka, X.-H. Zeng, N. Ueno and S. Kera. Band Dispersion and Hole Effective Mass of Methylammonium Lead Iodide Perovskite. *Solar Rapid Research Letters*, **2**, 10, 1800132 (2018). doi: 10.1002/solr.201800132.

[84] G. Giorgi, J.-I. Fujisawa, H. Segawa and K. Yamashita. Small Photocarrier Effective Masses Featuring Ambipolar Transport in Methylammonium Lead Iodide Perovskite: A Density Functional Analysis. *The Journal of Physical Chemistry Letters*, **4**, 24, 4213 (2013). doi: 10.1021/jz4023865.

[85] P. Umari, E. Mosconi and F. De Angelis. Relativistic GW Calculations on $CH_3NH_3PbI_3$ and $CH_3NH_3SnI_3$ Perovskites for Solar Cell Applications. *Scientific Reports*, **4**, 4467 (2014). doi: 10.1038/srep04467.

[86] E. Menéndez-Proupin, P. Palacios, P. Wahnón and J. C. Conesa. Self-Consistent Relativistic Band Structure of the $CH_3NH_3PbI_3$ Perovskite. *Physical Review B*, **90**, 4, 045207 (2014). doi: 10.1103/PhysRevB.90.045207.

[87] J. S. Blakemore. Semiconducting and Other Major Properties of Gallium Arsenide. *Journal of Applied Physics*, **53**, 10, R123 (1982). doi: 10.1063/1.331665.

[88] G. Xing, N. Mathews, S. Sun, S. S. Lim, Y. M. Lam, M. Grätzel, S. Mhaisalkar and T. C. Sum. Long-Range Balanced Electron- and Hole-Transport Lengths in Organic-Inorganic $CH_3NH_3PbI_3$. *Science*, **342**, 6156, 344 (2013). doi: 10.1126/science.1243167.

[89] S. D. Stranks, G. E. Eperon, G. Grancini, C. Menelaou, M. J. P. Alcocer, T. Leijtens, L. M. Herz, A. Petrozza and H. J. Snaith. Electron-Hole Diffusion Lengths Exceeding 1 Micrometer in an Organometal Trihalide Perovskite Absorber. *Science*, **342**, 6156, 341 (2013). doi: 10.1126/science.1243982.

[90] C. S. Ponseca, T. J. Savenije, M. Abdellah, K. Zheng, A. Yartsev, T. Pascher, T. Harlang, P. Chabera, T. Pullerits, A. Stepanov, J.-P. Wolf and V. Sundström. Organometal Halide Perovskite Solar Cell Materials Rationalized: Ultrafast Charge Generation, High and Microsecond-Long Balanced Mobilities, and Slow Recombination. *Journal of the American Chemical Society*, **136**, 14, 5189 (2014). doi: 10.1021/ja412583t.

[91] R. L. Milot, G. E. Eperon, H. J. Snaith, M. B. Johnston and L. M. Herz. Temperature-Dependent Charge-Carrier Dynamics in $CH_3NH_3PbI_3$ Perovskite Thin Films. *Advanced Functional Materials*, **25**, 39, 6218 (2015). doi: 10.1002/adfm.201502340.

[92] E. M. Hutter, G. E. Eperon, S. D. Stranks and T. J. Savenije. Charge Carriers in Planar and Meso-Structured Organic–Inorganic Perovskites: Mobilities, Lifetimes, and Concentrations of Trap States. *The Journal of Physical Chemistry Letters*, **6**, 15, 3082 (2015). doi: 10.1021/acs.jpclett.5b01361.

[93] D. H. Kim, J. Park, Z. Li, M. Yang, J.-S. Park, I. J. Park, J. Y. Kim, J. J. Berry, G. Rumbles and K. Zhu. 300% Enhancement of Carrier Mobility in Uniaxial-Oriented Perovskite Films Formed by Topotactic-Oriented Attachment. *Advanced Materials*, **29**, 23, 1606831 (2017). doi: 10.1002/adma.201606831.

[94] D. A. Valverde-Chávez, C. S. Ponseca, C. C. Stoumpos, A. Yartsev, M. G. Kanatzidis, V. Sundström and D. G. Cooke. Intrinsic Femtosecond Charge Generation Dynamics in Single Crystal $CH_3NH_3PbI_3$. *Energy & Environmental Science*, **8**, 12, 3700 (2015). doi: 10.1039/C5EE02503F.

[95] Q. Dong, Y. Fang, Y. Shao, P. Mulligan, J. Qiu, L. Cao and J. Huang. Electron-Hole Diffusion Lengths > 175 m in Solution-Grown $CH_3NH_3PbI_3$ Single Crystals. *Science*, **347**, 6225, 967 (2015). doi: 10.1126/science.aaa5760.

[96] I. Levine, S. Gupta, A. Bera, D. Ceratti, G. Hodes, D. Cahen, D. Guo, T. J. Savenije, J. Ávila, H. J. Bolink, O. Millo, D. Azulay and I. Balberg. Can We Use Time-Resolved Measurements to Get Steady-State Transport Data for Halide Perovskites? *Journal of Applied Physics*, **124**, 10, 103103 (2018). doi: 10.1063/1.5037637.

[97] Z. Chu, M. Yang, P. Schulz, D. Wu, X. Ma, E. Seifert, L. Sun, X. Li, K. Zhu and K. Lai. Impact of Grain Boundaries on Efficiency and Stability of Organic-Inorganic Trihalide Perovskites. *Nature Communications*, **8**, 1, 2230 (2017). doi: 10.1038/s41467-017-02331-4.

[98] R. Ciesielski, F. Schäfer, N. F. Hartmann, N. Giesbrecht, T. Bein, P. Docampo and A. Hartschuh. Grain Boundaries Act as Solid Walls for Charge Carrier Diffusion in Large Crystal MAPI Thin Films. *ACS Applied Materials Interfaces*, **10**, 9, 7974 (2018). doi: 10.1021/acsami.7b17938.

[99] J. Lim, M. T. Hörantner, N. Sakai, J. M. Ball, S. Mahesh, N. K. Noel, Y.-H. Lin, J. B. Patel, D. P. McMeekin, M. B. Johnston, B. Wenger and H. J. Snaith. Elucidating the Long-Range Charge Carrier Mobility in Metal Halide Perovskite Thin Films. *Energy & Environmental Science*, **12**, 1, 169 (2019). doi: 10.1039/C8EE03395A.

[100] C. Canali, C. Jacoboni, F. Nava, G. Ottaviani and A. Alberigi-Quaranta. Electron Drift Velocity in Silicon. *Physical Review B*, **12**, 6, 2265 (1975). doi: 10.1103/PhysRevB.12.2265.

[101] P. Y. Yu and M. Cardona. *Fundamentals of Semiconductors*. Springer (2010). doi: 10.1007/978-3-642-00710-1.

[102] H. Oga, A. Saeki, Y. Ogomi, S. Hayase and S. Seki. Improved Understanding of the Electronic and Energetic Landscapes of Perovskite Solar Cells: High Local Charge Carrier Mobility, Reduced Recombination, and Extremely Shallow Traps. *Journal of the American Chemical Society*, **136**, 39, 13818 (2014). doi: 10.1021/ja506936f.

[103] M. Karakus, S. A. Jensen, F. D'Angelo, D. Turchinovich, M. Bonn and E. Cánovas. Phonon–Electron Scattering Limits Free Charge Mobility in Methylammonium Lead Iodide Perovskites. *The Journal of Physical Chemistry Letters*, **6**, 24, 4991 (2015). doi: 10.1021/acs.jpclett.5b02485.

[104] S. Shrestha, G. J. Matt, A. Osvet, D. Niesner, R. Hock and C. J. Brabec. Assessing Temperature Dependence of Drift Mobility in Methylammonium Lead Iodide Perovskite Single Crystals. *The Journal of Physical Chemistry C*, **122**, 11, 5935 (2018). doi: 10.1021/acs.jpcc.8b00341.

[105] A. Biewald, N. Giesbrecht, T. Bein, P. Docampo, A. Hartschuh and R. Ciesielski. Temperature-Dependent Ambipolar Charge Carrier Mobility in Large-Crystal Hybrid Halide Perovskite Thin Films. *ACS Applied Materials Interfaces*, **11**, 23, 20838 (2019). doi: 10.1021/acsami.9b04592.

[106] Y. Wang, Y. Zhang, P. Zhang and W. Zhang. High Intrinsic Carrier Mobility and Photon Absorption in the Perovskite $CH_3NH_3PbI_3$. *Physical Chemistry Chemical Physics*, **17**, 17, 11516 (2015). doi: 10.1039/C5CP00448A.

[107] T. Zhao, W. Shi, J. Xi, D. Wang and Z. Shuai. Intrinsic and Extrinsic Charge Transport in $CH_3NH_3PbI_3$ Perovskites Predicted from First-Principles. *Scientific Reports*, **6**, 19968 (2016). doi: 10.1038/srep19968.

[108] A. D. Wright, C. Verdi, R. L. Milot, G. E. Eperon, M. A. Pérez-Osorio, H. J. Snaith, F. Giustino, M. B. Johnston and L. M. Herz. Electron–Phonon Coupling in Hybrid Lead Halide Perovskites. *Nature Communications*, **7**, 11755 (2016). doi: 10.1038/ncomms11755.

[109] A. Filippetti, A. Mattoni, C. Caddeo, M. I. Saba and P. Delugas. Low Electron-Polar Optical Phonon Scattering as a Fundamental Aspect of Carrier Mobility in Methylammonium Lead Halide $CH_3NH_3PbI_3$ Perovskites. *Physical Chemistry Chemical Physics*, **18**, 22, 15352 (2016). doi: 10.1039/C6CP01402J.

[110] S. Poncé, M. Schlipf and F. Giustino. Origin of Low Carrier Mobilities in Halide Perovskites. *ACS Energy Letters*, **4**, 2, 456 (2019). doi: 10.1021/acsenergylett.8b02346.

[111] L. M. Herz. Charge-Carrier Mobilities in Metal Halide Perovskites: Fundamental Mechanisms and Limits. *ACS Energy Letters*, **2**, 7, 1539 (2017). doi: 10.1021/acsenergylett.7b00276.

[112] F. Zheng and L.-w. Wang. Large Polaron Formation and its Effect on Electron Transport in Hybrid Perovskites. *Energy & Environmental Science*, **12**, 4, 1219 (2019). doi: 10.1039/C8EE03369B.

[113] M. Sendner, P. K. Nayak, D. A. Egger, S. Beck, C. Müller, B. Epding, W. Kowalsky, L. Kronik, H. J. Snaith, A. Pucci and R. Lovrinčić. Optical Phonons in Methylammonium Lead Halide Perovskites and Implications for Charge Transport. *Materials Horizons*, **3**, 6, 613 (2016). doi: 10.1039/C6MH00275G.

[114] D. A. Egger, A. Bera, D. Cahen, G. Hodes, T. Kirchartz, L. Kronik, R. Lovrincic, A. M. Rappe, D. R. Reichman and O. Yaffe. What Remains Unexplained about the Properties of Halide Perovskites? *Advanced Materials*, **30**, 20, 1800691 (2018). doi: 10.1002/adma.201800691.

[115] D. Shi, V. Adinolfi, R. Comin, M. Yuan, E. Alarousu, A. Buin, Y. Chen, S. Hoogland, A. Rothenberger, K. Katsiev, Y. Losovyj, X. Zhang, P. A. Dowben, O. F. Mohammed, E. H. Sargent and O. M. Bakr. Low Trap-State Density and Long Carrier Diffusion in Organolead Trihalide Perovskite Single Crystals. *Science*, **347**, 6221, 519 (2015). doi: 10.1126/science.aaa2725.

[116] F. Zhang, B. Yang, Y. Li, W. Deng and R. He. Extra Long Electron–Hole Diffusion Lengths in $CH_3NH_3PbI_{3-x}Cl_x$ perovskite single crystals. *Journal of Materials Chemistry C*, **5**, 33, 8431 (2017). doi: 10.1039/C7TC02802D.

[117] S. Liu, L. Wang, W.-C. Lin, S. Sucharitakul, C. Burda and X. P. A. Gao. Imaging the Long Transport Lengths of Photo-Generated Carriers in Oriented Perovskite Films. *Nano Letters*, **16**, 12, 7925 (2016). doi: 10.1021/acs.nanolett.6b04235.

[118] Z. Xiao, Q. Dong, C. Bi, Y. Shao, Y. Yuan and J. Huang. Solvent Annealing of Perovskite-Induced Crystal Growth for Photovoltaic-Device Efficiency Enhancement. *Advanced Materials*, **26**, 37, 6503 (2014). doi: 10.1002/adma.201401685.

[119] Y. Zhao, A. M. Nardes and K. Zhu. Solid-State Mesostructured Perovskite $CH_3NH_3PbI_3$ Solar Cells: Charge Transport, Recombination, and Diffusion Length. *The Journal of Physical Chemistry Letters*, **5**, 3, 490 (2014). doi: 10.1021/jz500003v.

[120] Y. Deng, E. Peng, Y. Shao, Z. Xiao, Q. Dong and J. Huang. Scalable Fabrication of Efficient Organolead Trihalide Perovskite Solar Cells With Doctor-Bladed Active Layers. *Energy & Environmental Science*, **8**, 5, 1544 (2015). doi: 10.1039/C4EE03907F.

[121] S. A. Kulkarni, T. Baikie, P. P. Boix, N. Yantara, N. Mathews and S. Mhaisalkar. Band-Gap Tuning of Lead Halide Perovskites Using a Sequential Deposition Process. *Journal of Materials Chemistry A*, **2**, 24, 9221 (2014). doi: 10.1039/C4TA00435C.

[122] N. Kitazawa, Y. Watanabe and Y. Nakamura. Optical Properties of $CH_3NH_3PbX_3$ (X = halogen) and their Mixed-Halide Crystals. *Journal of Materials Science*, **37**, 17, 3585 (2002). doi: 10.1023/a:1016584519829.

[123] G. E. Eperon, S. D. Stranks, C. Menelaou, M. B. Johnston, L. M. Herz and H. J. Snaith. Formamidinium Lead Trihalide: A Broadly Tunable Perovskite for Efficient Planar Heterojunction Solar Cells. *Energy & Environmental Science*, **7**, 3, 982 (2014). doi: 10.1039/C3EE43822H.

[124] T. Jesper Jacobsson, J.-P. Correa-Baena, M. Pazoki, M. Saliba, K. Schenk, M. Grätzel and A. Hagfeldt. Exploration of the Compositional Space for Mixed Lead Halogen Perovskites for High Efficiency Solar Cells. *Energy & Environmental Science*, **9**, 5, 1706 (2016). doi: 10.1039/C6EE00030D.

[125] F. Hao, C. C. Stoumpos, R. P. H. Chang and M. G. Kanatzidis. Anomalous Band Gap Behavior in Mixed Sn and Pb Perovskites Enables Broadening of Absorption Spectrum in Solar Cells. *Journal of the American Chemical Society*, **136**, 22, 8094 (2014). doi: 10.1021/ja5033259.

[126] N. N. Lal, Y. Dkhissi, W. Li, Q. Hou, Y.-B. Cheng and U. Bach. Perovskite Tandem Solar Cells. *Advanced Energy Materials*, **7**, 18, 1602761 (2017). doi: 10.1002/aenm.201602761.

[127] T. Leijtens, K. A. Bush, R. Prasanna and M. D. McGehee. Opportunities and Challenges for Tandem Solar Cells Using Metal Halide Perovskite Semiconductors. *Nature Energy*, **3**, 10, 828 (2018). doi: 10.1038/s41560-018-0190-4.

[128] M. Ahmadi, T. Wu and B. Hu. A Review on Organic–Inorganic Halide Perovskite Photodetectors: Device Engineering and Fundamental Physics. *Advanced Materials*, **29**, 41, 1605242 (2017). doi: 10.1002/adma.201605242.

[129] J. Miao and F. Zhang. Recent Progress on Highly Sensitive Perovskite Photodetectors. *Journal of Materials Chemistry C*, **7**, 7, 1741 (2019). doi: 10.1039/C8TC06089D.

[130] Q. Zhang, M. M. Tavakoli, L. Gu, D. Zhang, L. Tang, Y. Gao, J. Guo, Y. Lin, S.-F. Leung, S. Poddar, Y. Fu and Z. Fan. Efficient Metal Halide Perovskite Light-Emitting Diodes with Significantly Improved Light Extraction on Nanophotonic Substrates. *Nature Communications*, **10**, 1, 727 (2019). doi: 10.1038/s41467-019-08561-y.

[131] W. Xu, Q. Hu, S. Bai, C. Bao, Y. Miao, Z. Yuan, T. Borzda, A. J. Barker, E. Tyukalova, Z. Hu, M. Kawecki, H. Wang, Z. Yan, X. Liu, X. Shi, K. Uvdal, M. Fahlman, W. Zhang, M. Duchamp, J.-M. Liu, A. Petrozza, J. Wang, L.-M. Liu, W. Huang and F. Gao. Rational Molecular Passivation for High-Performance Perovskite Light-Emitting Diodes. *Nature Photonics*, **13**, 6, 418 (2019). doi: 10.1038/s41566-019-0390-x.

[132] S. A. Veldhuis, P. P. Boix, N. Yantara, M. Li, T. C. Sum, N. Mathews and S. G. Mhaisalkar. Perovskite Materials for Light-Emitting Diodes and Lasers. *Advanced Materials*, **28**, 32, 6804 (2016). doi: 10.1002/adma.201600669.

[133] Z. Li, J. Moon, A. Gharajeh, R. Haroldson, R. Hawkins, W. Hu, A. Zakhidov and Q. Gu. Room-Temperature Continuous-Wave Operation of Organometal Halide Perovskite Lasers. *ACS Nano*, **12**, 11, 10968 (2018). doi: 10.1021/acsnano.8b04854.

[134] Q. Chen, J. Wu, X. Ou, B. Huang, J. Almutlaq, A. A. Zhumekenov, X. Guan, S. Han, L. Liang, Z. Yi, J. Li, X. Xie, Y. Wang, Y. Li, D. Fan, D. B. L. Teh, A. H. All, O. F. Mohammed, O. M. Bakr, T. Wu, M. Bettinelli, H. Yang, W. Huang and X. Liu. All-Inorganic Perovskite Nanocrystal Scintillators. *Nature*, **561**, 7721, 88 (2018). doi: 10.1038/s41586-018-0451-1.

[135] H. Wei and J. Huang. Halide Lead Perovskites for Ionizing Radiation Detection. *Nature Communications*, **10**, 1, 1066 (2019). doi: 10.1038/s41467-019-08981-w.

[136] K. Tennakone, G. R. R. A. Kumara, A. R. Kumarasinghe, K. G. U. Wijayantha and P. M. Sirimanne. A Dye-Sensitized Nano-Porous Solid-State Photovoltaic Cell. *Semiconductor Science and Technology*, **10**, 12, 1689 (1995). doi: 10.1088/0268-1242/10/12/020.

[137] M. Kei, K. Ryuichiro, W. Yuji and Y. Shozo. Solid State Dye-Sensitized TiO_2 Solar Cell with Polypyrrole as Hole Transport Layer. *Chemistry Letters*, **26**, 5, 471 (1997). doi: 10.1246/cl.1997.471.

[138] U. Bach, D. Lupo, P. Comte, J. E. Moser, F. Weissörtel, J. Salbeck, H. Spreitzer and M. Grätzel. Solid-State Dye-Sensitized Mesoporous TiO_2 Solar Cells with High Photon-To-Electron Conversion Efficiencies. *Nature*, **395**, 6702, 583 (1998). doi: 10.1038/26936.

[139] J. Weickert and L. Schmidt-Mende. *Solid-State Dye-Sensitized Solar Cells*, 465–494. Wiley-VCH Verlag GmbH Co. KGaA (2014). doi: 10.1002/9783527656912.ch15.

[140] E. Hendry, M. Koeberg, B. O'Regan and M. Bonn. Local Field Effects on Electron Transport in Nanostructured TiO_2 Revealed by Terahertz Spectroscopy. *Nano Letters*, **6**, 4, 755 (2006). doi: 10.1021/nl0600225.

[141] M. H. Kumar, N. Yantara, S. Dharani, M. Graetzel, S. Mhaisalkar, P. P. Boix and N. Mathews. Flexible, Low-Temperature, Solution Processed ZnO-Based Perovskite Solid State Solar Cells. *Chemical Communications*, **49**, 94, 11089 (2013). doi: 10.1039/C3CC46534A.

[142] D. Bi, L. Yang, G. Boschloo, A. Hagfeldt and E. M. J. Johansson. Effect of Different Hole Transport Materials on Recombination in $CH_3NH_3PbI_3$ Perovskite-Sensitized Mesoscopic Solar Cells. *The Journal of Physical Chemistry Letters*, **4**, 9, 1532 (2013). doi: 10.1021/jz400638x.

[143] Y. Li, J. Zhu, Y. Huang, F. Liu, M. Lv, S. Chen, L. Hu, J. Tang, J. Yao and S. Dai. Mesoporous SnO_2 Nanoparticle Films as Electron-Transporting Material in Perovskite Solar Cells. *RSC Advances*, **5**, 36, 28424 (2015). doi: 10.1039/C5RA01540E.

[144] P. Gao, M. Gratzel and M. K. Nazeeruddin. Organohalide Lead Perovskites for Photovoltaic Applications. *Energy & Environmental Science*, **7**, 8, 2448 (2014). doi: 10.1039/C4EE00942H.

[145] J.-Y. Jeng, Y.-F. Chiang, M.-H. Lee, S.-R. Peng, T.-F. Guo, P. Chen and T.-C. Wen. $CH_3NH_3PbI_3$ Perovskite/Fullerene Planar-Heterojunction Hybrid Solar Cells. *Advanced Materials*, **25**, 27, 3727 (2013). doi: 10.1002/adma.201301327.

[146] C. Bi, Q. Wang, Y. Shao, Y. Yuan, Z. Xiao and J. Huang. Non-Wetting Surface-Driven High-Aspect-Ratio Crystalline Grain Growth for Efficient Hybrid Perovskite Solar Cells. *Nature Communications*, **6**, 7747 (2015). doi: 10.1038/ncomms8747.

[147] S. Ye, W. Sun, Y. Li, W. Yan, H. Peng, Z. Bian, Z. Liu and C. Huang. CuSCN-Based Inverted Planar Perovskite Solar Cell with an Average PCE of 15.6%. *Nano Letters*, **15**, 6, 3723 (2015). doi: 10.1021/acs.nanolett.5b00116.

[148] K.-G. Lim, H.-B. Kim, J. Jeong, H. Kim, J. Y. Kim and T.-W. Lee. Boosting the Power Conversion Efficiency of Perovskite Solar Cells Using Self-Organized Polymeric Hole Extraction Layers with High Work Function. *Advanced Materials*, **26**, 37, 6461 (2014). doi: 10.1002/adma.201401775.

[149] J. You, Z. Hong, Y. Yang, Q. Chen, M. Cai, T.-B. Song, C.-C. Chen, S. Lu, Y. Liu, H. Zhou and Y. Yang. Low-Temperature Solution-Processed Perovskite Solar Cells with High Efficiency and Flexibility. *ACS Nano*, **8**, 2, 1674 (2014). doi: 10.1021/nn406020d.

[150] Y. Hou, X. Du, S. Scheiner, D. P. McMeekin, Z. Wang, N. Li, M. S. Killian, H. Chen, M. Richter, I. Levchuk, N. Schrenker, E. Spiecker, T. Stubhan, N. A. Luechinger, A. Hirsch, P. Schmuki, H.-P. Steinrück, R. H. Fink, M. Halik, H. J. Snaith and C. J. Brabec. A Generic Interface to Reduce the Efficiency-Stability-Cost Gap of Perovskite Solar Cells. *Science* (2017). doi: 10.1126/science.aao5561.

[151] Q. Wang, C. Bi and J. Huang. Doped Hole Transport Layer for Efficiency Enhancement in Planar Heterojunction Organolead Trihalide Perovskite Solar Cells. *Nano Energy*, **15**, 275 (2015). doi: 10.1016/j.nanoen.2015.04.029.

[152] J. H. Heo, H. J. Han, D. Kim, T. K. Ahn and S. H. Im. Hysteresis-Less Inverted $CH_3NH_3PbI_3$ Planar Perovskite Hybrid Solar Cells with 18.1% Power Conversion Efficiency. *Energy & Environmental Science*, **8**, 5, 1602 (2015). doi: 10.1039/C5EE00120J.

[153] M. Liu, M. B. Johnston and H. J. Snaith. Efficient Planar Heterojunction Perovskite Solar Cells by Vapour Deposition. *Nature*, **501**, 395 (2013). doi: 10.1038/nature12509.

[154] J.-P. Correa-Baena, A. Abate, M. Saliba, W. Tress, T. Jesper Jacobsson, M. Grätzel and A. Hagfeldt. The Rapid Evolution of Highly Efficient Perovskite Solar Cells. *Energy & Environmental Science*, **10**, 3, 710 (2017). doi: 10.1039/C6EE03397K.

[155] V. Petrova-Koch. *Milestones of Solar Conversion and Photovoltaics*, 1–5. Springer, Berlin, Heidelberg (2009). doi: 10.1007/978-3-540-79359-5_1.

[156] A. Einstein. Über einen die Erzeugung und Verwandlung des Lichtes betreffenden heuristischen Gesichtspunkt. *Annalen der Physik*, **322**, 6, 132 (1905). doi: 10.1002/andp.19053220607.

[157] J. Fu, Q. Xu, G. Han, B. Wu, C. H. A. Huan, M. L. Leek and T. C. Sum. Hot Carrier Cooling Mechanisms in Halide Perovskites. *Nature Communications*, **8**, 1, 1300 (2017). doi: 10.1038/s41467-017-01360-3.

[158] D. Niesner, H. Zhu, K. Miyata, P. P. Joshi, T. J. S. Evans, B. J. Kudisch, M. T. Trinh, M. Marks and X. Y. Zhu. Persistent Energetic Electrons in Methylammonium Lead Iodide Perovskite Thin Films. *Journal of the American Chemical Society*, **138**, 48, 15717 (2016). doi: 10.1021/jacs.6b08880.

[159] J. Yang, X. Wen, H. Xia, R. Sheng, Q. Ma, J. Kim, P. Tapping, T. Harada, T. W. Kee, F. Huang, Y.-B. Cheng, M. Green, A. Ho-Baillie, S. Huang, S. Shrestha, R. Patterson and G. Conibeer. Acoustic-Optical Phonon Up-Conversion and Hot-Phonon Bottleneck in Lead-Halide Perovskites. *Nature Communications*, **8**, 14120 (2017). doi: 10.1038/ncomms14120.

[160] K. Chen, A. J. Barker, F. L. C. Morgan, J. E. Halpert and J. M. Hodgkiss. Effect of Carrier Thermalization Dynamics on Light Emission and Amplification in Organometal Halide Perovskites. *The Journal of Physical Chemistry Letters*, **6**, 1, 153 (2015). doi: 10.1021/jz502528c.

[161] M. Li, J. Fu, Q. Xu and T. C. Sum. Slow Hot-Carrier Cooling in Halide Perovskites: Prospects for Hot-Carrier Solar Cells. *Advanced Materials*, **0**, 0, 1802486 (2019). doi: 10.1002/adma.201802486.

[162] S. Kahmann and M. A. Loi. Hot Carrier Solar Cells and the Potential of Perovskites for Breaking the Shockley–Queisser Limit. *Journal of Materials Chemistry C*, **7**, 9, 2471 (2019). doi: 10.1039/C8TC04641G.

[163] J. Bisquert. *The Physics of Solar Cells: Perovskites, Organics, and Photovoltaic Fundamentals.* CRC Press, 10.1002/9783527618545 (2017). doi: 10.1201/b22380.

[164] U. Würfel, A. Cuevas and P. Wuerfel. Charge Carrier Separation in Solar Cells. *IEEE Journal of Photovoltaics*, **5**, 1, 461 (2014). doi: 10.1109/JPHOTOV.2014.2363550.

[165] T. Kirchartz, J. Bisquert, I. Mora-Sero and G. Garcia-Belmonte. Classification of Solar Cells According to Mechanisms of Charge Separation and Charge Collection. *Physical Chemistry Chemical Physics*, **17**, 6, 4007 (2015). doi: 10.1039/C4CP05174B.

[166] U. Rau and T. Kirchartz. Charge Carrier Collection and Contact Selectivity in Solar Cells. *Advanced Materials Interfaces*, **6**, 20, 1900252 (2019). doi: 10.1002/admi.201900252.

[167] S. Ravishankar, S. Gharibzadeh, C. Roldán-Carmona, G. Grancini, Y. Lee, M. Ralaiarisoa, A. M. Asiri, N. Koch, J. Bisquert and M. K. Nazeeruddin. Influence of Charge Transport Layers on Open-Circuit Voltage and Hysteresis in Perovskite Solar Cells. *Joule*, **2**, 4, 788 (2018). doi: 10.1016/j.joule.2018.02.013.

[168] I. Mora-Seró. How Do Perovskite Solar Cells Work? *Joule*, **2**, 4, 585 (2018). doi: 10.1016/j.joule.2018.03.020.

[169] V. W. Bergmann, Y. Guo, H. Tanaka, I. M. Hermes, D. Li, A. Klasen, S. A. Bretschneider, E. Nakamura, R. Berger and S. A. L. Weber. Local Time-Dependent Charging in a Perovskite Solar Cell. *ACS Applied Materials Interfaces*, **8**, 30, 19402 (2016). doi: 10.1021/acsami.6b04104.

[170] P. Würfel and U. Würfel. *Physics of Solar Cells: from Basic Principles to Advanced Concepts.* Wiley-VCH Verlag GmbH Co. (2016). doi: 10.1002/9783527618545.

[171] W. Shockley. The Theory of p-n Junctions in Semiconductors and p-n Junction Transistors. *The Bell System Technical Journal*, **28**, 3, 435 (1949). doi: 10.1002/j.1538-7305.1949.tb03645.x.

[172] A. Cuevas. The Recombination Parameter j_0. *Energy Procedia*, **55**, 53 (2014). doi: 10.1016/j.egypro.2014.08.073.

[173] K. Tvingstedt and C. Deibel. Temperature Dependence of Ideality Factors in Organic Solar Cells and the Relation to Radiative Efficiency. *Advanced Energy Materials*, **6**, 9, 1502230 (2016). doi: 10.1002/aenm.201502230.

[174] W. Tress, M. Yavari, K. Domanski, P. Yadav, B. Niesen, J. P. Correa Baena, A. Hagfeldt and M. Grätzel. Interpretation and Evolution of Open-Circuit Voltage, Recombination, Ideality Factor and Subgap Defect States During Reversible Light-Soaking and Irreversible Degradation of Perovskite Solar Cells. *Energy & Environmental Science*, **11**, 1, 151 (2018). doi: 10.1039/C7EE02415K.

[175] O. Dupré, R. Vaillon and M. A. Green. *Thermal Behavior of Photovoltaic Devices. Physics and Engineering*. Springer (2017). doi: 10.1007/978-3-319-49457-9.

[176] Y. Shao, Z. Xiao, C. Bi, Y. Yuan and J. Huang. Origin and Elimination of Photocurrent Hysteresis by Fullerene Passivation in $CH_3NH_3PbI_3$ Planar Heterojunction Solar Cells. *Nature Communications*, **5** (2014). doi: 10.1038/ncomms6784.

[177] N. Tessler and Y. Vaynzof. Preventing Hysteresis in Perovskite Solar Cells by Undoped Charge Blocking Layers. *ACS Applied Energy Materials*, **1**, 2, 676 (2018). doi: 10.1021/acsaem.7b00176.

[178] Z. Liu, Q. Chen, J.-W. Lee, Z. Zhao, X. Xu, Y.-T. Hsieh, L. Meng, P. Sun, N. D. Marco, H. Zhou, Y.-B. Cheng and Y. Yang. Rationally Induced Interfacial Dipole in Planar Heterojunction Perovskite Solar Cells for Reduced J–V Hysteresis. *Advanced Energy Materials*, **8**, 23, 1800568 (2018). doi: 10.1002/aenm.201800568.

[179] A. Guerrero, A. Bou, G. Matt, O. Almora, T. Heumüller, G. Garcia-Belmonte, J. Bisquert, Y. Hou and C. Brabec. Switching Off Hysteresis in Perovskite Solar Cells by Fine-Tuning Energy Levels of Extraction Layers. *Advanced Energy Materials*, **8**, 21, 1703376 (2018). doi: 10.1002/aenm.201703376.

[180] H.-W. Chen, N. Sakai, M. Ikegami and T. Miyasaka. Emergence of Hysteresis and Transient Ferroelectric Response in Organo-Lead Halide Perovskite Solar Cells. *The Journal of Physical Chemistry Letters*, **6**, 1, 164 (2015). doi: 10.1021/jz502429u.

[181] Y. Zhang, M. Liu, G. E. Eperon, T. C. Leijtens, D. McMeekin, M. Saliba, W. Zhang, M. de Bastiani, A. Petrozza, L. M. Herz, M. B. Johnston, H. Lin and H. J. Snaith. Charge Selective Contacts, Mobile Ions and Anomalous Hysteresis in Organic-Inorganic Perovskite Solar Cells. *Materials Horizons*, **2**, 3, 315 (2015). doi: 10.1039/C4MH00238E.

[182] Y. Wu, H. Shen, D. Walter, D. Jacobs, T. Duong, J. Peng, L. Jiang, Y. Cheng and K. Weber. On the Origin of Hysteresis in Perovskite Solar Cells. *Advanced Functional Materials*, **26**, 37, 6807 (2016). doi: 10.1002/adfm.201602231.

[183] X. Li, Y. Wang, M. Tai, X. Zhao, Y. Gu, J. Han, H. Shen, J. Li and H. Lin. New Insights into the Origin of Hysteresis Behavior in Perovskite Solar Cells. *Physical Chemistry Chemical Physics*, **20**, 23, 16285 (2018). doi: 10.1039/C8CP01432A.

[184] T. Bu, X. Liu, Y. Zhou, J. Yi, X. Huang, L. Luo, J. Xiao, Z. Ku, Y. Peng, F. Huang, Y.-B. Cheng and J. Zhong. A Novel Quadruple-Cation Absorber for Universal Hysteresis Elimination for High Efficiency and Stable Perovskite Solar Cells. *Energy & Environmental Science*, **10**, 12, 2509 (2017). doi: 10.1039/C7EE02634J.

[185] Z. Tang, T. Bessho, F. Awai, T. Kinoshita, M. M. Maitani, R. Jono, T. N. Murakami, H. Wang, T. Kubo, S. Uchida and H. Segawa. Hysteresis-Free Perovskite Solar Cells Made of Potassium-Doped Organometal Halide Perovskite. *Scientific Reports*, **7**, 1, 12183 (2017). doi: 10.1038/s41598-017-12436-x.

[186] B. Cao, L. Yang, S. Jiang, H. Lin, N. Wang and X. Li. Flexible Quintuple Cation Perovskite Solar Cells with High Efficiency. *Journal of Materials Chemistry A*, **7**, 9, 4960 (2019). doi: 10.1039/C8TA11945G.

[187] W. Tress, N. Marinova, T. Moehl, S. M. Zakeeruddin, M. K. Nazeeruddin and M. Grätzel. Understanding the Rate-Dependent J-V Hysteresis, Slow Time Component, and Aging in $CH_3NH_3PbI_3$ Perovskite Solar Cells: the Role of a Compensated Electric Field. *Energy & Environmental Science*, **8**, 3, 995 (2015). doi: 10.1039/C4EE03664F.

[188] X. Li, X. Wang, W. Zhang, Y. Wu, F. Gao and J. Fang. The Effect of External Electric Field on the Performance of Perovskite Solar Cells. *Organic Electronics*, **18**, 107 (2015). doi: 10.1016/j.orgel.2015.01.024.

[189] F. Wu, B. Bahrami, K. Chen, S. Mabrouk, R. Pathak, Y. Tong, X. Li, T. Zhang, R. Jian and Q. Qiao. Bias-Dependent Normal and Inverted J–V Hysteresis in Perovskite Solar Cells. *ACS Applied Materials Interfaces*, **10**, 30, 25604 (2018). doi: 10.1021/acsami.8b07298.

[190] H. J. Snaith, A. Abate, J. M. Ball, G. E. Eperon, T. Leijtens, N. K. Noel, S. D. Stranks, J. T.-W. Wang, K. Wojciechowski and W. Zhang. Anomalous Hysteresis in Perovskite Solar Cells. *The Journal of Physical Chemistry Letters*, **5**, 9, 1511 (2014). doi: 10.1021/jz500113x.

[191] E. L. Unger, E. T. Hoke, C. D. Bailie, W. H. Nguyen, A. R. Bowring, T. Heumüller, M. G. Christoforo and M. D. McGehee. Hysteresis and Transient Behavior in Current–Voltage Measurements of Hybrid-Perovskite Absorber Solar Cells. *Energy & Environmental Science*, **7**, 11, 3690 (2014). doi: 10.1039/C4EE02465F.

[192] C. Liu, J. Fan, X. Zhang, Y. Shen, L. Yang and Y. Mai. Hysteretic Behavior upon Light Soaking in Perovskite Solar Cells Prepared via Modified Vapor-Assisted Solution Process. *ACS Applied Materials Interfaces*, **7**, 17, 9066 (2015). doi: 10.1021/acsami.5b00375.

[193] L. K. Ono, S. R. Raga, S. Wang, Y. Kato and Y. Qi. Temperature-Dependent Hysteresis Effects in Perovskite-Based Solar Cells. *Journal of Materials Chemistry A*, **3**, 17, 9074 (2015). doi: 10.1039/C4TA04969A.

[194] D. Bryant, S. Wheeler, B. C. O'Regan, T. Watson, P. R. F. Barnes, D. Worsley and J. Durrant. Observable Hysteresis at Low Temperature in "Hysteresis Free" Organic–Inorganic Lead Halide Perovskite Solar Cells. *The Journal of Physical Chemistry Letters*, **6**, 16, 3190 (2015). doi: 10.1021/acs.jpclett.5b01381.

[195] M. Herman, M. Jankovec and M. Topic. Optimal I-V Curve Scan Time of Solar Cells and Modules in Light of Irradiance Level. *International Journal of Photoenergy*, **2012**, 11 (2012). doi: 10.1155/2012/151452.

[196] N. Koide and L. Han. Measuring Methods of Cell Performance of Dye-Sensitized Solar Cells. *Review of Scientific Instruments*, **75**, 9, 2828 (2004). doi: 10.1063/1.1784556.

[197] D. W. deQuilettes, W. Zhang, V. M. Burlakov, D. J. Graham, T. Leijtens, A. Osherov, V. Bulović, H. J. Snaith, D. S. Ginger and S. D. Stranks. Photo-Induced Halide Redistribution in Organic–Inorganic Perovskite Films. *Nature Communications*, **7**, 11683 (2016). doi: 10.1038/ncomms11683.

[198] J. M. Frost, K. T. Butler, F. Brivio, C. H. Hendon, M. van Schilfgaarde and A. Walsh. Atomistic Origins of High-Performance in Hybrid Halide Perovskite Solar Cells. *Nano Letters*, **14**, 5, 2584 (2014). doi: 10.1021/nl500390f.

[199] J. M. Frost, K. T. Butler and A. Walsh. Molecular Ferroelectric Contributions to Anomalous Hysteresis in Hybrid Perovskite Solar Cells. *APL Materials*, **2**, 8, 081506 (2014). doi: 10.1063/1.4890246.

[200] Z. Fan, J. Xiao, K. Sun, L. Chen, Y. Hu, J. Ouyang, K. P. Ong, K. Zeng and J. Wang. Ferroelectricity of $CH_3NH_3PbI_3$ Perovskite. *The Journal of Physical Chemistry Letters*, **6**, 7, 1155 (2015). doi: 10.1021/acs.jpclett.5b00389.

[201] A. Pecchia, D. Gentilini, D. Rossi, M. Auf der Maur and A. Di Carlo. Role of Ferroelectric Nanodomains in the Transport Properties of Perovskite Solar Cells. *Nano Letters*, **16**, 2, 988 (2016). doi: 10.1021/acs.nanolett.5b03957.

[202] A. Filippetti, P. Delugas, M. I. Saba and A. Mattoni. Entropy-Suppressed Ferroelectricity in Hybrid Lead-Iodide Perovskites. *The Journal of Physical Chemistry Letters*, **6**, 24, 4909 (2015). doi: 10.1021/acs.jpclett.5b02117.

[203] H. Röhm, T. Leonhard, M. J. Hoffmann and A. Colsmann. Ferroelectric Domains in Methylammonium Lead Iodide Perovskite Thin-Films. *Energy & Environmental Science*, **10**, 4, 950 (2017). doi: 10.1039/C7EE00420F.

[204] S. M. Vorpahl, R. Giridharagopal, G. E. Eperon, I. M. Hermes, S. A. L. Weber and D. S. Ginger. Orientation of Ferroelectric Domains and Disappearance upon Heating Methylammonium Lead Triiodide Perovskite from Tetragonal to Cubic Phase. *ACS Applied Energy Materials*, **1**, 4, 1534 (2018). doi: 10.1021/acsaem.7b00330.

[205] H. Röhm, T. Leonhard, A. D. Schulz, S. Wagner, M. J. Hoffmann and A. Colsmann. Ferroelectric Properties of Perovskite Thin Films and Their Implications for Solar Energy Conversion. *Advanced Materials*, **31**, 26, 1806661 (2019). doi: 10.1002/adma.201806661.

[206] L. M. Garten, D. T. Moore, S. U. Nanayakkara, S. Dwaraknath, P. Schulz, J. Wands, A. Rockett, B. Newell, K. A. Persson, S. Trolier-McKinstry and D. S. Ginley. The Existence and Impact of Persistent Ferroelectric Domains in $MAPbI_3$. *Science Advances*, **5**, 1, 9 (2019). doi: 10.1126/sciadv.aas9311.

[207] M. S. Alvar, M. Kumar, P. W. M. Blom, G.-J. A. H. Wetzelaer and K. Asadi. Absence of Ferroelectricity in Methylammonium Lead Iodide Perovskite. *AIP Advances*, **7**, 9, 095110 (2017). doi: 10.1063/1.4994957.

[208] A. Gómez, Q. Wang, A. R. Goñi, M. Campoy-Quiles and A. Abate. Ferroelectricity-Free Lead Halide Perovskites. *Energy & Environmental Science*, **12**, 8, 2537 (2019). doi: 10.1039/C9EE00884E.

[209] J. Wei, Y. Zhao, H. Li, G. Li, J. Pan, D. Xu, Q. Zhao and D. Yu. Hysteresis Analysis Based on the Ferroelectric Effect in Hybrid Perovskite Solar Cells. *The Journal of Physical Chemistry Letters*, **5**, 21, 3937 (2014). doi: 10.1021/jz502111u.

[210] A. M. A. Leguy, J. M. Frost, A. P. McMahon, V. G. Sakai, W. Kockelmann, C. Law, X. Li, F. Foglia, A. Walsh, B. C. O'Regan, J. Nelson, J. T. Cabral and P. R. F. Barnes. The Dynamics of Methylammonium Ions in Hybrid Organic–Inorganic Perovskite Solar Cells. *Nature Communications*, **6**, 1, 7124 (2015). doi: 10.1038/ncomms8124.

[211] B. Chen, M. Yang, S. Priya and K. Zhu. Origin of J–V Hysteresis in Perovskite Solar Cells. *The Journal of Physical Chemistry Letters*, **7**, 5, 905 (2016). doi: 10.1021/acs.jpclett.6b00215.

[212] P. Liu, W. Wang, S. Liu, H. Yang and Z. Shao. Fundamental Understanding of Photocurrent Hysteresis in Perovskite Solar Cells. *Advanced Energy Materials*, **9**, 13, 1803017 (2019). doi: 10.1002/aenm.201803017.

[213] K. Wojciechowski, S. D. Stranks, A. Abate, G. Sadoughi, A. Sadhanala, N. Kopidakis, G. Rumbles, C.-Z. Li, R. H. Friend, A. K. Y. Jen and H. J. Snaith. Heterojunction Modification for Highly Efficient Organic–Inorganic Perovskite Solar Cells. *ACS Nano*, **8**, 12, 12701 (2014). doi: 10.1021/nn505723h.

[214] J. Mizusaki, K. Arai and K. Fueki. Ionic Conduction of the Perovskite-Type Halides. *Solid State Ionics*, **11**, 3, 203 (1983). doi: 10.1016/0167-2738(83)90025-5.

[215] C. Eames, J. M. Frost, P. R. F. Barnes, B. C. O'Regan, A. Walsh and M. S. Islam. Ionic Transport in Hybrid Lead Iodide Perovskite Solar Cells. *Nature Communications*, **6** (2015). doi: 10.1038/ncomms8497.

[216] J. M. Azpiroz, E. Mosconi, J. Bisquert and F. De Angelis. Defect Migration in Methylammonium Lead Iodide and its Role in Perovskite Solar Cell Operation. *Energy & Environmental Science*, **8**, 7, 2118 (2015). doi: 10.1039/C5EE01265A.

[217] S. Meloni, T. Moehl, W. Tress, M. Franckevičius, M. Saliba, Y. H. Lee, P. Gao, M. K. Nazeeruddin, S. M. Zakeeruddin, U. Rothlisberger and M. Grätzel. Ionic Polarization-Induced Current–Voltage Hysteresis in $CH_3NH_3PbX_3$ Perovskite Solar Cells. *Nature Communications*, **7**, 1, 10334 (2016). doi: 10.1038/ncomms10334.

[218] A. Walsh and S. D. Stranks. Taking Control of Ion Transport in Halide Perovskite Solar Cells. *ACS Energy Letters*, **3**, 8, 1983 (2018). doi: 10.1021/acsenergylett.8b00764.

[219] Y. Yuan, Q. Wang, Y. Shao, H. Lu, T. Li, A. Gruverman and J. Huang. Electric-Field-Driven Reversible Conversion Between Methylammonium Lead Triiodide Perovskites and Lead Iodide at Elevated Temperatures. *Advanced Energy Materials*, **6**, 2, 1501803 (2016). doi: 10.1002/aenm.201501803.

[220] C. Li, S. Tscheuschner, F. Paulus, P. E. Hopkinson, J. Kießling, A. Köhler, Y. Vaynzof and S. Huettner. Iodine Migration and its Effect on Hysteresis in Perovskite Solar Cells. *Advanced Materials*, **28**, 12, 2446 (2016). doi: 10.1002/adma.201503832.

[221] M. H. Futscher, J. M. Lee, L. McGovern, L. A. Muscarella, T. Wang, M. I. Haider, A. Fakharuddin, L. Schmidt-Mende and B. Ehrler. Quantification of Ion Migration in $CH_3NH_3PbI_3$ Perovskite Solar Cells by Transient Capacitance Measurements. *Materials Horizons*, **6**, 7, 1497 (2019). doi: 10.1039/C9MH00445A.

[222] Z. Xiao, Y. Yuan, Y. Shao, Q. Wang, Q. Dong, C. Bi, P. Sharma, A. Gruverman and J. Huang. Giant Switchable Photovoltaic Effect in Organometal Trihalide Perovskite Devices. *Nature Materials*, **14**, 193 (2014). doi: 10.1038/nmat4150.

[223] Y. Yuan, J. Chae, Y. Shao, Q. Wang, Z. Xiao, A. Centrone and J. Huang. Photovoltaic Switching Mechanism in Lateral Structure Hybrid Perovskite Solar Cells. *Advanced Energy Materials*, **5**, 15, 1500615 (2015). doi: 10.1002/aenm.201500615.

[224] T. Leijtens, E. T. Hoke, G. Grancini, D. J. Slotcavage, G. E. Eperon, J. M. Ball, M. De Bastiani, A. R. Bowring, N. Martino, K. Wojciechowski, M. D. McGehee, H. J. Snaith and A. Petrozza. Mapping Electric Field-Induced Switchable Poling and Structural Degradation in Hybrid Lead Halide Perovskite Thin Films. *Advanced Energy Materials*, **5**, 20, 1500962 (2015). doi: 10.1002/aenm.201500962.

[225] J. Dhar, S. Sil, A. Dey, D. Sanyal and P. P. Ray. Investigation of Ion-Mediated Charge Transport in Methylammonium Lead Iodide Perovskite. *The Journal of Physical Chemistry C*, **121**, 10, 5515 (2017). doi: 10.1021/acs.jpcc.7b01047.

[226] A. Senocrate, I. Moudrakovski, T. Acartürk, R. Merkle, G. Y. Kim, U. Starke, M. Grätzel and J. Maier. Slow $CH_3NH_3^+$ Diffusion in $CH_3NH_3PbI_3$ under Light Measured by Solid-State NMR and Tracer Diffusion. *The Journal of Physical Chemistry C*, **122**, 38, 21803 (2018). doi: 10.1021/acs.jpcc.8b06814.

[227] G. E. Eperon and D. S. Ginger. B-Site Metal Cation Exchange in Halide Perovskites. *ACS Energy Letters*, **2**, 5, 1190 (2017). doi: 10.1021/acsenergylett.7b00290.

[228] D. Barboni and R. A. De Souza. The Thermodynamics and Kinetics of Iodine Vacancies in the Hybrid Perovskite Methylammonium Lead Iodide. *Energy & Environmental Science*, **11**, 11, 3266 (2018). doi: 10.1039/C8EE01697F.

[229] D. Meggiolaro, E. Mosconi and F. De Angelis. Formation of Surface Defects Dominates Ion Migration in Lead-Halide Perovskites. *ACS Energy Letters*, **4**, 3, 779 (2019). doi: 10.1021/acsenergylett.9b00247.

[230] Y. Shao, Y. Fang, T. Li, Q. Wang, Q. Dong, Y. Deng, Y. Yuan, H. Wei, M. Wang, A. Gruverman, J. Shield and J. Huang. Grain Boundary Dominated Ion Migration in Polycrystalline Organic–Inorganic Halide Perovskite Films. *Energy & Environmental Science*, **9**, 5, 1752 (2016). doi: 10.1039/C6EE00413J.

[231] W. Tress. Metal Halide Perovskites as Mixed Electronic–Ionic Conductors: Challenges and Opportunities – From Hysteresis to Memristivity. *The Journal of Physical Chemistry Letters*, **8**, 13, 3106 (2017). doi: 10.1021/acs.jpclett.7b00975.

[232] R. A. Belisle, W. H. Nguyen, A. R. Bowring, P. Calado, X. Li, S. J. C. Irvine, M. D. McGehee, P. R. F. Barnes and B. C. O'Regan. Interpretation of Inverted Photocurrent Transients in Organic Lead Halide Perovskite Solar Cells: Proof of the Field Screening by Mobile Ions and Determination of the Space Charge Layer Widths. *Energy & Environmental Science*, **10**, 1, 192 (2017). doi: 10.1039/C6EE02914K.

[233] S. van Reenen, M. Kemerink and H. J. Snaith. Modeling Anomalous Hysteresis in Perovskite Solar Cells. *The Journal of Physical Chemistry Letters*, **6**, 19, 3808 (2015). doi: 10.1021/acs.jpclett.5b01645.

[234] P. Calado, A. M. Telford, D. Bryant, X. Li, J. Nelson, B. C. O'Regan and P. R. F. Barnes. Evidence for Ion Migration in Hybrid Perovskite Solar Cells with Minimal Hysteresis. *Nature Communications*, **7**, 13831 (2016). doi: 10.1038/ncomms13831.

[235] A. Pockett and M. J. Carnie. Ionic Influences on Recombination in Perovskite Solar Cells. *ACS Energy Letters*, **2**, 7, 1683 (2017). doi: 10.1021/acsenergylett.7b00490.

[236] D. A. Jacobs, Y. Wu, H. Shen, C. Barugkin, F. J. Beck, T. P. White, K. Weber and K. R. Catchpole. Hysteresis Phenomena in Perovskite Solar Cells: The Many and Varied Effects of Ionic Accumulation. *Physical Chemistry Chemical Physics*, **19**, 4, 3094 (2017). doi: 10.1039/C6CP06989D.

[237] A. Pockett, G. E. Eperon, N. Sakai, H. J. Snaith, L. M. Peter and P. J. Cameron. Microseconds, Milliseconds and Seconds: Deconvoluting the Dynamic Behaviour of Planar Perovskite Solar Cells. *Physical Chemistry Chemical Physics*, **19**, 8, 5959 (2017). doi: 10.1039/C6CP08424A.

[238] D. W. Ferdani, S. R. Pering, D. Ghosh, P. Kubiak, A. B. Walker, S. E. Lewis, A. L. Johnson, P. J. Baker, M. S. Islam and P. J. Cameron. Partial Cation Substitution Reduces Iodide Ion Transport in Lead Iodide Perovskite Solar Cells. *Energy & Environmental Science*, **12**, 7, 2264 (2019). doi: 10.1039/C9EE00476A.

[239] Y. Hou, S. Scheiner, X. Tang, N. Gasparini, M. Richter, N. Li, P. Schweizer, S. Chen, H. Chen, C. O. R. Quiroz, X. Du, G. J. Matt, A. Osvet, E. Spiecker, R. H. Fink, A. Hirsch, M. Halik and C. J. Brabec. Suppression of Hysteresis Effects in Organohalide Perovskite Solar Cells. *Advanced Materials Interfaces*, **4**, 11, 1700007 (2017). doi: 10.1002/admi.201700007.

[240] D. Yang, R. Yang, K. Wang, C. Wu, X. Zhu, J. Feng, X. Ren, G. Fang, S. Priya and S. Liu. High Efficiency Planar-Type Perovskite Solar Cells with Negligible Hysteresis Using EDTA-Complexed SnO_2. *Nature Communications*, **9**, 1, 3239 (2018). doi: 10.1038/s41467-018-05760-x.

[241] R. S. Sanchez, V. Gonzalez-Pedro, J.-W. Lee, N.-G. Park, Y. S. Kang, I. Mora-Sero and J. Bisquert. Slow Dynamic Processes in Lead Halide Perovskite Solar Cells. Characteristic Times and Hysteresis. *The Journal of Physical Chemistry Letters*, **5**, 13, 2357 (2014). doi: 10.1021/jz5011187.

[242] Y. Rong, Y. Hu, S. Ravishankar, H. Liu, X. Hou, Y. Sheng, A. Mei, Q. Wang, D. Li, M. Xu, J. Bisquert and H. Han. Tunable Hysteresis Effect for Perovskite Solar Cells. *Energy & Environmental Science*, **10**, 11, 2383 (2017). doi: 10.1039/C7EE02048A.

[243] Z. L. Zhang, B. Q. Men, Y. F. Liu, H. P. Gao and Y. L. Mao. Effects of Precursor Solution Composition on the Performance and I-V Hysteresis of Perovskite Solar Cells Based on $CH_3NH_3PbI_{3-x}Cl_x$. *Nanoscale Research Letters*, **12**, 1, 84 (2017). doi: 10.1186/s11671-017-1872-8.

[244] Z. Li, J. Tinkham, P. Schulz, M. Yang, D. H. Kim, J. Berry, A. Sellinger and K. Zhu. Acid Additives Enhancing the Conductivity of Spiro-OMeTAD Toward High-Efficiency and Hysteresis-Less Planar Perovskite Solar Cells. *Advanced Energy Materials*, **7**, 4, 1601451 (2017). doi: 10.1002/aenm.201601451.

[245] S. N. Habisreutinger, N. K. Noel and H. J. Snaith. Hysteresis Index: A Figure without Merit for Quantifying Hysteresis in Perovskite Solar Cells. *ACS Energy Letters*, **3**, 10, 2472 (2018). doi: 10.1021/acsenergylett.8b01627.

[246] J. A. Christians, J. S. Manser and P. V. Kamat. Best Practices in Perovskite Solar Cell Efficiency Measurements. Avoiding the Error of Making Bad Cells Look Good. *The Journal of Physical Chemistry Letters*, **6**, 5, 852 (2015). doi: 10.1021/acs.jpclett.5b00289.

[247] E. Zimmermann, K. K. Wong, M. Müller, H. Hu, P. Ehrenreich, M. Kohlstädt, U. Würfel, S. Mastroianni, G. Mathiazhagan, A. Hinsch, T. P. Gujar, M. Thelakkat, T. Pfadler and L. Schmidt-Mende. Characterization of Perovskite Solar Cells: Towards a Reliable Measurement Protocol. *APL Materials*, **4**, 9, 091901 (2016). doi: 10.1063/1.4960759.

[248] Y. Wang, X. Liu, Z. Zhou, P. Ru, H. Chen, X. Yang and L. Han. Reliable Measurement of Perovskite Solar Cells. *Advanced Materials*, **31**, 47, 1803231 (2019). doi: 10.1002/adma.201803231.

[249] A. Förtig, J. Kniepert, M. Gluecker, T. Brenner, V. Dyakonov, D. Neher and C. Deibel. Nongeminate and Geminate Recombination in PTB7:PCBM Solar Cells. *Advanced Functional Materials*, **24**, 9, 1306 (2014). doi: 10.1002/adfm.201302134.

[250] Z. Wang, Q. Lin, B. Wenger, M. G. Christoforo, Y.-H. Lin, M. T. Klug, M. B. Johnston, L. M. Herz and H. J. Snaith. High Irradiance Performance of Metal Halide Perovskites for Concentrator Photovoltaics. *Nature Energy*, **3**, 10, 855 (2018). doi: 10.1038/s41560-018-0220-2.

[251] W. Shockley and W. T. Read. Statistics of the Recombinations of Holes and Electrons. *Physical Review*, **87**, 5, 835 (1952). doi: 10.1103/PhysRev.87.835.

[252] R. N. Hall. Electron-Hole Recombination in Germanium. *Physical Review*, **87**, 2, 387 (1952). doi: 10.1103/PhysRev.87.387.

[253] J. Nelson. *The Physics of Solar Cells*. Imperial College Press (2003). doi: 10.1142/p276.

[254] T. Kirchartz, D. Abou-Ras and U. Rau. *Introduction to Thin-Film Photovoltaics*, 1–32. Wiley-VCH Verlag GmbH Co. KGaA, Weinheim (2011). doi: 10.1002/9783527636280.ch1.

[255] N. G. Park, M. Grätzel and T. Miyasaka. *Organic-Inorganic Halide Perovskite Photovoltaics: From Fundamentals to Device Architectures*. Springer Nature (2016). doi: 10.1007/978-3-319-35114-8.

[256] T. Kirchartz, T. Markvart, U. Rau and D. A. Egger. Impact of Small Phonon Energies on the Charge-Carrier Lifetimes in Metal-Halide Perovskites. *The Journal of Physical Chemistry Letters*, **9**, 5, 939 (2018). doi: 10.1021/acs.jpclett.7b03414.

[257] T. Kirchartz, L. Krückemeier and E. L. Unger. Research Update: Recombination and Open-Circuit Voltage in Lead-Halide Perovskites. *APL Materials*, **6**, 10, 100702 (2018). doi: 10.1063/1.5052164.

[258] K. Huang, A. Rhys and N. F. Mott. Theory of Light Absorption and Non-Radiative Transitions in F-Centres. *Proceedings of the Royal Society of London. Series A. Mathematical and Physical Sciences*, **204**, 1078, 406 (1950). doi: 10.1098/rspa.1950.0184.

[259] R. Kubo and Y. Toyozawa. Application of the Method of Generating Function to Radiative and Non-Radiative Transitions of a Trapped Electron in a Crystal. *Progress of Theoretical Physics*, **13**, 2, 160 (1955). doi: 10.1143/ptp.13.160.

[260] B. K. Ridley. Multiphonon, Non-Radiative Transition Rate for Electrons in Semiconductors and Insulators. *Journal of Physics C: Solid State Physics*, **11**, 11, 2323 (1978). doi: 10.1088/0022-3719/11/11/023.

[261] G. D. Watkins. Defect Metastability and Bistability. *Materials Science Forum*, **38-41**, 39 (1989). doi: 10.4028/www.scientific.net/MSF.38-41.39.

[262] H. J. Queisser and E. E. Haller. Defects in Semiconductors: Some Fatal, Some Vital. *Science*, **281**, 5379, 945 (1998). doi: 10.1126/science.281.5379.945.

[263] J. Kim, S.-H. Lee, J. H. Lee and K.-H. Hong. The Role of Intrinsic Defects in Methylammonium Lead Iodide Perovskite. *The Journal of Physical Chemistry Letters*, **5**, 8, 1312 (2014). doi: 10.1021/jz500370k.

[264] W.-J. Yin, T. Shi and Y. Yan. Unusual Defect Physics in $CH_3NH_3PbI_3$ Perovskite Solar Cell Absorber. *Applied Physics Letters*, **104**, 6, 063903 (2014). doi: 10.1063/1.4864778.

[265] M.-H. Du. Density Functional Calculations of Native Defects in $CH_3NH_3PbI_3$: Effects of Spin–Orbit Coupling and Self-Interaction Error. *The Journal of Physical Chemistry Letters*, **6**, 8, 1461 (2015). doi: 10.1021/acs.jpclett.5b00199.

[266] W.-J. Yin, H. Chen, T. Shi, S.-H. Wei and Y. Yan. Origin of High Electronic Quality in Structurally Disordered $CH_3NH_3PbI_3$ and the Passivation Effect of Cl and O at Grain Boundaries. *Advanced Electronic Materials*, **1**, 6, 1500044 (2015). doi: 10.1002/aelm.201500044.

[267] H. Uratani and K. Yamashita. Charge Carrier Trapping at Surface Defects of Perovskite Solar Cell Absorbers: A First-Principles Study. *The Journal of Physical Chemistry Letters*, **8**, 4, 742 (2017). doi: 10.1021/acs.jpclett.7b00055.

[268] A. Baumann, S. Väth, P. Rieder, M. C. Heiber, K. Tvingstedt and V. Dyakonov. Identification of Trap States in Perovskite Solar Cells. *The Journal of Physical Chemistry Letters*, **6**, 12, 2350 (2015). doi: 10.1021/acs.jpclett.5b00953.

[269] G. Gordillo, C. A. Otálora and M. A. Reinoso. Trap Center Study in Hybrid Organic-Inorganic Perovskite Using Thermally Stimulated Current (TSC) Analysis. *Journal of Applied Physics*, **122**, 7, 075304 (2017). doi: 10.1063/1.4999297.

[270] H.-S. Duan, H. Zhou, Q. Chen, P. Sun, S. Luo, T.-B. Song, B. Bob and Y. Yang. The Identification and Characterization of Defect States in Hybrid Organic-Inorganic Perovskite Photovoltaics. *Physical Chemistry Chemical Physics*, **17**, 1, 112 (2015). doi: 10.1039/C4CP04479G.

[271] M. Samiee, S. Konduri, B. Ganapathy, R. Kottokkaran, H. A. Abbas, A. Kitahara, P. Joshi, L. Zhang, M. Noack and V. Dalal. Defect Density and Dielectric Constant in Perovskite Solar Cells. *Applied Physics Letters*, **105**, 15, 153502 (2014). doi: 10.1063/1.4897329.

[272] M. Yang, Y. Zeng, Z. Li, D. H. Kim, C.-S. Jiang, J. van de Lagemaat and K. Zhu. Do Grain Boundaries Dominate Non-Radiative Recombination in $CH_3NH_3PbI_3$ Perovskite Thin Films? *Physical Chemistry Chemical Physics*, **19**, 7, 5043 (2017). doi: 10.1039/C6CP08770A.

[273] V. Adinolfi, M. Yuan, R. Comin, E. S. Thibau, D. Shi, M. I. Saidaminov, P. Kanjanaboos, D. Kopilovic, S. Hoogland, Z.-H. Lu, O. M. Bakr and E. H. Sargent. The In-Gap Electronic State Spectrum of Methylammonium Lead Iodide Single-Crystal Perovskites. *Advanced Materials*, **28**, 17, 3406 (2016). doi: 10.1002/adma.201505162.

[274] H. Jin, E. Debroye, M. Keshavarz, I. G. Scheblykin, M. B. J. Roeffaers, J. Hofkens and J. A. Steele. It's a Trap! On the Nature of Localised States and Charge Trapping in Lead Halide Perovskites. *Materials Horizons* (2019). doi: 10.1039/C9MH00500E.

[275] A. Zakutayev, C. M. Caskey, A. N. Fioretti, D. S. Ginley, J. Vidal, V. Stevanovic, E. Tea and S. Lany. Defect Tolerant Semiconductors for Solar Energy Conversion. *The Journal of Physical Chemistry Letters*, **5**, 7, 1117 (2014). doi: 10.1021/jz5001787.

[276] J. Benduhn, K. Tvingstedt, F. Piersimoni, S. Ullbrich, Y. Fan, M. Tropiano, K. A. McGarry, O. Zeika, M. K. Riede, C. J. Douglas, S. Barlow, S. R. Marder, D. Neher, D. Spoltore and K. Vandewal. Intrinsic Non-Radiative Voltage Losses in Fullerene-Based Organic Solar Cells. *Nature Energy*, **2**, 17053 (2017). doi: 10.1038/nenergy.2017.53.

[277] W. van Roosbroeck and W. Shockley. Photon-Radiative Recombination of Electrons and Holes in Germanium. *Physical Review*, **94**, 6, 1558 (1954). doi: 10.1103/PhysRev.94.1558.

[278] C. L. Davies, M. R. Filip, J. B. Patel, T. W. Crothers, C. Verdi, A. D. Wright, R. L. Milot, F. Giustino, M. B. Johnston and L. M. Herz. Bimolecular Recombination in Methylammonium Lead Triiodide Perovskite is an Inverse Absorption Process. *Nature Communications*, **9**, 1, 293 (2018). doi: 10.1038/s41467-017-02670-2.

[279] R. Brenes, D. Guo, A. Osherov, N. K. Noel, C. Eames, E. M. Hutter, S. K. Pathak, F. Niroui, R. H. Friend, M. S. Islam, H. J. Snaith, V. Bulović, T. J. Savenije and S. D. Stranks. Metal Halide Perovskite Polycrystalline Films Exhibiting Properties of Single Crystals. *Joule*, **1**, 1, 155 (2017). doi: 10.1016/j.joule.2017.08.006.

[280] T. Trupke, M. A. Green, P. Würfel, P. P. Altermatt, A. Wang, J. Zhao and R. Corkish. Temperature Dependence of the Radiative Recombination Coefficient of Intrinsic Crystalline Silicon. *Journal of Applied Physics*, **94**, 8, 4930 (2003). doi: 10.1063/1.1610231.

[281] E. M. Hutter, M. C. Gélvez-Rueda, A. Osherov, V. Bulović, F. C. Grozema, S. D. Stranks and T. J. Savenije. Direct–Indirect Character of the Bandgap in Methylammonium Lead Iodide Perovskite. *Nature Materials*, **16**, 115 (2016). doi: 10.1038/nmat4765.

[282] F. Zheng, L. Z. Tan, S. Liu and A. M. Rappe. Rashba Spin–Orbit Coupling Enhanced Carrier Lifetime in $CH_3NH_3PbI_3$. *Nano Letters*, **15**, 12, 7794 (2015). doi: 10.1021/acs.nanolett.5b01854.

[283] D. W. deQuilettes, K. Frohna, D. Emin, T. Kirchartz, V. Bulovic, D. S. Ginger and S. D. Stranks. Charge-Carrier Recombination in Halide Perovskites. *Chemical Reviews*, **119**, 20, 11007 (2019). doi: 10.1021/acs.chemrev.9b00169.

[284] J. M. Richter, K. Chen, A. Sadhanala, J. Butkus, J. P. H. Rivett, R. H. Friend, B. Monserrat, J. M. Hodgkiss and F. Deschler. Direct Bandgap Behavior in Rashba-Type Metal Halide Perovskites. *Advanced Materials*, **30**, 52, 1803379 (2018). doi: 10.1002/adma.201803379.

[285] L. M. Pazos-Outón, M. Szumilo, R. Lamboll, J. M. Richter, M. Crespo-Quesada, M. Abdi-Jalebi, H. J. Beeson, M. Vrućinić, M. Alsari, H. J. Snaith, B. Ehrler, R. H. Friend and F. Deschler. Photon Recycling in Lead Iodide Perovskite Solar Cells. *Science*, **351**, 6280, 1430 (2016). doi: 10.1126/science.aaf1168.

[286] J. M. Richter, M. Abdi-Jalebi, A. Sadhanala, M. Tabachnyk, J. P. H. Rivett, L. M. Pazos-Outón, K. C. Gödel, M. Price, F. Deschler and R. H. Friend. Enhancing Photoluminescence Yields in Lead Halide Perovskites by Photon Recycling and Light Out-Coupling. *Nature Communications*, **7**, 13941 (2016). doi: 10.1038/ncomms13941.

[287] T. Kirchartz, F. Staub and U. Rau. Impact of Photon Recycling on the Open-Circuit Voltage of Metal Halide Perovskite Solar Cells. *ACS Energy Letters*, **1**, 4, 731 (2016). doi: 10.1021/acsenergylett.6b00223.

[288] T. W. Crothers, R. L. Milot, J. B. Patel, E. S. Parrott, J. Schlipf, P. Müller-Buschbaum, M. B. Johnston and L. M. Herz. Photon Reabsorption Masks Intrinsic Bimolecular Charge-Carrier Recombination in $CH_3NH_3PbI_3$ Perovskite. *Nano Letters*, **17**, 9, 5782 (2017). doi: 10.1021/acs.nanolett.7b02834.

[289] W. Shockley and H. J. Queisser. Detailed Balance Limit of Efficiency of p-n Junction Solar Cells. *Journal of Applied Physics*, **32**, 3, 510 (1961). doi: 10.1063/1.1736034.

[290] L. M. Herz. Charge-Carrier Dynamics in Organic-Inorganic Metal Halide Perovskites. *Annual Review of Physical Chemistry*, **67**, 1, 65 (2016). doi: 10.1146/annurev-physchem-040215-112222.

[291] J. L. Gray. *The Physics of the Solar Cell.* John Wiley Sons, Ltd (2011). doi: 10.1002/9780470974704.ch3.

[292] T. Kirchartz. High Open-Circuit Voltages in Lead-Halide Perovskite Solar Cells: Experiment, Theory and Open Questions. *Philosophical Transactions of the Royal Society A: Mathematical, Physical and Engineering Sciences*, **377**, 2152, 20180286 (2019). doi: 10.1098/rsta.2018.0286.

[293] J. R. Poindexter, E. S. Barnard, R. C. Kurchin and T. Buonassisi. Charge-Carrier Lifetime Measurements in Early-Stage Photovoltaic Materials: Intuition, Uncertainties, and Opportunities. *arXiv preprint*, **arXiv:1805.05832** (2018).

[294] A. Pivrikas, B. Philippa, R. D. White and G. Juska. Photocarrier Lifetime and Recombination Losses in Photovoltaic Systems. *Nature Photonics*, **10**, 282 (2016). doi: 10.1038/nphoton.2016.78.

[295] S. D. Stranks and A. Petrozza. Revisiting Photocarrier Lifetimes in Photovoltaics. *Nature Photonics*, **10**, 9, 562 (2016). doi: 10.1038/nphoton.2016.164.

[296] W. Tress. *Maximum Efficiency and Open-Circuit Voltage of Perovskite Solar Cells*. Springer International Publishing, Cham (2016). doi: 10.1007/978-3-319-35114-8$_3$.

[297] C. M. Wolff, P. Caprioglio, M. Stolterfoht and D. Neher. Nonradiative Recombination in Perovskite Solar Cells: The Role of Interfaces. *Advanced Materials*, **31**, 52, 1902762 (2019). doi: 10.1002/adma.201902762.

[298] P. Calado, D. Burkitt, J. Yao, J. Troughton, T. M. Watson, M. J. Carnie, A. M. Telford, B. C. O'Regan, J. Nelson and P. R. F. Barnes. Identifying Dominant Recombination Mechanisms in Perovskite Solar Cells by Measuring the Transient Ideality Factor. *Physical Review Applied*, **11**, 4, 044005 (2019). doi: 10.1103/PhysRevApplied.11.044005.

[299] T. Kirchartz, K. Ding and U. Rau. *Fundamental Electrical Characterization of Thin-Film Solar Cells*. Wiley-VCH Verlag GmbH Co. (2016). doi: 10.1002/9783527636280.ch2.

[300] B. C. O'Regan, P. R. F. Barnes, X. Li, C. Law, E. Palomares and J. M. Marin-Beloqui. Optoelectronic Studies of Methylammonium Lead Iodide Perovskite Solar Cells with Mesoporous TiO_2: Separation of Electronic and Chemical Charge Storage, Understanding Two Recombination Lifetimes, and the Evolution of Band Offsets during J–V Hysteresis. *Journal of the American Chemical Society*, **137**, 15, 5087 (2015). doi: 10.1021/jacs.5b00761.

[301] A. Rajagopal, K. Yao and A. K.-Y. Jen. Toward Perovskite Solar Cell Commercialization: A Perspective and Research Roadmap Based on Interfacial Engineering. *Advanced Materials*, **30**, 32, 1800455 (2018). doi: 10.1002/adma.201800455.

[302] O. Malinkiewicz, A. Yella, Y. H. Lee, G. M. Espallargas, M. Graetzel, M. K. Nazeeruddin and H. J. Bolink. Perovskite Solar Cells Employing Organic Charge-Transport Layers. *Nature Photonics*, **8**, 2, 128 (2014). doi: 10.1038/nphoton.2013.341.

[303] B. Dänekamp, N. Droseros, D. Tsokkou, V. Brehm, P. P. Boix, M. Sessolo, N. Banerji and H. J. Bolink. Influence of Hole Transport Material Ionization Energy on the Performance of Perovskite Solar Cells. *Journal of Materials Chemistry C*, **7**, 3, 523 (2019). doi: 10.1039/C8TC05372C.

[304] A. Rockett. *The Materials Science of Semiconductors*. Springer Science+Business Media, Boston (2008). doi: 10.1007/978-0-387-68650-9.

[305] C. Momblona, L. Gil-Escrig, E. Bandiello, E. M. Hutter, M. Sessolo, K. Lederer, J. Blochwitz-Nimoth and H. J. Bolink. Efficient Vacuum Deposited p-i-n and n-i-p Perovskite Solar Cells Employing Doped Charge Transport Layers. *Energy & Environmental Science*, **9**, 11, 3456 (2016). doi: 10.1039/C6EE02100J.

[306] F. Palazon, D. Pérez-del Rey, B. Dänekamp, C. Dreessen, M. Sessolo, P. P. Boix and H. J. Bolink. Room-Temperature Cubic Phase Crystallization and High Stability of Vacuum-Deposited Methylammonium Lead Triiodide Thin Films for High-Efficiency Solar Cells. *Advanced Materials*, **31**, 39, 1902692 (2019). doi: 10.1002/adma.201902692.

[307] D. Zhao, M. Sexton, H.-Y. Park, G. Baure, J. C. Nino and F. So. High-Efficiency Solution-Processed Planar Perovskite Solar Cells with a Polymer Hole Transport Layer. *Advanced Energy Materials*, **5**, 6, 1401855 (2015). doi: 10.1002/aenm.201401855.

[308] J. Lee, H. Kang, G. Kim, H. Back, J. Kim, S. Hong, B. Park, E. Lee and K. Lee. Achieving Large-Area Planar Perovskite Solar Cells by Introducing an Interfacial Compatibilizer. *Advanced Materials*, **29**, 22, 1606363 (2017). doi: 10.1002/adma.201606363.

[309] Q. J. Sun, J. H. Hou, C. H. Yang, Y. F. Li and Y. Yang. Enhanced Performance of White Polymer Light-Emitting Diodes Using Polymer Blends as Hole-Transporting Layers. *Applied Physics Letters*, **89**, 15, 153501 (2006). doi: 10.1063/1.2360248.

[310] X. Xu, C. Ma, Y. Cheng, Y.-M. Xie, X. Yi, B. Gautam, S. Chen, H.-W. Li, C.-S. Lee, F. So and S.-W. Tsang. Ultraviolet-Ozone Surface Modification for Non-Wetting Hole Transport Materials Based Inverted Planar Perovskite Solar Cells with Efficiency Exceeding 18%. *Journal of Power Sources*, **360**, 157 (2017). doi: 10.1016/j.jpowsour.2017.06.013.

[311] J. Höcker, D. Kiermasch, P. Rieder, K. Tvingstedt, A. Baumann and V. Dyakonov. Efficient Solution Processed $CH_3NH_3PbI_3$ Perovskite Solar Cells with PolyTPD Hole Transport Layer. *Zeitschrift für Naturforschung A*, **74**, 8, 665 (2019). doi: 10.1515/zna-2019-0127.

[312] B. J. Worfolk, S. C. Andrews, S. Park, J. Reinspach, N. Liu, M. F. Toney, S. C. B. Mannsfeld and Z. Bao. Ultrahigh Electrical Conductivity in Solution-Sheared Polymeric Transparent Films. *Proceedings of the National Academy of Sciences of the United States of America*, **112**, 46, 14138 (2015). doi: 10.1073/pnas.1509958112.

[313] M. Petrosino, P. Vacca, R. Miscioscia, G. Nenna, C. Minarini and A. Rubino. Effect of PEDOT:PSS Ratio on the Electrical and Optical Properties of OLEDs. *Microtechnologies for the New Millennium*, **6593** (2007). doi: 10.1117/12.722022.

[314] F. Zabihi, Y. Xie, S. Gao and M. Eslamian. Morphology, Conductivity, and Wetting Characteristics of PEDOT:PSS Thin Films Deposited by Spin and Spray Coating. *Applied Surface Science*, **338**, 163 (2015). doi: 10.1016/j.apsusc.2015.02.128.

[315] K. Sun, S. Zhang, P. Li, Y. Xia, X. Zhang, D. Du, F. H. Isikgor and J. Ouyang. Review on Application of PEDOTs and PEDOT:PSS in Energy Conversion and Storage Devices. *Journal of Materials Science: Materials in Electronics*, **26**, 7, 4438 (2015). doi: 10.1007/s10854-015-2895-5.

[316] K. M. Reza, S. Mabrouk and Q. Qiao. A Review on Tailoring PEDOT:PSS Layer for Improved Performance of Perovskite Solar Cells. *Proceedings of the Nature Research Society*, **2**, 02004 (2018). doi: 10.11605/j.pnrs.201802004.

[317] H. W. Kroto, J. R. Heath, S. C. O'Brien, R. F. Curl and R. E. Smalley. C_{60}: Buckminsterfullerene. *Nature*, **318**, 6042, 162 (1985). doi: 10.1038/318162a0.

[318] W. Krätschmer, L. D. Lamb, K. Fostiropoulos and D. R. Huffman. Solid C_{60}: a New Form of Carbon. *Nature*, **347**, 6291, 354 (1990). doi: 10.1038/347354a0.

[319] H. Ajie, M. M. Alvarez, S. J. Anz, R. D. Beck, F. Diederich, K. Fostiropoulos, D. R. Huffman, W. Kraetschmer and Y. Rubin. Characterization of the Soluble All-Carbon Molecules C_{60} and C_{70}. *The Journal of Physical Chemistry*, **94**, 24, 8630 (1990). doi: 10.1021/j100387a004.

[320] N. Mendil, M. Daoudi, Z. Berkai and A. Belghachi. Disorder Effect on Carrier Mobility in Fullerene Organic Semiconductor. *Journal of Physics: Conference Series*, **647**, 012057 (2015). doi: 10.1088/1742-6596/647/1/012057.

[321] A. B. Sieval and J. C. Hummelen. *Fullerene-Based Acceptor Materials*, 209–238. Wiley-VCH Verlag GmbH Co. KGaA (2014). doi: 10.1002/9783527656912.ch07.

[322] P. Peumans, A. Yakimov and S. R. Forrest. Small Molecular Weight Organic Thin-Film Photodetectors and Solar Cells. *Journal of Applied Physics*, **93**, 7, 3693 (2003). doi: 10.1063/1.1534621.

[323] T. Rabenau, A. Simon, R. K. Kremer and E. Sohmen. The Energy Gaps of Fullerene C_{60} and C_{70} Determined from the Temperature Dependent Microwave Conductivity. *Zeitschrift für Physik B Condensed Matter*, **90**, 1, 69 (1993). doi: 10.1007/bf01321034.

[324] J. C. Hummelen, B. W. Knight, F. LePeq, F. Wudl, J. Yao and C. L. Wilkins. Preparation and Characterization of Fulleroid and Methanofullerene Derivatives. *The Journal of Organic Chemistry*, **60**, 3, 532 (1995). doi: 10.1021/jo00108a012.

[325] V. Mihailetchi, J. van Duren, P. Blom, J. Hummelen, R. Janssen, J. Kroon, M. Rispens, W. Verhees and M. Wienk. Electron Transport in a Methanofullerene. *Advanced Functional Materials*, **13**, 1, 43 (2003). doi: 10.1002/adfm.200390004.

[326] P. Peumans and S. R. Forrest. Very-High-Efficiency Double-Heterostructure Copper Phthalocyanine/C_{60} Photovoltaic Cells. *Applied Physics Letters*, **79**, 1, 126 (2001). doi: 10.1063/1.1384001.

[327] C. Chen, S. Zhang, S. Wu, W. Zhang, H. Zhu, Z. Xiong, Y. Zhang and W. Chen. Effect of BCP Buffer Layer on Eliminating Charge Accumulation for High Performance of Inverted Perovskite Solar Cells. *RSC Advances*, **7**, 57, 35819 (2017). doi: 10.1039/C7RA06365B.

[328] N. Shibayama, H. Kanda, T. W. Kim, H. Segawa and S. Ito. Design of BCP Buffer Layer for Inverted Perovskite Solar Cells Using Ideal Factor. *APL Materials*, **7**, 3, 031117 (2019). doi: 10.1063/1.5087796.

[329] H. Kim, C. M. Gilmore, A. Piqué, J. S. Horwitz, H. Mattoussi, H. Murata, Z. H. Kafafi and D. B. Chrisey. Electrical, Optical, and Structural Properties of Indium–Tin–Oxide Thin Films for Organic Light-Emitting Devices. *Journal of Applied Physics*, **86**, 11, 6451 (1999). doi: 10.1063/1.371708.

[330] M. Xiao, F. Huang, W. Huang, Y. Dkhissi, Y. Zhu, J. Etheridge, A. Gray-Weale, U. Bach, Y.-B. Cheng and L. Spiccia. A Fast Deposition-Crystallization Procedure for Highly Efficient Lead Iodide Perovskite Thin-Film Solar Cells. *Angewandte Chemie International Edition*, **53**, 37, 9898 (2014). doi: 10.1002/anie.201405334.

[331] N. J. Jeon, J. H. Noh, Y. C. Kim, W. S. Yang, S. Ryu and S. I. Seok. Solvent Engineering for High-Performance Inorganic–Organic Hybrid Perovskite Solar Cells. *Nature Materials*, **13**, 897 (2014). doi: 10.1038/nmat4014.

[332] N. Ahn, D.-Y. Son, I.-H. Jang, S. M. Kang, M. Choi and N.-G. Park. Highly Reproducible Perovskite Solar Cells with Average Efficiency of 18.3% and Best Efficiency of 19.7% Fabricated via Lewis Base Adduct of Lead(II) Iodide. *Journal of the American Chemical Society*, **137**, 27, 8696 (2015). doi: 10.1021/jacs.5b04930.

[333] M. Saliba, J.-P. Correa-Baena, C. M. Wolff, M. Stolterfoht, N. Phung, S. Albrecht, D. Neher and A. Abate. How to Make over 20% Efficient Perovskite Solar Cells in Regular (n–i–p) and Inverted (p–i–n) Architectures. *Chemistry of Materials*, **30**, 13, 4193 (2018). doi: 10.1021/acs.chemmater.8b00136.

[334] Z. Xiao, C. Bi, Y. Shao, Q. Dong, Q. Wang, Y. Yuan, C. Wang, Y. Gao and J. Huang. Efficient, High Yield Perovskite Photovoltaic Devices Grown by Interdiffusion of Solution-Processed Precursor Stacking Layers. *Energy & Environmental Science*, **7**, 8, 2619 (2014). doi: 10.1039/C4EE01138D.

[335] Y. Xie, F. Shao, Y. Wang, T. Xu, D. Wang and F. Huang. Enhanced Performance of Perovskite $CH_3NH_3PbI_3$ Solar Cell by Using CH_3NH_3I as Additive in Sequential Deposition. *ACS Applied Materials Interfaces*, **7**, 23, 12937 (2015). doi: 10.1021/acsami.5b02705.

[336] T. Zhang, M. Yang, Y. Zhao and K. Zhu. Controllable Sequential Deposition of Planar $CH_3NH_3PbI_3$ Perovskite Films via Adjustable Volume Expansion. *Nano Letters*, **15**, 6, 3959 (2015). doi: 10.1021/acs.nanolett.5b00843.

[337] J. Ávila, C. Momblona, P. P. Boix, M. Sessolo and H. J. Bolink. Vapor-Deposited Perovskites: The Route to High-Performance Solar Cell Production? *Joule*, **1**, 3, 431 (2017). doi: 10.1016/j.joule.2017.07.014.

[338] S. R. Lederhandler and L. J. Giacoletto. Measurement of Minority Carrier Lifetime and Surface Effects in Junction Devices. *Proceedings of the IRE*, **43**, 4, 477 (1955). doi: 10.1109/JRPROC.1955.277857.

[339] N. W. Duffy, L. M. Peter, R. M. G. Rajapakse and K. G. U. Wijayantha. Investigation of the Kinetics of the Back Reaction of Electrons with Tri-Iodide in Dye-Sensitized Nanocrystalline Photovoltaic Cells. *The Journal of Physical Chemistry B*, **104**, 38, 8916 (2000). doi: 10.1021/jp001185z.

[340] A. Zaban, M. Greenshtein and J. Bisquert. Determination of the Electron Lifetime in Nanocrystalline Dye Solar Cells by Open-Circuit Voltage Decay Measurements. *ChemPhysChem*, **4**, 8, 859 (2003). doi: 10.1002/cphc.200200615.

[341] K. Sudheendra Rao and Y. N. Mohapatra. Open Circuit Voltage Decay Transients and Recombination in Bulk-Heterojunction Solar Cells. *Applied Physics Letters*, **104**, 20, 203303 (2014). doi: 10.1063/1.4879278.

[342] A. Baumann, K. Tvingstedt, M. C. Heiber, S. Väth, C. Momblona, H. J. Bolink and V. Dyakonov. Persistent Photovoltage in Methylammonium Lead Iodide Perovskite Solar Cells. *APL Materials*, **2**, 8, 081501 (2014). doi: 10.1063/1.4885255.

[343] P. G. Wilson. Recombination in Silicon p-π-n Diodes. *Solid-State Electronics*, **10**, 2, 145 (1967). doi: 10.1016/0038-1101(67)90032-9.

[344] P. R. F. Barnes, K. Miettunen, X. Li, A. Y. Anderson, T. Bessho, M. Grätzel and B. C. O'Regan. Interpretation of Optoelectronic Transient and Charge Extraction Measurements in Dye-Sensitized Solar Cells. *Advanced Materials*, **25**, 13, 1881 (2013). doi: 10.1002/adma.201201372.

[345] D. T. Stevenson and R. J. Keyes. Measurement of Carrier Lifetimes in Germanium and Silicon. *Journal of Applied Physics*, **26**, 2, 190 (1955). doi: 10.1063/1.1721958.

[346] C. G. Shuttle, B. O'Regan, A. M. Ballantyne, J. Nelson, D. D. C. Bradley, J. de Mello and J. R. Durrant. Experimental Determination of the Rate Law for Charge Carrier Decay in a Polythiophene: Fullerene Solar Cell. *Applied Physics Letters*, **92**, 9, 093311 (2008). doi: 10.1063/1.2891871.

[347] A. Maurano, C. G. Shuttle, R. Hamilton, A. M. Ballantyne, J. Nelson, W. Zhang, M. Heeney and J. R. Durrant. Transient Optoelectronic Analysis of Charge Carrier Losses in a Selenophene/Fullerene Blend Solar Cell. *The Journal of Physical Chemistry C*, **115**, 13, 5947 (2011). doi: 10.1021/jp109697w.

[348] V. Roiati, S. Colella, G. Lerario, L. De Marco, A. Rizzo, A. Listorti and G. Gigli. Investigating Charge Dynamics in Halide Perovskite-Sensitized Mesostructured Solar Cells. *Energy & Environmental Science*, **7**, 6, 1889 (2014). doi: 10.1039/C3EE43991G.

[349] C. Law, L. Miseikis, S. Dimitrov, P. Shakya-Tuladhar, X. Li, P. R. F. Barnes, J. Durrant and B. C. O'Regan. Performance and Stability of Lead Perovskite/TiO_2, Polymer/PCBM, and Dye Sensitized Solar Cells at Light Intensities up to 70 Suns. *Advanced Materials*, **26**, 36, 6268 (2014). doi: 10.1002/adma.201402612.

[350] P. R. F. Barnes, A. Y. Anderson, M. Juozapavicius, L. Liu, X. Li, E. Palomares, A. Forneli and B. C. O'Regan. Factors Controlling Charge Recombination under Dark and Light Conditions in Dye Sensitised Solar Cells. *Physical Chemistry Chemical Physics*, **13**, 8, 3547 (2011). doi: 10.1039/C0CP01855D.

[351] T. M. Clarke, C. Lungenschmied, J. Peet, N. Drolet and A. J. Mozer. A Comparison of Five Experimental Techniques to Measure Charge Carrier Lifetime in Polymer/Fullerene Solar Cells. *Advanced Energy Materials*, **5**, 4, 1401345 (2015). doi: 10.1002/aenm.201401345.

[352] J. Jiménez-López and E. Palomares. Interfacial Recombination Kinetics in Aged Perovskite Solar Cells Measured Using Transient Photovoltage Techniques. *Nanoscale*, **11**, 42, 20024 (2019). doi: 10.1039/C9NR06278E.

[353] S. De, T. Pascher, M. Maiti, K. G. Jespersen, T. Kesti, F. Zhang, O. Inganäs, A. Yartsev and V. Sundström. Geminate Charge Recombination in Alternating Polyfluorene Copolymer/Fullerene Blends. *Journal of the American Chemical Society*, **129**, 27, 8466 (2007). doi: 10.1021/ja068909q.

[354] J.-F. Guillemoles, T. Kirchartz, D. Cahen and U. Rau. Guide for the Perplexed to the Shockley–Queisser Model for Solar Cells. *Nature Photonics*, **13**, 8, 501 (2019). doi: 10.1038/s41566-019-0479-2.

[355] K. Tvingstedt, L. Gil-Escrig, C. Momblona, P. Rieder, D. Kiermasch, M. Sessolo, A. Baumann, H. J. Bolink and V. Dyakonov. Removing Leakage and Surface Recombination in Planar Perovskite Solar Cells. *ACS Energy Letters*, **2**, 2, 424 (2017). doi: 10.1021/acsenergylett.6b00719.

[356] M. B. Johnston and L. M. Herz. Hybrid Perovskites for Photovoltaics: Charge-Carrier Recombination, Diffusion, and Radiative Efficiencies. *Accounts of Chemical Research*, **49**, 1, 146 (2016). doi: 10.1021/acs.accounts.5b00411.

[357] T. Leijtens, G. E. Eperon, A. J. Barker, G. Grancini, W. Zhang, J. M. Ball, A. R. S. Kandada, H. J. Snaith and A. Petrozza. Carrier Trapping and Recombination: The Role of Defect Physics in Enhancing the Open Circuit Voltage of Metal Halide Perovskite Solar Cells. *Energy & Environmental Science*, **9**, 11, 3472 (2016). doi: 10.1039/C6EE01729K.

[358] F. Staub, T. Kirchartz, K. Bittkau and U. Rau. Manipulating the Net Radiative Recombination Rate in Lead Halide Perovskite Films by Modification of Light Outcoupling. *The Journal of Physical Chemistry Letters*, **8**, 20, 5084 (2017). doi: 10.1021/acs.jpclett.7b02224.

[359] Y. Yamada, T. Nakamura, M. Endo, A. Wakamiya and Y. Kanemitsu. Photocarrier Recombination Dynamics in Perovskite $CH_3NH_3PbI_3$ for Solar Cell Applications. *Journal of the American Chemical Society*, **136**, 33, 11610 (2014). doi: 10.1021/ja506624n.

[360] C. M. Wolff, F. Zu, A. Paulke, L. P. Toro, N. Koch and D. Neher. Reduced Interface-Mediated Recombination for High Open-Circuit Voltages in $CH_3NH_3PbI_3$ Solar Cells. *Advanced Materials*, **29**, 28, 1700159 (2017). doi: 10.1002/adma.201700159.

[361] L. G. Kudriashova, D. Kiermasch, P. Rieder, M. Campbell, K. Tvingstedt, A. Baumann, G. V. Astakhov and V. Dyakonov. Impact of Interfaces and Laser Repetition Rate on Photocarrier Dynamics in Lead Halide Perovskites. *The Journal of Physical Chemistry Letters*, **8**, 19, 4698 (2017). doi: 10.1021/acs.jpclett.7b02087.

[362] Y. Bi, E. M. Hutter, Y. Fang, Q. Dong, J. Huang and T. J. Savenije. Charge Carrier Lifetimes Exceeding 15 μs in Methylammonium Lead Iodide Single Crystals. *The Journal of Physical Chemistry Letters*, **7**, 5, 923 (2016). doi: 10.1021/acs.jpclett.6b00269.

[363] L. Bertoluzzi, P. P. Boix, I. Mora-Sero and J. Bisquert. Theory of Impedance Spectroscopy of Ambipolar Solar Cells with Trap-Mediated Recombination. *The Journal of Physical Chemistry C*, **118**, 30, 16574 (2014). doi: 10.1021/jp411004e.

[364] I. Mora-Seró, G. Garcia-Belmonte, P. P. Boix, M. A. Vázquez and J. Bisquert. Impedance Spectroscopy Characterisation of Highly Efficient Silicon Solar Cells under Different Light Illumination Intensities. *Energy & Environmental Science*, **2**, 6, 678 (2009). doi: 10.1039/B812468J.

[365] L. Contreras-Bernal, S. Ramos-Terrón, A. Riquelme, P. P. Boix, J. Idígoras, I. Mora-Seró and J. A. Anta. Impedance Analysis of Perovskite Solar Cells: A Case Study. *Journal of Materials Chemistry A*, **7**, 19, 12191 (2019). doi: 10.1039/C9TA02808K.

[366] I. Zonno, H. Zayani, M. Grzeslo, B. Krogmeier and T. Kirchartz. Extracting Recombination Parameters from Impedance Measurements on Organic Solar Cells. *Physical Review Applied*, **11**, 5, 054024 (2019). doi: 10.1103/PhysRevApplied.11.054024.

[367] V. V. Brus, C. M. Proctor, N. A. Ran and T.-Q. Nguyen. Capacitance Spectroscopy for Quantifying Recombination Losses in Nonfullerene Small-Molecule Bulk Heterojunction Solar Cells. *Advanced Energy Materials*, **6**, 11, 1502250 (2016). doi: 10.1002/aenm.201502250.

[368] D. Jarzab, F. Cordella, J. Gao, M. Scharber, H.-J. Egelhaaf and M. A. Loi. Low-Temperature Behaviour of Charge Transfer Excitons in Narrow-Bandgap Polymer-Based Bulk Heterojunctions. *Advanced Energy Materials*, **1**, 4, 604 (2011). doi: 10.1002/aenm.201100083.

[369] A. J. Pearson, P. E. Hopkinson, E. Couderc, K. Domanski, M. Abdi-Jalebi and N. C. Greenham. Critical Light Instability in CB/DIO Processed PBDTTT-EFT:PC71BM Organic Photovoltaic Devices. *Organic Electronics*, **30**, 225 (2016). doi: 10.1016/j.orgel.2015.12.024.

[370] T. Du, J. Kim, J. Ngiam, S. Xu, P. R. Barnes, J. R. Durrant and M. A. McLachlan. Elucidating the Origins of Subgap Tail States and Open-Circuit Voltage in Methylammonium Lead Triiodide Perovskite Solar Cells. *Advanced Functional Materials*, **28**, 32, 1801808 (2018). doi: 10.1002/adfm.201801808.

[371] J.-S. Zhao, H.-Y. Wang, M. Yu, M.-Y. Hao, S. Yuan, Y. Qin, L.-M. Fu, J.-P. Zhang and X.-C. Ai. Charge Carrier Recombination Dynamics in a Bi-Cationic Perovskite Solar Cell. *Physical Chemistry Chemical Physics*, **21**, 10, 5409 (2019). doi: 10.1039/C8CP07461E.

[372] Hamamatsu S1787-04 Si Photodiode Product Overview. *URL: https://www.hamamatsu.com/eu/en/product/type/S1787-04/index.html* (accessed 20.11.2019).

[373] A. Pockett, G. E. Eperon, T. Peltola, H. J. Snaith, A. Walker, L. M. Peter and P. J. Cameron. Characterization of Planar Lead Halide Perovskite Solar Cells by Impedance Spectroscopy, Open-Circuit Photovoltage Decay, and Intensity-Modulated Photovoltage/Photocurrent Spectroscopy. *The Journal of Physical Chemistry C*, **119**, 7, 3456 (2015). doi: 10.1021/jp510837q.

[374] M. Wolf and H. Rauschenbach. Series Resistance Effects on Solar Cell Measurements. *Advanced Energy Conversion*, **3**, 2, 455 (1963). doi: 10.1016/0365-1789(63)90063-8.

[375] E. Rodrigues, R. Melicio, V. M. F. Mendes and J. Catalão. Simulation of a solar cell considering single-diode equivalent circuit mode. *Renewable Energy and Power Quality Journal*, 369–373 (2011). doi: 10.24084/repqj09.339.

[376] T. Kirchartz, K. Ding and U. Rau. *Fundamental Electrical Characterization of Thin-Film Solar Cells*. Wiley-VCH Verlag GmbH Co. KGaA, Weinheim (2011). doi: 10.1002/9783527636280.ch2.

[377] M. A. Cappelletti, G. A. Casas, A. P. Cédola, E. L. Peltzer y Blancá and B. Marí Soucase. Study of the Reverse Saturation Current and Series Resistance of p-p-n Perovskite Solar Cells Using the Single and Double-Diode Models. *Superlattices and Microstructures*, **123**, 338 (2018). doi: 10.1016/j.spmi.2018.09.023.

[378] R. Gottesman, P. Lopez-Varo, L. Gouda, J. Jimenez-Tejada, J. Hu, S. Tirosh, A. Zaban and J. Bisquert. Dynamic Phenomena at Perovskite/Electron-Selective Contact Interface as Interpreted from Photovoltage Decays. *Chem*, **1**, 5, 776 (2016). doi: 10.1016/j.chempr.2016.10.002.

[379] J. Hu, R. Gottesman, L. Gouda, A. Kama, M. Priel, S. Tirosh, J. Bisquert and A. Zaban. Photovoltage Behavior in Perovskite Solar Cells under Light-Soaking Showing Photoinduced Interfacial Changes. *ACS Energy Letters*, **2**, 5, 950 (2017). doi: 10.1021/acsenergylett.7b00212.

[380] E. H. Hellen. Verifying the Diode–Capacitor Circuit Voltage Decay. *American Journal of Physics*, **71**, 8, 797 (2003). doi: 10.1119/1.1578070.

[381] D. A. Jacobs, H. Shen, F. Pfeffer, J. Peng, T. P. White, F. J. Beck and K. R. Catchpole. The Two Faces of Capacitance: New Interpretations for Electrical Impedance Measurements of Perovskite Solar Cells and Their Relation to Hysteresis. *Journal of Applied Physics*, **124**, 22, 225702 (2018). doi: 10.1063/1.5063259.

[382] Y. Jiang, E. J. Juarez-Perez, Q. Ge, S. Wang, M. R. Leyden, L. K. Ono, S. R. Raga, J. Hu and Y. Qi. Post-Annealing of $MAPbI_3$ Perovskite Films with Methylamine for Efficient Perovskite Solar Cells. *Materials Horizons*, **3**, 6, 548 (2016). doi: 10.1039/C6MH00160B.

[383] F. Ebadi, N. Taghavinia, R. Mohammadpour, A. Hagfeldt and W. Tress. Origin of Apparent Light-Enhanced and Negative Capacitance in Perovskite Solar Cells. *Nature Communications*, **10**, 1, 1574 (2019). doi: 10.1038/s41467-019-09079-z.

[384] J. Lee, J. Kong, H. Kim, S.-O. Kang and K. Lee. Direct Observation of Internal Potential Distributions in a Bulk Heterojunction Solar Cell. *Applied Physics Letters*, **99**, 24, 243301 (2011). doi: 10.1063/1.3669533.

[385] L. Castañer, E. Vilamajó, J. Llabería and J. Garrido. Investigations of the OCVD Transients in Solar Cells. *Journal of Physics D: Applied Physics*, **14**, 10, 1867 (1981). doi: 10.1088/0022-3727/14/10/019.

[386] L. Castañer, J. Llabería, J. Garrido and E. Vilamajó. Numerical Simulation of Solar Cell Open Circuit Voltage Decay. *Electronics Letters*, **17**, 20, 745 (1981). doi: 10.1049/el:19810524.

[387] J. E. Mahan and D. L. Barnes. Depletion Layer Effects in the Open-Circuit-Voltage-Decay Lifetime Measurement. *Solid-State Electronics*, **24**, 10, 989 (1981). doi: 10.1016/0038-1101(81)90124-6.

[388] J. Bisquert, F. Fabregat-Santiago, I. Mora-Seró, G. Garcia-Belmonte and S. Giménez. Electron Lifetime in Dye-Sensitized Solar Cells: Theory and Interpretation of Measurements. *The Journal of Physical Chemistry C*, **113**, 40, 17278 (2009). doi: 10.1021/jp9037649.

[389] R. A. Street. Localized State Distribution and its Effect on Recombination in Organic Solar Cells. *Physical Review B*, **84**, 7, 075208 (2011). doi: 10.1103/PhysRevB.84.075208.

[390] W. M. M. Lin, D. Bozyigit, O. Yarema and V. Wood. Transient Photovoltage Measurements in Nanocrystal-Based Solar Cells. *The Journal of Physical Chemistry C*, **120**, 23, 12900 (2016). doi: 10.1021/acs.jpcc.6b03695.

[391] O. J. Sandberg, K. Tvingstedt, P. Meredith and A. Armin. Theoretical Perspective on Transient Photovoltage and Charge Extraction Techniques. *The Journal of Physical Chemistry C*, **123**, 23, 14261 (2019). doi: 10.1021/acs.jpcc.9b03133.

[392] J. Kniepert, A. Paulke, L. Perdigón-Toro, J. Kurpiers, H. Zhang, F. Gao, J. Yuan, Y. Zou, V. M. L. Corre, L. J. A. Koster and D. Neher. Reliability of Charge Carrier Recombination Data Determined with Charge Extraction Methods. *Journal of Applied Physics*, **126**, 20, 205501 (2019). doi: 10.1063/1.5129037.

[393] J. Shi, D. Li, Y. Luo, H. Wu and Q. Meng. Opto-Electro-Modulated Transient Photovoltage and Photocurrent System for Investigation of Charge Transport and Recombination in Solar Cells. *Review of Scientific Instruments*, **87**, 12, 123107 (2016). doi: 10.1063/1.4972104.

[394] Y. Li, Y. Li, J. Shi, H. Li, H. Zhang, J. Wu, D. Li, Y. Luo, H. Wu and Q. Meng. Photocharge Accumulation and Recombination in Perovskite Solar Cells Regarding Device Performance and Stability. *Applied Physics Letters*, **112**, 5, 053904 (2018). doi: 10.1063/1.5009040.

[395] M. C. Heiber, T. Okubo, S.-J. Ko, B. R. Luginbuhl, N. A. Ran, M. Wang, H. Wang, M. A. Uddin, H. Y. Woo, G. C. Bazan and T.-Q. Nguyen. Measuring the Competition Between Bimolecular Charge Recombination and Charge Transport in Organic Solar Cells under Operating Conditions. *Energy & Environmental Science*, **11**, 10, 3019 (2018). doi: 10.1039/C8EE01559G.

[396] K. X. Steirer, P. Schulz, G. Teeter, V. Stevanovic, M. Yang, K. Zhu and J. J. Berry. Defect Tolerance in Methylammonium Lead Triiodide Perovskite. *ACS Energy Letters*, **1**, 2, 360 (2016). doi: 10.1021/acsenergylett.6b00196.

[397] M. Stolterfoht, P. Caprioglio, C. M. Wolff, J. A. Márquez, J. Nordmann, S. Zhang, D. Rothhardt, U. Hörmann, Y. Amir, A. Redinger, L. Kegelmann, F. Zu, S. Albrecht, N. Koch, T. Kirchartz, M. Saliba, T. Unold and D. Neher. The Impact of Energy Alignment and Interfacial Recombination on the Internal and External Open-Circuit Voltage of Perovskite Solar Cells. *Energy & Environmental Science*, **12**, 9, 2778 (2019). doi: 10.1039/C9EE02020A.

[398] V. M. Le Corre, M. Stolterfoht, L. Perdigón Toro, M. Feuerstein, C. Wolff, L. Gil-Escrig, H. J. Bolink, D. Neher and L. J. A. Koster. Charge Transport Layers Limiting the Efficiency of Perovskite Solar Cells: How To Optimize Conductivity, Doping, and Thickness. *ACS Applied Energy Materials*, **2**, 9, 6280 (2019). doi: 10.1021/acsaem.9b00856.

[399] F. Staub, H. Hempel, J.-C. Hebig, J. Mock, U. W. Paetzold, U. Rau, T. Unold and T. Kirchartz. Beyond Bulk Lifetimes: Insights into Lead Halide Perovskite Films from Time-Resolved Photoluminescence. *Physical Review Applied*, **6**, 4, 044017 (2016). doi: 10.1103/PhysRevApplied.6.044017.

[400] A. Paulke, S. D. Stranks, J. Kniepert, J. Kurpiers, C. M. Wolff, N. Schön, H. J. Snaith, T. J. K. Brenner and D. Neher. Charge Carrier Recombination Dynamics in Perovskite and Polymer Solar Cells. *Applied Physics Letters*, **108**, 11, 113505 (2016). doi: 10.1063/1.4944044.

[401] D. Kiermasch, P. Rieder, K. Tvingstedt, A. Baumann and V. Dyakonov. Improved Charge Carrier Lifetime in Planar Perovskite Solar Cells by Bromine Doping. *Scientific Reports*, **6**, 39333 (2016). doi: 10.1038/srep39333.

[402] N. F. Montcada, J. M. Marín-Beloqui, W. Cambarau, J. Jiménez-López, L. Cabau, K. T. Cho, M. K. Nazeeruddin and E. Palomares. Analysis of Photoinduced Carrier Recombination Kinetics in Flat and Mesoporous Lead Perovskite Solar Cells. *ACS Energy Letters*, **2**, 1, 182 (2017). doi: 10.1021/acsenergylett.6b00600.

[403] T. Kirchartz and J. Nelson. Meaning of Reaction Orders in Polymer:Fullerene Solar Cells. *Physical Review B*, **86**, 16, 165201 (2012). doi: 10.1103/PhysRevB.86.165201.

[404] F. Deledalle, P. Shakya Tuladhar, J. Nelson, J. R. Durrant and T. Kirchartz. Understanding the Apparent Charge Density Dependence of Mobility and Lifetime in Organic Bulk Heterojunction Solar Cells. *The Journal of Physical Chemistry C*, **118**, 17, 8837 (2014). doi: 10.1021/jp502948y.

[405] C. Deibel, A. Wagenpfahl and V. Dyakonov. Origin of Reduced Polaron Recombination in Organic Semiconductor Devices. *Physical Review B*, **80**, 7, 075203 (2009). doi: 10.1103/PhysRevB.80.075203.

[406] I. Gelmetti, L. Cabau, N. F. Montcada and E. Palomares. Selective Organic Contacts for Methyl Ammonium Lead Iodide (MAPI) Perovskite Solar Cells: Influence of Layer Thickness on Carriers Extraction and Carriers Lifetime. *ACS Applied Materials Interfaces*, **9**, 26, 21599 (2017). doi: 10.1021/acsami.7b06638.

[407] J. Jiménez-López, W. Cambarau, L. Cabau and E. Palomares. Charge Injection, Carriers Recombination and HOMO Energy Level Relationship in Perovskite Solar Cells. *Scientific Reports*, **7**, 1, 6101 (2017). doi: 10.1038/s41598-017-06245-5.

[408] S. Wheeler, D. Bryant, J. Troughton, T. Kirchartz, T. Watson, J. Nelson and J. R. Durrant. Transient Optoelectronic Analysis of the Impact of Material Energetics and Recombination Kinetics on the Open-Circuit Voltage of Hybrid Perovskite Solar Cells. *The Journal of Physical Chemistry C*, **121**, 25, 13496 (2017). doi: 10.1021/acs.jpcc.7b02411.

[409] J. Burschka, N. Pellet, S.-J. Moon, R. Humphry-Baker, P. Gao, M. K. Nazeeruddin and M. Gratzel. Sequential Deposition as a Route to High-Performance Perovskite-Sensitized Solar Cells. *Nature*, **499**, 7458, 316 (2013). doi: 10.1038/nature12340.

[410] D. Pérez-del Rey, P. P. Boix, M. Sessolo, A. Hadipour and H. J. Bolink. Interfacial Modification for High-Efficiency Vapor-Phase-Deposited Perovskite Solar Cells Based on a Metal Oxide Buffer Layer. *The Journal of Physical Chemistry Letters*, **9**, 5, 1041 (2018). doi: 10.1021/acs.jpclett.7b03361.

[411] D. Liu, M. K. Gangishetty and T. L. Kelly. Effect of $CH_3NH_3PbI_3$ Thickness on Device Efficiency in Planar Heterojunction Perovskite Solar Cells. *Journal of Materials Chemistry A*, **2**, 46, 19873 (2014). doi: 10.1039/C4TA02637C.

[412] K. Wang, C. Liu, P. Du, L. Chen, J. Zhu, A. Karim and X. Gong. Efficiencies of Perovskite Hybrid Solar Cells Influenced by Film Thickness and Morphology of $CH_3NH_3PbI_{3-x}Cl_x$ Layer. *Organic Electronics*, **21**, 19 (2015). doi: 10.1016/j.orgel.2015.02.023.

[413] G. E. Eperon, V. M. Burlakov, P. Docampo, A. Goriely and H. J. Snaith. Morphological Control for High Performance, Solution-Processed Planar Heterojunction Perovskite Solar Cells. *Advanced Functional Materials*, **24**, 1, 151 (2014). doi: 10.1002/adfm.201302090.

[414] M. . Reinoso, C. A. Otálora and G. Gordillo. Improvement Properties of Hybrid Halide Perovskite Thin Films Prepared by Sequential Evaporation for Planar Solar Cells. *Materials*, **12**, 9, 1394 (2019). doi: 10.3390/ma12091394.

[415] W. Zhang, M. Saliba, D. T. Moore, S. K. Pathak, M. T. Hörantner, T. Stergiopoulos, S. D. Stranks, G. E. Eperon, J. A. Alexander-Webber, A. Abate, A. Sadhanala, S. Yao, Y. Chen, R. H. Friend, L. A. Estroff, U. Wiesner and H. J. Snaith. Ultrasmooth Organic–Inorganic Perovskite Thin-Film Formation and Crystallization for Efficient Planar Heterojunction Solar Cells. *Nature Communications*, **6** (2015). doi: 10.1038/ncomms7142.

[416] N.-G. Park. Perovskite Solar Cells: An Emerging Photovoltaic Technology. *Materials Today*, **18**, 2, 65 (2015). doi: 10.1016/j.mattod.2014.07.007.

[417] C. Momblona, O. Malinkiewicz, C. Roldán-Carmona, A. Soriano, L. Gil-Escrig, E. Bandiello, M. Scheepers, E. Edri and H. J. Bolink. Efficient Methylammonium Lead Iodide Perovskite Solar Cells with Active Layers from 300 to 900 nm. *APL Materials*, **2**, 8, 081504 (2014). doi: 10.1063/1.4890056.

[418] S. Glunz, J. Nekarda, H. Mäckel and A. Cuevas. Analyzing Back Contacts of Silicon Solar Cells by Suns-Voc-Measurements at High Illumination Densities. *2nd European Photovoltaic Solar Energy Conference and Exhibition*, 849–853 (2007).

[419] O. Gunawan, T. Gokmen and D. B. Mitzi. Suns-V_{OC} Characteristics of High Performance Kesterite Solar Cells. *Journal of Applied Physics*, **116**, 8, 084504 (2014). doi: 10.1063/1.4893315.

[420] T. Kirchartz, F. Deledalle, P. S. Tuladhar, J. R. Durrant and J. Nelson. On the Differences between Dark and Light Ideality Factor in Polymer:Fullerene Solar Cells. *The Journal of Physical Chemistry Letters*, **4**, 14, 2371 (2013). doi: 10.1021/jz4012146.

[421] S. Ullbrich, A. Fischer, Z. Tang, J. Ávila, H. J. Bolink, S. Reineke and K. Vandewal. Electrothermal Feedback and Absorption-Induced Open-Circuit-Voltage Turnover in Solar Cells. *Physical Review Applied*, **9**, 5, 051003 (2018). doi: 10.1103/PhysRevApplied.9.051003.

[422] Y. Hou, W. Chen, D. Baran, T. Stubhan, N. A. Luechinger, B. Hartmeier, M. Richter, J. Min, S. Chen, C. O. R. Quiroz, N. Li, H. Zhang, T. Heumueller, G. J. Matt, A. Osvet, K. Forberich, Z.-G. Zhang, Y. Li, B. Winter, P. Schweizer, E. Spiecker and C. J. Brabec. Overcoming the Interface Losses in Planar Heterojunction Perovskite-Based Solar Cells. *Advanced Materials*, **28**, 25, 5112 (2016). doi: 10.1002/adma.201504168.

[423] O. Bubnova, Z. U. Khan, H. Wang, S. Braun, D. R. Evans, M. Fabretto, P. Hojati-Talemi, D. Dagnelund, J.-B. Arlin, Y. H. Geerts, S. Desbief, D. W. Breiby, J. W. Andreasen, R. Lazzaroni, W. M. Chen, I. Zozoulenko, M. Fahlman, P. J. Murphy, M. Berggren and X. Crispin. Semi-Metallic Polymers. *Nature Materials*, **13**, 2, 190 (2014). doi: 10.1038/nmat3824.

[424] H. Liu, X. Li, L. Zhang, Q. Hong, J. Tang, A. Zhang and C.-Q. Ma. Influence of the Surface Treatment of PEDOT:PSS Layer with High Boiling Point Solvent on the Performance of Inverted Planar Perovskite Solar Cells. *Organic Electronics*, **47**, 220 (2017). doi: 10.1016/j.orgel.2017.05.025.

[425] M. Neophytou, J. Griffiths, J. Fraser, M. Kirkus, H. Chen, C. B. Nielsen and I. McCulloch. High Mobility, Hole Transport Materials for Highly Efficient PEDOT:PSS Replacement in Inverted Perovskite Solar Cells. *Journal of Materials Chemistry C*, **5**, 20, 4940 (2017). doi: 10.1039/C7TC00858A.

[426] N. F. Montcada, M. Mendez, K. T. Cho, M. K. Nazeeruddin and E. Palomares. Photo-Induced Dynamic Processes in Perovskite Solar Cells: the Influence of Perovskite Composition in the Charge Extraction and the Carrier Recombination. *Nanoscale*, **10**, 13, 6155 (2018). doi: 10.1039/C8NR00180D.

[427] J.-H. Im, H.-S. Kim and N.-G. Park. Morphology-Photovoltaic Property Correlation in Perovskite Solar Cells: One-Step Versus Two-Step Deposition of $CH_3NH_3PbI_3$. *APL Materials*, **2**, 8, 081510 (2014). doi: 10.1063/1.4891275.

[428] J.-W. Lee, T.-Y. Lee, P. J. Yoo, M. Gratzel, S. Mhaisalkar and N.-G. Park. Rutile TiO_2-Based Perovskite Solar Cells. *Journal of Materials Chemistry A*, **2**, 24, 9251 (2014). doi: 10.1039/C4TA01786B.

[429] D. Liu, Y. Li, J. Yuan, Q. Hong, G. Shi, D. Yuan, J. Wei, C. Huang, J. Tang and M.-K. Fung. Improved Performance of Inverted Planar Perovskite Solar Cells with F4-TCNQ Doped PEDOT:PSS Hole Transport Layers. *Journal of Materials Chemistry A*, **5**, 12, 5701 (2017). doi: 10.1039/C6TA10212C.

[430] H. Choi, C.-K. Mai, H.-B. Kim, J. Jeong, S. Song, G. C. Bazan, J. Y. Kim and A. J. Heeger. Conjugated Polyelectrolyte Hole Transport Layer for Inverted-Type Perovskite Solar Cells. *Nature Communications*, **6**, 1, 7348 (2015). doi: 10.1038/ncomms8348.

[431] A. Förtig, A. Baumann, D. Rauh, V. Dyakonov and C. Deibel. Charge Carrier Concentration and Temperature Dependent Recombination in Polymer-Fullerene Solar Cells. *Applied Physics Letters*, **95**, 5, 052104 (2009). doi: 10.1063/1.3202389.

[432] S. Colella, M. Mazzeo, A. Rizzo, G. Gigli and A. Listorti. The Bright Side of Perovskites. *The Journal of Physical Chemistry Letters*, **7**, 21, 4322 (2016). doi: 10.1021/acs.jpclett.6b01799.

[433] C. Wehrenfennig, G. E. Eperon, M. B. Johnston, H. J. Snaith and L. M. Herz. High Charge Carrier Mobilities and Lifetimes in Organolead Trihalide Perovskites. *Advanced Materials*, **26**, 10, 1584 (2014). doi: 10.1002/adma.201305172.

[434] A. Förtig, J. Rauh, V. Dyakonov and C. Deibel. Shockley Equation Parameters of P3HT:PCBM Solar Cells Determined by Transient Techniques. *Physical Review B*, **86**, 11, 115302 (2012). doi: 10.1103/PhysRevB.86.115302.

[435] R. Hamilton, C. G. Shuttle, B. O'Regan, T. C. Hammant, J. Nelson and J. R. Durrant. Recombination in Annealed and Nonannealed Polythiophene/Fullerene Solar Cells: Transient Photovoltage Studies versus Numerical Modeling. *The Journal of Physical Chemistry Letters*, **1**, 9, 1432 (2010). doi: 10.1021/jz1001506.

[436] A. Petersen, A. Ojala, T. Kirchartz, T. A. Wagner, F. Würthner and U. Rau. Field-Dependent Exciton Dissociation in Organic Heterojunction Solar Cells. *Physical Review B*, **85**, 24, 245208 (2012). doi: 10.1103/PhysRevB.85.245208.

[437] d. y. Son, J.-W. Lee, Y. J. Choi, I.-H. Jang, S. Lee, P. J. Yoo, H. Shin, N. Ahn, M. Choi, D. Kim and N.-G. Park. Self-Formed Grain Boundary Healing Layer for Highly Efficient $CH_3NH_3PbI_3$ Perovskite Solar Cells. *Nature Energy*, **1**, 16081 (2016). doi: 10.1038/nenergy.2016.81.

[438] S. S. Shin, E. J. Yeom, W. S. Yang, S. Hur, M. G. Kim, J. Im, J. Seo, J. H. Noh and S. I. Seok. Colloidally Prepared La-doped $BaSnO_3$ Electrodes for Efficient, Photostable Perovskite Solar Cells. *Science*, **356**, 6334, 167 (2017). doi: 10.1126/science.aam6620.

[439] D. Kiermasch, L. Gil-Escrig, H. J. Bolink and K. Tvingstedt. Effects of Masking on Open-Circuit Voltage and Fill Factor in Solar Cells. *Joule*, **3**, 1, 16 (2019). doi: 10.1016/j.joule.2018.10.016.

[440] M. A. Green. Solar Cell Fill Factors: General Graph and Empirical Expressions. *Solid-State Electronics*, **24**, 8, 788 (1981). doi: 10.1016/0038-1101(81)90062-9.

[441] K. Tvingstedt, O. Malinkiewicz, A. Baumann, C. Deibel, H. J. Snaith, V. Dyakonov and H. J. Bolink. Radiative Efficiency of Lead Iodide Based Perovskite Solar Cells. *Scientific Reports*, **4**, 6071 (2014). doi: 10.1038/srep06071.

[442] W. Tress, N. Marinova, O. Inganäs, M. K. Nazeeruddin, S. M. Zakeeruddin and M. Grätzel. Predicting the Open-Circuit Voltage of $CH_3NH_3PbI_3$ Perovskite Solar Cells Using Electroluminescence and Photovoltaic Quantum Efficiency Spectra: the Role of Radiative and Non-Radiative Recombination. *Advanced Energy Materials*, **5**, 3, 1400812 (2015). doi: 10.1002/aenm.201400812.

[443] M. Stolterfoht, C. M. Wolff, Y. Amir, A. Paulke, L. Perdigon-Toro, P. Caprioglio and D. Neher. Approaching the Fill Factor Shockley-Queisser Limit in Stable, Dopant-Free Triple Cation Perovskite Solar Cells. *Energy & Environmental Science*, **10**, 6, 1530 (2017). doi: 10.1039/C7EE00899F.

[444] J. Diekmann, P. Caprioglio, M. Arvind, T. Unold, T. Kirchartz, D. Neher, M. Stolterfoht and D. Rothhardt. Pathways Towards 30% Efficient Single-Junction Perovskite Solar Cells. *arXiv preprint*, **arXiv:1910.07422** (2019).

[445] Y. Hu, E. M. Hutter, P. Rieder, I. Grill, J. Hanisch, M. F. Aygüler, A. G. Hufnagel, M. Handloser, T. Bein, A. Hartschuh, K. Tvingstedt, V. Dyakonov, A. Baumann, T. J. Savenije, M. L. Petrus and P. Docampo. Understanding the Role of Cesium and Rubidium Additives in Perovskite Solar Cells: Trap States, Charge Transport, and Recombination. *Advanced Energy Materials*, **8**, 16, 1703057 (2018). doi: 10.1002/aenm.201703057.

[446] D. W. deQuilettes, S. Koch, S. Burke, R. K. Paranji, A. J. Shropshire, M. E. Ziffer and D. S. Ginger. Photoluminescence Lifetimes Exceeding 8 μs and Quantum Yields Exceeding 30% in Hybrid Perovskite Thin Films by Ligand Passivation. *ACS Energy Letters*, **1**, 2, 438 (2016). doi: 10.1021/acsenergylett.6b00236.

[447] I. L. Braly, D. W. deQuilettes, L. M. Pazos-Outón, S. Burke, M. E. Ziffer, D. S. Ginger and H. W. Hillhouse. Hybrid Perovskite Films Approaching the Radiative Limit with Over 90% Photoluminescence Quantum Efficiency. *Nature Photonics*, **12**, 6, 355 (2018). doi: 10.1038/s41566-018-0154-z.

[448] D. Luo, W. Yang, Z. Wang, A. Sadhanala, Q. Hu, R. Su, R. Shivanna, G. F. Trindade, J. F. Watts, Z. Xu, T. Liu, K. Chen, F. Ye, P. Wu, L. Zhao, J. Wu, Y. Tu, Y. Zhang, X. Yang, W. Zhang, R. H. Friend, Q. Gong, H. J. Snaith and R. Zhu. Enhanced Photovoltage for Inverted Planar Heterojunction Perovskite Solar Cells. *Science*, **360**, 6396, 1442 (2018). doi: 10.1126/science.aap9282.

[449] Z. Liu, L. Krückemeier, B. Krogmeier, B. Klingebiel, J. A. Márquez, S. Levcenko, S. Öz, S. Mathur, U. Rau, T. Unold and T. Kirchartz. Open-Circuit Voltages Exceeding 1.26 V in Planar Methylammonium Lead Iodide Perovskite Solar Cells. *ACS Energy Letters*, 110–117 (2018). doi: 10.1021/acsenergylett.8b01906.

[450] Y. Yang, M. Yang, D. Moore, Y. Yan, E. Miller, K. Zhu and M. Beard. Top and Bottom Surfaces Limit Carrier Lifetime in Lead Iodide Perovskite Films. *Nature Energy*, **2**, 16207 (2017). doi: 10.1038/nenergy.2016.207.

[451] M. Stolterfoht, P. Caprioglio, C. M. Wolff, J. A. Márquez, J. Nordmann, S. Zhang, D. Rothhart, U. Hörmann, A. Redinger, L. Kegelmann, S. Albrecht, T. Kirchartz, M. Saliba, T. Unold and D. Neher. The Perovskite/Transport Layer Interfaces Dominate Non-Radiative Recombination in Efficient Perovskite Solar Cells. *arXiv preprint*, **arXiv:1810.01333** (2018).

[452] M. Stolterfoht, C. M. Wolff, J. A. Márquez, S. Zhang, C. J. Hages, D. Rothhardt, S. Albrecht, P. L. Burn, P. Meredith, T. Unold and D. Neher. Visualization and Suppression of Interfacial Recombination for High-Efficiency Large-Area PIN Perovskite Solar Cells. *Nature Energy*, **3**, 10, 847 (2018). doi: 10.1038/s41560-018-0219-8.

[453] G. Divitini, S. Cacovich, F. Matteocci, L. Cinà, A. Di Carlo and C. Ducati. In Situ Observation of Heat-Induced Degradation of Perovskite Solar Cells. *Nature Energy*, **1**, 15012 (2016). doi: 10.1038/nenergy.2015.12.

[454] A. F. Akbulatov, S. Y. Luchkin, L. A. Frolova, N. N. Dremova, K. L. Gerasimov, I. S. Zhidkov, D. V. Anokhin, E. Z. Kurmaev, K. J. Stevenson and P. A. Troshin. Probing the Intrinsic Thermal and Photochemical Stability of Hybrid and Inorganic Lead Halide Perovskites. *The Journal of Physical Chemistry Letters*, **8**, 6, 1211 (2017). doi: 10.1021/acs.jpclett.6b03026.

[455] J. P. Bastos, G. Uytterhoeven, W. Qiu, U. W. Paetzold, D. Cheyns, S. Surana, J. Rivas, M. Jaysankar, W. Song, T. Aernouts, J. Poortmans and R. Gehlhaar. Model for the Prediction of the Lifetime and Energy Yield of Methyl Ammonium Lead Iodide Perovskite Solar Cells at Elevated Temperatures. *ACS Applied Materials Interfaces*, **11**, 18, 16517 (2019). doi: 10.1021/acsami.9b00923.

[456] F. Matsumoto, S. M. Vorpahl, J. Q. Banks, E. Sengupta and D. S. Ginger. Photodecomposition and Morphology Evolution of Organometal Halide Perovskite Solar Cells. *The Journal of Physical Chemistry C*, **119**, 36, 20810 (2015). doi: 10.1021/acs.jpcc.5b06269.

[457] Z. Safari, M. B. Zarandi and M. R. Nateghi. Improved Environmental Stability of HTM Free Perovskite Solar Cells by a Modified Deposition Route. *Chemical Papers*, **73**, 11, 2667 (2019). doi: 10.1007/s11696-019-00818-6.

[458] T. Mahmoudi, Y. Wang and Y.-B. Hahn. Stability Enhancement in Perovskite Solar Cells with Perovskite/Silver–Graphene Composites in the Active Layer. *ACS Energy Letters*, **4**, 1, 235 (2019). doi: 10.1021/acsenergylett.8b02201.

[459] C. Chen, H. Kang, S. Hsiao, P. Yang, K. Chiang and H. Lin. Efficient and Uniform Planar-Type Perovskite Solar Cells by Simple Sequential Vacuum Deposition. *Advanced Materials*, **26**, 38, 6647 (2014). doi: 10.1002/adma.201402461.

[460] Y. H. Lee, J. Luo, M.-K. Son, P. Gao, K. T. Cho, J. Seo, S. M. Zakeeruddin, M. Grätzel and M. K. Nazeeruddin. Enhanced Charge Collection with Passivation Layers in Perovskite Solar Cells. *Advanced Materials*, **28**, 20, 3966 (2016). doi: 10.1002/adma.201505140.

[461] D. H. Cao, C. C. Stoumpos, C. D. Malliakas, M. J. Katz, O. K. Farha, J. T. Hupp and M. G. Kanatzidis. Remnant PbI_2, an Unforeseen Necessity in High-Efficiency Hybrid Perovskite-Based Solar Cells? *APL Materials*, **2**, 9, 091101 (2014). doi: 10.1063/1.4895038.

[462] G.-J. A. H. Wetzelaer, M. Scheepers, A. M. Sempere, C. Momblona, J. Ávila and H. J. Bolink. Trap-Assisted Non-Radiative Recombination in Organic–Inorganic Perovskite Solar Cells. *Advanced Materials*, **27**, 11, 1837 (2015). doi: 10.1002/adma.201405372.

[463] H. K. H. Lee, J. Barbé, S. M. P. Meroni, T. Du, C.-T. Lin, A. Pockett, J. Troughton, S. M. Jain, F. De Rossi, J. Baker, M. J. Carnie, M. A. McLachlan, T. M. Watson, J. R. Durrant and W. C. Tsoi. Outstanding Indoor Performance of Perovskite Photovoltaic Cells – Effect of Device Architectures and Interlayers. *Solar Rapid Research Letters*, 1800207 (2018). doi: 10.1002/solr.201800207.

[464] A. Guerrero, J. You, C. Aranda, Y. S. Kang, G. Garcia-Belmonte, H. Zhou, J. Bisquert and Y. Yang. Interfacial Degradation of Planar Lead Halide Perovskite Solar Cells. *ACS Nano*, **10**, 1, 218 (2016). doi: 10.1021/acsnano.5b03687.

[465] B. Rivkin, P. Fassl, Q. Sun, A. D. Taylor, Z. Chen and Y. Vaynzof. Effect of Ion Migration-Induced Electrode Degradation on the Operational Stability of Perovskite Solar Cells. *ACS Omega*, **3**, 8, 10042 (2018). doi: 10.1021/acsomega.8b01626.

[466] C. Li, A. Guerrero, Y. Zhong, A. Gräser, C. A. M. Luna, J. Köhler, J. Bisquert, R. Hildner and S. Huettner. Real-Time Observation of Iodide Ion Migration in Methylammonium Lead Halide Perovskites. *Small*, **13**, 42, 1701711 (2017). doi: 10.1002/smll.201701711.

[467] H. Lee and C. Lee. Analysis of Ion-Diffusion-Induced Interface Degradation in Inverted Perovskite Solar Cells via Restoration of the Ag Electrode. *Advanced Energy Materials*, **8**, 11, 1702197 (2018). doi: 10.1002/aenm.201702197.

[468] Y. Kato, L. K. Ono, M. V. Lee, S. Wang, S. R. Raga and Y. Qi. Silver Iodide Formation in Methyl Ammonium Lead Iodide Perovskite Solar Cells with Silver Top Electrodes. *Advanced Materials Interfaces*, **2**, 13, 1500195 (2015). doi: 10.1002/admi.201500195.

[469] O. Almora, C. Aranda, E. Mas-Marzá and G. Garcia-Belmonte. On Mott-Schottky Analysis Interpretation of Capacitance Measurements in Organometal Perovskite Solar Cells. *Applied Physics Letters*, **109**, 17, 173903 (2016). doi: 10.1063/1.4966127.

[470] M. Fischer, K. Tvingstedt, A. Baumann and V. Dyakonov. Doping Profile in Planar Hybrid Perovskite Solar Cells Identifying Mobile Ions. *ACS Applied Energy Materials*, **1**, 10, 5129 (2018). doi: 10.1021/acsaem.8b01119.

[471] L. M. Pazos-Outón, T. P. Xiao and E. Yablonovitch. Fundamental Efficiency Limit of Lead Iodide Perovskite Solar Cells. *The Journal of Physical Chemistry Letters*, 1703–1711 (2018). doi: 10.1021/acs.jpclett.7b03054.

[472] Q. Jiang, Y. Zhao, X. Zhang, X. Yang, Y. Chen, Z. Chu, Q. Ye, X. Li, Z. Yin and J. You. Surface Passivation of Perovskite Film for Efficient Solar Cells. *Nature Photonics*, **13**, 7, 460 (2019). doi: 10.1038/s41566-019-0398-2.

[473] M. A. Green and A. W. Y. Ho-Baillie. Pushing to the Limit: Radiative Efficiencies of Recent Mainstream and Emerging Solar Cells. *ACS Energy Letters*, **4**, 7, 1639 (2019). doi: 10.1021/acsenergylett.9b01128.

[474] A. D. Sheikh, R. Munir, M. A. Haque, A. Bera, W. Hu, P. Shaikh, A. Amassian and T. Wu. Effects of High Temperature and Thermal Cycling on the Performance of Perovskite Solar Cells: Acceleration of Charge Recombination and Deterioration of Charge Extraction. *ACS Applied Materials Interfaces*, **9**, 40, 35018 (2017). doi: 10.1021/acsami.7b11250.

[475] L. T. Schelhas, J. A. Christians, J. J. Berry, M. F. Toney, C. J. Tassone, J. M. Luther and K. H. Stone. Monitoring a Silent Phase Transition in $CH_3NH_3PbI_3$ Solar Cells via Operando X-ray Diffraction. *ACS Energy Letters*, **1**, 5, 1007 (2016). doi: 10.1021/acsenergylett.6b00441.

[476] H. M. N. Ferdous, I. Nazifah, L. Zhen, R. Guofeng, Z. Kai and F. Zhaoyang. Ionic and Optical Properties of Methylammonium Lead Iodide Perovskite across the Tetragonal–Cubic Structural Phase Transition. *ChemSusChem*, **9**, 18, 2692 (2016). doi: 10.1002/cssc.201600949.

[477] H. Tsai, R. Asadpour, J.-C. Blancon, C. C. Stoumpos, O. Durand, J. W. Strzalka, B. Chen, R. Verduzco, P. M. Ajayan, S. Tretiak, J. Even, M. A. Alam, M. G. Kanatzidis, W. Nie and A. D. Mohite. Light-Induced Lattice Expansion Leads to High-Efficiency Perovskite Solar Cells. *Science*, **360**, 6384, 67 (2018). doi: 10.1126/science.aap8671.

[478] C. Zhu, X. Niu, Y. Fu, N. Li, C. Hu, Y. Chen, X. He, G. Na, P. Liu, H. Zai, Y. Ge, Y. Lu, X. Ke, Y. Bai, S. Yang, P. Chen, Y. Li, M. Sui, L. Zhang, H. Zhou and Q. Chen. Strain Engineering in Perovskite Solar Cells and its Impacts on Carrier Dynamics. *Nature Communications*, **10**, 1, 815 (2019). doi: 10.1038/s41467-019-08507-4.

[479] T. W. Jones, A. Osherov, M. Alsari, M. Sponseller, B. C. Duck, Y.-K. Jung, C. Settens, F. Niroui, R. Brenes, C. V. Stan, Y. Li, M. Abdi-Jalebi, N. Tamura, J. E. Macdonald, M. Burghammer, R. H. Friend, V. Bulović, A. Walsh, G. J. Wilson, S. Lilliu and S. D. Stranks. Lattice Strain Causes Non-Radiative Losses in Halide Perovskites. *Energy & Environmental Science*, **12**, 2, 596 (2019). doi: 10.1039/C8EE02751J.

[480] K. Nishimura, D. Hirotani, M. A. Kamarudin, Q. Shen, T. Toyoda, S. Iikubo, T. Minemoto, K. Yoshino and S. Hayase. Relationship between Lattice Strain and Efficiency for Sn-Perovskite Solar Cells. *ACS Applied Materials Interfaces*, **11**, 34, 31105 (2019). doi: 10.1021/acsami.9b09564.

[481] K. B. Lohmann, J. B. Patel, M. U. Rothmann, C. Q. Xia, R. D. J. Oliver, L. M. Herz, H. J. Snaith and M. B. Johnston. Control over Crystal Size in Vapor Deposited Metal-Halide Perovskite Films. *ACS Energy Letters*, 710–717 (2020). doi: 10.1021/acsenergylett.0c00183.

[482] C. Yang, J. Wang, X. Bao, J. Gao, Z. Liu and R. Yang. Grain-Boundary Effect and Post Treatment of Active Layer for Efficient Inverted Planar Perovskite Solar Cells. *Electrochimica Acta*, **281**, 9 (2018). doi: 10.1016/j.electacta.2018.05.114.

[483] H. Zhang, X. Ren, X. Chen, J. Mao, J. Cheng, Y. Zhao, Y. Liu, J. Milic, W.-J. Yin, M. Grätzel and W. C. H. Choy. Improving the Stability and Performance of Perovskite Solar Cells via Off-The-Shelf Post-Device Ligand Treatment. *Energy & Environmental Science*, **11**, 8, 2253 (2018). doi: 10.1039/C8EE00580J.

[484] G. Rumbles, M. O. Reese and A. Marshall. *Chapter 1: Reliably Measuring the Performance of Emerging Photovoltaic Solar Cells*. The Royal Society of Chemisty (2017). doi: 10.1039/9781782626749-00001.

[485] K. A. Emery. Solar Simulators and I–V Measurement Methods. *Solar Cells*, **18**, 3, 251 (1986). doi: 10.1016/0379-6787(86)90124-9.

[486] Solar Cell Woes. *Nature Photonics*, **8**, 9, 665 (2014). doi: 10.1038/nphoton.2014.212.

[487] R. B. Dunbar, B. C. Duck, T. Moriarty, K. F. Anderson, N. Duffy, C. J. Fell, J. Kim, A. Ho-Baillie, D. Vak, T. Duong, Y. Wu, K. Weber, A. Pascoe, Y.-B. Cheng, Q. Lin, P. L. Burn, R. Bhattacharjee, H. Wang and G. J. Wilson. How Reliable are Efficiency Measurements of Perovskite Solar Cells? The First Inter-Comparison, Tetween Two Accredited and Eight Non-Accredited Laboratories. *Journal of Materials Chemistry A*, **5**, 43, 22542 (2017). doi: 10.1039/C7TA05609E.

[488] E. Zimmermann, P. Ehrenreich, T. Pfadler, J. A. Dorman, J. Weickert and L. Schmidt-Mende. Erroneous Efficiency Reports Harm Organic Solar Cell Research. *Nature Photonics*, **8**, 9, 669 (2014). doi: 10.1038/nphoton.2014.210.

[489] A. Cravino, P. Schilinsky and C. Brabec. Characterization of Organic Solar Cells: the Importance of Device Layout. *Advanced Functional Materials*, **17**, 18, 3906 (2007). doi: 10.1002/adfm.200700295.

[490] S. Ito, M. K. Nazeeruddin, P. Liska, P. Comte, R. Charvet, P. Péchy, M. Jirousek, A. Kay, S. M. Zakeeruddin and M. Grätzel. Photovoltaic Characterization of Dye-Sensitized Solar Cells: Effect of Device Masking on Conversion Efficiency. *Progress in Photovoltaics: Research and Applications*, **14**, 7, 589 (2006). doi: 10.1002/pip.683.

[491] H. J. Snaith. How Should You Measure Your Excitonic Solar Cells? *Energy & Environmental Science*, **5**, 4, 6513 (2012). doi: 10.1039/C2EE03429H.

[492] H. J. Snaith. The Perils of Solar Cell Efficiency Measurements. *Nature Photonics*, **6**, 6, 337 (2012). doi: 10.1038/nphoton.2012.119.

[493] A Solar Checklist. *Nature Photonics*, **9**, 11, 703 (2015). doi: 10.1038/nphoton.2015.233.

[494] J.-H. Im, C.-R. Lee, J.-W. Lee, S.-W. Park and N.-G. Park. 6.5 % Efficient Perovskite Quantum-Dot-Sensitized Solar Cell. *Nanoscale*, **3**, 10, 4088 (2011). doi: 10.1039/C1NR10867K.

[495] J. M. Ball, M. M. Lee, A. Hey and H. J. Snaith. Low-Temperature Processed Meso-Superstructured to Thin-Film Perovskite Solar Cells. *Energy & Environmental Science*, **6**, 6, 1739 (2013). doi: 10.1039/C3EE40810H.

[496] M. A. Green, Y. Hishikawa, E. D. Dunlop, D. H. Levi, J. Hohl-Ebinger, M. Yoshita and A. W. Ho-Baillie. Solar Cell Efficiency Tables (Version 53). **27**, 1, 3 (2019). doi: 10.1002/pip.3102.

[497] X. Xu, J. Shi, H. Wu, Y. Yang, J. Xiao, Y. Luo, D. Li and Q. Meng. The Influence of Different Mask Aperture on the Open-Circuit Voltage Measurement of Perovskite Solar Cells. *Journal of Renewable and Sustainable Energy*, **7**, 4, 043104 (2015). doi: 10.1063/1.4926481.

[498] A. M. Goodman and A. Rose. Double Extraction of Uniformly Generated Electron-Hole Pairs from Insulators with Noninjecting Contacts. *Journal of Applied Physics*, **42**, 7, 2823 (1971). doi: 10.1063/1.1660633.

[499] S. Albrecht, W. Schindler, J. Kurpiers, J. Kniepert, J. C. Blakesley, I. Dumsch, S. Allard, K. Fostiropoulos, U. Scherf and D. Neher. On the Field Dependence of Free Charge Carrier Generation and Recombination in Blends of PCPDTBT/PC70BM: Influence of Solvent Additives. *The Journal of Physical Chemistry Letters*, **3**, 5, 640 (2012). doi: 10.1021/jz3000849.

[500] M. W. Denhoff and N. Drolet. The Effect of the Front Contact Sheet Resistance on Solar Cell Performance. *Solar Energy Materials and Solar Cells*, **93**, 9, 1499 (2009). doi: 10.1016/j.solmat.2009.03.028.

[501] M. Seeland and H. Hoppe. Comparison of Distributed vs. Lumped Series Resistance Modeling of Thin-Film Solar Cells and Modules: Influence on the Geometry-Dependent Efficiency. *Physica Status Solidi (a)*, **212**, 9, 1991 (2015). doi: 10.1002/pssa.201431886.

[502] P. Schilinsky, C. Waldauf, J. Hauch and C. J. Brabec. Simulation of Light Intensity Dependent Current Characteristics of Polymer Solar Cells. *Journal of Applied Physics*, **95**, 5, 2816 (2004). doi: 10.1063/1.1646435.

[503] S. A. Gevorgyan, J. Eggert Carlé, R. Søndergaard, T. Trofod Larsen-Olsen, M. Jørgensen and F. C. Krebs. Accurate Characterization of OPVs: Device Masking and Different Solar Simulators. *Solar Energy Materials and Solar Cells*, **110**, 24 (2013). doi: 10.1016/j.solmat.2012.11.020.

A. Publications and Conference Contribution

Peer-reviewed Publications

1. **D. Kiermasch**, L. Gil-Escrig, A. Baumann, H. J. Bolink, K. Tvingstedt and V. Dyakonov. High open-circuit voltages above 1.18 V in planar perovskite solar cells due to post-annealing: insights into charge carrier dynamics from transient electrical techniques. *In preparation* (2020)
2. J. Höcker, **D. Kiermasch**, P. Rieder, K. Tvingstedt, A. Baumann und V. Dyakonov. Efficient Solution Processed, $CH_3NH_3PbI_3$ Perovskite Solar Cells with PolyTPD Hole Transport Layer. *Zeitschrift für Naturforschung A*, 74, 8, 665-672 (2019) DOI: 10.1515/zna-2019-0127
3. **D. Kiermasch**, L. Gil-Escrig, A. Baumann, H. J. Bolink, V. Dyakonov and K. Tvingstedt. Unravelling steady-state bulk recombination dynamics in thick efficient vacuum-deposited perovskite solar cells by transient methods. *Journal of Materials Chemistry A*, 7, 14712 (2019). DOI: 10.1039/c9ta04367e
4. **D. Kiermasch**, L. Gil-Escrig, H. J. Bolink and K. Tvingstedt. Effects of Masking on Open-Circuit Voltage and Fill Factor in Solar Cells. *Joule*, 3, 16-26 (2019) DOI: 10.1016/j.joule.2018.10.016
5. **D. Kiermasch**, A. Baumann, M. Fischer, V. Dyakonov and K. Tvingstedt. Revisiting lifetimes from transient electrical characterization of thin film solar cells; a capacitive concern evaluated for silicon, organic and perovskite devices. *Energy Environmental Science*, 11, 629-640 (2018) DOI: 10.1039/c7ee03155f
6. L. Kudriashova, **D. Kiermasch**, P. Rieder, M. Campbell, K. Tvingstedt, A. Baumann, G. V. Astakhov and V. Dyakonov. Impact of Interfaces and Laser Repetition Rate on Photocarrier Dynamics in Lead Halide Perovskites. *Journal of Physical Chemistry Letters*, 8, 19, 4698-4703 (2017) DOI: 10.1021/acs.jpclett.7b02087

7. K. Tvingstedt, L. Gil-Escrig, C. Momblona, P. Rieder, **D. Kiermasch**, M. Sessolo, A. Baumann, H. J. Bolink and V. Dyakonov. Removing Leakage and Surface Recombination in Planar Perovskite Solar Cells. *ACS Energy Letters*, 2, 2, 424-430 (2017) DOI: 10.1021/acsenergylett.6b00719
8. **D. Kiermasch**, P. Rieder, K. Tvingstedt, A. Baumann and V. Dyakonov. Improved charge carrier lifetime in planar perovskite solar cells by bromine doping. *Scientific Reports*, 6, 39333 (2016) DOI: 10.1038/srep39333

Contributed Talks

1. Identifying recombination dynamics in efficient perovskite solar cells with transient opto-electrical techniques via active layer thickness alteration. *DPG Frühjahrstagung*, Regensburg (2019)
2. Recombination dynamics in hybrid perovskite solar cells probed by electrical time-resolved methods. *7th SolTech Conference*, Würzburg (2018)
3. Impact of bromine doping on recombination kinetics in perovskite solar cells. *DPG Frühjahrstagung*, Dresden (2017)
4. Recombination of photogenerated charge carriers in planar methylammonium lead halide perovskite solar cells. *DPG Frühjahrstagung*, Regensburg (2016)

Poster Presentations

1. Charge carrier recombination in planar n-i-p and p-i-n perovskite solar cells – the role of interfaces. *DPG Frühjahrstagung*, Berlin (2018)
   acknowledged with the “**Outstanding Poster Award**” by the DPG
2. Charge carrier recombination in planar n-i-p and p-i-n perovskite solar cells probed by transient electrical techniques. *3rd International Conference on Perovskite Solar Cells and Optoelectronics*, Oxford, UK (2017)
3. Improved charge carrier lifetime in planar perovskite solar cells by bromine doping. *Materials Research Society Fall Meeting*, Boston, USA (2016)
4. Improved charge carrier lifetime in planar perovskite solar cells by bromine doping. *Bundesministerium für Bildung und Forschung – Workshop “Perovskite Photovoltaics”*, Würzburg (2016)

B. Danksagung

An dieser Stelle möchte ich mich bei allen Personen bedanken, die mich während des Studiums und natürlich während der Promotion begleitet, unterstützt und zum erfolgreichen Gelingen dieser Arbeit beigetragen haben. Insbesondere geht der Dank an...

- Prof. Dr. Vladimir Dyakonov für die Möglichkeit die Promotion am Lehrstuhl für Experimentelle Physik VI anzufertigen und das entgegengebrachte Vertrauen in den letzten Jahren, welches mir ermöglicht hat Verantwortung zu übernehmen und eigenständig zu arbeiten. Weiterhin möchte ich dir für die sehr gute Betreuung, die zahlreichen Korrekturen und Verbesserungen zu Publikationen und Vorträgen und die vielen wissenschaftlichen Diskussionsrunden in den Meetings danken, die dabei geholfen haben die eigene Arbeit voran zu bringen auch wenn die Thematik alles andere als einfach war. Ich habe die Zeit hier sehr genossen!
- Dr. Christian Schneider für das Interesse an meiner Arbeit und die unkomplizierte Bereitschaft das Zweitgutachten zu übernehmen.
- Dr. Kristofer Tvingstedt für die zahlreichen Diskussionen und Gespräche sowohl wissenschaftlicher als auch privater Natur. Ich bin dir dankbar, dass du mir dabei geholfen hast Licht ins Dunkel der Messungen und der dazugehörigen Daten zu bringen und dadurch maßgeblich zum Verständnis, welches diese Dissertation versucht zu vermitteln, beigetragen hast. Ich konnte viel über das sorgfältige wissenschaftliche Arbeiten von dir lernen und bin froh mit dir zusammengearbeitet zu haben.
- Dr. Andreas Baumann für die Betreuung in den vergangenen Jahren seit Beginn der Masterarbeit. Du hast mich an die experimentellen Methoden herangeführt und letztlich mein Interesse an Perowskit-Solarzellen geweckt. Ich danke dir für die freundschaftliche Atmosphäre in unserer Arbeitsgruppe und den stetigen Zuspruch von Vertrauen, welcher mir ermöglicht hat auch schwierige Situationen zu meistern. Ich hoffe, dass du deine Gruppenleiterfähigkeiten konservieren und in zukünftigen Aufgaben genauso wieder zum Einsatz bringen kannst.
- the project partners from Valencia Dr. Henk J. Bolink and Lidón Gil-Escrig, who provided numerous samples. Without your solar cells this work would not have been possible. Gracias!

- meine langjährigen Perowskit-Mitstreiter aus dem Büro: Philipp Rieder, Mathias Fischer und Julian Höcker. Ihr habt das Überleben im alltäglichen Kampf mit dem Perowskit überhaupt erst erträglich gemacht und dabei zur Entlastung beigetragen. Ich danke euch für Zusammenarbeit in den vergangenen Jahren und sämtlichen Spaß den wir sowohl innerhalb als auch außerhalb des Büros hatten. Vielen Dank auch an Philipp für die stetige Versorgung mit Frischluft und an Julian und Mathias für die Korrekturen zu dieser Arbeit.
- Christian Kasper für die überragenden Analysen der Transferpolitik aller Fussballvereine und der aktuellen Entwicklungen in der Automobilindustrie. Danke auch an Nikolai Bunzmann und Sebastian Weißenseel für die gemeinsame Zeit und sämtliche Unternehmungen, wie das Fussball spielen oder das Analysieren der Dart WM. Vielen Dank auch an Liudmila Kudriashova für die abwechslungsreichen Diskussionsthemen und das Erstellen von psychologischer Gutachten, weshalb der Gang in die Mensa jeden Tag aufs neue interessant war. Ihr alle seid zu echten Freunden geworden!
- die Bacheloranden und Masteranden, die ich betreuen durfte.
- Dr. Andreas Sperlich für die Hilfe rund um IT-Probleme sämtlicher Art und viele Gespräche unterschiedlichster Natur.
- André Thiem-Riebe für den reibungslosen Ablauf im Labor. Vieles wäre ohne deine Hilfe und deinen Einsatz nicht möglich gewesen. Danke auch an Valentin Baianov für die Hilfe bei der Laserjustage und den optischen Aufbauten.
- Diep Phan für die blitzschnelle Lösung sämtlicher organisatorischer Hürden. Der Lehrstuhl kann sich glücklich schätzen so einen sicheren Rückhalt zu haben.
- das ZAE und Stephan Braxmeier für die Elektronenmikroskopaufnahmen.
- die zahlreichen Personen, die nicht namentlich erwähnt sind und die gesamte Experimentelle Physik VI für die kollegiale Zusammenarbeit und das beste Arbeitsklima, dass man sich nur wünschen kann. Die vielen Unternehmungen, wie z.B. das Lasertag spielen, haben zur Abwechslung vom Alltag beigetragen.
- an Alle, die mich auch außerhalb der Universität diesen langen Weg über begleitet haben. Vielen Dank auch an Yannik und Clare für die Korrekturen.

Zum Schluss gilt ein großer Dank natürlich auch meiner Familie, insbesondere meinen Eltern und meinem Bruder ohne die das Studium nicht möglich gewesen wäre. Vielen Dank dafür, dass ihr mir den Rücken freigehalten habt und ich mich vollständig auf das Wesentliche konzentrieren konnte. Nicht zuletzt geht auch ein besonderer Dank an dich, Isabell, dafür dass du diesen Weg gemeinsam mit mir gegangen bist und mich jederzeit dabei unterstützt hast.